LNGS Laboratori Nazionali del Gran Sasso
CERN European Laboratory for Particle Physics

CERN/SPSC 2002-027
SPSC-P-323
August 7, 2002

A Second-Generation Proton Decay Experiment and Neutrino Observatory at the Gran Sasso Laboratory

By the ICARUS Collaboration

LNGS Laboratory Nazionali del Gran Sasso
CERN European Laboratory for Particle Physics

CERN/SPSC 2002-027
SPSC-P-323
August 7, 2002
Updated from
LNGS-EXP 13/89 add. 2/01
ICARUS-TM/2001-09
November 26, 2001

THE ICARUS EXPERIMENT

A Second-Generation Proton
Decay Experiment
and
Neutrino Observatory at
the Gran Sasso Laboratory

ADDENDUM:

Cloning of T600 modules to reach the design sensitive mass

(This document appeared as an Addendum to LNGS proposal LNGS-94/99 I&II)

by the ICARUS Collaboration

Abstract

The study of very rare nuclear signals, like those related to the neutrino interactions, requires the use of very massive detectors , better if characterized by a granularity as thin as possible. The liquid Argon "Time Projection Chamber" (TPC) technology gives an answer to this problem. Since 1985, the ICARUS Collaboration has been developing the TPC innovative technique for nuclear particle detection. The first Proposal of Experiment, presented in 1985, described a very big monolithic detector (4500 m^3) to be installed in the Hall C of the LNGS. After a long R&D activity, in 1994 an upgraded version for a 4000 m^3 detector was published and later, in 1997, a Revised Version was presented, introducing the concept of "modularity". A number of test devices with rising dimensions have been successfully tested over the years. Recently, a 270m^3 detector (ICARUS T600) has been tested, with fully satisfactory results. ICARUS can now be considered ready for the experimental applications.

We propose to concentrate the activities of the ICARUS Collaboration in the near future along two main parallel lines:

1. the transport of the first T600 module to the LNGS: the first part of the physics programme will include the collection of a substantial number of atmospheric neutrino events, a first search for proton decay with a background-free technique, and a detection of ^{8}B solar neutrinos. This work is essential in order to understand better the performance of this type of detector with actual physics events and to bring to maturity the LAr technology in an underground laboratory, including backgrounds, actual event signatures and, very important, all the specific operational and safety aspects.

2. Within the framework of the 1997 proposal, and on the basis of the experience of the T600 module, the design and assembly of "clones" of the present prototype module in a series of units, in order to reach the originally foreseen sensitive mass. This is inevitably a graded programme, in which the mass will be increased in a number of successive steps.

Updated Collaboration member list

P. Aprili, F. Arneodo, O. Palamara
Laboratori Nazionali di Gran Sasso, INFN, s.s. 17bis, km 18+910, Assergi (AQ), Italy

B. Babussinov, M. Baldo-Ceolin, S. Centro, D. Gibin, A. Guglielmi, G. Meng, M. Nicoletto, D. Pascoli, F. Pietropaolo, S. Ventura
Dipartimento di Fisica e INFN, Università di Padova, via Marzolo 8, Padova, Italy

A. Badertscher, M. Bischofberger, P. Crivelli, Z. Dai, M. Felcini, Y. Ge, I. Gil-Botella, M. Laffranchi, L. Knecht, S. Navas-Concha, G. Natterer, J. Rico, A. Rubbia, P. Sala[1]
Institute for Particle Physics, ETH Hönggerberg, Zürich, Switzerland

G. Battistoni, D. Cavalli, S. Muraro, T. Rancati
Dipartimento di Fisica e INFN, Università di Milano, via Celoria 16, Milano, Italy

P. Benetti, A. Borio di Tigliole, R. Brunetti, E. Calligarich, R. Dolfini, A. Gigli Berzolari, L. Grandi, F. Mauri, C. Montanari, A. Piazzoli, A. Rappoldi, G.L. Raselli, M. Rossella, **C. Rubbia**[2], D. Scannicchio, C. Vignoli, C. De Vecchi
Dipartimento di Fisica e INFN, Università di Pavia, via Bassi 6, Pavia, Italy

A. Cesana, M. Terrani
Politecnico di Milano (CESNF), Università di Milano, via Ponzio 34/3, Milano, Italy

F. Cavanna, F. Ferri, S. Galli, G. Piano Mortari, E. Segreto
Dipartimento di Fisica e INFN, Università dell'Aquila, via Vetoio, L'Aquila, Italy

P. Cennini, A. Ferrari[3]
CERN, CH 1211 Geneva 23, Switzerland

C. Chen, Y. Chen, K. He, X. Huang, Z. Li, F. Lu, J. Ma, G. Xu, C. Zhang, Q. Zhang, S. Zhen
IHEP – Academia Sinica, 19 Yuqnan Road, Beijing, People's Republic of China

D. Cline, B. Lisowski, N. Makrouchina, C. Matthey, S. Otwinowski, Y. Seo, H. Wang, X. Yang
University of California, Los Angeles, Department of Physics & Astronomy, Los Angeles, CA 90095-1547, USA

P. Picchi[4]
Dipartimento di Fisica, Università di Torino, Torino, Italy

---

[1] On leave of absence from Dipartimento di Fisica e INFN, Università di Milano, via Celoria 16, Milano, Italy.

[2] Spokesman

[3] Also at Dipartimento di Fisica e INFN, Università di Milano, via Celoria 16, Milano, Italy.

[4] Also at Laboratori Nazionali di Frascati (LNF), INFN, Frascati, Italy and IFSI del CNR sezione presso LNF.

G. Mannocchi[5]
Laboratori Nazionali di Frascati (LNF), INFN, Frascati, Italy

L. Periale[6]
IFSI (CNR), Sezione di Torino, Torino, Italy

F. Sergiampietri[7]
INFN Sezione di Pisa, via Livornese 1291, 56100 San Piero a Grado (PI), Italy

B.Bekman, J.Holeczek, J.Kisiel, W.Zipper
Institute of Physics, University of Silesia, Katowice, Poland

M.Markiewicz, W.Półchłopek
Faculty of Physics and Nuclear Techniques, University of Mining and Metallurgy, Kraków, Poland

A.Dąbrowska, M.Stodulski, M.Szarska, A.Zalewska
H.Niewodniczański Institute of Nuclear Physics, Kraków, Poland

M.Wójcik
Institute of Physics, Jagellonian University, Kraków, Poland

T.Kozłowski, E.Rondio, J.Stepaniak, M.Szeptycka, J.Zalipska
A.Sołtan Institute for Nuclear Studies, Warszawa, Poland

B.Badełek, D.Kiełczewska, J.Łagoda
Institute of Experimental Physics, Warsaw University, Warszawa, Poland

M.Daszkiewicz, K.Graczyk, C.Juszczak, J.Sobczyk
Institute of Theoretical Physics, Wrocław University, Wrocław, Poland

H.Kuna-Ciskal
Institute of Mechanics and Machine Design, Cracow University of Technology, Kraków, Poland

Since the LNGS proposal in November 2001, the following Institutes have joined the Collaboration:

S. Amoruso, R. Bruzzese, F. Carbonara, A. Ereditato, G. Fiorillo, G. Mangano, N. Spinelli, R. Velotta
Dipartimento di Fisica e INFN, Università di Napoli, via Cintia ed. G, 80126 Napoli, Italy

X. Wang
Istituto Nazionale di Fisica della Materia, Unità di Napoli, via Cintia ed. G, 80126 Napoli, Italy

A. Bueno
Departamento de Física Teórica y del Cosmos & Centro Andaluz de Física de Partículas Elementales (C.A.F.P.E.), Universidad de Granada, Spain

[5]Also at IFSI del CNR, sezione presso LNF.
[6]Sezione INFN, Torino, Italy.
[7]Also at University of California, Los Angeles, Department of Physics & Astronomy, Los Angeles, CA 90095-1547, USA

Contents

Chapter 1

FOREWORD

The study of very rare nuclear signals, like those related to the neutrino interactions, requires the use of very massive detectors , better if characterized by a granularity as thin as possible. The liquid Argon "Time Projection Chamber" (TPC) technology[1] gives an answer to this problem.

Since 1985, the ICARUS Collaboration has been developing the TPC innovative technique for nuclear particle detection[2]. The liquid Argon in a very pure condition (less then 0.1 part of one billion of contaminant) allows a long "mean lifetime" of the order of the 10^{-3} s of the free electrons, generated in the interactions between charged particles and Argon nuclei ("ionization electrons"). In such a long time an electric field can drift the negative charges through a path, as long as several meters, onto an anode, on which they will dynamically produce a "map" that represents an actual section of the ionizing event produced inside the liquid. The anode, realised as a matrix of wires (few millimeters pitch, arranged in parallel planes and kept at adequate voltages), is continuously sensitive to the signals and thus reconstruct the full 3D pattern of the event.

The first Proposal of Experiment[3], presented in 1985, described a very big monolithic detector (4500 m^3) to be installed in the Hall C of the LNGS. After a long R&D activity[4, 5, 6, 7, 8, 9, 10, 11] in 1994 an upgraded version for a 4000 m^3 detector was published[12] and later, in 1997, a Revised Version was presented[13], introducing the concept of "modularity"[14].

A number of test devices with rising dimensions have been successfully tested over the years[15, 16, 17]. Recently, a $270m^3$ detector (ICARUS T600) has been tested, with fully satisfactory results. ICARUS can now be considered ready for the experimental applications.

We remark that the proposal, on which the T600 is based, has been presented in 1995, far before the decision of the CNGS neutrino beam, although this concept had been discussed by the Collaboration already in the eighties. It is evident that this powerful addition to the LNGS should be exploited within the ICARUS programme. Indeed, the extremely competitive potentialities of the ICARUS detector *also in this domain* have been amply illustrated in a series of submitted documents[18] and are further developed here.

We now propose to concentrate the activities of the ICARUS Collaboration in the near future along two main parallel lines:

- The transport of the first T600 module to the LNGS should start as soon as possible, pending on the realization of the necessary infrastructure in the underground hall. This task will be performed in close connection with the technical staff of LNGS, in particular in order to fulfill the safety requirements. The commissioning of the T600 prototype will be complete once the detector is installed inside the LNGS tunnel and operated for a reasonable period of time in order to collect physics events, which although relatively limited in number, are of physics value because of absence of biases[19]. The first part of the programme will include the collection of a substantial number of atmospheric neutrino events, a first search for proton decay with a background-free technique, and a detection of ^{8}B solar neutrinos. This work is essential in order to understand better the performance of this type of detector with actual physics events and to bring to maturity the LAr technology in an underground laboratory, including backgrounds, actual event signatures and, very important, all the specific operational and safety aspects.

- Within the framework of the 1997 proposal, and on the basis of the experience of the T600 module, the design and assembly of "clones" of the present prototype module in a series of units, in order to reach the originally foreseen sensitive mass. This is inevitably a graded programme, in which the mass will be increased in a number of successive steps. On the basis of the experience acquired in the realization of the first T600 prototype, we believe that four additional modules (T600 equivalent) can be realistically readied for the time of arrival of the CNGS beam, with a mass of the order of 2500 tons. This represents half of the modules depicted in the 1997 figure in Hall B.

Chapter 2

INTRODUCTION

2.1 A multikton liquid Argon TPC

A Liquid Argon time projection chamber (TPC), as developed by the ICARUS Collaboration, working as a electronic bubble chamber, continuously sensitive, self-triggering, with the ability to provide 3D imaging of any ionizing event, together with excellent calorimetric response, offers the possibility to perform complementary and simultaneous measurements of neutrinos, as those of the CERN to Gran Sasso beam (CNGS), those from cosmic ray events, and even those from the Sun and from Supernovae. The same class of detector can also be envisaged for high precision measurements at a neutrino factory and can be used to perform background-free searches for nucleon decays. Hence an extremely rich and broad physics programme, encompassing both accelerator and non-accelerator physics, will be addressed. These will answer fundamental questions about neutrino properties and about the possible physics of the nucleon decay.

2.2 Physics perspectives of a 5 kton detector

Large underground detectors are mandatory to study rare neutrino interactions or to look for the stability of matter via nucleon decay.

The reference mass for such underground detectors is now set by the SuperKamiokande detector, which is of the order of 30 ktons. However, the rather coarse nature of the Cherenkov ring detection is capable to reconstruct only part of the features of the events occurring in the large water volume.

New generation underground experiments are now facing challenges, for which novel and more powerful technologies are required.

The overall performance of an underground detector is primarily determined by two factors: its **total mass** and its **geometrical granularity**. A large total mass is of course of importance, because the number of potential signal events is proportional to it. However, the geometrical granularity, which determines the quality with which signal events can be reconstructed, and hence separated from backgrounds, is equally important, since the significance of the results depends on the total number of signal events observed over the expected background.

The main motivation for putting the ICARUS detector inside the LNGS tunnel is the ability to perform simultaneously accelerator and non-accelerator physics.

An instrumented target of 5 ktons would provide the following:

- *Atmospheric neutrinos*: about one thousand atmospheric electron and muon charged current (CC) events per year and 500 neutral current (NC) atmospheric events. In addition, about 5 tau charged current events per year coming from neutrino oscillations are expected, assuming $\nu_\mu \rightarrow \nu_\tau$ oscillations with $\sin^2 2\theta = 1$ and $\Delta m^2 \approx 10^{-3}$ eV^2.

- *Solar and supernovae neutrinos*: about $16200 \times f_B$ solar neutrino electron scattering and absorption events per year with an electron detection threshold of 5 MeV, where f_B is the Boron flux suppression factor. A supernova at a distance of 10 kpc would produce about 360 events, in a similar energy range.

- *CERN-NGS neutrinos*: A total of 13600 ν_μ CC events per year (4.5×10^{19} pots) and accompanying smaller samples of $\bar{\nu_\mu}$, ν_e and $\bar{\nu_e}$ flavors. In addition, 455 ν_τ CC events for $\nu_\mu \rightarrow \nu_\tau$ oscillations with $\Delta m^2 = 3 \times 10^{-3}$ eV^2 and $\sin^2 2\theta = 1$.

- *Neutrino factory*: 6150 ν_μ CC events for 10^{21} decays of 5 GeV μ^- at a distance of $L = 730$ km; and 1130 ν_μ CC events per 10^{20} decays of 30 GeV μ^- at a distance of $L = 7400$ km (FNAL-LNGS).

- *Nucleon decays*: 3×10^{33} nucleons, which translates into background-free searches up to 2×10^{32} years for $p \rightarrow e^+\pi^0$ and 6×10^{32} years for $p \rightarrow K^+\bar{\nu}$ after 1 year of running.

Chapter 3

THE PERFORMANCE OF LIQUID ARGON IMAGING

3.1 Event Imaging out of liquid Argon

This detector technology, first proposed by C. Rubbia [1] in 1977, combines the characteristics of a bubble chamber with the advantages of the electronic read-out. The detector is essentially a large cryogenic pool equipped with an electronic readout system and it is an ideal device to study particle interactions: it is continuously sensitive, self-triggering, cost effective and simple to build in modular form, sufficiently safe to be located underground (no pressure, no flammable gas, etc.). This detector is also a superb calorimeter of very fine granularity and high accuracy.

The choice of Argon as the liquid medium is justified by the fact that it must be a noble gas in order to permit long electron drifts. Out of the stable 5 noble gases in nature (He, Ne, Ar, Kr and Xe) the first two cannot be used in the liquid form, since a micro-bubble forms around the electron, slowing down the drift process. Of the two remaining liquids, only Argon has reached the industrial exploitation which is commensurate to our task. Argon is a by-product of the liquefaction of air and consequent production of liquid Nitrogen and Oxygen. Argon is relatively abundant since it makes about 0.9% of air. The cost in the liquid form is relatively modest, ≈ 0.5 Euro/kg, corresponding to 0.5 MEuro (0.8 MSF) for 1 kiloton, less than the price of standard iron plates.

After the original proposal, the feasibility of these goals has been amply demonstrated by an extensive R&D programme which included ten years of studies on small volumes prototypes (proof of principle, purification methods, readout schemes, mixtures of Argon-methane, diffusion coefficients, electronics) and five years of studies with several detectors at CERN (purification technology, real events, pattern recognition, event simulations, long duration tests, doping, readout technology). The largest of these devices has a mass of 3 tons. A 50 liters prototype has been exposed to the CERN neutrino beam and, recently, tracks with electron drift paths of about ≈ 140 cm have been obtained. The ICARUS project has now reached an industrial phase, with the construction and the successful test of the T600 (a 600 ton detector for the LNGS) prototype described in Section 3.5.

The following sections of this proposal will be devoted to an in-depth description of the detector principles, the technological break-through that make it feasible and finally

the near term physics programme of the ICARUS collaboration at the LNGS.

3.1.1 Electric detection of ionizing events

The simplest detector of ionizing events consists of a pair of electrodes immersed in a dielectric liquid and connected to a power supply (Figure 3.1). As a consequence of the passage of an ionizing particle, electrons and positive ions are formed and are subject to forces pushing them towards the electrodes with opposite polarities. Let us assume that both electrons and positive ions can move under the influence of the electric field E, with constant velocities $v^-(E) \gg v^+(E)$, and that they have no appreciable attachment to electronegative impurities. The effect of a charged particle passing through the liquid on the external circuit can be estimated from the "work" performed by the electric field in order to keep the charges moving:

$$dW = eE(v^+ + v^-)dt = V_0 i_0 dt \tag{3.1}$$

where i_0 is the current in the circuit. This relation can be written as

$$i_0 = e(v^+ + v^-)/d \tag{3.2}$$

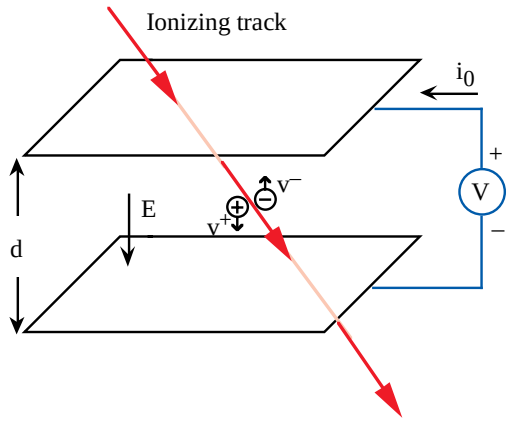

Figure 3.1: Schematic diagram of an electron-ion pair produced inside a plane electrode detector. The current flowing in the power supply is observed.

Note that, contrary to what is naively expected, the current starts to flow immediately after the ion-electron pair has been formed and long before they hit the electrodes. Since the electron mobility is several orders of magnitude larger than that of positive ions, only electrons will contribute significantly to the current:

$$i_0 \approx ev^-/d \tag{3.3}$$

and, therefore, the "free" electron signal is dominant. The signal observed from a single electron starting at position x within the gap is then:

$$Q^-(x) = \int_0^t (d)_t(x) i_0 dt = e\frac{v^-}{d}\frac{(d-x)}{v^-} = e(d-x)/d \tag{3.4}$$

Liquid	Density (g/cm^3)	dE/dx (MeV/cm)	Radiation length (cm)	Collision length (cm)	Boiling point (°C)	Mobility (cm^2/Vs)
Argon	1.394	2.10	14.0	54.8	-185.7	500
krypton	2.410	3.00	4.85	29.0	-153.1	1200
xenon	3.057	3.79	2.77	33.6	-107.1	2200
methane	0.425	1.02	109.4	128.7	-164.0	400
TMS	0.645	1.36	52.4	94.5	26.5	90
TMP	0.720	1.58	62.4	79.2	233.0	40

Table 3.1: Parameters of some liquids with relatively high mobility.

Note that the signal $Q^+(x)$ produced by the positive ion starting at the same place is:

$$Q^+(x) = ex/d \tag{3.5}$$

which ensures that the sum $Q^+ + Q^-$ is always one elementary charge. Because of the much smaller mobility of the ions, the signal Q^+ is spread out over a much larger time, hence the only useful information for imaging is given by Q^-.

The detection of ionizing events in a liquid faces, therefore, two main problems:

1. Signals are very small: typically 1 mm of a minimum ionizing track delivers less than 10^4 electrons in most of dielectric liquids. The signal is even smaller at low electric field because a significant amount of electron-ion pairs recombine immediately after formation (Onsager effect).

2. Liquids must be ultra-pure: an electron in the liquid undergoes about 10^{12} molecular collision per second. Hence impurities with large attachment probability must be kept at very low level, in the order or less that 1 *ppb*, to achieve electron lifetimes in excess of several hundreds microseconds.

The electron's mobility $\mu = v/E$ in several liquids is shown in Table 3.1 (together with some other important properties). One can see that liquified noble gases like Argon, krypton and xenon have very high mobility, indicating that the electrons are essentially free. On the other hand Helium and Neon have incredibly low mobility ($\approx 0.01 cm^2/Vs$). This is due to the fact that in these liquids electrostatic effects around the electronic charge produce a sort of "bubble" which must be carried along with the electron, slowing it down considerably. Methane is the only non-polar hydrocarbon showing mobility very similar to those of noble gases due to its very simple and compact molecular structure. Tetra-methyl-silane (TMS) and tetra-methyl-pentane (TMP) are interesting hydrocarbons because they are liquid at room temperature. Argon is the most widely used cryogenic liquid because it is easily available in large quantity at a reasonably low price.

3.1.2 Imaging of events

The imaging of ionizing events inside the volume of liquid detectors is made possible because of (1) the long lifetime of the drifting electrons (in excess of several milliseconds) and (2) the sensitivity of the modern low noise jFET-input charge sensitive amplifiers that

are capable of sensing the signal due to few thousands electrons (namely the one produced by a few millimeters of minimum ionizing track). The read-out of the information, therefore, follows very closely the techniques used traditionally in the case of ionization chambers, since in both instances there is no gas amplification. However the read-out cannot simply be a charge-collecting process: a non-destructive read-out is necessary to ensure the simultaneous imaging in at least three different views and the determination of the so called t=0 signal. The latter provides the measurement of the absolute drift time hence the distance travelled by the drifting electrons.

A non-destructive read-out can be realized by replacing the plane electrodes with a number of wire planes or grids which are highly transparent to the electrons of the event. The transparency of a grid to electrons drifting along the electric field lines has been calculated in the literature; it is a function of the ratio of the fields E_1 and E_2 in front and behind the grid respectively and of the ratio $\rho = 2\pi r/p$ where r is the wire mesh radius and p is the wire spacing (pitch). For equal field values at both sides of the grid the transparency is given by $1 - 4r/p$, i.e. exactly twice the geometrical cross-section of the grid itself. Full transparency will be reached when the following condition is satisfied:

$$\frac{E_2}{E_1} > \frac{1+\rho}{1-\rho} \tag{3.6}$$

This condition has to be balanced against the requirement that the grid has to act as an electrostatic shielding between the spaces above and below it. If this condition is satisfied, a drifting charge will be sensed by the electrodes below the grid only when the grid itself is crossed. Detailed calculations show that the shielding power, σ, of a grid is approximately given by the following formula:

$$\sigma = \frac{p}{2\pi d} \log\left(\frac{p}{2\pi r}\right) \tag{3.7}$$

where d is the distance between the grid and the next electrode, assumed to be continuous. Note that unshieldings of few percent are acceptable.

The drifting electrons, following the electric field lines, can cross a succession of several planes of stretched wires oriented in different directions (Figure 3.2) where the electrical conditions mentioned above are verified. While approaching a plane, the electrons induce a current only on the wires near which they are drifting; when moving away a current of opposite sign will be recorded. Integrating the current with a charge sensitive amplifier will produce a signal which has an approximately triangular time dependent shape. Due to the shielding of the adjacent grids, the signals have a limited duration. The signals on the wires of the first grid are "prompt", i.e. start as soon as the ionizing particle crosses the chamber. Therefore the initial time $t = 0$ can also be recorded. A detailed analysis of the induced signals for the geometry displayed in Figure 3.2 has been performed by Gatti et al. [20].

A number of significant advantages can be noticed:

1. The very uniform response to single electron produces a signal pulse height proportional to the charge passing through the electrodes (hence a precise measurement of the deposited energy).

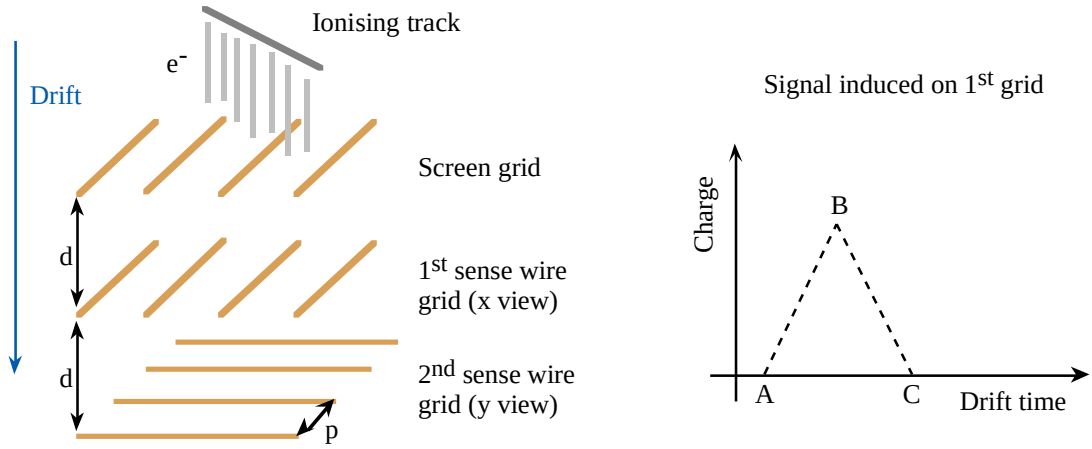

Figure 3.2: Geometry of the grids for multi-dimensional, inductive readout. As an example, the signal induced by drifting electrons on a wire of the 1st grid is also shown: (A) electrons cross the screen grid, (B) electrons cross the 1st sense wire grid, (C) electrons cross the 2nd sense wire grid.

2. The electrostatic separation between sensing wires allows a very sharp localization of the drifting charge (hence a good space resolution).

3. Each of the wire planes of the read-out system provides a two-dimensional projection of the event image where one coordinate is given by the wire position and the other by the drift time (directly proportional, through the electron velocity, to the drift distance). Thus the various projections have a common coordinate (the drift time); this allows the three-dimensional reconstruction of the event. The basic 3-D pixel (or "bubble") size is given by the wire pitch.

4. The drift-time technique and the continuous read-out permit to digitize (by means of flash ADC's) and electronically record the complete image of any ionizing track. Therefore this detection technique is essentially bias free and allows to detect a very broad class of events.

Technical improvements [21] have been made on this basic structure in order to optimize its response to the drifting charges or to increase the mechanical reliability. Nevertheless the principles and performances are not far from the one illustrated here.

3.2 The 3 ton prototype

The first phase of the ICARUS programme has been an intensive R&D activity based on a reasonable scale prototype detector (3 ton) where the feasibility of the LAr TPC has been successfully verified by solving the main technological problems [22].

1. **Argon purification**: Liquid Argon must be ultra-pure, even in the presence of a large number of feedthroughs for the signals and the high voltage and with wire

chambers, cables, etc. in the clean volume. The contamination of electronegative molecules must be kept to around 0.1 *ppb* to allow drifts on long distances (meters) without capture of the ionization electrons. This has been achieved using commercial gas purification systems to remove oxygen and polar molecules (H_2O, CO_2, fluorinated and chlorinated compounds) combined with ultra-high-vacuum techniques to avoid recontamination of the liquid through leaks and with the use of low outgassing materials for the detector components. Electrons lifetime higher than 3 ms ($\approx$ 0.1 ppb) are easily and constantly reachable. Liquid phase purification allows fast filling of large detectors. Continuous recirculation of the liquid through the purifier during normal operation is used to keep the lifetime stable (against micro-leaks and outgassing).

2. **Wire chambers**: The wire chambers must be able to perform non-destructive readout with several wire planes with a few millimeters pitch; they must be built out of non-contaminating materials and must stand the thermal stress of going from room to liquid Argon temperatures; the precision and the reliability of the mechanics must be high and a good knowledge of the electric field in the detector must be granted.

3. **Analogue electronics**: In order to obtain a good signal to noise ratio, very low noise electron preamplifiers must be developed. Since the signal is very small ($\approx$ 10.000 electrons for a minimum ionizing track in a 2 mm wire pitch) the equivalent noise charge must be less than 1000 electrons. This has been reached by means of jFET technology. Since the noise depends on temperature and input capacitance, a further improvement can be obtained placing the preamplifiers in liquid Argon near the sense wires.

4. **Data Acquisition**: The ICARUS detector readout system behaves as a large multi-channel wave form recorder. The digital conversion is performed by means of FADC's continuously active sampling at a rate of 5 MHz. The system effectively stores the charge information collected by each sense wire during a time corresponding at least to the maximum drift time of the electrons (few milliseconds). The high resolution that has to be achieved, both in space and time sampling, brings the size of a single event to over hundreds of kilobytes. The useful signal occupies only a small fraction of the data sample. Although in the initial phases of the experiment the complete information is useful for trouble shooting and debugging purposes, this is the real bottleneck of the whole data taking system, overloading both the on-line and off-line processing. To speed up the performances of the detector and reduce the dead times, a great effort has been devoted to the development of the software architecture and the algorithms for data reduction.

The three ton prototype detector is shown schematically in Figure 3.3. It consists of a cylindrical dewar filled with liquid Argon split vertically into two sections by a frame running along a diameter and holding two wire chambers. Each chamber supports two orthogonal read-out views with 2 mm pitch and a total of 2000 electronic channels. They face, in opposite directions, the active volume where a uniform electric field

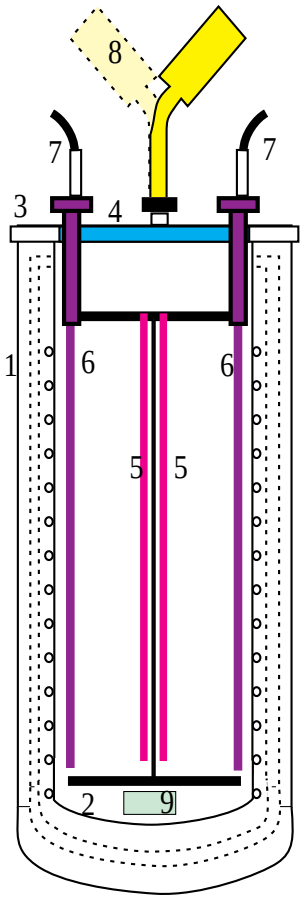

Figure 3.3: Schematic view of the three ton LAr TPC. 1 Outer vessel. 2 Inner vessel. 3 Annular flange. 4 Circular flange. 5 Wire chambers. 6 Cathodes. 7 High voltage feed-throughs. 8 Cooled boxes containing the front end preamplifiers. 9 Purity monitor.

($max. \approx 1kV/cm$) is applied by means of field shaping electrodes. The maximum drift distance is 42 cm.

A large amount of data has been collected with the 3 ton prototype, during more than four years of operation, using cosmic rays and gamma rays sources to study the response of the detector to a wide range of energies (from a few MeV to several GeV).

3.2.1 The readout

The readout is performed with a chamber consisting of three parallel wire planes located at the end of the drift length. We call z the coordinate along the electric field, x and y the coordinates on the plane of the chamber. The absolute z coordinate is given by a measurement of the drift time, provided that $t = 0$ time and drift speed are known.

The drifting electrons reach and cross in sequence the following wire planes:

1. A plane of wires running in the y direction, functioning as the screening grid;

2. A plane of wires (2 mm pitch) running again in the y direction, located at a distance of 2 mm below the screening grid, where its function is to measure by induction the x coordinate (called "induction plane" thereafter);

3. A plane of wires running in the x direction, with 2 mm pitch, located at a distance of 2 mm below the induction plane; its function is to measure the y coordinate. Since this is the last sensitive plane the electric field is arranged to collect the drifting electrons (collection plane).

The ratio of the electric fields above the screening grid (E_1) and between it and the induction plane (E_2) is chosen to achieve full transparency of the grid. Figure 3.4 shows the average charge produced by a minimum ionizing track and collected by the single sense wires as a function of $E_2 : E_1$. As predicted by the Buneman's formula 3.6, full transparency is reached at $E_2 : E_1 = 1.4$. We will discuss data collected at $E_2 : E_1 = 1.5$.

The collection plane is made of sense wires at a 2 mm pitch separated by screen wires. The fields above (E_2) and below the induction plane (E_3) are chosen to assure complete transparency of the induction plane. Figure 3.5 shows the average charge collected by the single sense wires produced by a minimum ionizing track as a function of $E_3 : E_2$. As predicted, full transparency is reached at $E_3 : E_2 = 3.1$. The data to be discussed here have been collected at $E_3 : E_2 = 3.5$.

The current signals from each sense wire of the induction plane and of the collection plane are integrated by charge sensitive preamplifiers. The preamplifiers are located close to the signal feedthroughs to minimize the input capacitance and hence the noise.

For a minimum ionizing track parallel to the chamber the shape of the charge signal from the induction plane is triangular with a maximum of about 6,000 electrons for a 2 mm sample (depending on the field intensity). Figure 3.6 shows an example of a digitized induction signal, where two tracks are present, sampled with a 200 ns period. As expected from our calculations, the induced charge is not the full charge crossing the wire plane, but only 60% of it.

The charge signal from the collection plane is a step function followed by the exponential discharge of the capacitor that holds the charge. The height of the step is around 10,000 electrons for a 2 mm sample. Figure 3.7 shows an example of a digitized collection signal, sampled with a 200 ns period, together with the curve resulting from the filtering and fitting procedure we will describe. Two close tracks contribute to the signal: their distance in time is 4.6 μs (from fit). The drift velocity is 1.24 $mm/\mu s$: the distance between the two tracks along the drift direction is then 5.7 mm. It is clear from the example that the two track resolution is close to the 2 mm length of the gaps between the wire planes. The value of the rise time obtained from fit is 2.4 μs.

We notice that the signal may become very long, several microseconds, if the track has a large dip angle. This requires that the low frequency components must be accepted by the amplifier without distortion.

The capacitance at the input of the amplifiers is the sum of the wire and of the cable capacitances, the latter being the larger. The input capacitance range from 100 pF for the upper collection wires to 200 pF for the induction wires. The corresponding design equivalent noise charge (ENC) evaluated with 1 μs shaping time is ENC (electrons) = 500+2.5 C, where C is the input capacitance in picofarad, corresponding to values

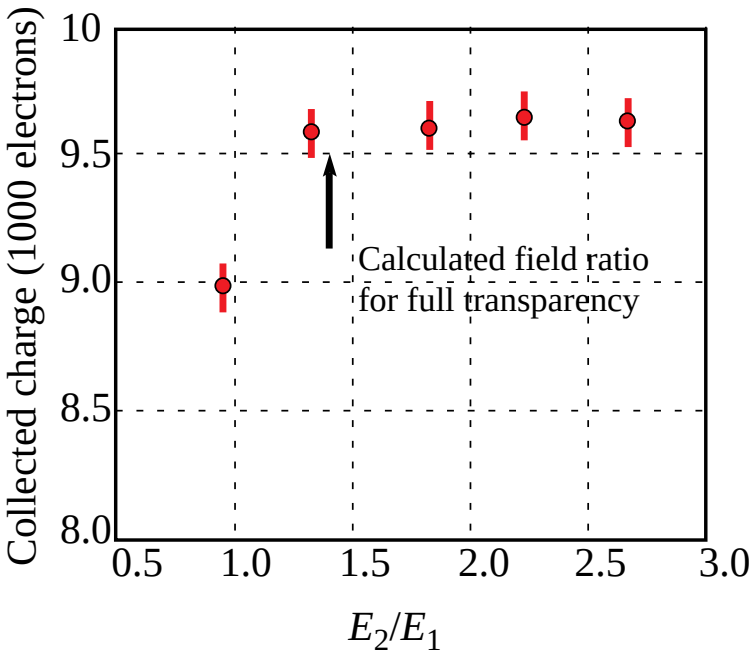

Figure 3.4: Charge collected by the induction wires as a function of the field ratio across the grid.

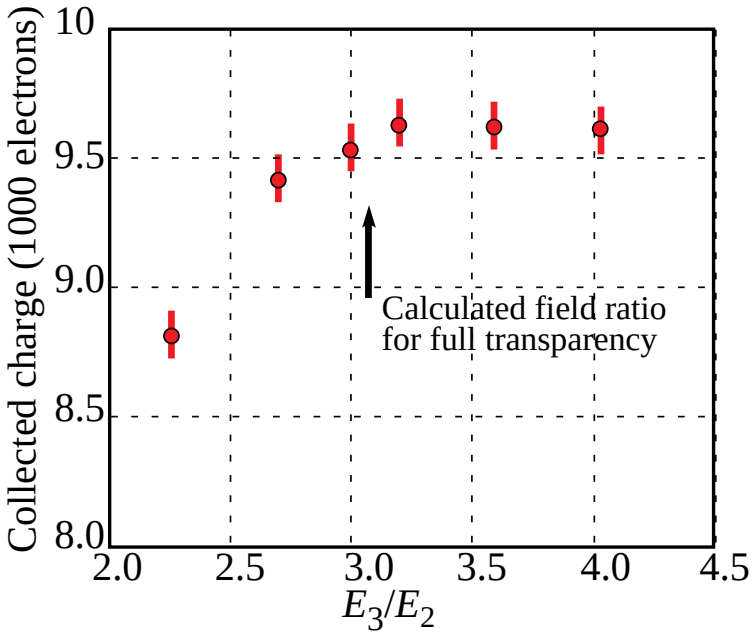

Figure 3.5: Charge collected by the induction wires as a function of field ratio across the induction plane.

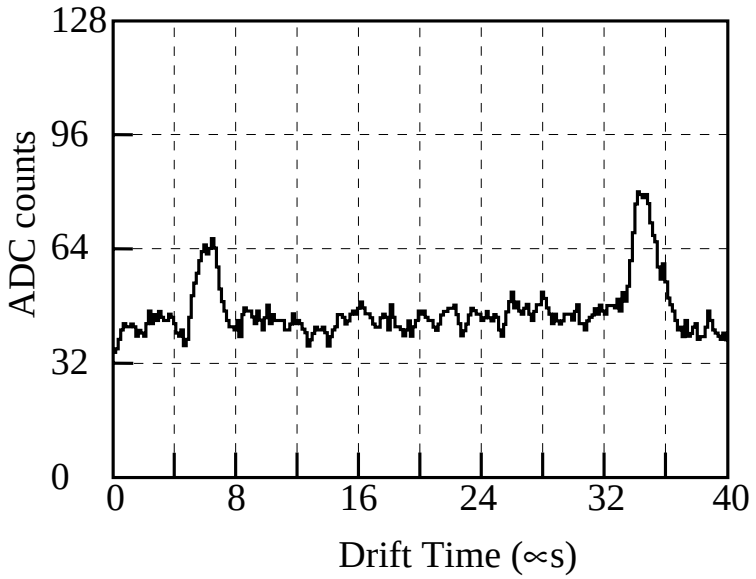

Figure 3.6: A digitized induction signal, showing the presence of two tracks. Sampling period is 200 ns.

between 700 electrons and 1000 electrons. These values have been confirmed by direct measurements on the detector.

The charge signals are sampled with flash ADCs (one per channel) at a frequency that provides several measurements for each pulse. The sampling period ranges from 50 ns to 400 ns; we have used 200 ns period in the data collection described in this work. The complete readout system is described in [20]. The charge measurement calibration is obtained for all channels by injecting the same voltage pulse on test capacitances (one per channel). The test capacitances have been measured with 0.5% accuracy. The gains have been periodically measured and found to be stable within 2%.

Two different types of cross-talk are present between electronic channels. The first one is the cross talk between two contiguous wires: its average value is 1.2%. The second one is due to the structure of our cables. The signals from groups of 8 contiguous wires are brought from the chamber to the amplifiers by specially designed flat cables. A number (32) of these flat cables are sandwiched together to form a stack as described in [1]. The cross talk between a wire in one cable and the octet that it faces is on average 1%.

A good overview of the imaging capability of the LAr TPC is given by the cosmic ray electromagnetic/hadronic shower recorded with the 3 ton prototype and shown in Figure 3.8. The quality of the image (approximately 40×60 cm^2 wide) is of bubble chamber grade. The grey level of the pixels codes the pulse height, proportional to the collected charge. Very fine details of the event are noticeable: the electromagnetic shower is initiated by γ ray, its conversion vertex is visible in the upper-right corner of the picture; a stopping pion decaying into a muon (whose kinetic energy of 3 MeV is deposited within one wire) that in turn decays into an electron are also visible, the increase in ionization near the pion stopping point is evident; heavily ionizing particles, probably low energy protons produced by neutron interactions, accompany the shower; a low energy pair is easily identifiable and measurable (top left); finally, the small black dots are not noise but

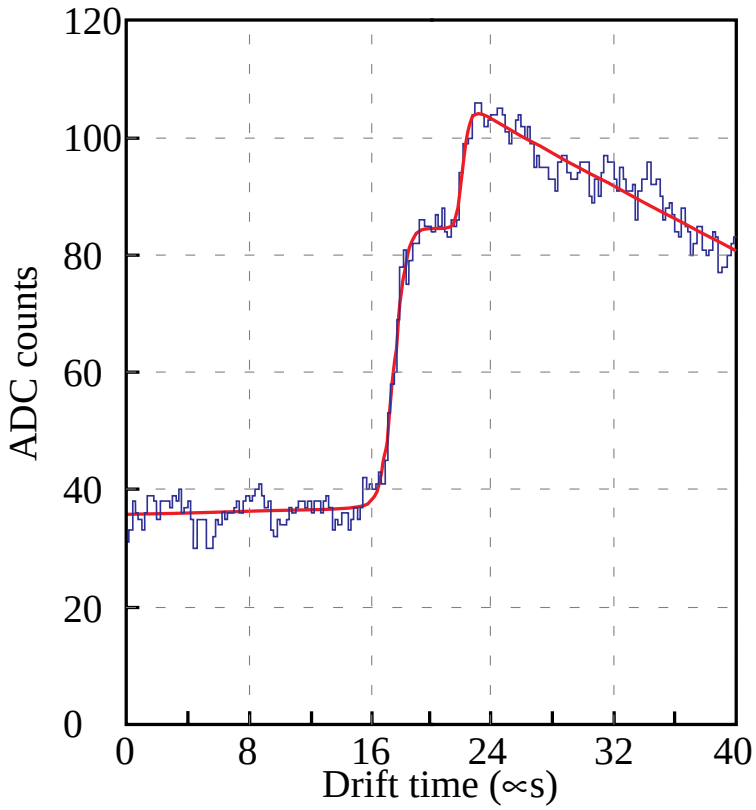

Figure 3.7: A digitized signal from one collection wire due to two tracks separated by 5.7 mm. The curve is the result of the fitting procedure described in the text.

real part of the event: they are Compton electrons with energy around 1 MeV.

The physical parameters characterizing the detector have been found to be consistent with the expectation; their stability in time has been also extensively verified.

1. The electron lifetime was always above 4 ms corresponding to an attenuation length of more than 8 meters (@ 1kV/cm). As a consequence, drift distances of about two meters are reachable without major loss of drifting charge.

2. The electron diffusion coefficient, estimated from the width of signal rise time, is consistent with the value foreseen for thermalized electrons (4 cm^2/s). This means that a point-like charge, after two meters of drift, is spread over less than 1 mm namely less than the wire pitch. Hence the space resolution should not be seriously affected by this factor.

3. The electron drift velocity have been measured as a function of the electric field from 50 to 1000 V/cm. It depends linearly on the field up to 200 V/cm ($\mu = v/E \approx 500\ cm^2/Vs$) then it starts saturating ($v \approx 2\ mm/\mu s$ at 1 kV/cm). The free electron yield (i.e. the fraction of free electrons remaining along a minimum ionizing track after the electron-ion recombination) shows as well a slight dependence on the fields (from 50 to 75 % in the measured range). Both measures indicate that the working electric field can be chosen quite low with clear advantage for the high voltage system when drift of few meters are considered (HV $\approx$ 100 kV).

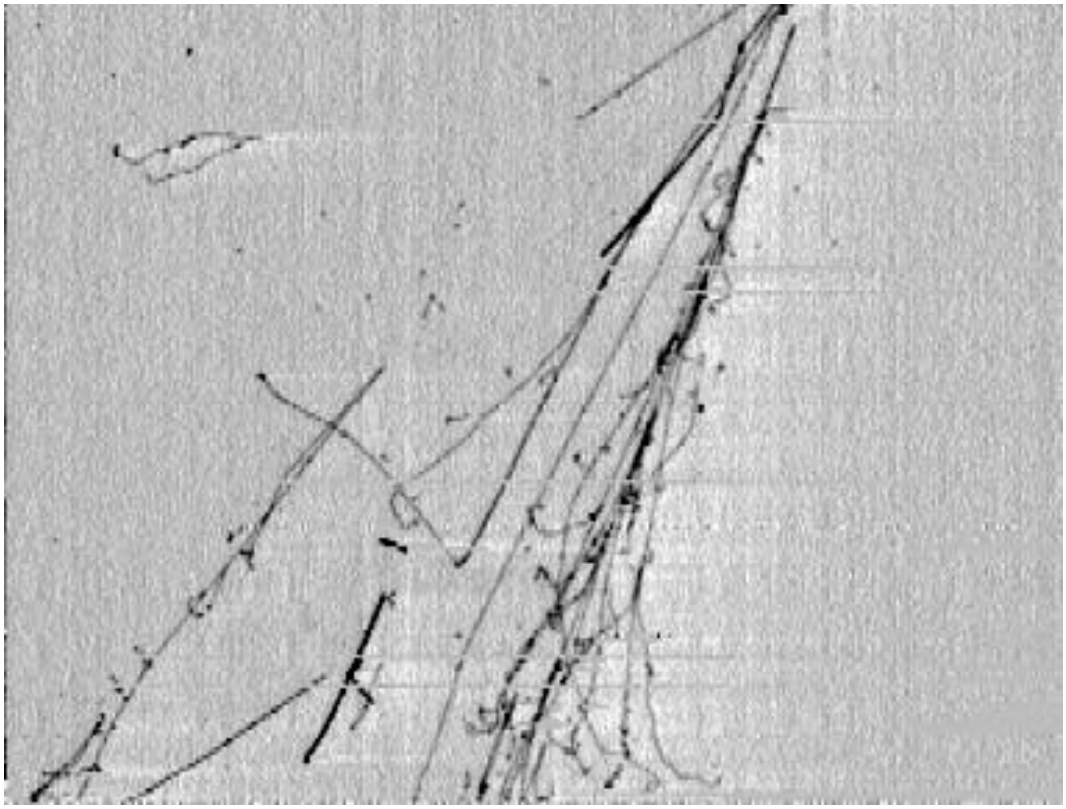

Figure 3.8: Electronic image of a cosmic ray induced shower. The overall drift time (horizontal axis) corresponds to about 40 cm of drift distance. The vertical coordinate is the wire numbering; around 40 cm are shown.

3.2.2 Performance of the 3 ton prototype

The main results concerning the performance of the LAr TPC have been obtained through the analysis of the wide variety of events occurring in the detector [23]. They can be summarized as follows.

(a) Space resolution. Through-going cosmic muons have been used to evaluate the single point space resolution along the drift coordinate. The contribution of multiple scattering has been avoided by taking in turn the drift times measured on any three contiguous collection wires; we then take the distance d from the line through the two outer points to the middle one. The resolution is then $\sigma_z = \sqrt{(2/3 < d^2 >)}$, where $< d^2 >$ is the root mean square value of the distrbution. Values of about 150 μm are the norm and appear to be independent on the field in our range of intensities. Instead they strongly depend on the signal to noise ratio (≈ 10 in our case). In fact specific tests on small scale detectors have shown that resolutions of less that 50 μm are reachable with a signal to noise ratio of ≈ 20. The space resolution on the other two coordinates are strictly related to the wire pitch p: $\sigma_{x,y} \approx p/\sqrt{12}$.

(b) Energy resolution. Always by means of through-going minimum ionizing muons we measured the distribution of the charge deposited over 2 mm. Its width is the

convolution of a Landau function with the gaussian electronic noise and is directly related to resolution on the energy deposited by ionization. A comparison with a test pulse distribution shows that the noise is the main contribution to the width. Hence an energy resolution of $\leq 10\%$ over 2 mm track is the typical value in the 3 ton prototype.

(c) Energy resolution in the MeV range. It has been evaluated by studying the Compton spectrum and the pair production peak produced by a 4.43 MeV monochromatic gamma ray source placed outside the dewar. This spectrum has been fitted with a Monte Carlo simulation including, as a free parameter, smearing caused by the detector response. The best fit gave a resolution of 7% at 4 MeV in agreement with the calorimetric measurement found in the literature.

(d) Particle identification. This very important feature is directly related to the ability of measuring the dE/dx along the range of a stopping particle. A study of cosmic muons and protons stopping in the 3 ton prototype has shown that the charge deposited along the track is not proportional to the energy deposited because of the recombination effect that strongly depends on the ionization density. This non-linear response may degrade the particle identification capability of the LAr TPC.

3.3 The test in the CERN ν beam

The 50 liter liquid Argon TPC is a detector built and successfully operated at CERN for R&D purposes within the ICARUS programme. In the year 1997 it has been exposed at the CERN neutrino beam for the entire SPS neutrino run period as proposed and approved at the SPSLC of January 1997 [24]. The detector, complemented with scintillators acting as veto, trigger counters and pre-shower counters, was installed in front of the NOMAD detector. The year 1997 was scheduled to be the last for the operation of the West Area Neutrino Facility. It was important to take this last opportunity for a parasitic exposure, which did not interfere with running experiments, of an already existing and operating liquid Argon TPC. As we had expected, the collected data brought important information for a better understanding of the performance of liquid Argon TPC's which should be useful for the entire ICARUS programme.

The exposure of the prototype has given a substantial sample of quasi-elastic $\nu_\mu + n \rightarrow p + \mu^-$ events. In addition, further experience with real neutrino events has been gained. This experience has provided general information useful for the study of atmospheric neutrinos, proton decay and high energy neutrinos from CERN. For example the test has led to the optimization of the readout chain in view of best extracting the features of these events.

3.3.1 The 50 liter TPC

The detector structure consists in a stainless steel cylindrical main vessel, 70 cm diameter, 90 cm height, whose upper face is an UHV flange housing the feedthrough's for vacuum, liquid Argon filling, high voltages and readout electronics. Inside the main vessel an

ICARUS type liquid Argon TPC is mounted. The TPC has the shape of a parallelepiped whose opposite horizontal faces (32×32 cm^2) act as cathode and anode, while the side faces, 47 cm long, support the field-shaping electrodes. The mass of the liquid Argon contained in the active volume is 65 kg.

The readout electrodes, forming the anode, are two parallel wire planes spaced by 4 mm. Each plane is made of stainless steel wires, 100 μm diameter and 2.54 mm pitch. The first plane (facing the drift volume) works in induction mode while the second collects the drifting electrons. The wire direction on the induction plane runs orthogonally to that on the collection plane (cfr. with the ICARUS 600 ton set-up where the three planes are foreseen at 60^o to each other). The wire geometry is the simplest version of the ICARUS readout technique [25] since both the screening grid and field wires in between sense wires have been eliminated. The wires are soldered on a vetronite frame which supports also the high voltage distribution and the de-coupling capacitors.

The front-end electronics for the 256 read-out channels is mounted directly on the frame in order to minimize the input capacitance of the preamplifiers which are foreseen to work immersed in liquid Argon [26].

The cathode and the field shaping electrodes have been obtained with a printed board technique. The wires were soldered on a vetronite frame, which supported also the voltage distributions and the de-coupling capacitors. The front-end electronics was mounted directly on the wire frame in order to reduce the input capacitance of the preamplifiers, which were designed to work immersed in liquid Argon. A quasi-current configuration of the electronic chain was adopted with a RC constant of $\approx 3\ \mu s$. The cathode and the field shaping electrodes were obtained by metallization of vetronite boards. The boards were glued on honeycomb structure to ensure rigidity. The field shaping electrodes were horizontal strips, 1.27 cm wide, spaced 2.54 cm. A high voltage divider, made of a series of 14 MOhm resistors interconnecting the strips, supplied the correct voltage to the strips. The drift high voltage ($< 15kV$) was brought to the cathode by a commercial ceramic feedthrough.

The whole main vessel is immersed in a thermal bath of commercial liquid Argon, contained in an open air stainless steel dewar. The Argon evaporation from the open-air dewar is about 50 liters/day. The detector is equipped with a standard ICARUS recirculation-purification system [27]. The full set-up was already tested and successfully operated in CERN for R&D purposes.

The layout of the experimental setup is sketched in Figure 3.9. Since muon identification and momentum measurement were essential for the studies we wished to perform, the chamber had to be complemented with a muon identifier and a spectrometer. Together with the NOMAD collaboration we came to the conclusion that the NOMAD detector could perform these tasks.

Given the size of the TPC and the radiation length of liquid Argon ($X_0 = 14$ cm), π^0's produced in neutrino interactions may escape detection, thus $\mu - p - \pi^0$ events, with undetected π^0, could fake quasi-elastic interactions with large missing P_T. The installation of a pre-shower counter downstream of the TPC was implemented in order to attempt to identify gammas leaving the chamber.

The detector has been installed in CERN hall 191 between CHORUS and NOMAD detectors. Dewar, Argon purification system, vacuum pumps, veto and trigger

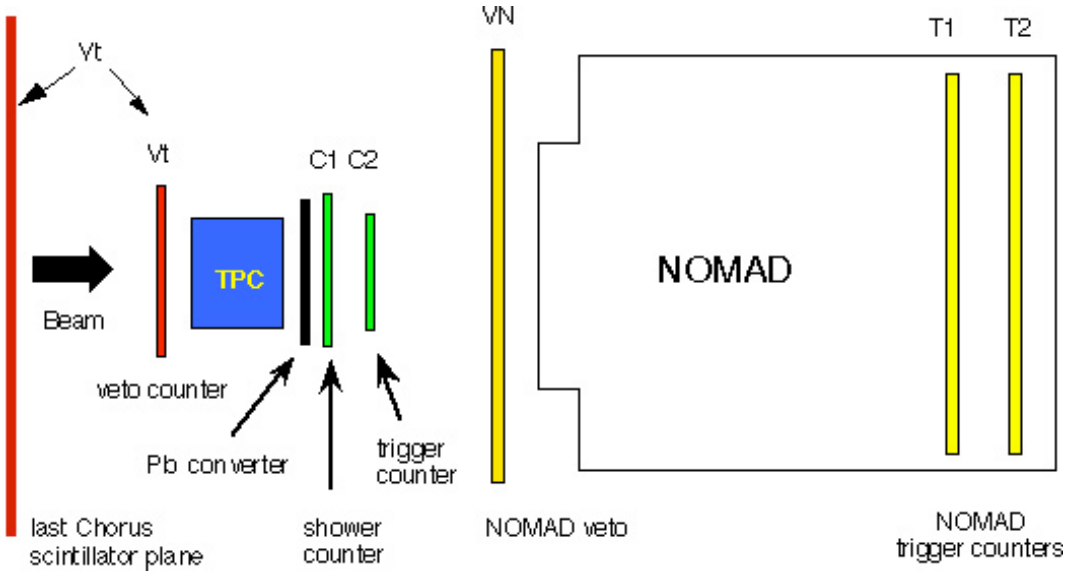

Figure 3.9: Experimental setup of the 50 liter liquid Argon TPC in the CERN ν beam.

scintillators, trigger and readout electronics and data acquisition system, have been placed on a platform at 3.90 m from ground level. An Argon tank of 5000 liters has been installed outside of the hall. Liquid Argon, for periodic re-filling, has been brought from the outer tank to the dewar containing the TPC by isolated pipes running in protected position on the floor of the hall and reaching the platform along its scaffolding.

Immediately upstream of the chamber a double plane of scintillators, acting as a veto counter, have been installed; downstream of the chamber there is a 6 mm thick lead sheet followed by a plane of scintillators, acting as trigger and pre-shower counter.

A standard ICARUS readout of the 256 channels was implemented allowing to acquire up to 4 triggers per neutrino burst. Being the electron drift velocity about 1 mm/μs and the signals sampled by FADC at 400 ns, to span the total drift space one needs about 2 kb per channel or about 600 kb/event.

The events were written in raw-data format without any zero suppression; they were stored locally on disk and automatically transferred to the main CERN tape facility using the network. The trigger of the TPC readout was based on coincidences between the downstream scintillators and the NOMAD muon trigger planes. The upstream scintillators, OR-ed with signals from the CHORUS muon spectrometer scintillator planes were used to veto passing through particles (mostly muons produced by neutrino interactions upstream). At the beginning of each spill NOMAD sent, as pulse trains on standard BNC cables, run number and burst number, which have been recorded by scalers readout by the TPC acquisition system. This allowed off-line matching of events in the TPC with muons reconstructed by NOMAD. For some specific periods of time (calibration, gamma rays source, etc.) we also self-triggered the chamber exploiting the analog-sum of the collection wires.

The dead time of the TPC data acquisition was measured to be lower than 5%, while the NOMAD dead time was around 15%.

3.3.2 Experience with the chamber operation

The detector was filled with ultra-pure liquid Argon flown through the ICARUS purification system in liquid phase (at a rate of 60 liter/hour) [28].

- The initial lifetime was about 100 μs. The recirculation/purification system, circulating about 5 liters of LAr/hour allowed to increase this value to more than 8 ms in three weeks (see Figure 3.10). This performance was excellent since the maximum drift time was 400 μs and therefore the attenuation of the ionization over the drift distance was negligible.
- This purity level was kept stable for all the running period of 9 months.
- The same recirculation system allowed to dissolve in pure LAr a small concentration of TMG (few ppm) necessary to recover the linearity response in deposited energy [29].
- The total LAr consumption necessary to circulate the pure LAr and to compensate the heat losses of the set-up was about 200 liter/day.
- The planned operating value for the drift high voltage was 25 kV to reach the nominal drift field of 500 V/cm. Unfortunately we experienced some instabilities of uncertain origin which forced us to operate at a safe value of 10 kV. We believe that most likely this limitation was due to residual humidity in the HV feedthrough at the level of the LAr interface. In the newly designed feedthrough this problem should not arise. Given the achieved Argon purity and the relatively short drift length, the reduced drift field did not affect significantly the performance of the chamber.
- The new wire chamber configuration appeared to be sound. The visibility of the induction signal was optimized by varying the ratio of the fields in the drift and gap regions.

3.3.3 Experience gained with the front-end electronics

In Figure 3.11 we show, as an example, a neutrino event recorded with the 50 liter LAr TPC exposed at the CERN neutrino beam. From the inspection of many similar events and from the analysis of simulations of neutrino interactions in liquid Argon, we decided to adopt a front-end configuration based on a current amplifier with a feed-back resistance of $R_f = 5\mathrm{M}\Omega$.

With this configuration we obtained a signal-to-noise ratio $S/N = 11$ with *mip* signal equivalent to 10 ADC counts. This choice was satisfactory because the risk of pile-up in events containing electromagnetic showers was highly suppressed. This is essentially due to the fact that the duration of the signal was comparable with the distance between tracks in electromagnetic showers.

A further consequence of the front-end choice was that the digital dynamic range of 8 bits was sufficient even for the case of electromagnetic showers. A detailed analysis of the performance of the adopted front-end scheme can be found in reference [30].

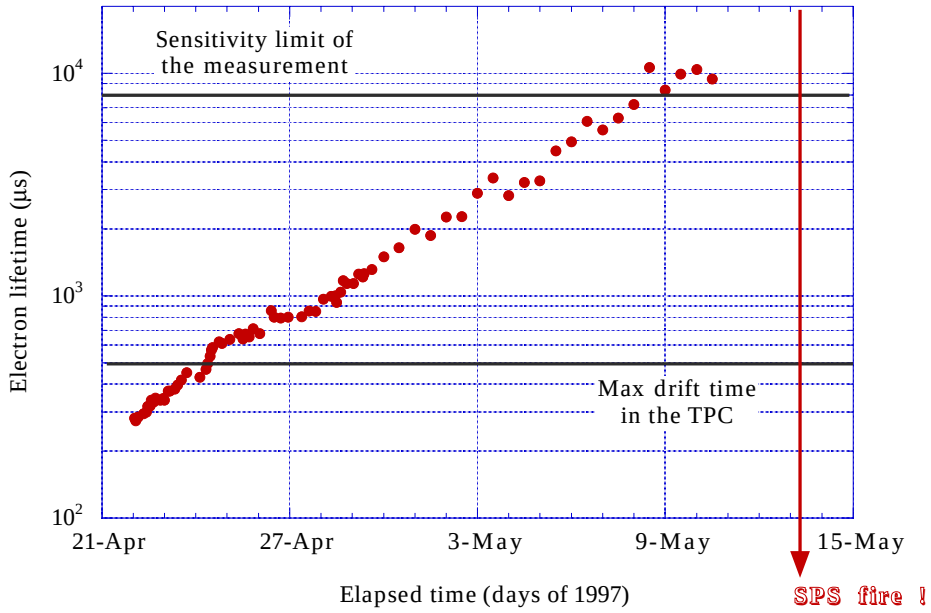

Figure 3.10: Lifetime of the drifting electrons in the 50 liter liquid Argon TPC at the CERN ν beam. The filling of the chamber with LAr was performed on the fourth of April 1997.

3.4 The $10m^3$ prototype

A prototype of 14 t of LAr ("$10m^3$ prototype") was built in 1997. This prototype has undergone several cooling and filling tests in Pavia; this phase successfully ended in July 1999 [31]. The $10m^3$ was then transported to LNGS for a test run[32]. A number of modifications have been performed in order to transform the $10m^3$ from a test facility into a fully operational detector module, including the construction of the HV and field shaping system, cabling of the wires and installation of two PMT's for light detection in LAr. The trigger and T_0 signal was provided either by the coincidence of an external system of scintillator planes, or by Čerenkov and scintillation light collected with the two PMTs placed in the LAr volume. Several cosmic ray data runs have been taken with various field intensities, up to 500 V/cm.

We have acquired a large number of cosmic rays events, with a wide variety of geometrical topologies and different energies. A large number of events with track-length up to about 3.5 m, have been collected using the external trigger system and the internal PMTs trigger.
Combining the information from drift time and hits separately from each of the two wire planes, two views for each event are obtained (as shown, for example, in Fig.3.12 and Fig.3.13).

Figure 3.11: An example of recorded neutrino interaction in the 50 liter liquid Argon chamber prototype located at the CERN ν beam. The neutrino comes from the top of the picture. The horizontal axis is the time axis (drift direction) and vertically is the wire number. The visible area corresponds to $47 \times 32\ cm^2$

Given the different behaviour of collection and induction view waveforms, different fitting functions have been used. The analytical expression for the collection view is the following function of the drift time (t):

$$F_c(t) = A_c \cdot \frac{e^{(t_0-t)/\tau}}{1+e^{(t_0-t)/R_t}} + B_c \tag{3.8}$$

where t_0 is the signal peak time, τ is the signal decay time (mainly dependent on the amplifier decay constant), R_t is the signal rise-time (mainly dependent on the inclination of the track), B_c is the signal baseline and A_c is a normalization factor (depending on the peak pulse height). An example is given in Fig. 3.14. The function chosen and optimized to fit induction view waveforms, which has the peculiarity of describing both unipolar and bipolar shapes, is the following:

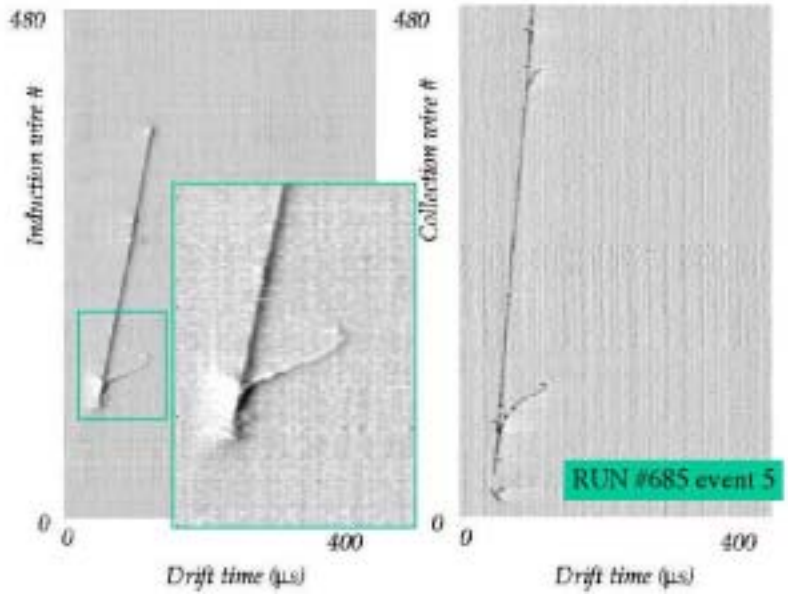

Figure 3.12: Induction and collection views of a muon track with a δ-ray (also shown in the zoom) well separated along the main track.

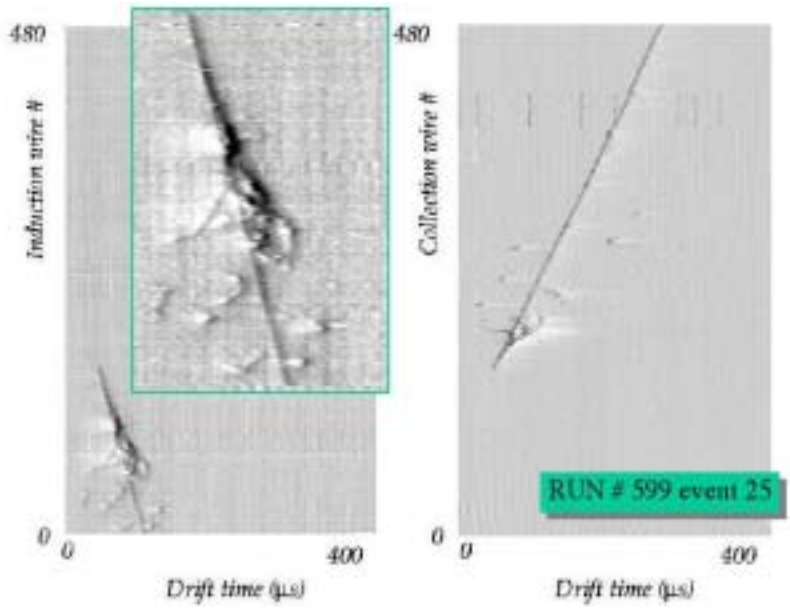

Figure 3.13: Induction and collection views of a muon track, with well distinguished δ-rays.

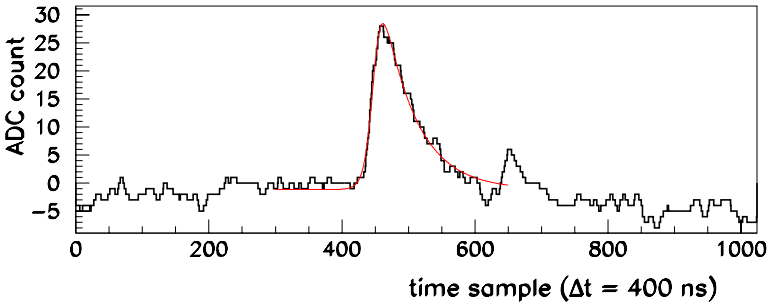

Figure 3.14: Collection view wire waveform. The continuous line shows the result of the fit , in a time window around the Region of Interest (ROI).

$$F_i(t) = A_i \cdot \frac{e^{-(t_0-t)/R_2}}{1+e^{-(t_0-t)/R_1}} \cdot \left[\frac{\frac{e^{-(t_0-t)/R_1}}{1+e^{-(t_0-t)/R_1}}}{R_1} - \frac{1}{R_2}\right] + B_i \tag{3.9}$$

where t_0 is the point of inflection of the function, R_1 is the positive amplitude signal rise-time, R_2 is the negative amplitude signal rise-time, B_i is the signal baseline and A_i is a normalization factor. Examples of the results of the fit are given in Fig. 3.15.

Event reconstruction consists in (1) a pattern recognition stage, based on the search for a set of aligned points amongst the hits selected by the hit finding algorithm, and (2) a linear fit procedure through the aligned hits, to calculate track parameters in a 2D reference frame. To accomplish a 3D reconstruction, we have used an analytical approach: the track in space is obtained combining the two projected tracks parameters (slopes and intercepts), as reconstructed by the tracking algorithm, to obtain the track direction in space. In Fig.3.16 we show, as an example, the 3D reconstruction of a sample of single muon events recorded in one run, triggered by the coincidence of the external system of scintillator planes.

The drift electron lifetime has also been obtained from the collected events, from the level of degradation in the signal amplitude, as a function of the electron drift distance from the wire chamber. After the 3D reconstruction of the events, corrections of the signal amplitude on each wire for the actual track direction in space, give the charge collected per unit track length (dQ/dx). We considered the distribution of dQ/dx measured on the collection wires, as a function of the drift coordinate, dividing the sample of events in bins, 2.5 cm wide, of the measured drift coordinate. For this measurement we have considered separately groups of consecutive runs taken in periods of 24 h each. As an example, in Fig. 3.17 we show the distributions corresponding to the first four slices, relative to one period of data taking. Once this procedure is applied to all slices, the exponential fit

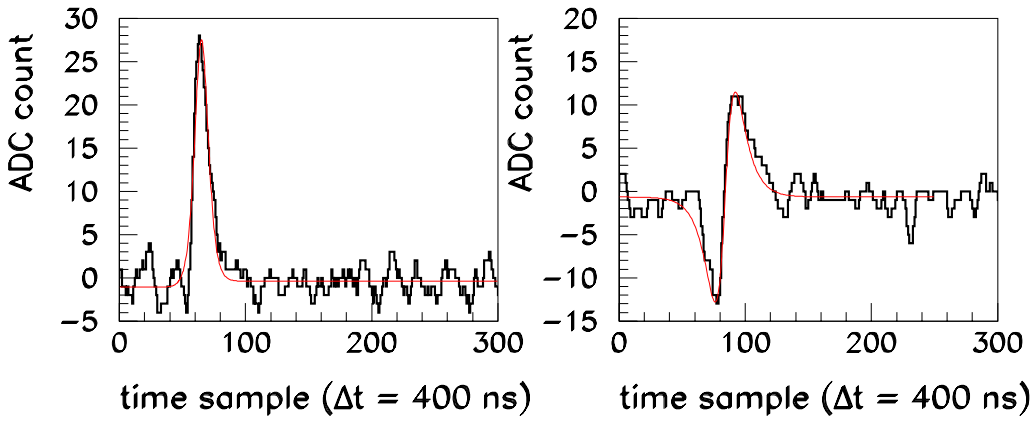

Figure 3.15: Induction view wire unipolar (left) and bipolar (right) waveforms in a time window around the Region of Interest (ROI). The continuous lines show the results of the fit.

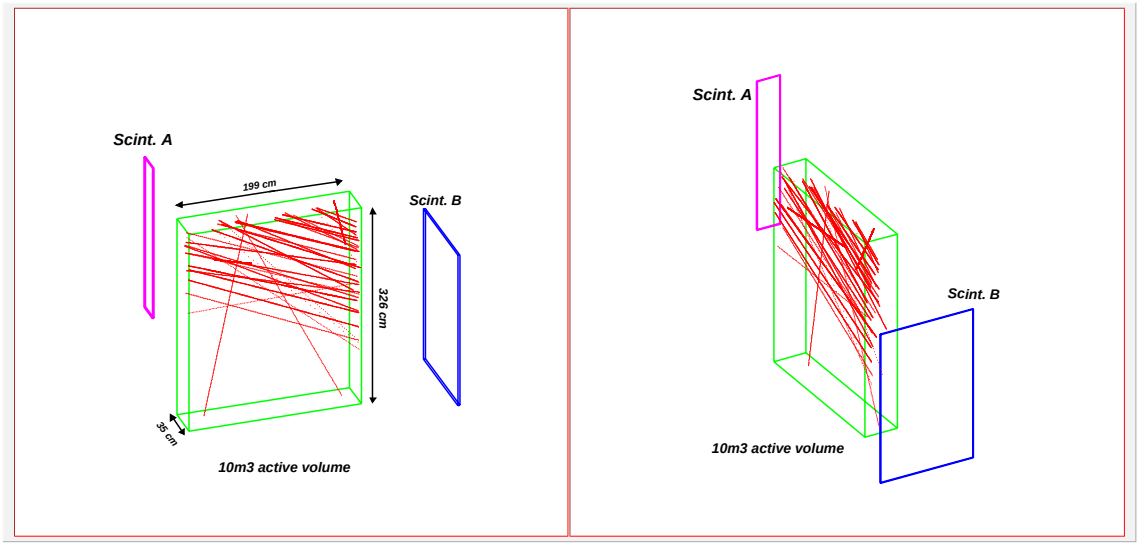

Figure 3.16: 3D reconstruction algorithm: sample of superimposed muon tracks crossing the $10m^3$ active volume (viewed from two different angles), identified by the linear fit procedure. The trigger is provided, in this case, by the external system of scintillator planes (also shown).

of the most probable charge measured per unit track length as a function of the drift coordinate, reported in Fig. 3.18, gives the electron lifetime. The intercept of the fit gives an electron yield of about 5×10^4 e$^-$/cm) and the slope gives an electron mean free path of about 140 cm. For this data sample the measured electron drift velocity is 1.18 mm/μs, therefore the value of the electron lifetimes is $\tau \simeq 1.2$ ms.

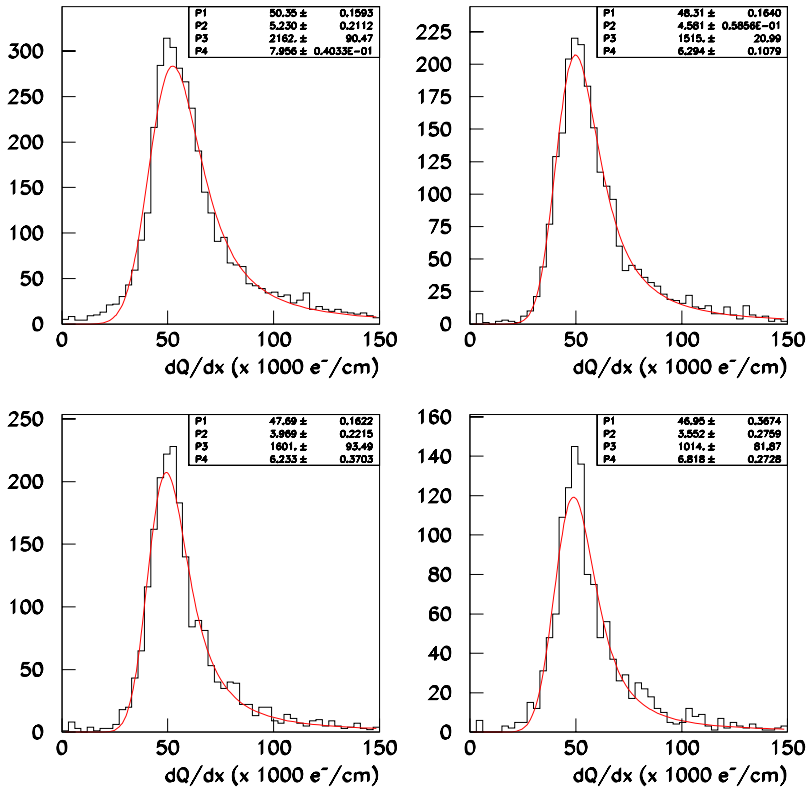

Figure 3.17: Distributions of the charge measured on the collection wires per unit track length in four different ranges of the drift coordinate ($[0, 2.5]$, $[2.5, 5]$, $[5, 7.5]$ and $[7.5, 10]$ respectively), fitted with a Landau-Gaussian function (continuous line). The electronic noise and the electron diffusion contributions (width of the Gaussian distribution) ranges from about (6000 $\div$ 8000) electrons per cm (RMS)

We have then accomplished the calorimetric reconstruction of the events. The electron charge yield in LAr at the passage of an ionizing particle depends on the intensity of the drift electric field[23]. The distribution of dE/dx for the $10m^3$ data sample collected using the internal PMTs trigger system is shown in Fig. 3.19. The result for average energy release in LAr is $< dE/dx_{data} >$=1.91 MeV/cm. This value corresponds to the average energy deposited by a m.i.p. muon in LAr. It does not represent the total energy released in the LAr at the passage of the ionizing particles, since it does not include the energy

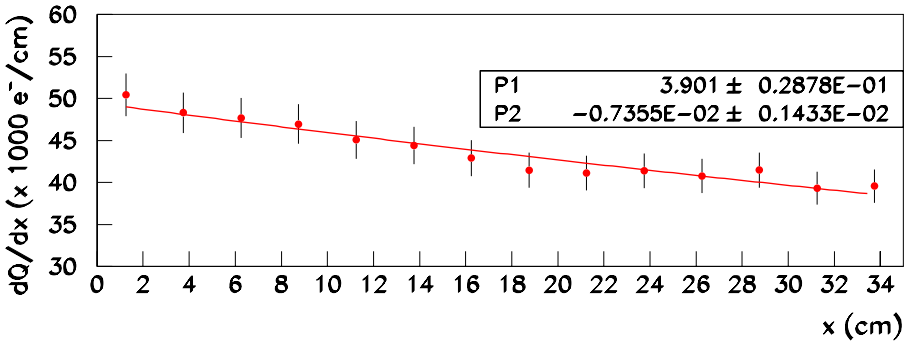

Figure 3.18: Exponential fit of the most probable value of the charge measured on the collection wires per unit track length as a function of the electron drift time. The intercept gives the electron yield ($N_0 = e^{P_1} \simeq 5 \times 10^4$ e$^-$/cm), while the slope gives the inverse of the electron mean free path ($\lambda = 1/P_2 \simeq 140$ cm).

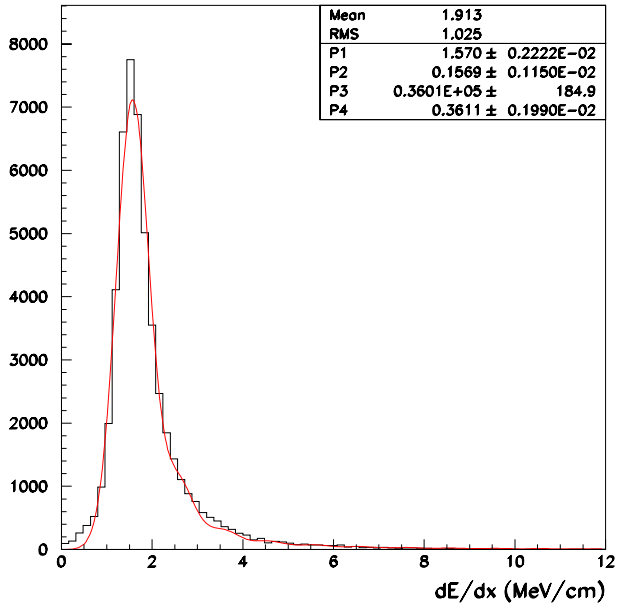

Figure 3.19: Distribution of the energy deposited by m.i.p. muons per unit track length, for the $10m^3$ data collected using the internal PMTs trigger system.

released by δ-rays. In fact the algorithms we have applied to the signal waveforms to identify signal hits and then the hit clustering procedures, through which 2D straight line track projections are identified, select the pattern of the main track, while secondaries are discarded, at this level.

3.5 Performance of the 600 ton prototype

3.5.1 Three views readout

As a consequence of the passage of an ionizing particle through the active LAr volume, electrons and positive ions are formed. They are immediately subject to forces pushing them in the direction parallel to the electric field, towards the electrodes with opposite polarities.

For each wire chamber there are three wire planes, the first, facing the drift region, with horizontal wires, the other two with the wires at $\pm 60^0$ from the horizontal direction. Drifting electrons can be read by several wire planes as the readout is non destructive.

For each plane, the common drift time coordinate and the particular wire coordinate at which the signal is detected, are recorded. Therefore, for every wire plane, the acquired signal can be displayed as a function of the drift and wire coordinates. This produces a two dimensional projection of the event in the plane perpendicular to the considered wire set. Table 3.5.1 summarizes the orientation of the wires and of the produced projection plane (view) with respect to the horizontal, for the different wire planes of the right side wire chamber. For the left side wire chamber, the *Induction II* (60^0) and *Collection* planes orientation changes sign.

In addition, the *Induction I* (0^0) wires (along the z coordinate) are one half the total detector length. Thus, there exist two independent set of wires for the front and the back halves. They produce two independent 90 degrees views, corresponding to each half of the chamber.

Wire plane	Wire orientation (deg)	View orientation (deg)
Induction I	0	90
Induction II	60	-30
Collection	-60	30

Table 3.2: Summary of wire and view orientation for the three wire planes of the right side wire chamber.

3.5.2 Signal shapes

As explained in Section 3.5.1, the drifting electrons, following the electric field lines, can cross a succession of several planes of stretched wires oriented in different directions. While approaching a plane, the electrons induce a current only on the wires near which they are drifting; when moving away, a current of opposite sign will be recorded. The signals on the wires of the first grid (*Induction* plane (0^0)) start as soon as the ionizing particle crosses the detector and the charge is finally integrated in the last plane (*Collection* plane). In this way, each wire of the readout planes senses a segment of track. Some examples of signal shapes recorded in the three wire planes with the T600 detector are presented in the following Sections.

Induction planes:

The current in the first wire plane (*Induction I*) starts to flow immediately after the ion-electron pair has been formed and long before the drifting electrons hit the wire.

The Figure 3.20 is a clear example of this phenomenon. It shows the shape of the signal detected by a wire in terms of ADC counts versus drift time (in 400 ns sampling time units) and corresponds to the detection of a minimum ionizing particle (*mip*). The top figure is the full spectrum of the digitalized signal and the bottom corresponds to a zoom of the interesting region around the peak (at $\sim$3700$\times$400 ns). Looking at the distribution from left to right, one can clearly appreciate how the wire "sees" the charge of the shower approaching, which translates in a negative signal. Then, the drifting electrons cross the wire plane inducing a change on the signal sign (at $\sim$3690$\times$400 ns) that becomes positive. The signal reaches a maximum (35 ADC counts) and then drops down very quickly. Finally, beyond $\sim$3750$\times$400 ns one finds the baseline (10 ADC counts).

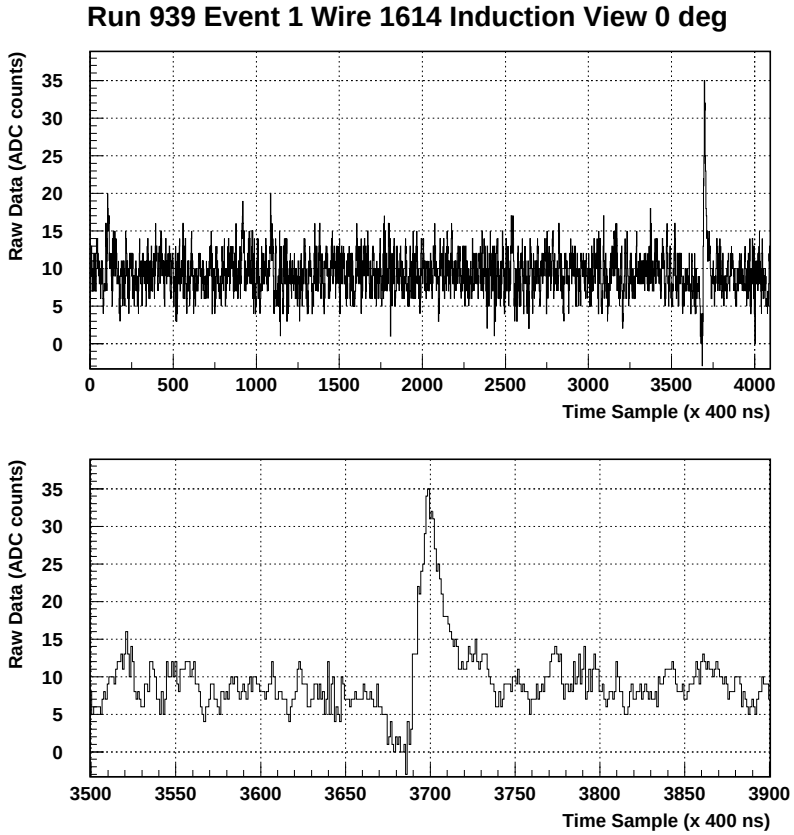

Figure 3.20: Shape of a single hit signal from a *mip* recorded in the *Induction I* plane (0^0), corresponding to wire no.1614 (Run 939, Event 1). The full spectrum (top) and a zoom around the signal peak (bottom) are shown.

The signal generated by the passage of the drifting electrons when crossing the second *Induction* plane is integrated, appearing with a triangular shape. A nice example is shown in Figure 3.21 where the full spectrum (top) and the zoom on the signal peak (bottom)

are shown. The signal, 21 ADC counts over a baseline of 10, corresponds to the passage of a *mip*.

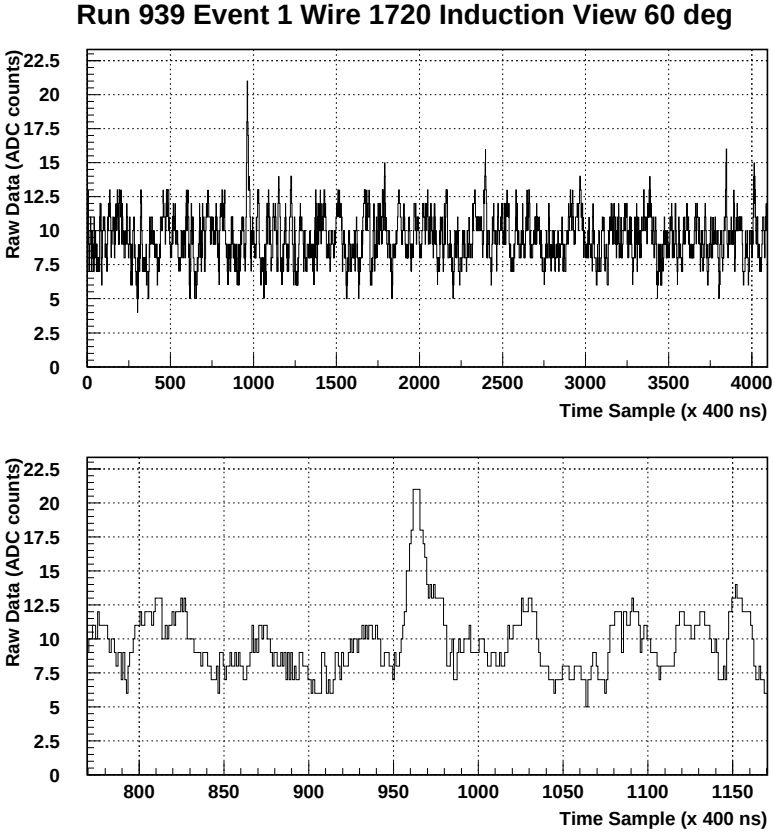

Figure 3.21: Shape of a single hit signal from a *mip* recorded in the *Induction II* plane (60^0), corresponding to wire no.1720 (Run 939, Event 1). The full spectrum (top) and a zoom around the signal peak (bottom) are shown.

Collection plane:

When the drifting electrons reach the last plane (*Collection* plane) they are collected on the wires and give a step signal proportional to the collected charge. Integrating the current with a charge sensitive amplifier will produce a signal which can be approximated by a step function followed by an exponential.

Figure 3.22 shows an example of the signal recorded by a wire in this last plane after the passage of a minimum ionizing particle. A peak of $\sim$27 ADC counts is clearly visible over a baseline of $\sim$10 ADC counts.

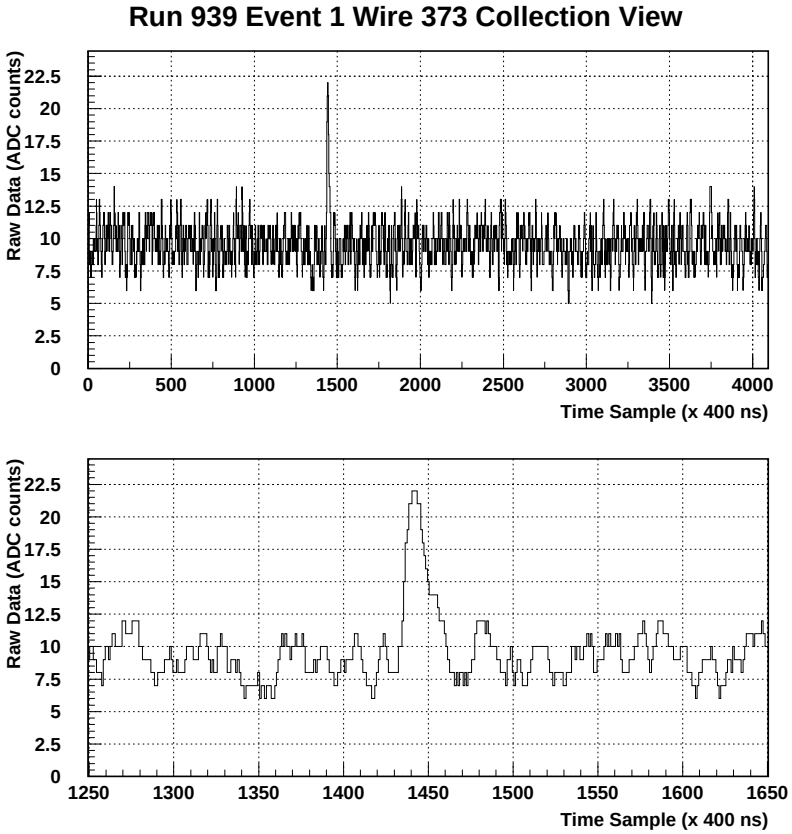

Figure 3.22: Shape of a single hit signal from a *mip* recorded in the *Collection* plane, corresponding to wire no.373 (Run 939, Event 1). The full spectrum (top) and a zoom around the signal peak (bottom) are shown.

The previous examples concerned signals generated by minimum ionizing particles. When detecting electromagnetic or hadronic cascades the signal shapes can be slightly modified. Figures 3.23 and 3.24 are two examples of signal shapes generated by the same electromagnetic cascade (the one shown in Figure 3.43). The first one corresponds to a wire which "sees" the beginning of the cascade, while the second one, with much more detected charge, "sees" the middle of the cascade, getting saturated. They can be compared to the *mip* spectrum (Figure 3.20).

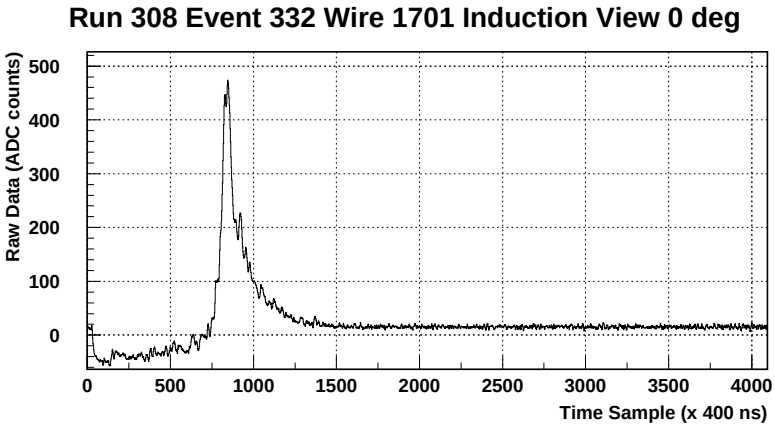

Figure 3.23: Shape of a single hit signal corresponding to an electromagnetic shower recorded in the *Induction I* plane (0^0), corresponding to wire no.1701 (Run 308, Event 332).

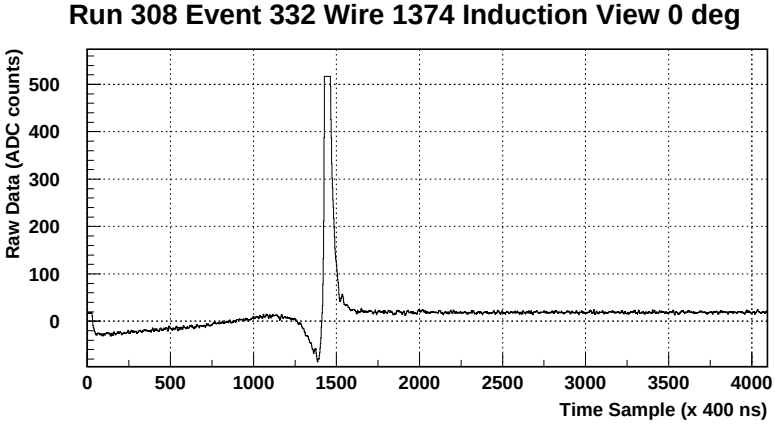

Figure 3.24: Shape of a single hit signal corresponding to an electromagnetic shower recorded in the *Induction I* plane (0^0), corresponding to wire no.1374 (Run 308, Event 332).

Regarding now the *Induction II* plane (60^0), as an example we show the shape of a signal generated by the detection of a hadronic interaction (see Figure 3.37) in Figure 3.25. The under-shoot of the signal after the first jump is a feature of the electronics.

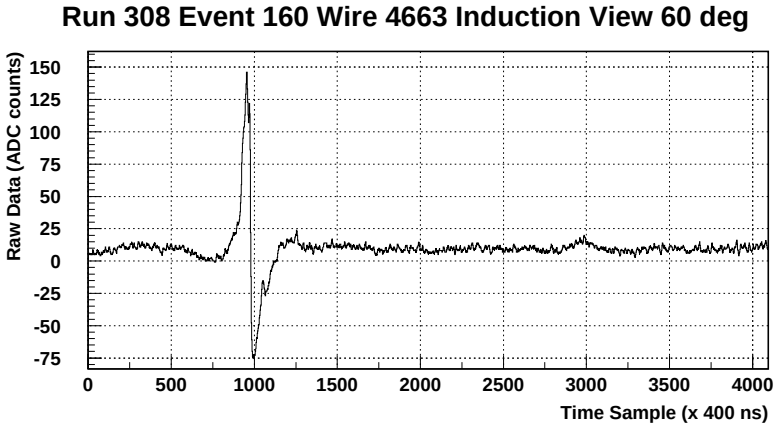

Figure 3.25: Shape of a single hit signal recorded in the *Induction II* plane (60^0), corresponding to wire no.4663 (Run 308, Event 160).

3.5.3 Examples of recorded cosmic data

A full test of the T600 experimental set-up has been carried out in a technical run during 2001. A large statistics of cosmic ray events have been recorded with different configurations of the trigger system. In this Section some kind of events collected during this test are reported and discussed.

Low energy event

Figure 3.26 shows a zoomed region containing a low energy event in the *Induction II* view (60^0). A short track (T_1) can be seen together with two spots of about 0.8 MeV (T_2 and T_3) located in the surrounding area.

The leading track can be an electron spanning over 19 wires in the *Induction II* plane and 30 wires in the *Collection* plane (Figure 3.27). The length of the track is about 11 cm in space. Considering that a *mip* deposits 2 MeV per cm, the energy of this electron track is at least 22 MeV.

The wire near the end point of a track usually collects more charge than the one close to the main vertex. The view of the event in the *Collection* plane shows that the end point corresponds to a drift time of 0.73 ms (left end of the track).

The electron track enters the detector and crosses the wire plane, producing a negative signal when the charge is before the plane ("white" wires at the right end of the track) and a positive signal as soon as the track traverses the plane.

The two spots of 0.8 MeV near the electron track in the *Induction II* view could be associated to Compton electrons coming from the same main vertex (right end of the leading track). However, the spot corresponding to a drift time of 0.97 ms (T_3) is not in the vicinity of the leading electron track in the other views. Therefore, it cannot be the Compton conversion of a gamma generated at the same vertex as the electron, but an independent track.

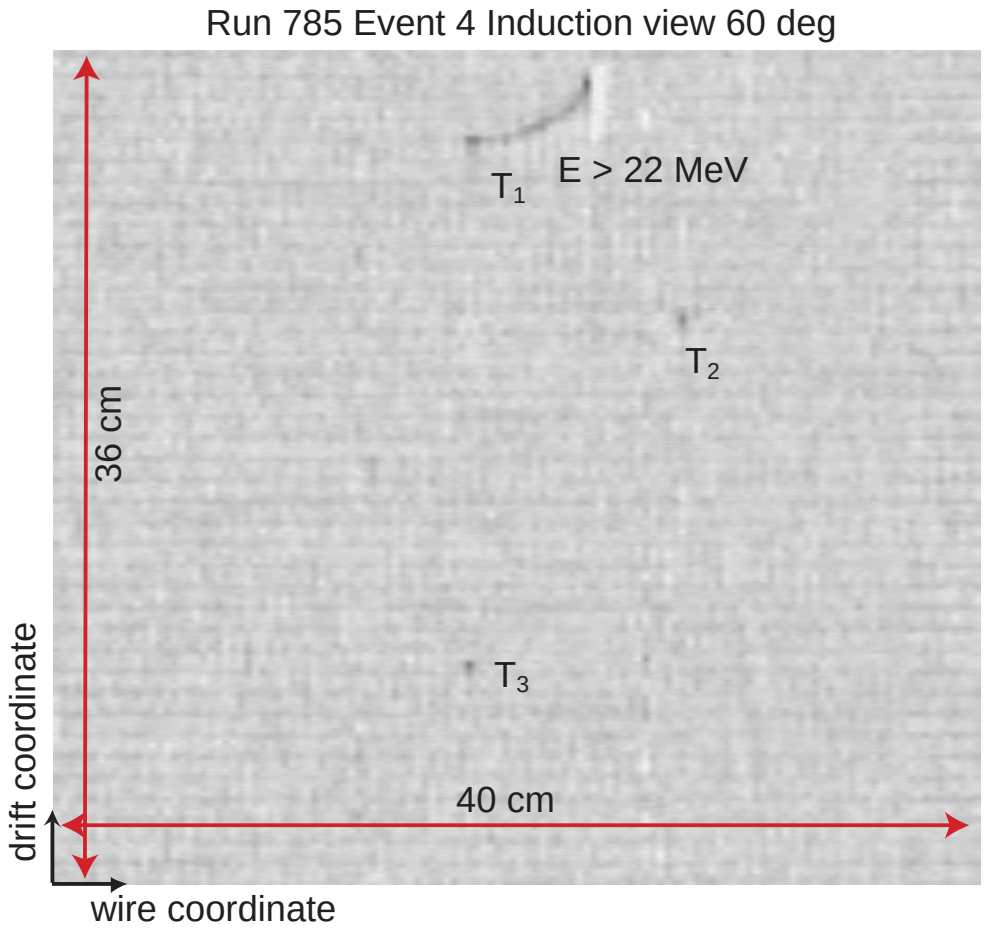

Figure 3.26: Run 785, Event 4, second *Induction* view (60^0).

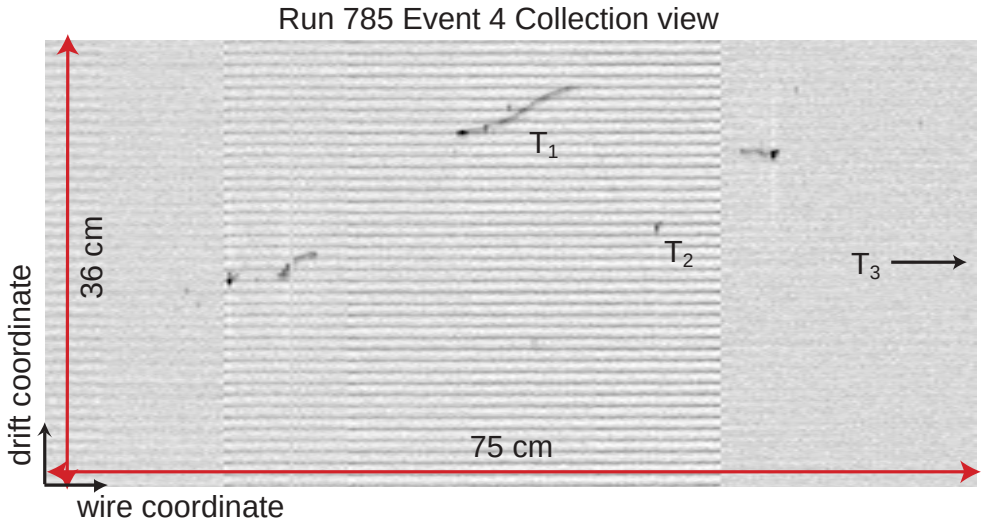

Figure 3.27: Run 785, Event 4, *Collection* view. The leading track enters the detector crossing the wire plane.

Atmospheric shower

Figure 3.28 shows the *Collection* view of an impressive cosmic event composed by hundreds of parallel tracks. The event extends to the full length (about 18 m) and drift (1.5 m) of the detector, as shown in the upper image. The zoomed region contains several electromagnetic and hadronic showers, muon tracks and low energy photons converting into electrons.

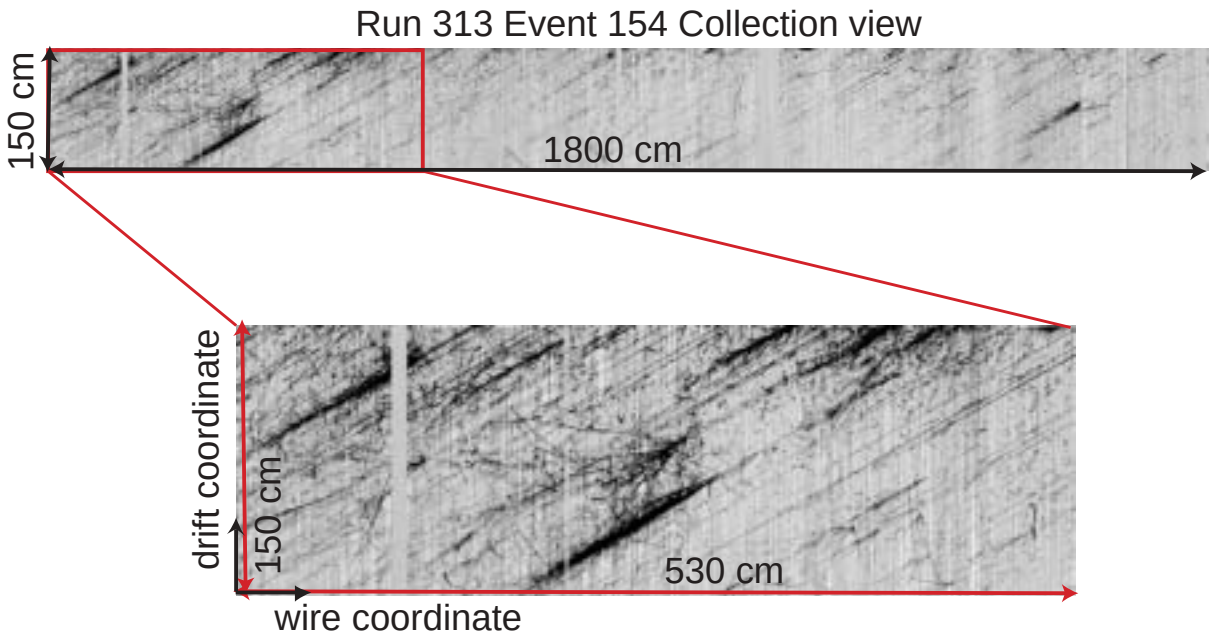

Figure 3.28: Run 313, Event 154, *Collection* view.

Stopping muon

Some of the muons entering the detector deposit all their energy, stop and decay in the LAr active volume. These kind of events are easily recognized by the presence of a low energy muon track followed by an electron emission. The muon track, due to the low momentum, undergoes large angle multiple scattering, and the ionization increases rapidly near the end point. Since the muon decays at rest in the detector, producing one electron plus two undetected neutrinos, the directions of the electron and muon are uncorrelated. The electron energy ranges between 0 and about 53 MeV.

Figure 3.29 shows the *Collection* view of an event matching the previous pattern. The muon extends about 60 cm in the increasing wire coordinate. The last part of the track shows the increasing energy deposition pattern, indicating that the muon stopped rather than decayed on flight. The small track corresponds to the emitted electron. The track presents many direction changes, due to multiple Coulomb scattering. The fitted energy deposition of the electron is about 20 MeV.

Figures 3.30 and 3.31 correspond to the *Induction I* (0^0) and *II* (60^0) views, respectively, of the same event.

Another example of a stopping muon event is shown in Figures 3.32, 3.33 and 3.34 for the *Collection*, first and second *Induction* views respectively. Again, the muon shows large angle multiple scattering, and produces an increased energy deposition in the region close to the end point. The energy of the electron is estimated to be about 15 MeV.

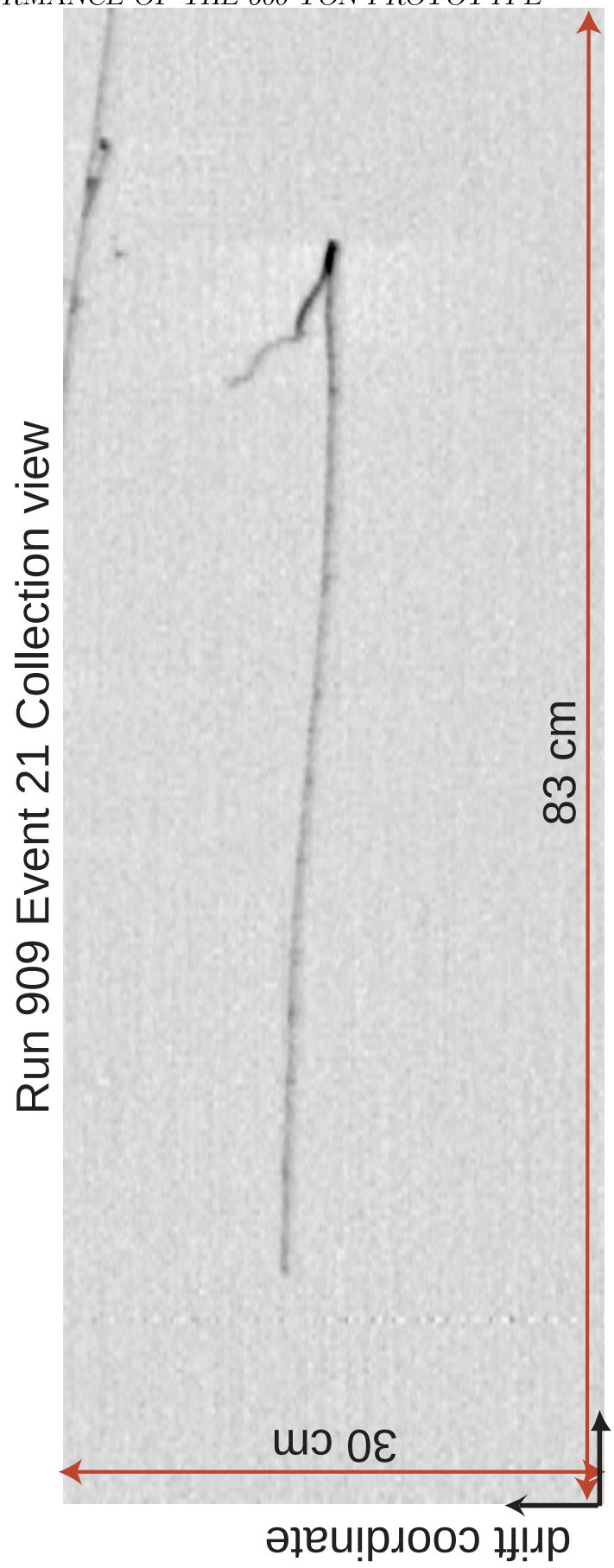

Figure 3.29: Run 909, Event 21, *Collection* view.

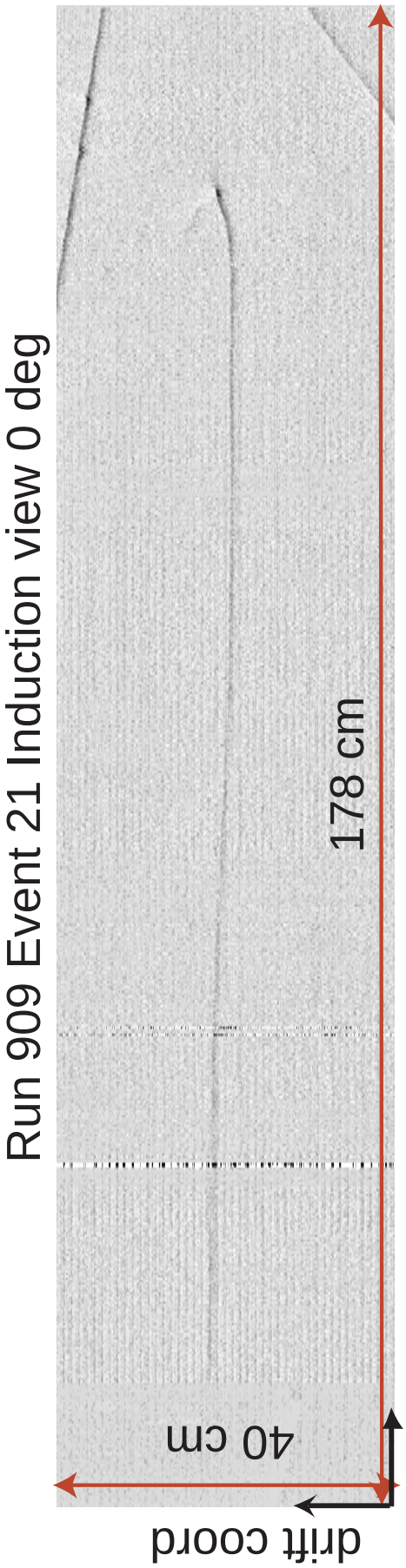

Figure 3.30: Run 909, Event 21, first *Induction* view (0^0).

Figure 3.31: Run 909, Event 21, second *Induction* view (60^0).

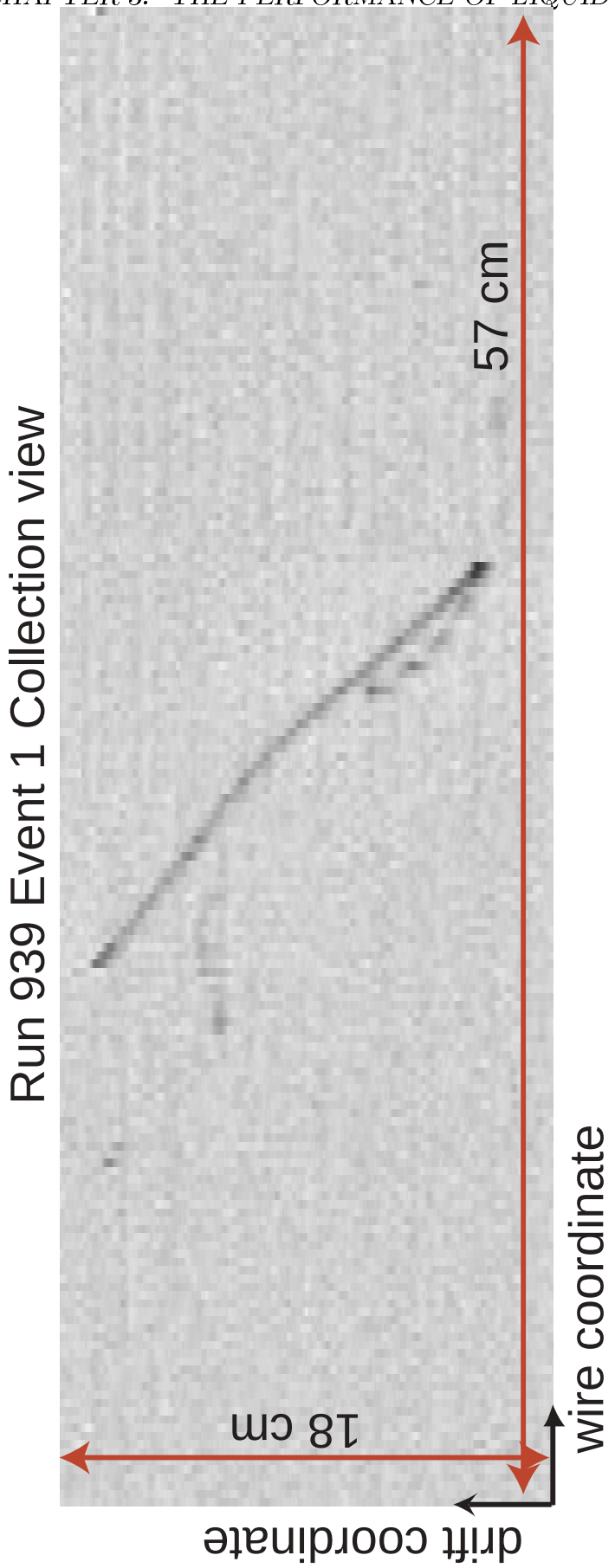

Figure 3.32: Run 939, Event 1, *Collection* view.

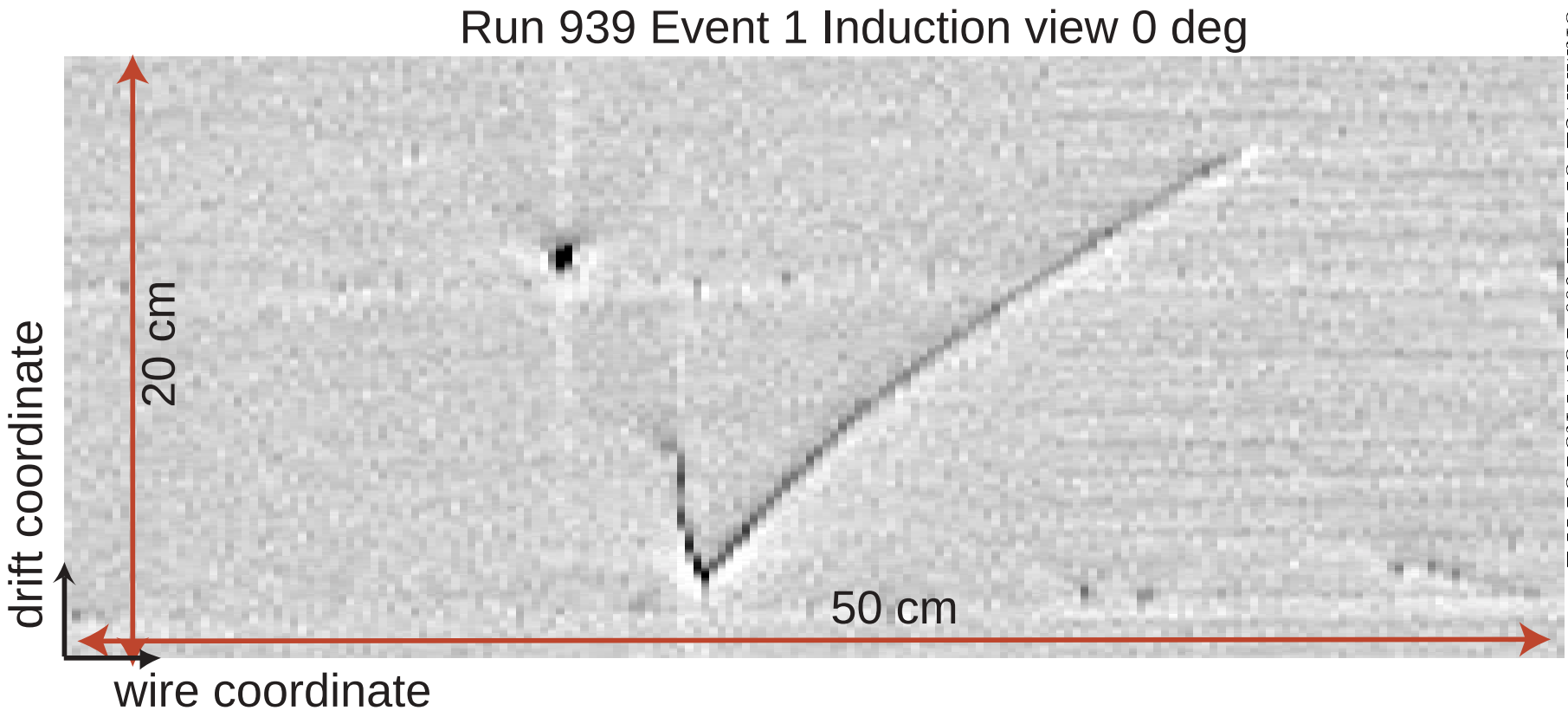

Figure 3.33: Run 939, Event 1, first *Induction* view (0^0).

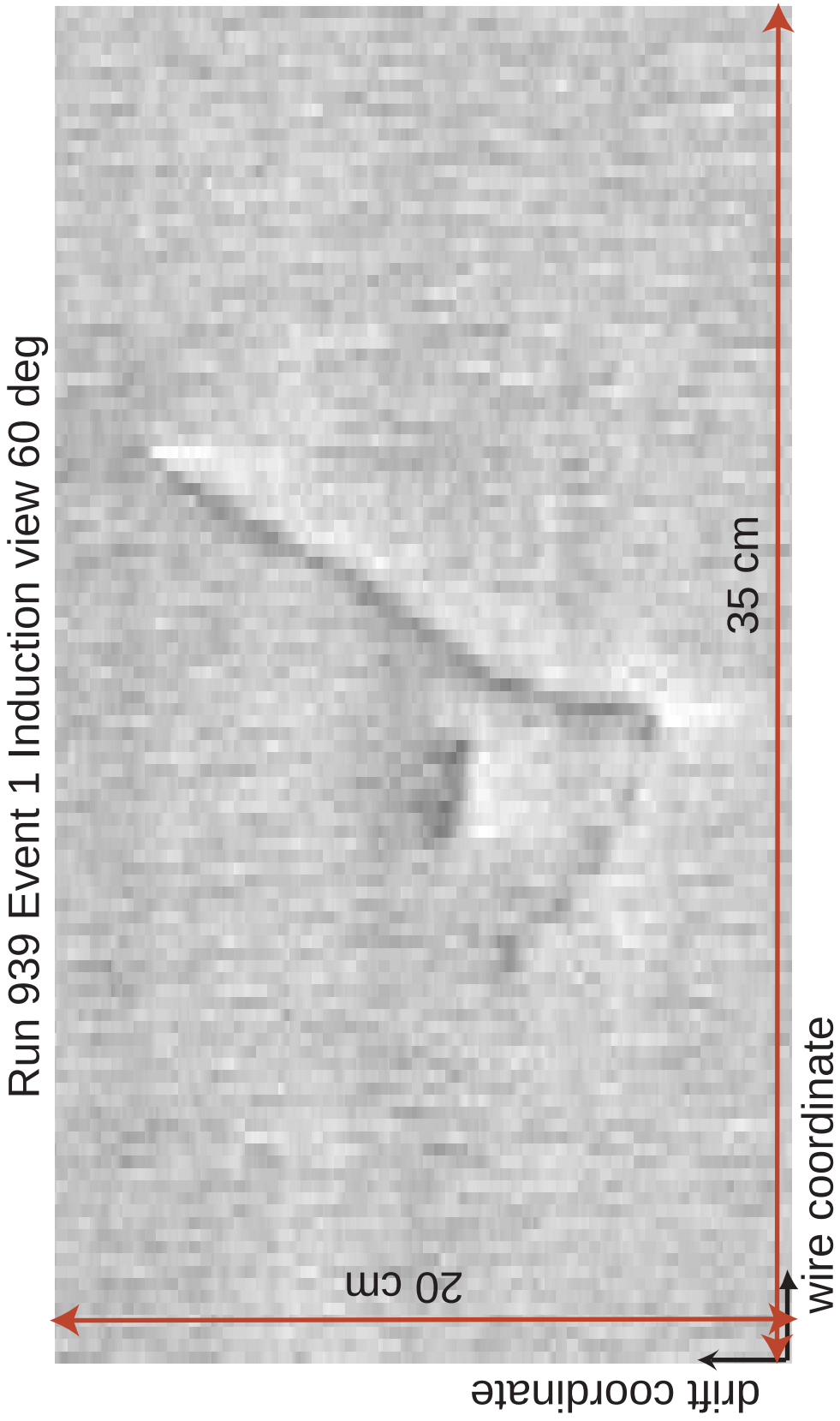

Figure 3.34: Run 939, Event 1, second *Induction* view (60^0).

Hadronic interaction

Figure 3.35 shows the complete three views of a hadronic interaction inside the detector. The squares in every view indicate the selected regions where the interaction is located. As mentioned in Section 3.5.1, the *Induction I* plane gives two independent views corresponding to each half of a chamber along the z coordinate.

A zoomed image of the region selected in the *Induction I* view (0^0) is shown in Figure 3.36. A charged hadron enters the detector from the top and travels around 1 m in LAr before interacting. Then, several secondary particles are produced and undergo different interactions. The event is also visible in the *Induction II* (60^0) plane (Figure 3.37).

A cleanest image of the interaction is shown in the *Collection* view (Figure 3.38). A δ ray is produced at the beginning of the hadron track. Among the secondary particles, it is possible to distinguish in the bottom part of the picture the conversion of a pair of photons, most likely coming from the decay of a π^0. A neutral particle (possibly a neutron) could also be produced, giving an additional hadronic interaction in the upper part of the figure. One of the charged hadrons coming from the main interaction vertex travels around 1.7 m undergoing secondary hadronic interactions along its path. Soft secondary heavily ionizing nuclear debris are also visible.

The shape of the signal corresponding to the interaction point of the event detected by a wire in the *Collection* plane is shown in Figure 3.39. About 160 ADC counts over a baseline of $\sim$10 are detected in the wire. This can be compared to Figure 3.22, which corresponds to the signal recorded by a wire after the passage of a minimum ionizing particle. Moreover, we are able to distinguish the signals of different secondary tracks that hit the same wire, as shown in Figure 3.40.

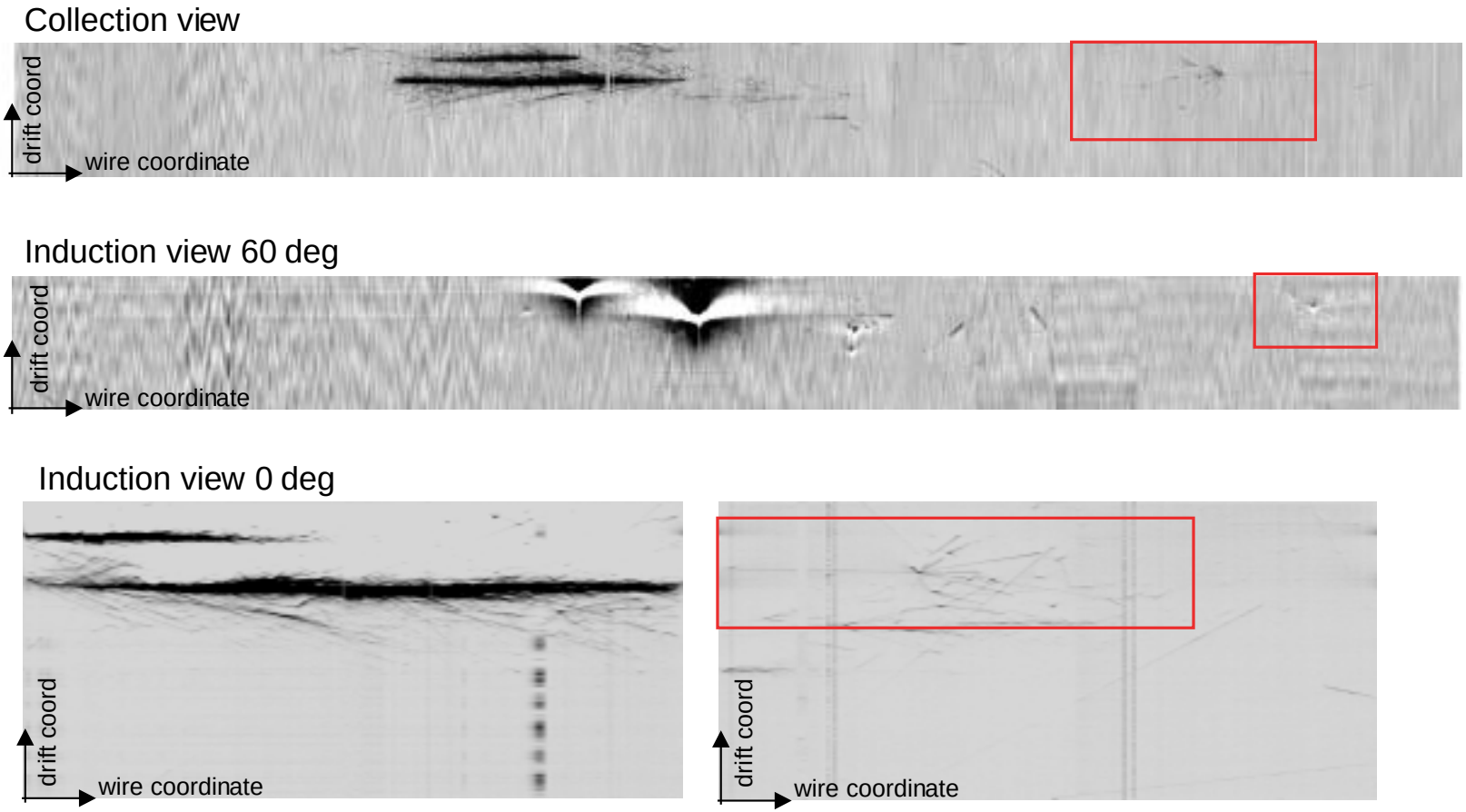

Figure 3.35: Run 308, Event 160, the three views.

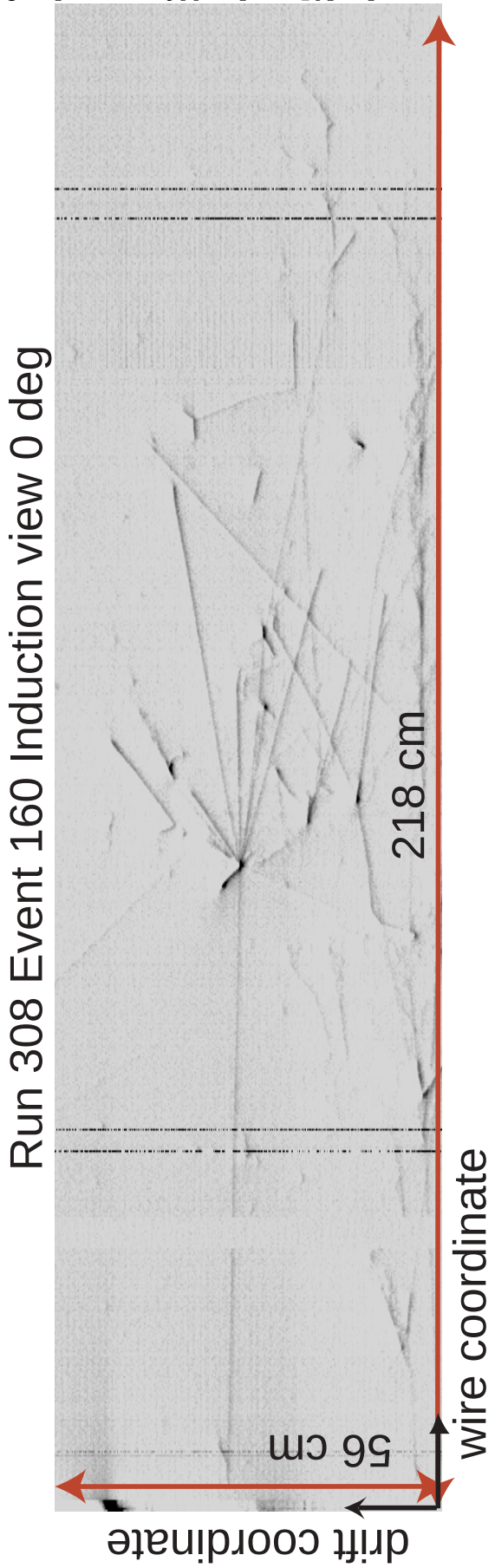

Figure 3.36: Run 308, Event 160, *Induction view* (0^0).

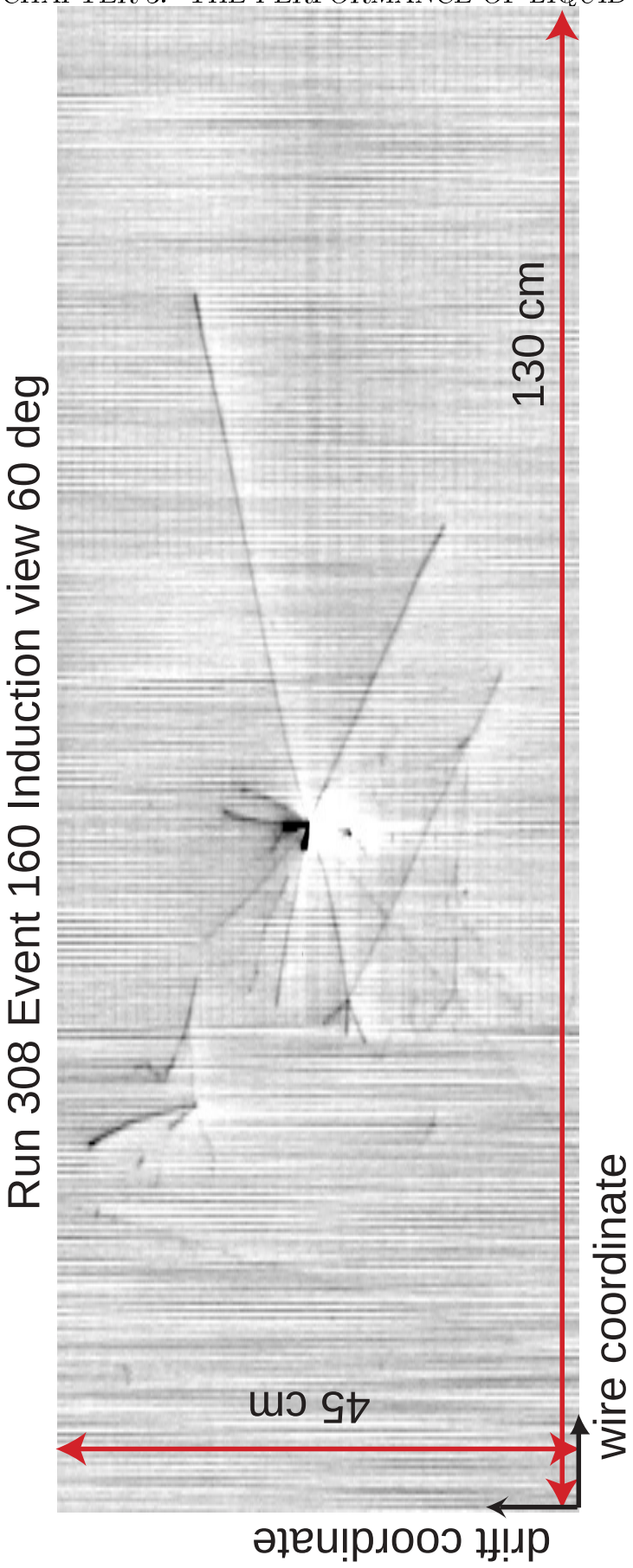

Figure 3.37: Run 308, Event 160, *Induction view* (60^0).

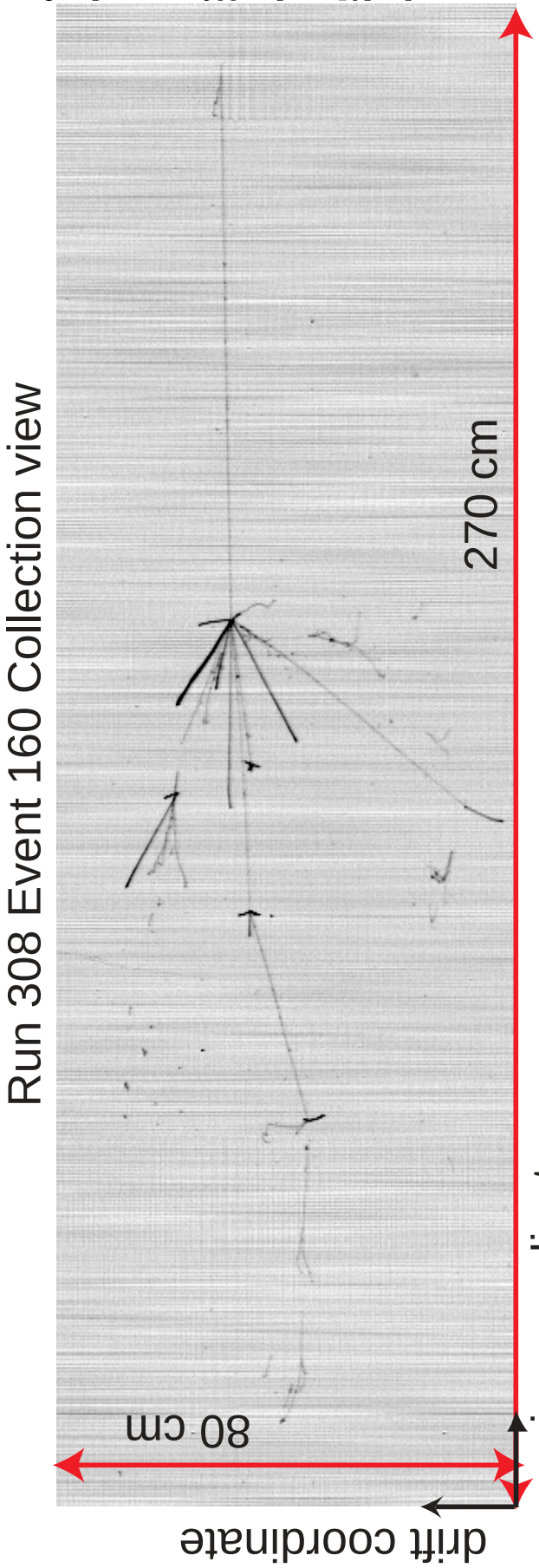

Figure 3.38: Run 308, Event 160, *Collection* view.

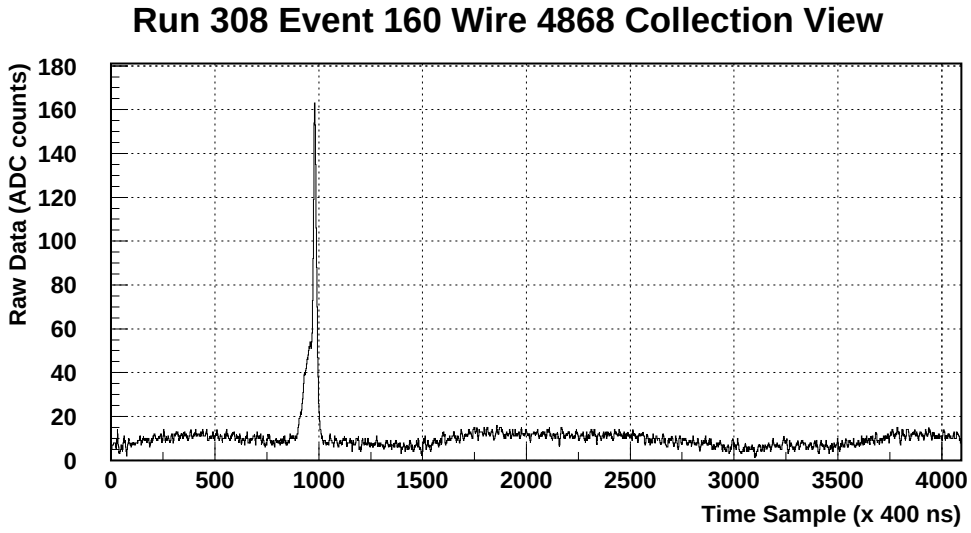

Figure 3.39: Signal corresponding to the main vertex of the hadronic interaction.

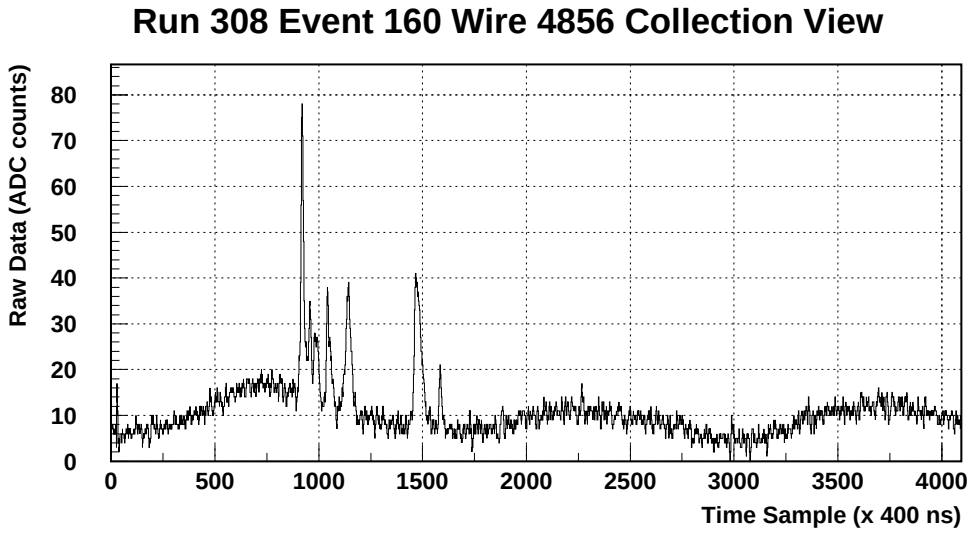

Figure 3.40: Multiple hits detection in a single wire of the *Collection* plane.

V0 event

Figure 3.41 shows the typical signature of a V0 event. This event can be associated to the decay of a K^0 into a pair of pions ($K^0 \rightarrow \pi^+ + \pi^-$) or a Λ particle flying a few centimeters and decaying into a pion and a proton ($\Lambda \rightarrow p + \pi^-$).

Two tracks are coming from the same interaction vertex and they are traveling towards the right part of the detector. Since there is not any other track in the opposite direction, the two tracks should be produced by the disintegration of a neutral particle.

The longest track deposits an energy of about 85 MeV and escapes the detector. The other track has a total energy of about 50 MeV and stops inside the detector, depositing the maximal energy at the end point.

The *Induction II* view (60^0) of the event (Figure 3.42) clearly shows again the two tracks coming from the same vertex.

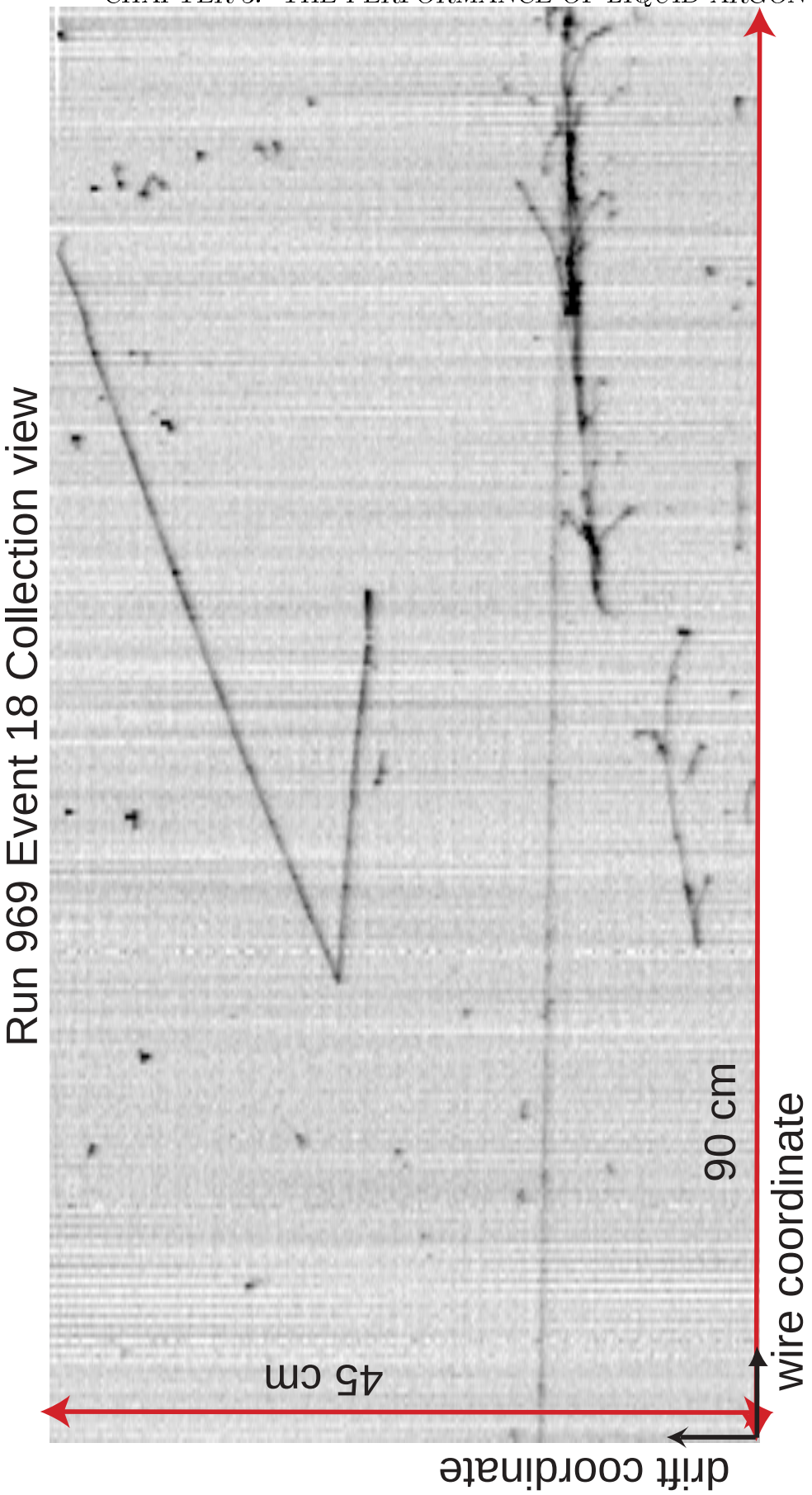

Figure 3.41: Run 969, Event 18, *Collection* view.

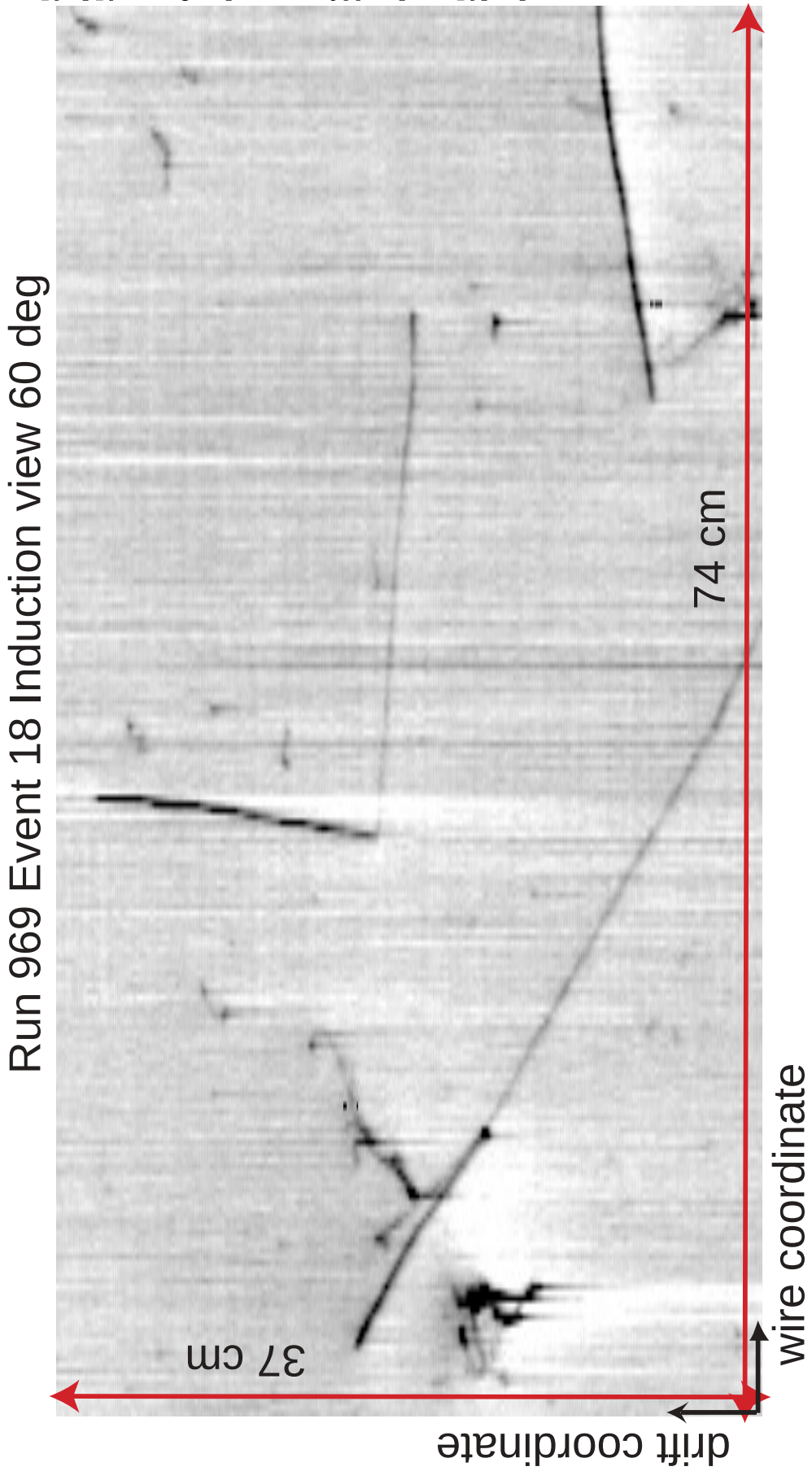

Figure 3.42: Run 969, Event 18, *Induction* view (60^0).

Electromagnetic shower

A good example of the imaging capabilities of the LAr TPC is given by the electromagnetic shower shown in Figure 3.43. The image is about 75×170 cm^2 wide. The electron initiates an electromagnetic cascade (bottom-left corner of the figure) as pair production and bremsstrahlung generate more electrons and photons with lower energy. The grey level of the pixels codes the electronic pulse height, proportional to the collected charge, so that the longitudinal and transverse developments of the cascade can be easily studied.

The black dots that appear all around the main shower are Compton electrons of very low energy ($\sim$ 1 MeV), which shows the excellent performances of the electronic LAr imaging.

The overall drift time (vertical axis) corresponds to about 75 cm of drift distance, while the shower spreads over $\sim$15 radiation lengths.

Figures 3.44 and 3.45 show the two *Induction* views of the event at 0^0 and 60^0, respectively. The shower spreads over 3 meters (5 m) with 76 cm (90 cm) of drift distance in the 0^0 (60^0) projection.

While in the *Collection* view (Figure 3.43) the shower is clearly recognized as a big black cloud in a light grey background, the two *Induction* views show, in addition, a "white" cloud correlated to the black one. The reason for this second band is found in the bipolar nature of the signals recorded by the *Induction* wires (see Section 3.5.2). As an example, Figure 3.23 shows the signal observed in wire no.1701 of this event, placed in the 0^0 *Induction* plane. Starting from the left of the plot, the wire "sees" the charge of the shower approaching (time sample $<700 \times 400$ ns), which translates in a negative signal and appears in the display (Figure 3.44) as "white". The crossing of the charge on the wire corresponds to the positive peak in the figure (at around 850×400 ns), which appears black in the display. Finally, above $\sim 1500 \times 400$ ns one finds the baseline, grey in the display.

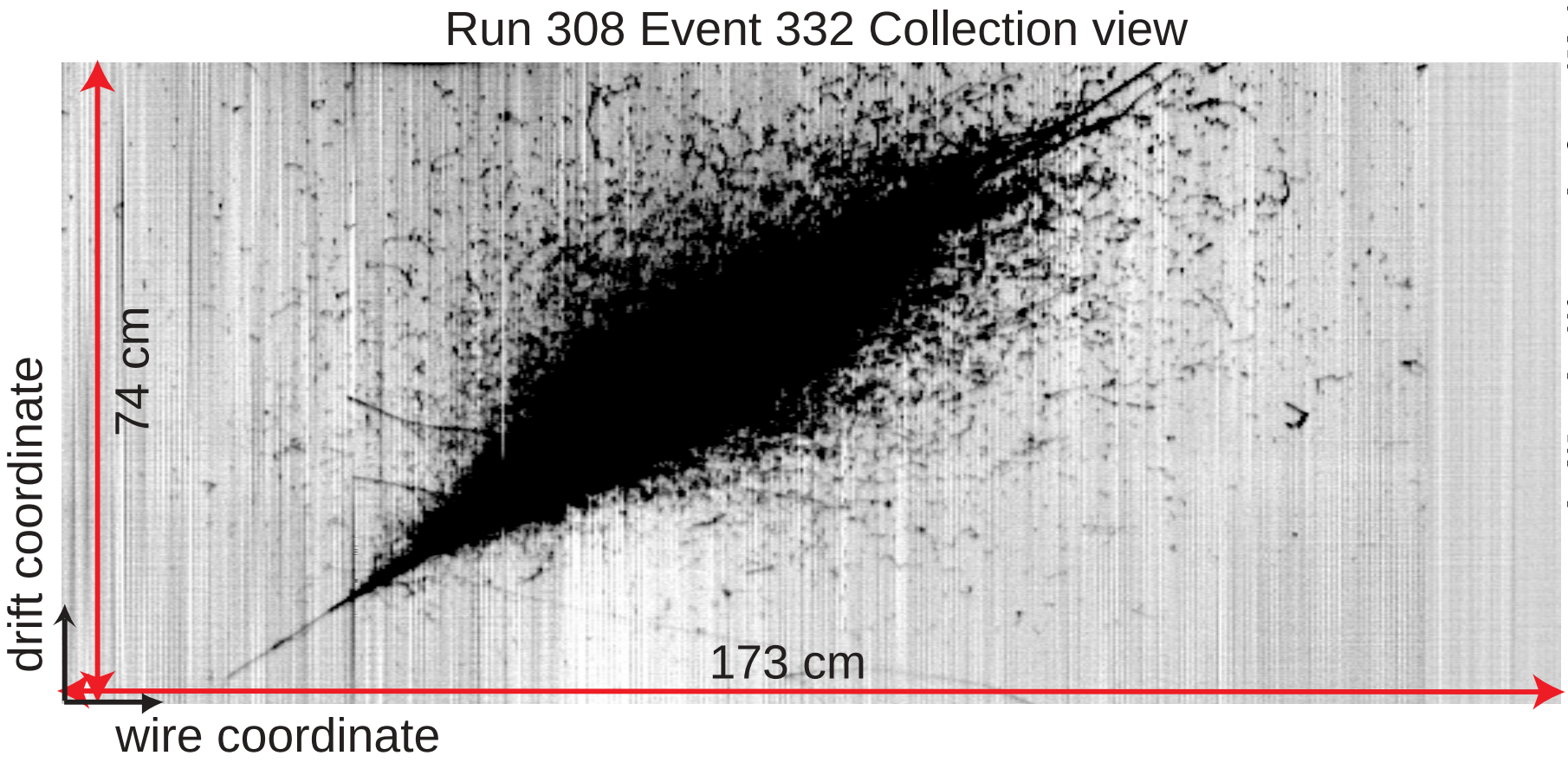

Figure 3.43: Run 308, Event 332, *Collection* view. Electromagnetic shower.

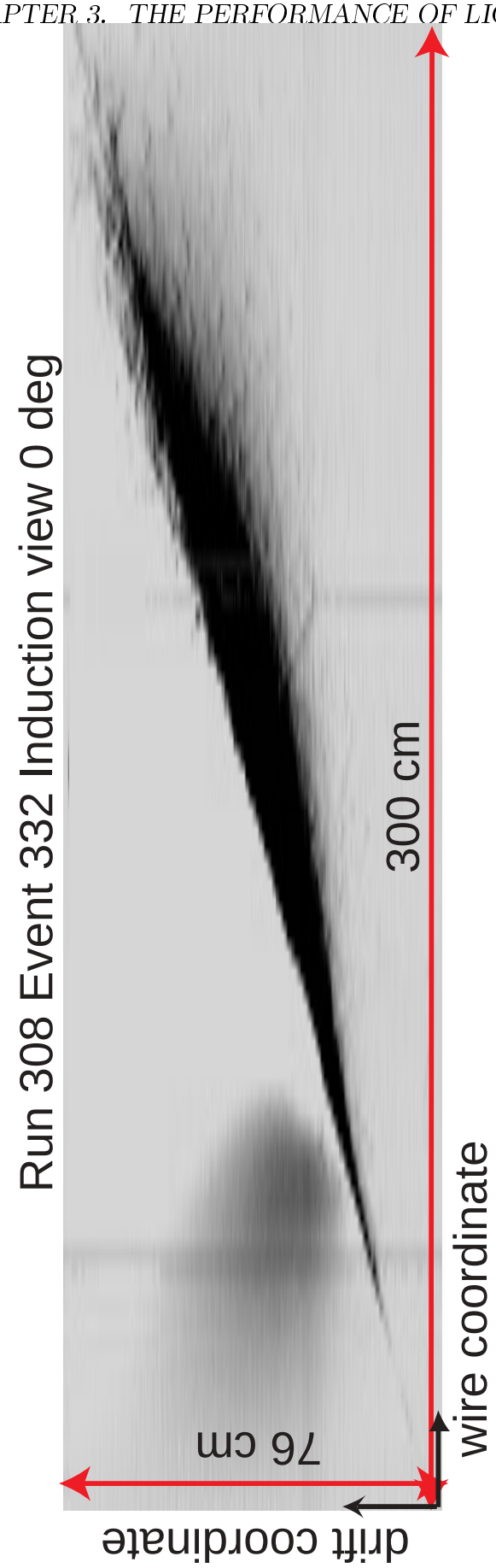

Figure 3.44: Run 308, Event 332, *Induction view* (0^0). Electromagnetic shower.

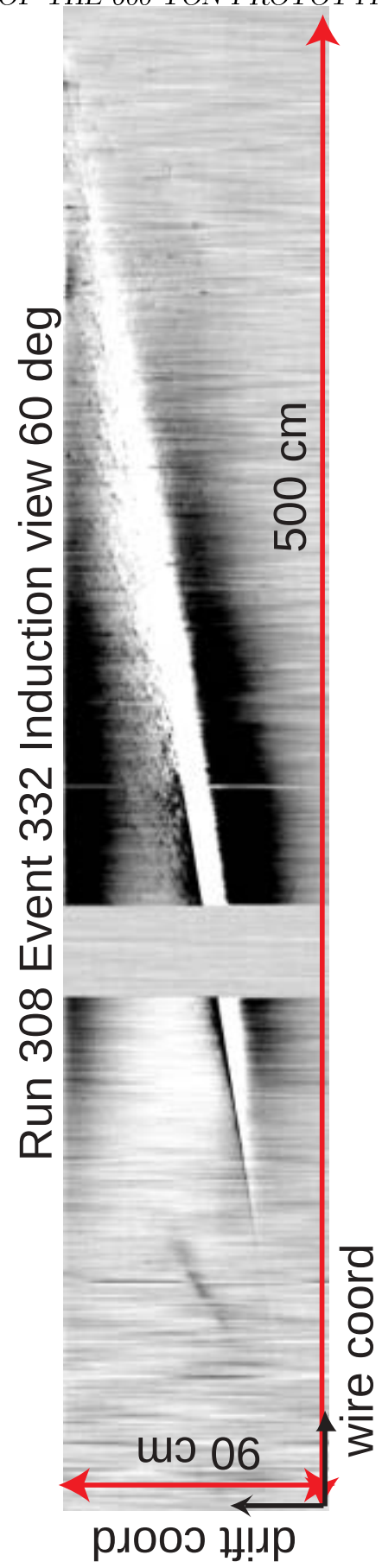

Figure 3.45: Run 308, Event 332, *Induction view* (60^0). Electromagnetic shower.

Hadronic shower

A nice example of a hadronic interaction is shown in Figure 3.46, where a high energetic charged hadron enters the detector from the top flying to the bottom for more than 1 meter (from left to right in Figure 3.46). The interaction generates a spectacular shower where one can identify some secondary hadronic interactions accompanied by a high electromagnetic activity. The projection of the event in this view (*Induction I*), reveals a $\sim$2 meters long shower, quite collimated and almost fully contained in the detector. In addition, the hadron enters near the anode (small drift distances) flying in the direction of the cathode (from bottom to top in Figure 3.46), the maximum drift distance being $\sim$70 cm.

The beauty of the event is also shown in Figures 3.47 (*Collection* view) and 3.48 (*Induction II*), where one can appreciate that it extends for more than 2 meters in both projections.

Figure 3.46: Run 308, Event 7, *Induction* view (0^0). Hadronic interaction candidate.

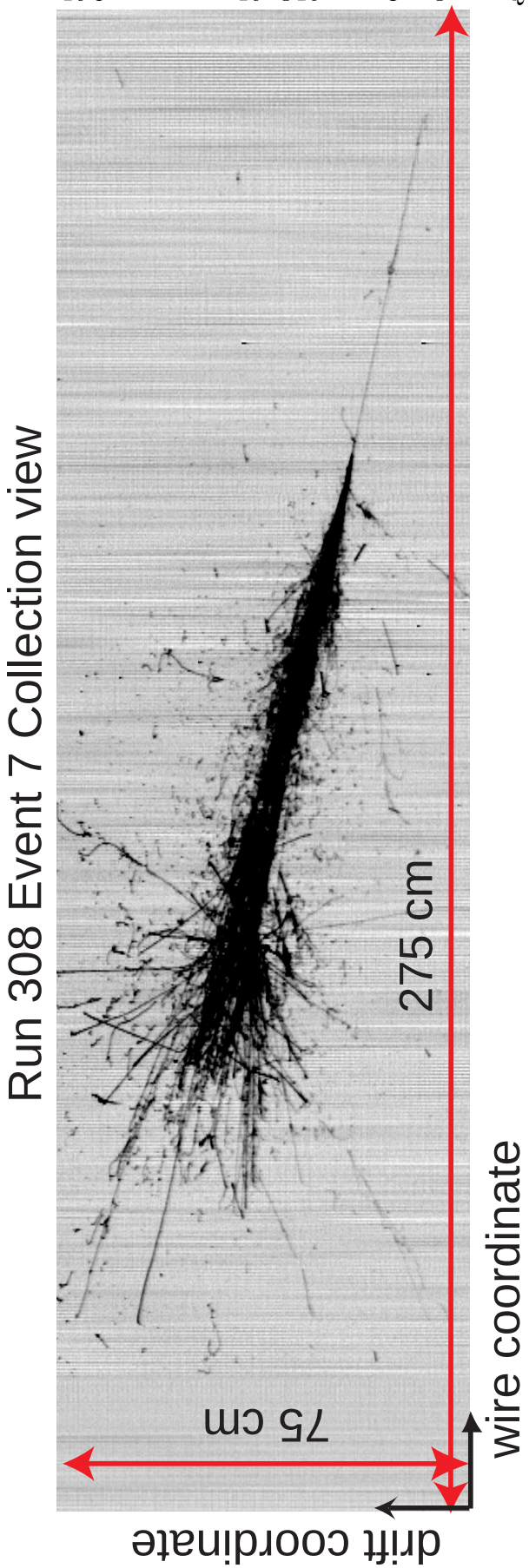

Figure 3.47: Run 308, Event 7, *Collection* view. Hadronic interaction candidate.

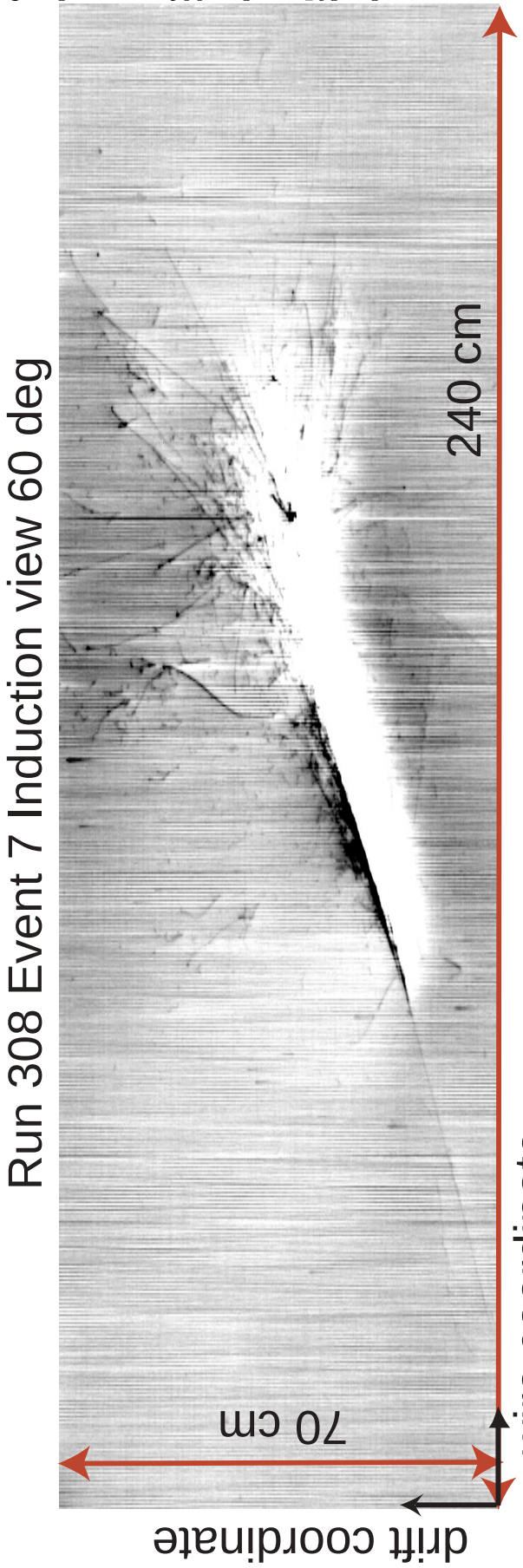

Figure 3.48: Run 308, Event 7, *Induction* view (60^0). Hadronic interaction candidate.

3.5.4 Wire diagnostics

A basic wire classification is performed based on the dispersion of the wire output signal within a given run. The RMS of the wire output signal distribution in a event discriminates between wires having collected any ionization signal and those showing only electronic noise. Due to the high density of ionizing particles traversing the detector, all wires are expected to be "touched" by the ionization signal at least once in the run. Therefore, wires with systematic low RMS value are cataloged as disconnected. The selection cut for disconnected channels is set to an average RMS lower than 11.5 ADC counts along a run. Figure 3.49 shows the distribution of the average wire output signal RMS in run 939. The distribution at the left and right sides of the cut corresponds to the disconnected and connected wires respectively.

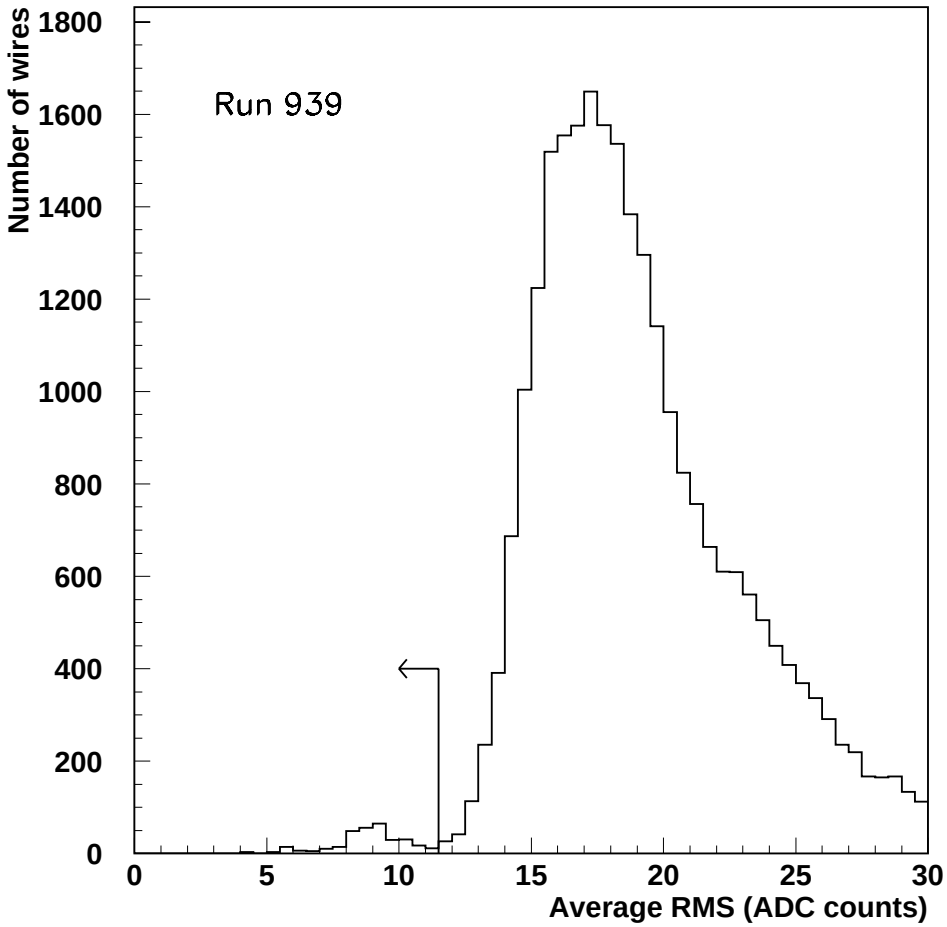

Figure 3.49: Average wire output signal RMS distribution for run 939. The arrow marks the cut selecting the disconnected wires.

Connected wires are further classified according to their noise conditions. In order

Run number	disconnected (%)	dead channel (%)	unstable (%)
227	1.0	4.5	6.0
335	1.4	2.5	3.7
446	0.4	2.0	0.7
550	1.1	1.9	0.9
663	1.2	0.0	0.6
781	1.1	0.0	0.8
841	1.2	0.0	0.7
939	1.1	0.0	1.0

Table 3.3: Disconnected, dead channel and unstable wires rates for several runs along the data taking period.

to remove the contribution of the ionization signal from the total wire output signal, the mean and RMS are computed iteratively after successively removing values at more than 3 times the RMS value from the mean. After three iterations, the ionization signal contribution (in the tails of the signal distribution) is ensured to be removed. The resulting mean value is the baseline signal of the wire in the given event. The RMS quantifies the noise amplitude (see Figures 3.50 and 3.51).

The dispersion of the baseline values within a given run provides a criterion for the classification of connected wires. The mean of the baseline distribution along the run is taken as the baseline of the wire in the given run. The corresponding RMS is used to establish the following classification:

- RMS = 0: dead channel wire. The wire signal is constant during the whole run. The electronics channel reading this wire is out of work.
- $0 < \text{RMS} \leq 2.5$: stable wire. The relatively small dispersion of the baseline along the run allows us to use a common baseline value for the run.
- $2.5 < \text{RMS}$: unstable wire. No baseline value can be taken for the run.

Dead channel wires are discarded in the data analysis. The baseline values for a given run are stored in a database for all stable wires, whereas for the unstable wires the baseline is computed in an event by event basis. Table 3.3 shows the rate of disconnected, dead channel, and unstable wires (over the whole number of read wires) for several runs along the data taking period. The rate of disconnected wires stays around 1% whereas the dead channels and unstable wires' rates are considerably reduced (to 0% and 1% respectively) thanks to the electronics optimization performed along the technical run.

3.5.5 Electronic noise

High noise conditions, mainly in the low frequency part of the spectrum, were found in the initial runs in the *Induction II* and *Collection* wire planes. A modification on the wire planes high voltage configuration was performed, aiming to the reduction of the noise conditions.

Voltages at the different wire planes have to increase in the drift direction. Thus, in a first configuration, the *Induction I* plane was grounded, and the *Induction II* and *Collection* planes were set to growing positive potentials. The voltages configuration was typically ($V_{Induction1}$, $V_{Induction2}$, $V_{Collection}$) = (0,280,480) V. Since the microphonic noise contributes mainly to the low frequency part of the spectrum proportionally to the absolute value of the voltage, an improvement on the noise conditions was achieved by grounding the *Induction II* wire plane, and setting negative and positive voltages for the *Induction I* and *Collection* planes respectively. An optimization of the noise conditions was found for the configuration (-220,0,280) V. The price to be paid is an increase in the low frequency noise in the *Induction I* plane.

Figures 3.50 and 3.51 show the average noise amplitude as a function of the wire number for the different wire planes, in runs 335 (initial wires high voltage configuration) and 939 (final wires' high voltage configuration), respectively. The noise conditions are highly improved for *Induction II* and *Collection* planes, while the increase in *Induction I* is marginal. Figure 3.52 shows the comparison of the noise spectrum for a single wire from each of the three wire planes, for runs 227 and 939. Again, the plot shows how a reduction of the low frequency noise is achieved for both *Induction II* and *Collection* planes (of about one order of magnitude in the case of the *Induction II*). In the case of *Induction I* plane, even though the amplitude of the low frequencies is slightly increased, the noise level is maintained at low level.

3.5.6 Zero-suppression

The data acquisition in the ICARUS detector produces a very large amount of data (about 200 Mbytes per event in the 300 ton prototype), whereas signals of interest take only a little fraction. The acquisition rate is limited by the bandwidth of the building network, which introduces a non negligible dead-time when acquiring "full image" events. The implementation of an on-line data reduction system, aiming to a factor 100 reduction of the event size, bypasses the dead-time problem and allows a faster off-line data handling. This function is performed by the DAEDALUS chip, within the read-out chain, which selects the Regions of Interest (ROI) [33, 34, 35].

A ROI is defined as a time window around a rising edge (hit). To identify a rising slope, first we compute the differences between every two consecutive signal samples inside a time-sliding window of fixed size (*window size*). Positive differences are accumulated whereas occurrences of negative and null differences are counted. A hit is found when, for the given time window, the positive sum is above a given threshold (*rising_sum_threshold*) and the two counters values are below two other thresholds (*rising_zero_count* and *rising_negative_count*).

The end of the rising edge is detected when two conditions are met: the positive sum is below a given threshold (*falling_sum_threshold*) and at least one of the two counters is above its corresponding threshold (*falling_zero_count* and *falling_negative_count*).

After having passed through the DAEDALUS chip, the filtered data are organized into tiles by the *trigger logic* unit. One tile groups 16 channels together. Three parameters (*Nbuf*, *Npre* and *Npost*), can be adjusted to select the number of samples entering a tile and the duration of the inhibit window.

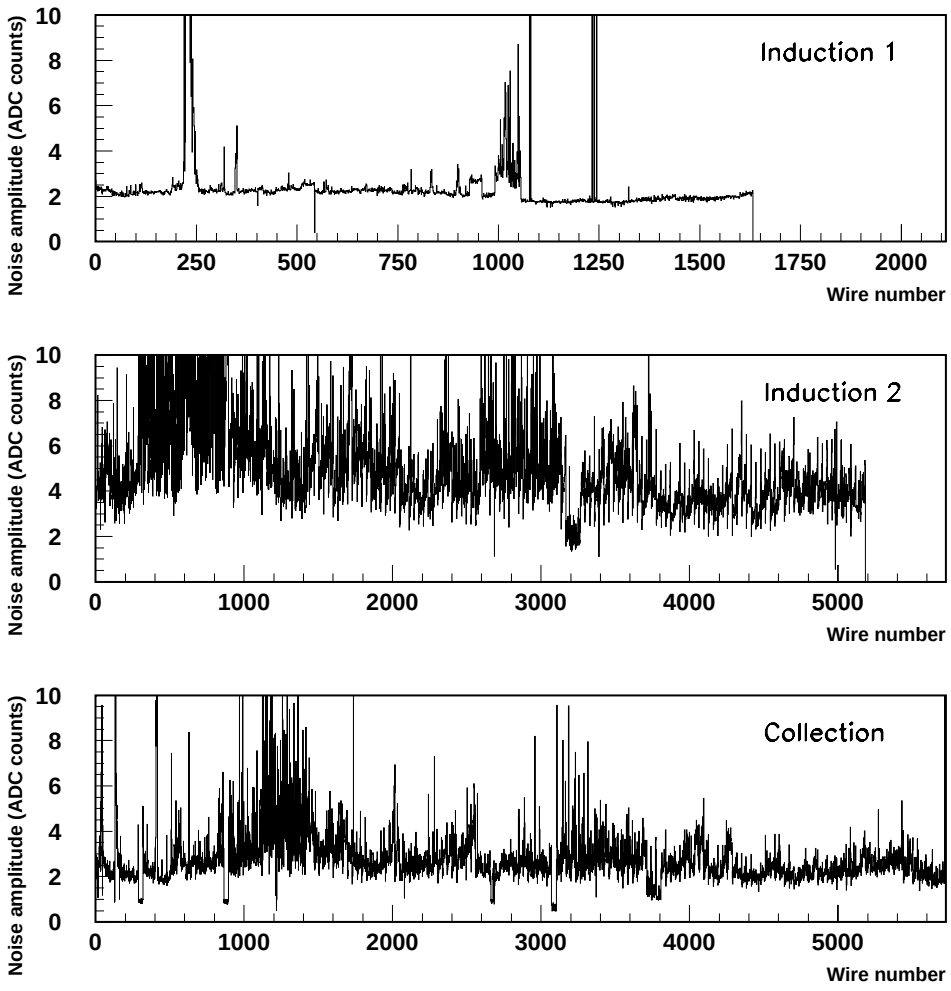

Figure 3.50: Noise amplitude as a function of the wire number for the *Induction I* (top), *Induction II* (middle) and *Collection* (bottom) wire planes in run 335.

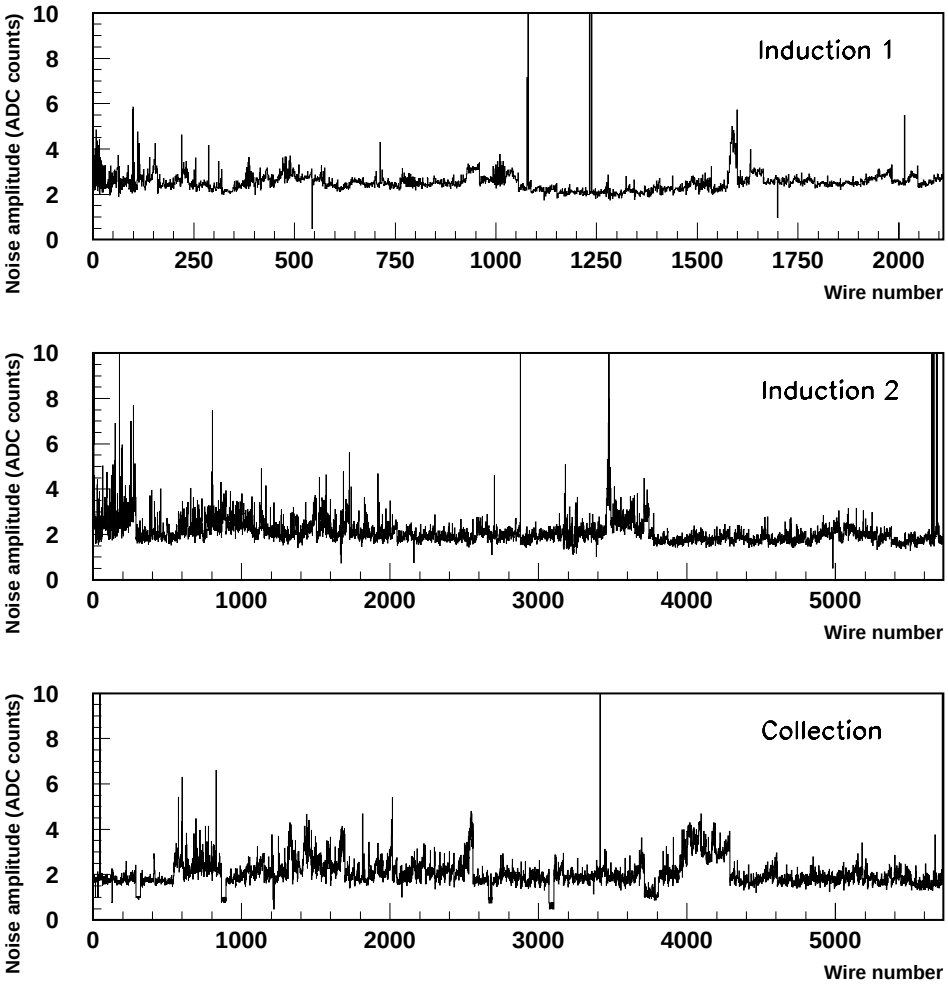

Figure 3.51: Noise amplitude as a function of the wire number for the *Induction I* (top), *Induction II* (middle) and *Collection* (bottom) wire planes in run 939.

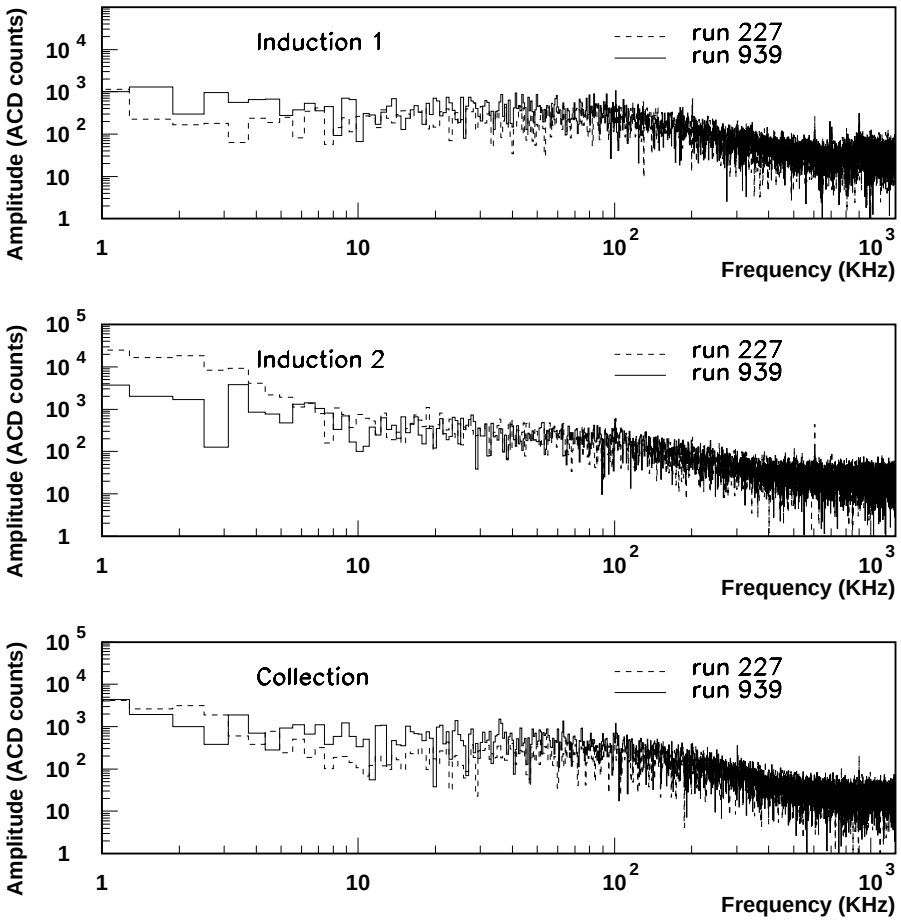

Figure 3.52: Noise spectrum for a single wire in the *Induction I* (top), *Induction II* (middle) and *Collection* (bottom) wire planes compared for runs 227 (dashed) and 939 (solid).

The DAEDALUS parameters need to be tuned on the specific signal shapes. We perform an off-line simulation of the DAEDALUS behaviour, and use the data collected during the technical run to find the set of parameters that optimizes the track detection efficiency and minimizes the collection of spurious signals. These parameters will be used for the on-line data reduction in the next runs.

For our analysis, we select about two hundred tracks from the *Collection* wire plane. The track detection efficiency is defined as the fraction of the track length selected by the DAEDALUS. The collection of spurious signal regions is quantified by the ratio of the area of the selected zones where no track or coherent noise is present over the area of the whole selected zone.

The parameters of the DAEDALUS chip allow us to select a wide range of signal shapes, both in *Induction* and *Collection*. Here we describe the results concerning the *Collection* plane.

For the *Collection* view, the detection efficiency depends mainly on the parameters *rising_sum_threshold* and *window_size*. *rising_sum_threshold* is related to the signal amplitude respect to the baseline. A signal with a little amplitude can be generated by a *mip* or by an event occurring far from the anode (when part of the ionization charge is captured by LAr impurities). Setting a low *rising_sum_threshold* value, the DAEDALUS chip selects this kind of events, but also electronic noise. On the other hand, high *rising_sum_threshold* values avoid fake signals selection but reduces the efficiency on ROI's selection. For this reason, *rising_sum_threshold* is set as low as possible.

The *window_size* is related to the signal rising-time. Its value must be larger than the width of the signal rising-edge.

Further selection efficiency improvement is achieved by tuning *rising_negative_count* and *rising_zero_count* parameters. Setting them to low values avoids noise selection. In order to further reduce the amount of spurious tracks, we require a minimum number of wires for every 16 wires group (*majority*) to have an identified hit. In such a case a tile is built. A dramatic reduction of selected spurious hits (from 8% to 3%) is achieved by selection *majority*= 3. Nevertheless, a value greater than 1 involves the risk of decreasing the capability of detecting tracks with few hits. The usage of this parameter requires a deep investigation about detection efficiency of low energy events.

A set of parameters that allow 100% track detection efficiency over a wide range of event topologies is shown in Table 3.4. Figures 3.53 and 3.54 show the result of the DAEDALUS selection on a T600 full *Collection* view signal.

3.5.7 Residuals

To estimate the energy deposited by an ionizing particle in the liquid Argon, we perform a least-square fit to the wire output signal, using an analytical function that reproduces well the expected signal shapes. For instance, in the *Collection* plane, the expected charge signal corresponds to a step function followed by the exponential discharge of the capacitor that holds the charge; hence a description of the signal shape as a function of time (t) can be obtained by means of:

$$S(t) = B + A\frac{e^{(t-t_0)/\tau_1}}{1 + e^{(t-t_0)/\tau_2}} \tag{3.10}$$

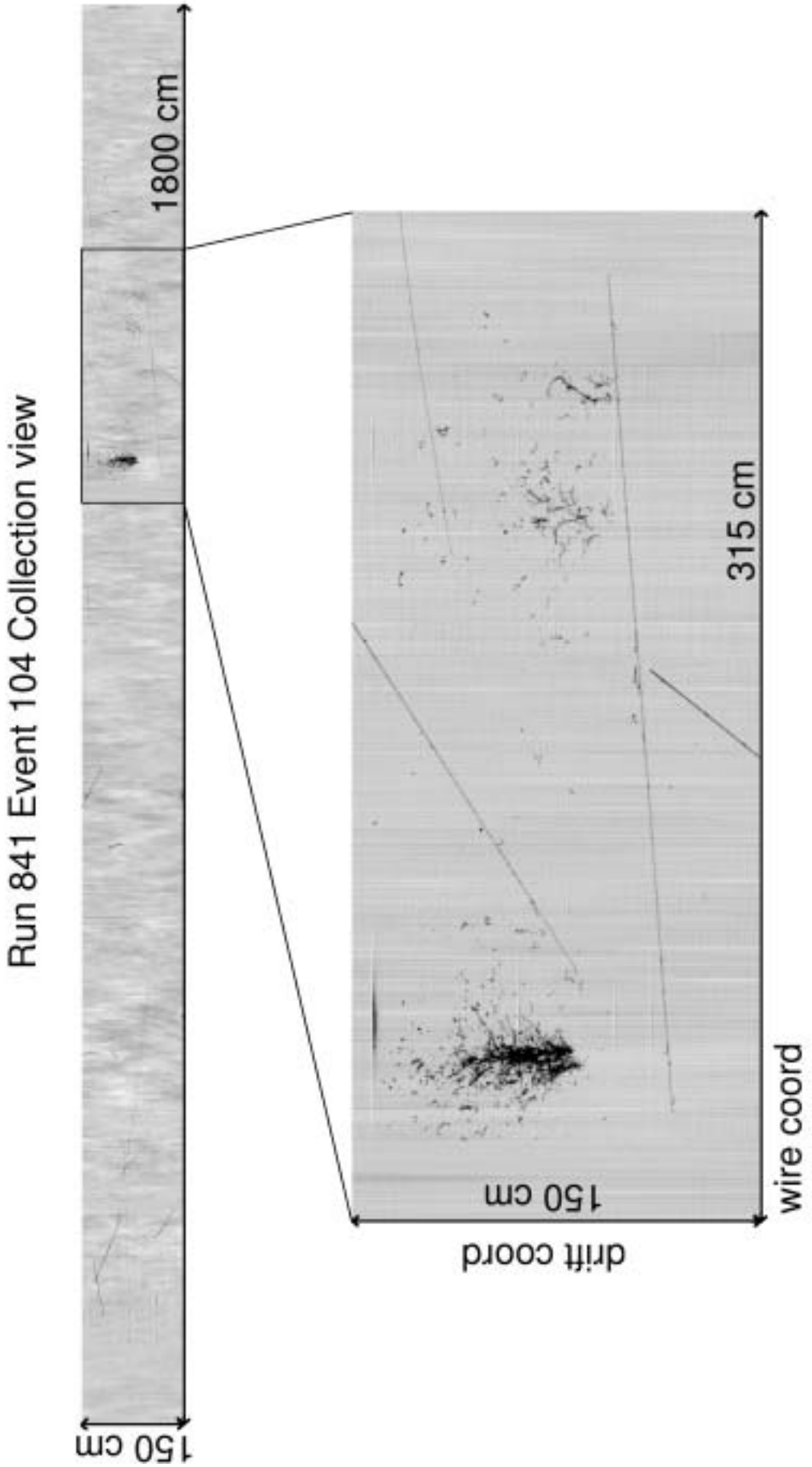

Figure 3.53: *Collection* plane signals for Run 841 event 104.

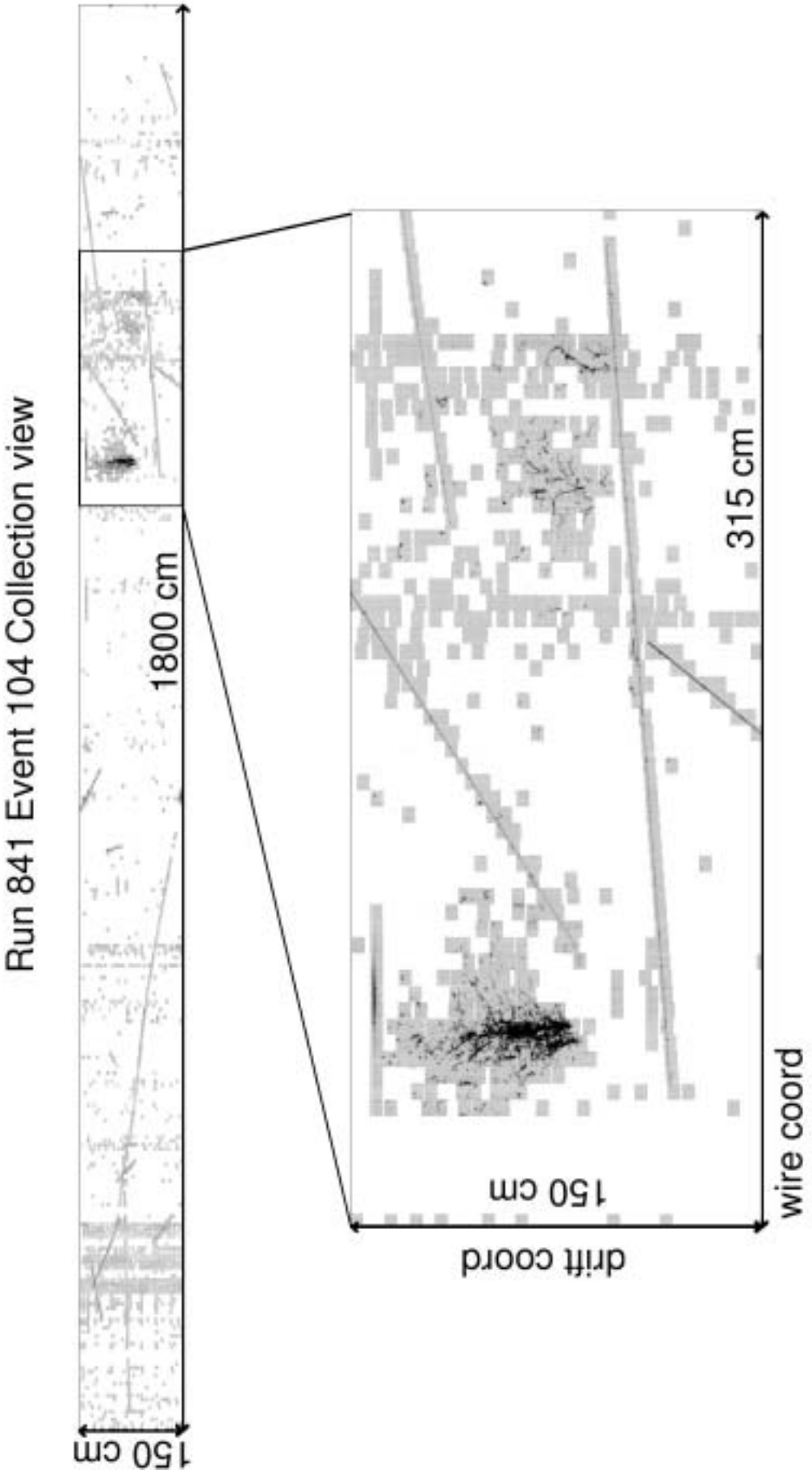

Figure 3.54: *Collection* plane signals after Daedalus simulation for Run 841 event 104.

Daedalus parameter	Used value
median_size	5
window_size	6
rising_sum_threshold	5
falling_sum_threshold	6
rising_negative_count	0
falling_negative_count	2
rising_zero_count	1
falling_zero_count	0
polarity	0
Nbuf	128
Npre	25
Npost	25
majority	3

Table 3.4: Set of parameters used for the data reduction in the image.

Three out of the five quantities used to parametrize the signal are relevant for physics analysis: the peak time position (t_0), which gives the drift coordinate; the pulse height (A), proportional to the collected charge; and the rise time (τ_1), which depends on both the track angle with respect to the wire plane and on the diffusion of the electron cloud during the drift. The signal baseline B and the amplifier decay time τ_2 are are also taken into account.

The determination of the parameters proceeds as follows: A hit is built in the region where some signal is detected over the electronic noise. Subsequently a least-square fit to the digitized signal is performed for each individual hit using equation 3.10.

The error assign during the fit to an individual point corresponds to the r.m.s. value of the electronic noise(1.5 ADC counts). The time region, where the fit is performed, should be large enough to cope with inclined track signals and multiple neighboring hits due to the presence of close tracks. A range of ± 50 time samples around the peak is enough to fulfill these requirements.

Figure 3.55 shows an example of a digitized signal in the *Collection* plane, sampled with a period of 400 ns. Superimposed is the result of the fit. The analytical function used accurately describes the signal shape. The fit value for the rise time is 1.4μs.

Figure 3.56 shows the digitized *Collection* signals from four hits along the track of a muon stopping inside the detector. Increasing peak areas (from left to right and top to bottom) exemplify the increase of the dE/dx towards the end point of the track.

The fit procedure allows not only a measurement of the energy deposited by individual tracks in the detector, but also to obtain an estimation of the resolution along the drift time coordinate.

The major contribution to the spatial resolution along the drift coordinate comes from electronic noise (i.e., the signal to noise, S/N, ratio). The effects produced by wire misalignment and diffusion of the electron cloud during drift have been observed to be less important.

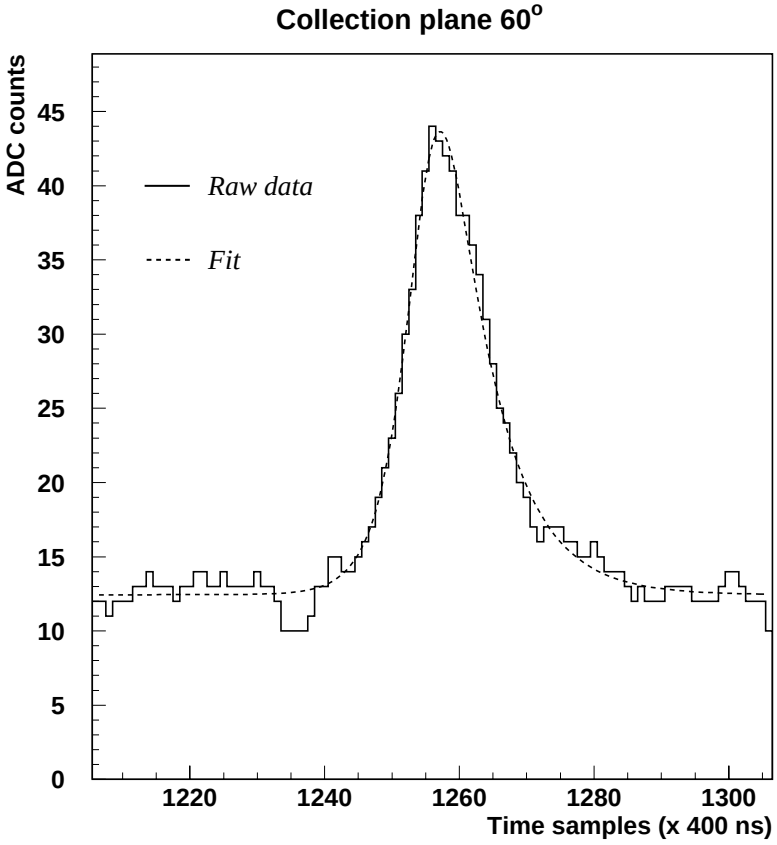

Figure 3.55: Digitized signal from a collection wire (solid histogram). The dashed line is the result of the signal shape fit as described in the text. The fit rise time value is 1.4μs.

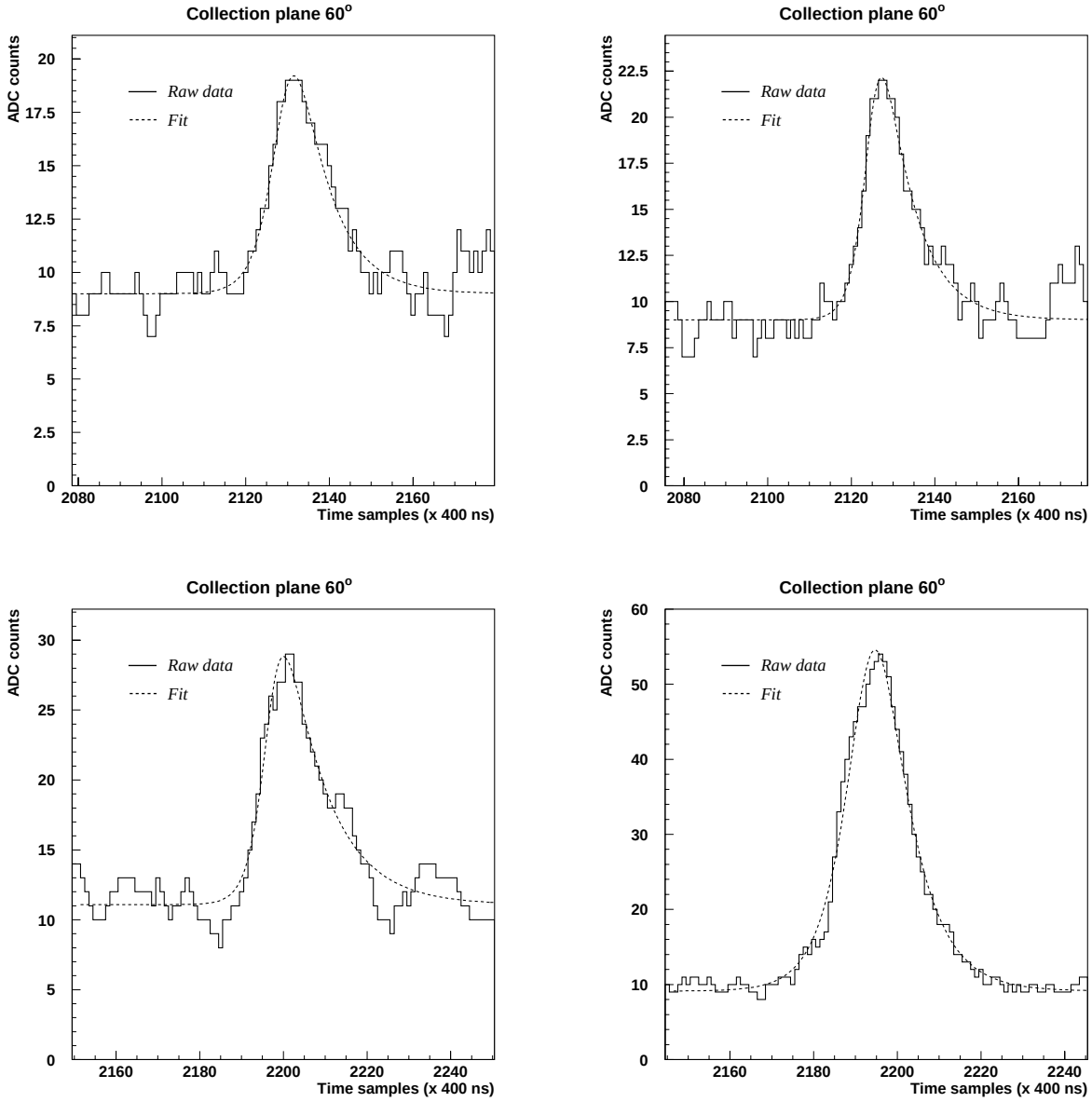

Figure 3.56: *Collection* signals from four hits along the track of a muon stopping inside the detector. Increasing peak areas (from left to right and top to bottom) exemplify the increase of the dE/dx towards the end point of the track.

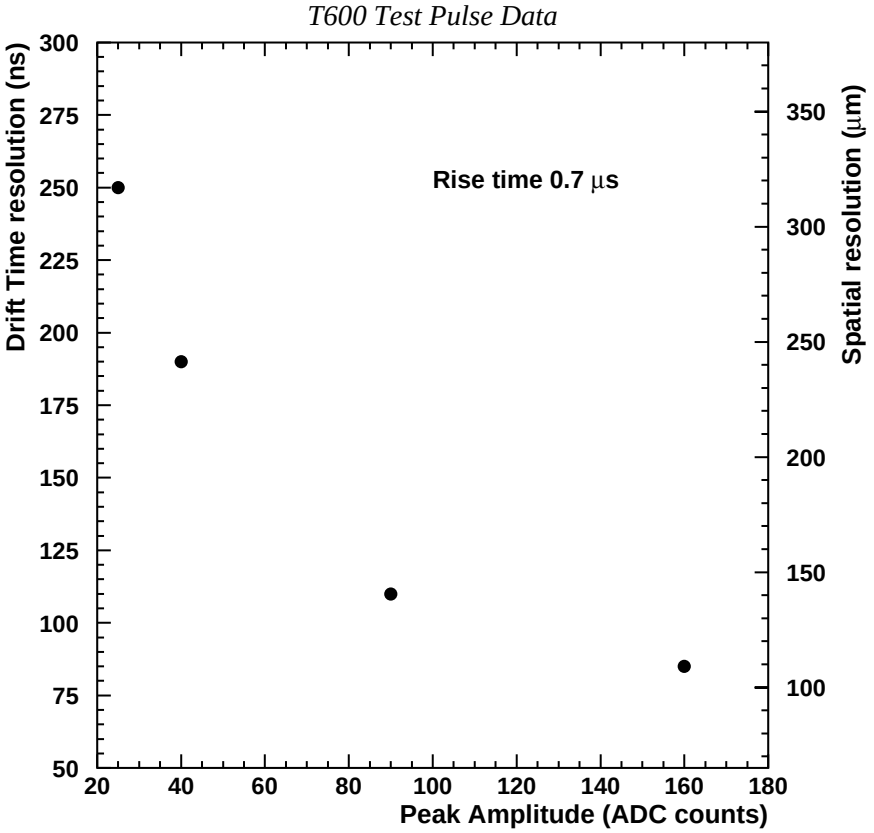

Figure 3.57: Contribution of the S/N ratio to the resolution in the drift time measurement (left-hand side). The x-axis shows the value of the peak amplitude (in ADC counts) for test pulse data of 10, 20, 50 and 100 mV. In the right hand side, the corresponding spatial resolution has been calculated using the measured value of 1.59 mm/μs

To study how the S/N ratio affects the space resolution, we fit test pulse data with rise times similar to those expected for a typical signal. Four different test pulse amplitudes have been studied (100, 50, 20 and 10 mV) corresponding to four different S/N ratios. Figure 3.57 shows the drift time resolution in nanoseconds as a function of the peak amplitude (in ADC counts). The time resolution varies from $\simeq$ 75 ns for the highest amplitude to a value of 250 ns when the 10 mV test pulse signal is considered. The right-hand side axis shows the corresponding spatial resolution (computed taking a drift velocity equal to the measured value of 1.59 mm/μs).

The measurement of the space resolution along the drift coordinate has been performed using cosmic ray muons. To avoid multiple scattering contributions, we estimate the spatial resolution through consecutive fits of hit triplets occurring in consecutive wires. The outer hits define a straight line. The distance (d) of the middle hit to the straight line is then computed. The spatial resolution, σ, is finally given by $\sigma = \sqrt{(2/3) < d^2 >}$, where $< d^2 >$ is the root mean square value of the distribution of distance measurements along the track.

Figure 3.58 shows the drift time resolution for a sample of cosmic ray muons. For a field intensity of 500 V/m and signal sampling of 400 ns, minimum ionizing particles show a spatial resolution in the drift coordinate of $\simeq$ 400 μm. This result agrees with the estimations obtained using test pulse data. We have also observed that the spatial resolution does not sensibly vary as a function of the drift distance.

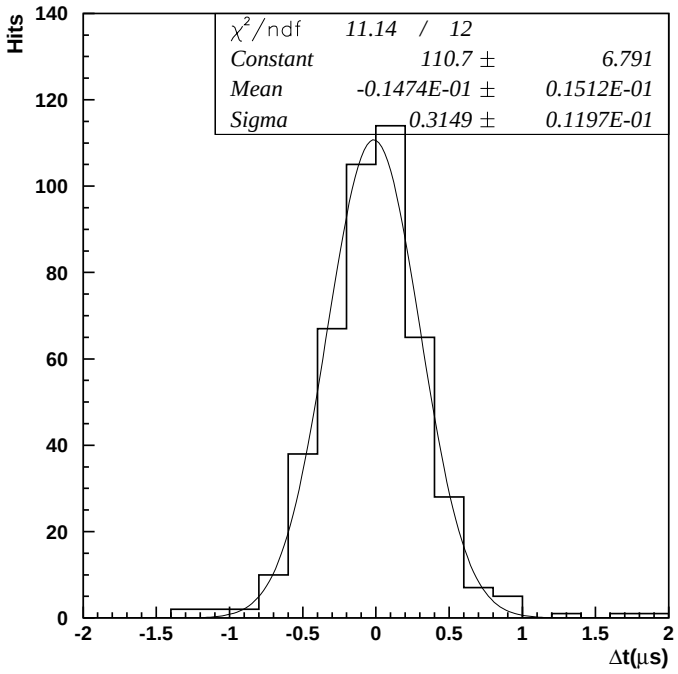

Figure 3.58: Drift time resolution for a data sample of cosmic ray muons. Assuming a drift velocity of 1.59 mm/μs, the single hit spatial resolution is $\simeq$ 400 μm.

3.5.8 Track reconstruction

The extraction of some basic parameters, namely: electron lifetime, uniformity of detector response, energy resolution, landau fluctuations, single point space resolution, particle identifications by dE/dx, 3D reconstruction, can be performed studying isolated tracks crossing or stopping in the T300 detector.

The reconstruction procedure consists of the following steps:

- calibrating the gain of the electronic readout chain by means of test pulse signals;
- finding the signal clusters on each wire applying an algorithm similar to that used in the Daedalus chip;
- fitting each cluster with a phenomenological function able to reproduce faithfully a wide range of signal shapes (see eq. 3.10).
- exploiting the fitted parameters to actually reconstruct the 3D geometry and the physics parameters associated to the tracks.

As a preliminary example, we show the results of 3D reconstruction on an isolated minimum ionizing track crossing a large fraction of the detector volume.

We recall that the *Collection* plane is read with current amplifiers hence the charge deposited on each wire is given by the area of the signal cluster.

The calibration of the readout chain has been checked fitting test pulse signals with function in Equation 3.10. Figure 3.59 shows the distribution of the test pulse areas over all collection wires. From the design values we expect gain non-uniformity smaller than few percent and a S/N better than 10: experimentally we find a spread of 8 percent which is probably due mainly to electronic noise. This allows to skip the equalization procedure for this preliminary analysis. A deeper investigation is planned to disentangle the two contributions.

For the track reconstruction, the projections on the wire planes are recognized visually and then are associated matching start and end points using the time coordinates. This allows to calculate the effective track length in 3D and the track angles with respect to the *Collection* planes where we measure the deposited charge. Due to the fact that the planes are at 60 degrees to each other, the effective track length is given by the following formula

$$\Delta L = \sqrt{\Delta t^2 + 4/3 \cdot (\Delta c^2 + \Delta i^2 - \Delta c \cdot \Delta i)} \tag{3.11}$$

where Δc and Δi are the projections on the *Collection* and *Induction* planes respectively.

On the *Collection* plane, signal clusters are searched and fitted along a line connecting the start to the end point. Figure 3.60 shows a track with 430 wires hit spanning a drift time of 0.57 ms. The effective track length seen by a collection wire is 4.87 mm.

Being the electron lifetime of the order of 1 ms (comparable to the drift time), the signal fitted charge has to be corrected by a factor $e^{\frac{t-t_{min}}{\tau}}$, where τ is the lifetime which has been measured from the track data (see Figure 3.61), t is the drift time and t_{min} is the drift coordinate of the cluster closest to the wire chamber.

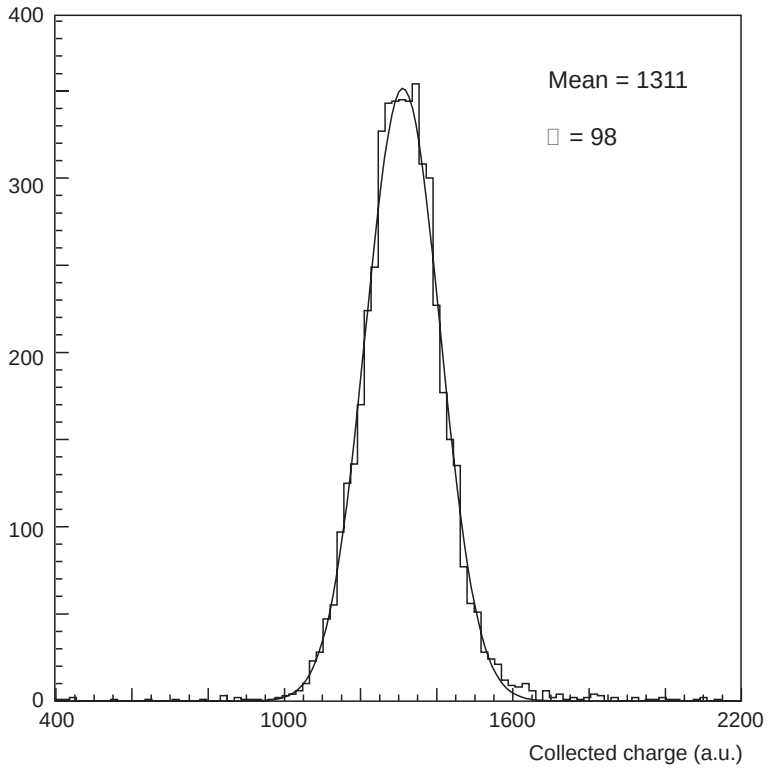

Figure 3.59: Distribution of the test pulse areas measured by all wires in a *Collection* plane. The pulse is injected on analog boards (amplitude= 10 mV, frequency= 1.5 kHz).

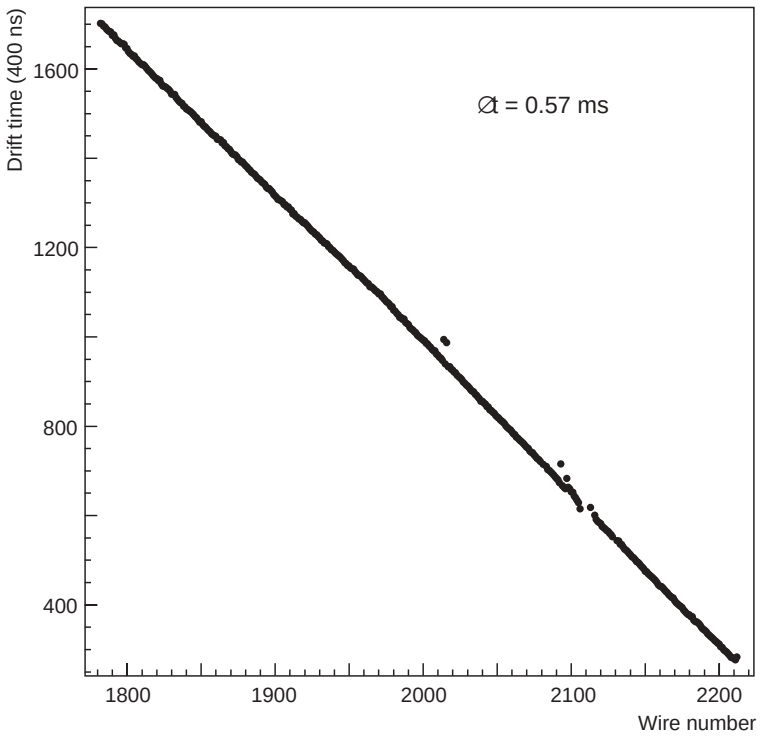

Figure 3.60: Bidimensional reconstruction of a track in the *Collection* plane: only the recognized and fitted hits are plotted.

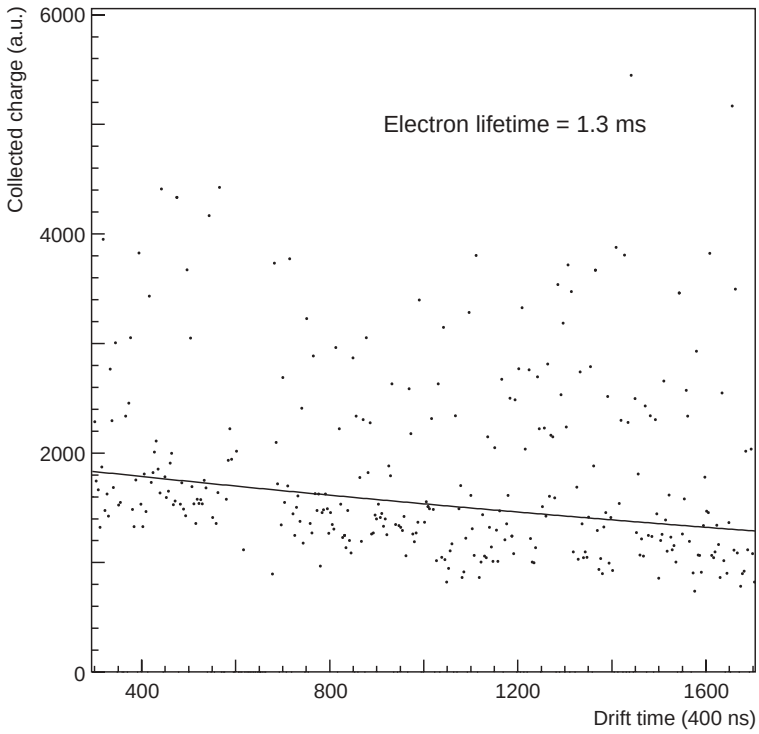

Figure 3.61: Collected charge vs. drift time: non-infinite electron lifetime is responsible of the reduction of the integral; lifetime is calculated fitting this distribution with a exponential function; large charge values haven't been used in the fit (truncated mean method).

3.5.9 Landau distribution

The fitted signals can be used to produce the distribution of the energy deposited by a *m.i.p.* in liquid argon (see Figure 3.62).

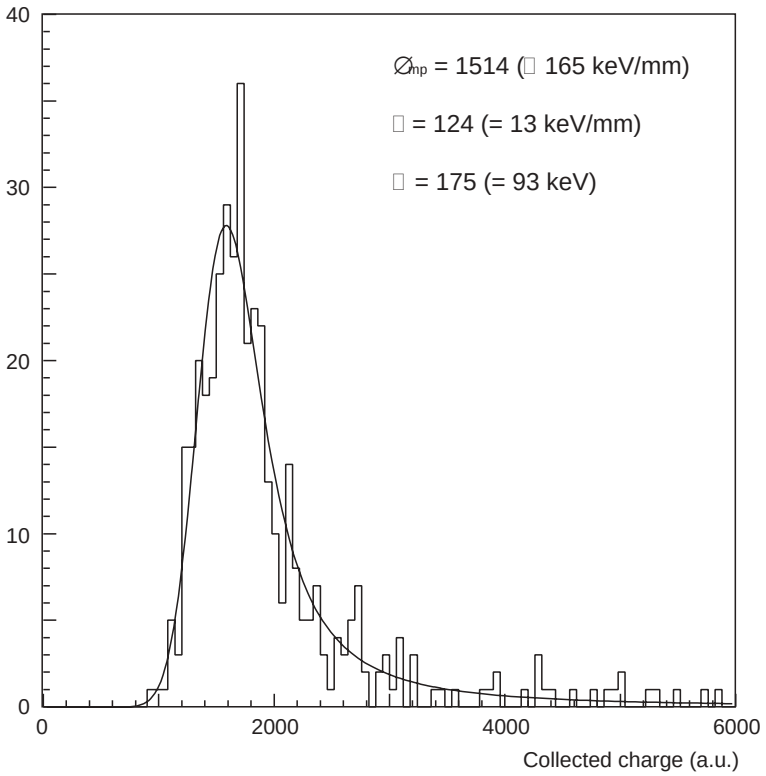

Figure 3.62: Distribution of a m.i.p. measured signals areas: Δ_{mp} is the most probable energy loss.

A fit with the convolution of a Landau with a Gaussian distributions reproduces quite well the experimental data and allows to extract the characteristic parameters: the most probable energy loss Δ_{mp} for LAr is easily calculable (165 keV/mm) and can be used to transform the units of the fit in energy. The mean energy loss per collision (Landau parameter) is then found to be 13 keV/mm (to be compared to the expected theoretical value of 10 keV/mm). The Gaussian component of the fit accounts for the electronic noise and gains smearing and is found to be 175 a.u. (93 keV). This number is larger than that obtained with the test pulses. Part of the increase can be explained by the correction factor applied for the finite lifetime. Without correction, the Gaussian spread is about 140 a.u. (75 keV). Both the Landau and Gaussian parameters are slightly larger than expected; the understanding of this requires further study on a larger sample of tracks.

Other parameters characterizing the detector performance could be extracted in a similar way and this will be done in the future.

Chapter 4

THE GENERAL LAYOUT

4.1 Detector considerations

In order to perform simultaneously LBL and atmospheric neutrino analysis and nucleon decay search, separating efficiently signal to background, this detector has to be operated underground and to have sophisticated imaging, calorimetric and μ-momentum capabilities.

Imaging should be provided by a modern bubble chamber-like technology since:

- it has to be able to provide high resolution, unbiased, three dimensional images of ionizing events;
- it has to provide an accurate measurement of the basic kinematical properties of the particles of the event, including particle identification.
- it has to accomplish simultaneously the two basic functions of target and detector.

Unlike traditional bubble chambers, limited by a short window of sensitivity after expansion and not self-triggerable, the detector should remain fully and continuously sensitive, self-triggering and readout without dead time. In addition, operating underground introduces severe safety requirements which exclude traditional flammable and/or pressurized liquids. Finally the mass of the largest bubble chamber ever constructed is about two orders of magnitude smaller than the one required here.

We consider the ICARUS technology as the ideal detector choice for rare event search such as proton decay and neutrino interactions.

The following main features of the liquid Argon detector technology have been carefully investigated and constitute the basis for the present proposal:

- The accuracy of localization of a single "bubble" is about 150 μm r.m.s., determined by the amplifier noise. Diffusion effects are small even for the longest drift lengths.
- The bubble diameter is about 3 mm, similar to the one of the famous GARGAMELLE bubble chamber.
- Unlike bubble chambers, the ionization measurement along the track is excellent and it can be used to determine the momentum (speed) of non relativistic particles with a good accuracy.

- The pure Argon is also an excellent calorimeter medium with very good energy resolution. Moreover, the calorimetric determination of highly ionizing tracks can be improved by doping.

- For long tracks in the liquid, like the case of the leading muon from ν_μ interactions, an excellent accuracy ($\approx 20\%$ for a 5 meter long track) of the muon momentum can be obtained by multiple scattering measurements. For short stopping tracks, the energy can be accurately measured from the range and the nature of the particle identified by the ionization as a function of the range.

- Liquid Argon is also an excellent scintillator. Scintillation light has an attenuation path of about 0.8 meters and it can be used for triggering purposes.

The superior quality of the event vertex inspection and reconstruction of the liquid Argon volumes would be ideally complemented by the addition of an external module capable of magnetic analysis of the muons escaping the chamber. Bubble chambers have in fact often been very similarly complemented in the past by external identifiers. An iron muon tracking spectrometer fulfills this job.

4.2 Detector layout

A detector suitable for long baseline neutrino experimental activity can be similar to that of a "classical" neutrino detector, segmented into almost independent supermodules and optionally complemented by a muon spectrometer. As a baseline configuation, we consider a detector consisting of T600+2×T1200 modules (see Figures 4.1, 4.2, 4.3, 4.4, and 4.5). This mass configuration can of course be enlarged with the help of additional T1200 modules in Hall B. Given the long-term nature of the ICARUS experiment, we consider this as a likely possibility.

The liquid Argon module is dedicated to extremely high resolution tracking, dE/dx measurements, full electromagnetic and hadronic calorimetry, where electrons and photons are identified and measured with extremely good precision and π/μ, K and p separation is possible at low momenta. The muon spectrometer has aim of providing the measurement of the sign and momentum of muons escaping the liquid Argon module. Such a system behaves as a complete building block, capable of identifying and measuring electrons, photons, muons and hadrons produced in the events.

The basic constraints in the current design are the following:

- Retaining as much as possible the basic features and know-how elaborated during the construction of the ICARUS T600 prototype;

- Optimization of the available space in Hall B at LNGS;

- Time scale (tradeoff between R&D and freezing of solutions).

The present design is based on a liquid Argon segmentation of 1200 tons of active mass. The spectrometer, in its simplest version, is foreseen to be composed of non-instrumented 3-meters-long magnetized iron, and will act only as a muon bender. The direction of a track will be measured in the liquid Argon modules before and after the iron spectrometer.

Figure 4.1: Perspective view of the baseline detector with 2 supermodules. Each liquid Argon module contains about 1200 tons of active Argon.

Figure 4.2: Side view of the ICARUS T600 (left) plus two T1200 detectors.

Figure 4.3: Top view of the ICARUS T600 (left) plus two T1200 detectors.

Figure 4.4: Front view of the ICARUS 2×T1200+T600 detector as seen from a neutrino coming from CERN.

Figure 4.5: Close view from the top of the ICARUS 2×T1200+T600 detector. The electronic racks are clearly visible. The computerized version of the famous physicist P. Picchi is visible on the lower-right corner of the figure.

The stacking of T600-like modules offers the advantage that the original construction strategy of the T600 is preserved: (i) each module can be built and tested outside the underground laboratory; (ii) more modules can be built in parallel if different working groups can be formed and then transported and installed independently in Hall B. Also, the serialization of the present T600 design could offer a number of obvious advantages, since the time and efforts required for the design are minimized and the testing of all the solutions has been achieved directly through the assembly of the first T600 detector.

4.3 The general guidelines for a large, massive detector

The leading constraints when designing new LAr TPC units are essentially three:

- Keeping the basic features of the ICARUS technology.
- Availability of underground space at LNGS.
- Time schedule.

A fundamental constraint, the availability of the necessary fundings, has not been explicitly considered at this stage. However evaluation of the overall cost breakdown is at the level of other detectors of comparable size.

We have decided to maintain the basic properties of the ICARUS T600 detector unchanged in order to benefit from the already acquired experience, available design and technical tools.

We assume the experiment will be installed in Hall B at the Gran Sasso underground laboratory. The transverse dimension of ICARUS should expand over the full hall cross-section, leaving all around the minimum space needed for the external services of the experiment and for the safety devices. The detector length is a critical issue. The longest possible extension, up to about 120 m (corresponding to 5 ICARUS T1200 modules), would guarantee the maximum sensitivity reach in terms of physics.

The combination of all these constraints led us to the definition of the basic element of the new ICARUS detector: the **ICARUS T1200 module**.
It guarantees the "modularity" requirements necessary to cope with the space and time limitations and preserves an internal flexibility, open to future technological refining and upgrades. At this stage, we propose the construction of two T1200 modules (see Figure 4.1) to be added to the existing T600 module with a total length of the experiment of about 60 m and a total mass of 3.7 kton of liquid argon[1].

In chapter 6, a description of the T1200 module is provided, including the main technological aspects and achievements that form the basis of the ICARUS proposal.

[1]Each basic T600 element contains about 750 tons of argon. The imaging region corresponds to 470 tons while the energy deposited in the rest of the argon is readout via "pads".

4.4 Solutions for the new liquid Argon modules.

The design of new ICARUS-type modules is the main topic of the present document. Obviously, this design includes all benefits from the experience gained in building and running the T600 module. We have chosen to consider a solution in which the new modules are made of an array of "T600-like" sub-modules (four sub-modules, arranged in two pairs, each one made of two sub-modules superimposed). There are obvious arguments in favour of a smaller number of larger detectors:

- Easier handling (fewer units);
- Lower construction and running costs:
- Fewer, non-scalable, auxiliary units (pumps, recirculators, controls, etc.);
- Fewer electronics channels;
- Better sensitive to total volume ratio;
- Lower heat transmission through the insulation (LN_2 consumption);
- Lower total length and better occupation of the Hall B volume.

On the other hand, increasing dimensions of the single sub-unit enhance the impact of some issues and tend to increase the complication of the associate technical solutions:

- LAr purity achievement and maintenance;
- Thermal stability;
- Assembly operations;
- Safety.

A significant modification of the present T600 structure would require a time (and a cost) for engineering and testing far beyond the present constraints imposed by the CNGS beam starting date. However, we keep open the possibility to modify the structure of additional modules, following the first or the second T1200, especially in view of a significant sensitive mass increase for proton decay and atmospheric neutrino searches.
We recall here the main criteria that have driven the actual design of the T600 module:

- the drift length (verified experimentally in stable conditions) of about 3 m induces a detector total width of about 4 m;
- in the orthogonal direction this dimension leads to a sensible wire length (60^o with respect to the vertical direction) of about 4 m; this value allows an excellent signal to noise ratio (the capacity of the sensible wires in the chambers is about 20 pF / m).
- the total detector length is defined to obtain a transportable cryostat.

These constraints lead to a LAr container (the so called "half-module") with internal dimensions of about $4 \times 4 \times 20$ m^3 (the actual internal dimensions of the T600 half-module are $3.6 \times 3.9 \times 19.6$ m^3 for a volume of about 275 m^3). With such dimensions the previous requirements are fulfilled. Moreover, the cryostat dimensions allow the use of a highly safe technology, i.e. the aluminum honeycomb panel structures. This solution, well known in aeronautics industry, provides high mechanical stability, with modest weight, as demonstrated during the T600 technical run. The major advantage of our approach is that the original construction strategy of the T600 is preserved:

- each module will be built and tested (for vacuum tightness and mechanical resistance) outside the underground laboratory;
- more modules can be built in parallel if different working groups can be formed and then transported and installed independently in Hall B.

The serial production of the current T600 design offers a number of obvious advantages, as well:

- the time and efforts required for the design are minimized;
- a test of all the solutions have been already achieved during the T600 module construction;
- the experience acquired during the T600 construction and run will be fully exploited by the collaboration and by the industries as well;
- the tooling and the auxiliary plants used for the T600 construction, test and run will be preserved.

In our design we have tried to maximize the occupancy of the Hall B cross-sectional area taking into account the existing facilities (crane) and the necessary technical volumes (for services, passageways, etc.). We only made few modifications of the present T600 basic structure:

- four LAr containers in two superposed pairs, supported by an appropriate stainless steel structure, have been grouped into a common insulation box to reduce the transverse area and minimize the LN_2 consumption rate;
- the maximum drift is 3 m instead of the present 1.5 m;
- calorimetric readout of the LAr non-imaging regions has been added to recover the energy deposition in the LAr volumes outside the main drift volume.

We finally recall that the installation of an array of T600 modules in Hall B was part of the original programme of the ICARUS Collaboration[13] and a study for the installation of 8 T600-like modules is part of the basic engineering design of the single T600 made by Air Liquide at the beginning of 1997.

Chapter 5

THE PHYSICS PROGRAMME

5.1 Overview

The ICARUS physics programme is rather broad: it covers in many complementary ways the questions related to neutrino oscillations with the direct observation of atmospheric neutrinos and with the study of CERN LBL neutrinos. In addition, ICARUS is also sensitive to solar and supernova neutrinos. The second important physics item is related to the stability of matter. ICARUS can provide background-free searches for nucleon decays in a wide variety of decay modes. In addition, we think that the ICARUS technology is a very competitive solution for future neutrino factories.

The ICARUS physics programme has been discussed in many occasions. We present in this section an overview of the programme refering the interrested reader to the available extensive literature on the subject.

We describe our physics programme in terms of exposure. Our physics estimations refer to a "baseline configuration" consisting of one T600 plus two T1200 modules. In this case, one year of running corresponds to an exposure of 2.35 kton×year, since every T600-equivalent module contributes to a fully imaging liquid Argon mass of 470 tons. This mass configuration can of course be enlarged with the help of additional T1200 modules in Hall B. Given the long-term nature of the ICARUS experiment, we consider this as a likely possibility.

We note that events occuring in the non-imaging part, whose deposited energy is read out by coarser "pads" (see Section 6.9), have for the moment not being considered for physics analyses. These events will of course be acquired in the experiment if they deposit energy in the imaging part or if they trigger the photomultipliers via scintillation. We foresee that a fraction of these events will be adequate for physics analyses, in particular for atmospheric neutrino studies, even though of coarser resolution.

5.2 Neutrino oscillation framework

The most important physics issue of the ICARUS physics programme is addressed to the question of neutrino masses and oscillations. Only new generation experiments with enhanced experimental capabilities may provide direct answers to this question. Within

this context, ICARUS provides, through a large variety of measurements, new information on the nature of the neutrino.

The "atmospheric neutrino anomaly", first published by Kamiokande in 1988 [36] and, at the time, quite controversial, has been strongly confirmed by the latest measurements from SuperKamiokande [37], Soudan-2 [38] and MACRO [39].

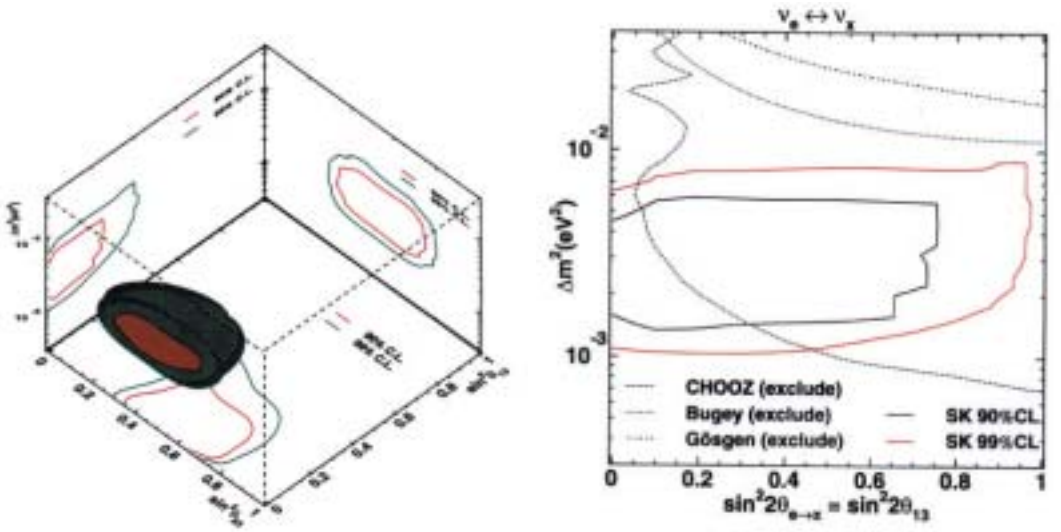

Figure 5.1: Three flavor mixing analysis of the SuperKamiokande data (from Ref.[40]).

The atmospheric anomaly, observed by various experiments employing different techniques, stands today as a clear and convincing evidence that muon neutrinos are "disappearing". The statistically strongest result is obtained by SuperKamiokande.

The CHOOZ[41] experiment, that has not seen any anomalous effect, tells us that the electron-neutrino ν_e does not significantly disappear in the atmospheric neutrino region. SuperKamiokande also shows no evidence for large ν_e disappearance.

The most natural explanation of the atmospheric anomaly is $\nu_\mu \leftrightarrow \nu_\tau$ oscillation. The Δm^2 parameter characterizing this oscillation seems to be smaller than initially suggested by Kamiokande. While the Kamiokande data seemed to favour Δm^2 values in the region of 10^{-2} eV^2, the new Superkamiokande results are centered around 3×10^{-3} eV^2. The oscillation parameters have been further constrained by Superkamiokande with a combined fit of their neutrino sample and their upward going muon samples. This fit is currently indicating a range within $1.6\times10^{-3} < \Delta m^2 < 3.6\times10^{-3}$ eV^2 at the 90%C.L.[37].

Since three flavors of light neutrinos are known to exist, the minimal framework to analyze neutrino oscillations should contain the 3×3 mixing matrix U, which relates the flavor eigenstates $\nu_\alpha(\alpha = e,\mu,\tau)$ to the mass eigenstates $\nu_i'(i = 1,2,3)$: $\nu_\alpha = U_{\alpha i}\nu_i'$. This matrix can be parameterized as:

$$U = \begin{pmatrix} c_{12}c_{13} & s_{12}c_{13} & s_{13}e^{-i\delta} \\ -s_{12}c_{23} - c_{12}s_{13}s_{23}e^{i\delta} & c_{12}c_{23} - s_{12}s_{13}s_{23}e^{i\delta} & c_{13}s_{23} \\ s_{12}s_{23} - c_{12}s_{13}c_{23}e^{i\delta} & -c_{12}s_{23} - s_{12}s_{13}c_{23}e^{i\delta} & c_{13}c_{23} \end{pmatrix} \qquad (5.1)$$

with $s_{ij} = \sin\theta_{ij}$ and $c_{ij} = \cos\theta_{ij}$.

A natural assignment of the mass difference squared Δm^2_{12} is to explain the solar neutrino deficit and the mass difference squared Δm^2_{32} to describe the atmospheric neutrino anomaly. This choice implies that $|\Delta m^2_{21}| < |\Delta m^2_{32}| \approx |\Delta m^2_{31}|$. In first approximation, the oscillation phenomena governed by the two mass differences decouple and the effects produced by Δm^2_{12} are small at high energy for the considered baselines. In the case of one-mass scale approximation, the oscillation probabilities are:

$$\begin{aligned}
P(\nu_e \to \nu_e, E, L) &= 1 - \sin^2(2\theta_{13})\Delta^2_{32} \\
P(\nu_e \to \nu_\mu, E, L) &= \sin^2(2\theta_{13})\sin^2(\theta_{23})\Delta^2_{32} \\
P(\nu_e \to \nu_\tau, E, L) &= \sin^2(2\theta_{13})\cos^2(\theta_{23})\Delta^2_{32} \\
P(\nu_\mu \to \nu_\mu, E, L) &= 1 - 4\cos^2(\theta_{13})\sin^2(\theta_{23})\left[1 - \cos^2(\theta_{13})\sin^2(\theta_{23})\right]\Delta^2_{32} \\
P(\nu_\mu \to \nu_\tau, E, L) &= \cos^4(\theta_{13})\sin^2(2\theta_{23})\Delta^2_{32}
\end{aligned} \tag{5.2}$$

where $\Delta^2_{32} = \sin^2\left((m^2_3 - m^2_2)L/4E\right)$.

The current experimental constraints on the oscillation parameters are shown in Figure 5.1(left). The current atmospheric data yields a rather poor constraint on the θ_{13} angle, because of the cancellation of the effect due to the subleading $\nu_\mu \to \nu_e$ and $\nu_e \to (\nu_\mu/\nu_\tau)$ transitions. The best constraint comes from CHOOZ[42] which yields $\sin^2 2\theta_{13} \lesssim 0.1$ (see Figure 5.1(right)). Hence, the relevant questions to be answered as far as the atmospheric neutrinos are concerned are the following: what is Δm^2_{32} and what are the angles θ_{23} and θ_{13} ? Further studies of the solar neutrinos and atmospheric neutrino at very low energy will shed light on the values of Δm^2_{12} and θ_{12}.

5.3 Physics simulation

In order to study the capabilities to reconstruct neutrino or rare events, we use fully simulated events generated using a detailed description of the different layers and materials of the T600 detector[43]. The FLUKA package is used to track all final state particles in the detector.

For the simulation the detector was divided in different regions of homogeneous material composition, as is shown in figure 5.2. The different components, from inside to outside the detector, are the following:

1. The ICARUS T600 detector **internal volume** consists of two identical, independent half-modules filled with liquid Argon. In each module a central vertical cathode plane is facing on each side a wire chamber made by three wire planes. Four different regions were considered inside the internal volume:

   - The LAr *active volume*, defined as the parallelepiped with a side surface equal to the wire chamber surface and a width equal to twice the distance between the first wire plane (0°) and the cathode.
   - A 7.6 mm thick *stainless steel layer* (AISI 304L) of 20 tons surrounding the active volume.
   - The LAr *inactive volume*, the dead space left between the wire chambers and the dewar walls.

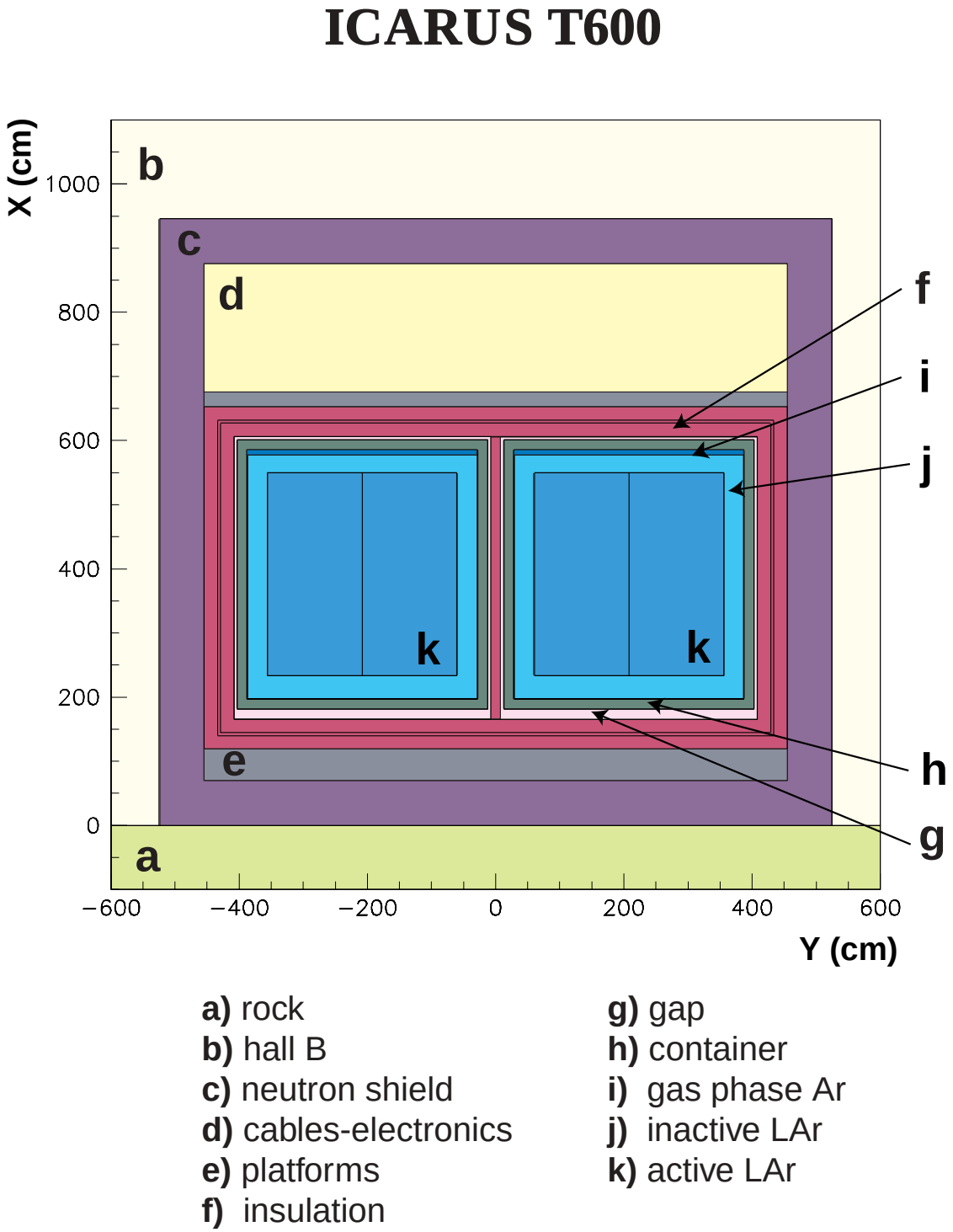

Figure 5.2: Transversal view of the ICARUS T600 detector showing the different layers considered in the simulation.

- A 8 cm *gas phase Argon* layer on the top of the internal volume.

2. The LAr volume of each half-module is contained inside a structure of aluminum honeycomb panels reinforced by aluminum frames. A homogeneous **aluminum honeycomb container** was considered in the simulation.

3. The two half-modules are surrounded by a common thermal **insulation layer** made of two Nomex (aramid fiber pre-impregnated paper) honeycomb panels with an intermediate aluminum shield cooled by nitrogen gas. An additional 15 cm thick Nomex insulation layer was generated between the two containers.

4. A 5 cm thick foam **gap** is located between the aluminum containers and the insulation layer.

5. Bottom and top aluminum **platforms**.

6. Upper empty space for **cables and electronics**.

7. The **shielding layer** against neutrons consists of a 70 cm thick layer of polyethylene tubes filled with boric acid. The inner radius of the tubes is 9 cm and the thickness is 1 cm. Taking into account these data, an average density of 0.621 g/cm^3 was computed and included in the simulation for this layer.

The neutrino-cross sections and the generation of neutrino interactions is based on the NUX[44] code. This code, benchmarked with the NOMAD experiment data, can be used from kinematical threshold up to neutrino energies in the range of tens of TeV. NUX includes all basic processes to properly describe neutrino interactions in different kinematical regimes. In particular, a distinction is made among the following processes: quasi-elastic process, inelastic process and charm production. These processes are appropriately matched to reproduce a total (inclusive) and existing exclusive experimental data to the best of current experimental knowledge (which unfortunately in the region here of interest is rather poor). The mass of the outgoing lepton and of the target nucleus are taken into account in all places. In order to take into account of nuclear effects, a primary nucleon is chosen by FLUKA, a neutrino event is then generated on this nucleon, then final state particles are propagated through the nucleus with PEANUT. Nuclear effects can be roughly divided in those of nuclear potential and those due to reinteractions of decay products. Reinteractions in the nuclear medium play an important role. Final state products can loose part of their energy in collisions, or even be absorbed in the same nucleus where they have been created. This is particularly true for pions, that have an important absorption cross section on nucleon pairs, while positive kaons have a very small interaction probability. Nuclear effects have also been benchmarked with NOMAD experimental data and found to be mandatory to reproduce the kinematical properties, in particular in the transverse plane, of the observed neutrino events.

5.4 Atmospheric neutrino experiment

The comprehensive investigation of atmospheric neutrino events beyond what already achieved in SuperKamiokande requires a fiducial mass of several ktons, in order to reach the level of at least one thousand events per year.

The physics goal of new atmospheric neutrino measurements are to firmly establish the evidence of neutrino oscillations with a different experimental technique, possibly free of systematic biases, measure the oscillation parameters and clarify the nature of the oscillation mechanism.

The capability to observe all separate processes, electron, muon and tau neutrino charged current events (CC) and all neutral currents (NC) without detector biases and down to kinematical threshold is also highly desirable.

A detector based on the ICARUS technique will provide an observation of atmospheric neutrinos of a very high quality, thanks to its unique performances in terms of resolution and precision.

Unlike measurements obtained up to now in water Cherenkov detectors, which are in practice limited to the analysis of "single-ring" events, complicated final states with multi-pion products, occurring mostly at energies higher than a few GeV, will be completely analyzed and reconstructed in ICARUS. This will be a significant improvement with respect to previous observations.

The perspective of ICARUS is to provide redundant, high precision measurement and minimize as much as possible the systematics uncertainties of experimental origin which affect the results of existing experiments. Improvements over existing methods are expected in

1. neutrino event selection
2. identification of ν_μ, ν_e and ν_τ flavors
3. identification of neutral currents

The physics performance of the ICARUS detector in the observation of the atmospheric neutrinos has been described in some details in the ICANOE proposal[18], in which a chapter was dedicated to it. We point out that these studies were based only on the liquid Argon target, and that the external spectrometer did not play any rôle. Hence the physics capabilities described in the ICANOE proposal remain unchanged.

We recall the expected atmospheric neutrino rates obtained per year in Table 5.1, with and without $\nu_\mu \rightarrow \nu_\tau$ oscillation hypothesis ($\sin^2 2\theta = 1$).

Muon-like events contain an identified muon and correspond to $\nu_\mu/\bar{\nu_\mu}$ CC events. Electron-like are events with an identified electron and are $\nu_e/\bar{\nu_e}$ CC events. Given the clean event reconstruction, the ratio R of "muon-like" to "electron-like" events can be determined free of large experimental systematic errors. In fact, the expected purity of the samples is above 99%. In particular, the contamination from π^0 in the "electron-like" sample is expected to be completely negligible.

We split further the muon-like events into contained and partially-contained samples. For the contained events (62% of the total), the muon energy is precisely determined by integration of the dE/dx measurements along the track. For partially contained events

	5 kton×year				
		Δm^2_{23} (eV^2)			
	No osci	5×10^{-4}	1×10^{-3}	3.5×10^{-3}	5×10^{-3}
Muon-like	675 ± 26	515 ± 23	495 ± 22	470 ± 22	455 ± 21
Contained	418 ± 20	319 ± 18	307 ± 18	291 ± 17	282 ± 17
Partially-Contained	257 ± 16	196 ± 14	188 ± 14	179 ± 13	173 ± 13
No proton	260 ± 16	190 ± 14	185 ± 14	170 ± 13	165 ± 13
One proton	205 ± 14	160 ± 13	150 ± 12	145 ± 12	140 ± 12
Multi-prong	210 ± 14	165 ± 13	160 ± 13	155 ± 12	150 ± 12
$P_{lepton} < 400$ MeV	285 ± 17	205 ± 14	200 ± 14	185 ± 14	175 ± 13
$P_{lepton} \geq 400$ MeV	390 ± 20	310 ± 18	295 ± 17	285 ± 17	280 ± 17
Electron-like	380 ± 19	380 ± 19	380 ± 19	380 ± 19	380 ± 19
No proton	160 ± 13	160 ± 13	160 ± 13	160 ± 13	160 ± 13
One proton	120 ± 11	120 ± 11	120 ± 11	120 ± 11	120 ± 11
Multi-prong	100 ± 10	100 ± 10	100 ± 10	100 ± 10	100 ± 10
$P_{lepton} < 400$ MeV	185 ± 14	185 ± 14	185 ± 14	185 ± 14	185 ± 14
$P_{lepton} \geq 400$ MeV	195 ± 14	195 ± 14	195 ± 14	195 ± 14	195 ± 14
NC	480 ± 22	480 ± 22	480 ± 22	480 ± 22	480 ± 22
TOTAL	1535 ± 39				

Table 5.1: Expected atmospheric neutrino rates in case no oscillations occur and assuming $\nu_\mu \rightarrow \nu_\tau$ oscillations with maximal mixing. Four different Δm^2 values have been considered. Errors are statistical only. With the considered detector configuration, this numbers correspond to two years of running.

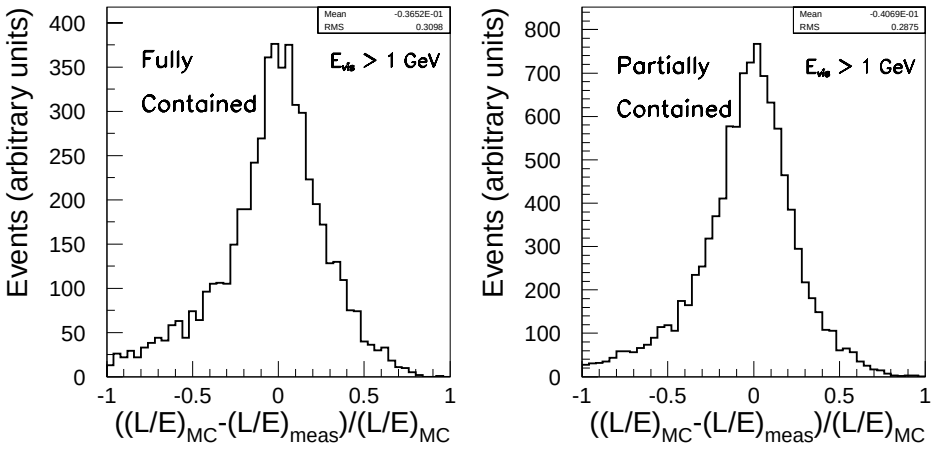

Figure 5.3: Full simulation of the L/E resolution in atmospheric events for contained and non-contained events.

(38% of the total, average neutrino energy 4.5 GeV), in which the muon escapes the detector active volume, the muon momentum is estimated via the multiple scattering method (see ICANOE proposal[18]).

We illustrate also the expected kind of events, classified according to their final state multiplicity. We see that approximately 40% of muon-like events contain no proton in the final state[1], corresponding to the "one-ring" sample. The rest of the events will contain a proton or multi-prongs final states, which will provide, thanks to the precise reconstruction of all particles, a precise determination of the incoming neutrino energy and direction (for events with $E_{vis} > 1GeV$).

Finally, we also point out that in ICARUS atmospheric neutrino events can be analyzed down to production threshold, given the excellent imaging. We illustrate this by classifying the events according to the energy of the leading lepton (electron or muon). We split the samples into $P_{lepton} < 400MeV$ and $P_{lepton} > 400MeV$, which correspond to the threshold used in Superkamiokande. Almost 50% of the expected rate lies below the threshold and hence ICARUS can really contribute to the understanding of the low energy part of the atmospheric neutrino spectrum.

An improved observation of about 220 neutral current (NC) events per year is also expected, given the clean classification of charged current events based on the presence of electron or muon in the final state. In this case, the excellent e/π^0 separation plays a fundamental role to select an unbiased, free of background neutral current sample.

We highlight the L/E reconstruction performance, which is determined by the resolution on the determination of the incoming neutrino energy E and on its direction $\cos\theta_Z$, where θ_Z is the zenith angle. The result of a full simulation of events in liquid Argon yields an L/E resolution for events with visible energy $E_{vis} > 1$ GeV (approx. 40% events) of $\approx 30\%$ RMS (see Figure 5.3). The L/E distribution of muon and electron like events assuming a three family mixing scenario with $\Delta m^2_{32} = 3.5 \times 10^{-3}$ eV^2, $\sin^2\theta_{23} = 1$

[1] A proton is identified if its kinetic energy is above 50 MeV.

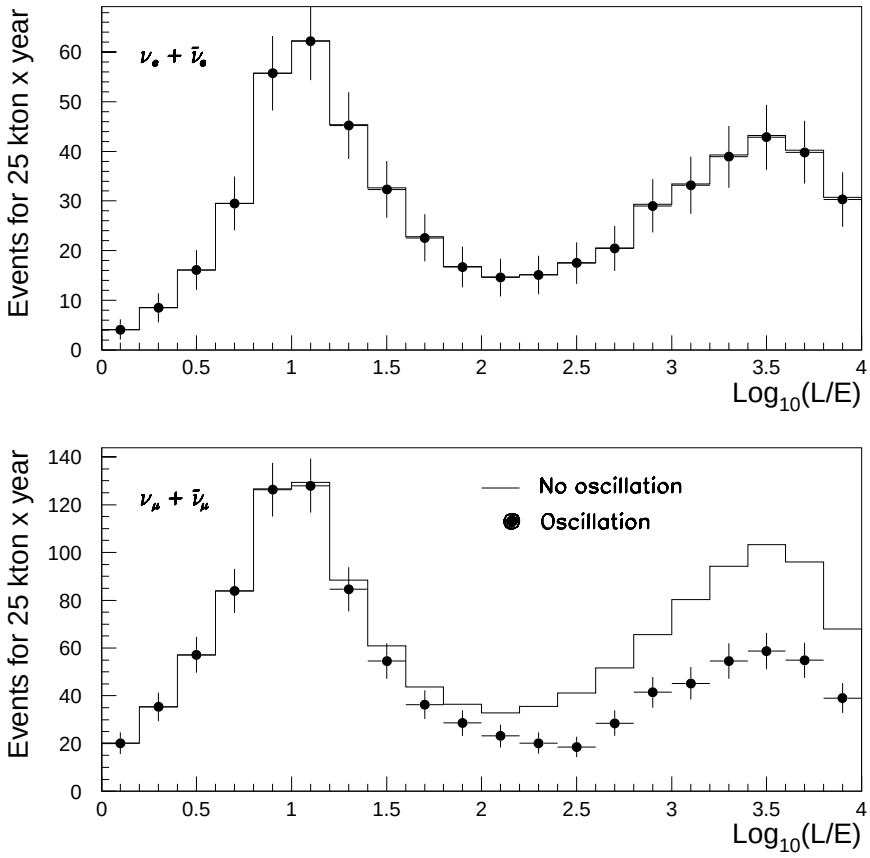

Figure 5.4: L/E distribution of muon and electron like events for three family mixing. The electron sample can be used as a reference sample. The plots are normalized to an exposure of 25 $kt \times year$ (corresponding to 10 years of data taking). A three-family mixing scenario was assumed with $\Delta m^2_{32} = 3.5 \times 10^{-3}$ eV^2, $\sin^2\theta_{23} = 1$ and $\sin^2 2\theta_{13} = 0.1$.

and $\sin^2 2\theta_{13} = 0.1$ is shown in Figure 5.4. The electron sample, essentially unaffected by the subleading $\nu_\mu \to \nu_e$ and $\nu_e \to (\nu_\mu/\nu_\tau)$ transitions, can be used as a reference sample. The plots are normalized to an exposure of 25 $kt \times year$.

More examples on the physics performance of a ICARUS liquid Argon detector can be found in the original ICANOE proposal [18]. In particular, tau appearance in the atmospheric "beam" is very attractive. Statistically significant signals require exposures of more than 20 kt $\times$ years.

Finally, an ICARUS detector can also measure upward–going muons from neutrinos interacting in the surrounding rock. In fact, the design and size of ICARUS are such to make it also a large area detector. The direction of the muon can be very well determined by looking at the direction of the delta-rays that accompany the muons as they traverse the liquid Argon volume (see Ref.[45]).

5.5 CNGS long-baseline experiment

In order to achieve a better understanding of neutrino phenomenology, it is fundamental to have coherent results from different kind of measurements, showing that all of them can be interpreted within an unique model. Therefore, the possibility of measuring atmospheric neutrinos with the same detector operating in the long–baseline beam is considered a fundamental feature in order to establish a robust confidence on the results.

The main reason for performing a long-baseline neutrino oscillation experiment is to adopt an L/E parameter coherent with the Δm^2_{23} parameter indicated by atmospheric neutrino events.

In the CERN-NGS beam, the expected ν_e and ν_τ contamination are of the order of 10^{-2} and 10^{-7} respectively compared to the dominant ν_μ composition. These properties allow to search for oscillations by looking at the appearance of ν_e or ν_τ charged current events. In this case, the detector must be able to tag efficiently the interaction of ν_e's and ν_τ's out of the bulk of ν_μ events. This requires a detailed event reconstruction that can be achieved only by means of a high granularity detector. This requirement is met by the liquid Argon target.

	20 kton×year			
		Δm^2_{23} (eV^2)		
	No osci	1×10^{-3}	3.5×10^{-3}	5×10^{-3}
ν_μ CC	54300	53820	49330	44910
$\bar{\nu_\mu}$ CC	1090	1088	1070	1057
ν_e CC	437	437	437	436
$\bar{\nu_e}$ CC	29	29	29	29
ν NC		17550		
$\bar{\nu}$ NC		410		
$\nu_\mu \to \nu_e$ CC	-	7	74	143
$\nu_\mu \to \nu_\tau$ CC	-	52	620	1250
$\bar{\nu_\mu} \to \bar{\nu_e}$ CC	-	< 1	< 1	1
$\bar{\nu_\mu} \to \bar{\nu_\tau}$ CC	-	< 1	6	13

Table 5.2: Expected event rates at CERN-NGS for an exposure of 20 kton× year in the liquid Argon (corresponds to 8 (5) years of running in "shared" ("dedicated") mode for the baseline T600+2×T1200 configuration). The 3-family mixing scenario was assumed with the following angles: $\theta_{23} = 45^o$ and $\theta_{13} = 7^o$.

The expected event rates after 8 (5) years of running in "shared" ("dedicated") mode (equivalent to a total of $8(5) \times 4.5(7.6) \times 10^{19}$ pots) are listed in Table 5.2. For the oscillation scenarios, we assume a three family mixing with Δm^2_{23} in the range allowed by SuperKamiokande and the following mixing angles: $\theta_{23} = 45^o$ and $\theta_{13} = 7^o$, corresponding to $\sin^2 2\theta_{13} = 0.06$, or about half the CHOOZ limit on $\sin^2 2\theta_{13}$.

5.5.1 $\nu_\mu \to \nu_\tau$ appearance – electron channel

To search for the appearance of ν_τ, we exploit the excellent electron measurement and identification capabilities available in ICARUS and concentrate on the $\tau \to e\nu\nu$ decay mode. Because of the high resolution on measuring kinematical quantities, the ν_τ appearance search is based on the kinematical suppression of the background using similar techniques to those of the NOMAD experiment, but with much less stringent requirements on the background suppression, since as shown below, for the central value of Δm^2 of Superkamiokande, we expect a statistically significant excess at low neutrino energy even prior to any cuts. To reconstruct the hadronic jet, the detector is used as an homogeneous calorimeter. We expect the main background of the intrinsic ν_e CC component of the beam to be suppressible to a few events, while keeping a $\approx 30\%$ efficiency for the signal.

The expected number of ν_τ CC with $\tau \to e\nu\nu$ for $\Delta m^2 = 3.5 \times 10^{-3}$ eV^2 is $\simeq 110$ events in eight years of "shared" running, while the background from $\nu_e, \bar{\nu}_e$ CC amounts to about 470 events, or a signal over background $S/\sqrt{B} = 5$.

A detailed investigation of the signal and background has been performed for the original ICANOE proposal[18]. At the time, a fiducial cut, loosing 12% of events, was imposed in order to restrict the analysis to contained events in the liquid Argon target. The non-contained beam events played no role and were not included. While we believe that those events can be partially recovered with a "shower-shape" analysis in the liquid Argon imaging, we will not consider them further.

Since the analysis made for the ICANOE proposal took into account only the contained events in the liquid Argon target, the expected performance remains valid even in the currently considered design of ICARUS.

The result of the investigation of the charged current backgrounds sources that included effects of kinematical reconstruction of the events (nuclear effects benchmarked on NOMAD data) and charm semileptonic decays from CC events obtained for the ICANOE proposal[18] showed that they can be comfortably suppressed.

To enhance the τ appearance sensitivity, we adopt an improved method which makes use of a multi-dimensional likelihood function which becomes the unique discriminant between signal and background (see [46] for a more detailed description). This approach offers the advantage of taking into account correlations between the chosen variables, hence, yielding a better separation between signal and background.

Ignoring jet and τ structure, an event is fully characterized from the kinematics point of view by five independent variables: two provide longitudinal information and three describe the transverse plane with respect to the incident neutrino direction. A complete likelihood function aiming at describing the event kinematics should thus contain five variables. However, in order to reduce the complexity of the problem, we limit ourselves to the discrimination power provided by the following three variables:

- $E_{visible}$.
- $\rho_l \equiv P_T^{lep}/(P_T^{miss} + P_T^{lep} + P_T^{had})$
- P_T^{miss}

We built one likelihood for the τ signal ($\mathcal{L}_\mathcal{S}$) and another for background events ($\mathcal{L}_\mathcal{B}$). The discrimination is obtained by taking the ratio of the two likelihoods

$$\ln\lambda \equiv \mathcal{L}([E_{visible}, P_T^{miss}, \rho_l]) = \frac{\mathcal{L}_\mathcal{S}([E_{visible}, P_T^{miss}, \rho_l])}{\mathcal{L}_\mathcal{B}([E_{visible}, P_T^{miss}, \rho_l])} \tag{5.3}$$

Events with primary interaction vertex inside the selected fiducial volume and having an electron candidate with momentum larger than 0.5 GeV are used. To avoid biases, the likelihood functions were built using only MC events with "odd" sequential number. Background and τ efficiency estimations were obtained after applying the described algorithm to MC events with "even" sequential number.

Results

Figure 5.5 shows the likelihood distributions for background and tau events normalized to five years of "shared" CNGS running (total exposure of 12 kton $\times$ year). Figure 5.6 shows the P_T^{miss} distribution of the surviving signal events selected for different likelihood cuts. We note that events with P_T^{miss} values down to 0.2 GeV are selected even when tight cuts (i.e. $\ln\lambda > 2$) are applied, showing the power of the multi-dimensional likelihood.

Table 5.3 shows, for different cuts of $\ln\lambda$, the expected number of tau and ν_e CC background events. The maximum sensitivity corresponds to $\ln\lambda > 2$. For this cut and assuming five CNGS "shared" years of operation, we expect 13 taus and less than one event background. When compared to the "classical" approach where a serie of sequential kinematical cuts is used, we observe that the number of taus is similar, however the background is a factor three smaller in the case of the multi-dimensional likelihood. The background rejection power is enhanced for the likelihood approach, since correlations among variables are taken into account.

ν_μ CC background rejection

Charged current muon neutrino events can contribute to the background. In case the muon is not identified, the event will appear as a neutral current event. The source of electrons which can induce backgrounds are Dalitz decays, γ conversions and $e/\pi^\pm$ misidentification. Kinematics rejection combined with imaging and dE/dx measurements reduce to a negligible level this sort of background [18].

A more important source of background specific to charged current interactions comes from the decays of charmed mesons. At the CNGS energies $\sigma(\nu_\mu N \to \mu\ c\ X)/\sigma(\nu_\mu N \to \mu X) \approx 5\%$, therefore, in five years of "shared" operation, we expect to collect about 160 events where a charmed meson decays into a positron and a neutrino. These events resemble kinematically the real ν_τ events, since they have a neutrino in the final state and possess a softer energy spectrum and a genuine sizable missing transverse momentum.

Kinematics criteria reduce contamination due to charm events by a factor 10^{-1} (see Table 5.4). This translates into 16 expected background events. These criteria alone are insufficient to bring down $\nu_\mu\ CC$ background to a tolerable level.

The rejection of these charmed events requires a muon "veto" based on the imaging capabilities. The adopted veto proceeds in two steps:

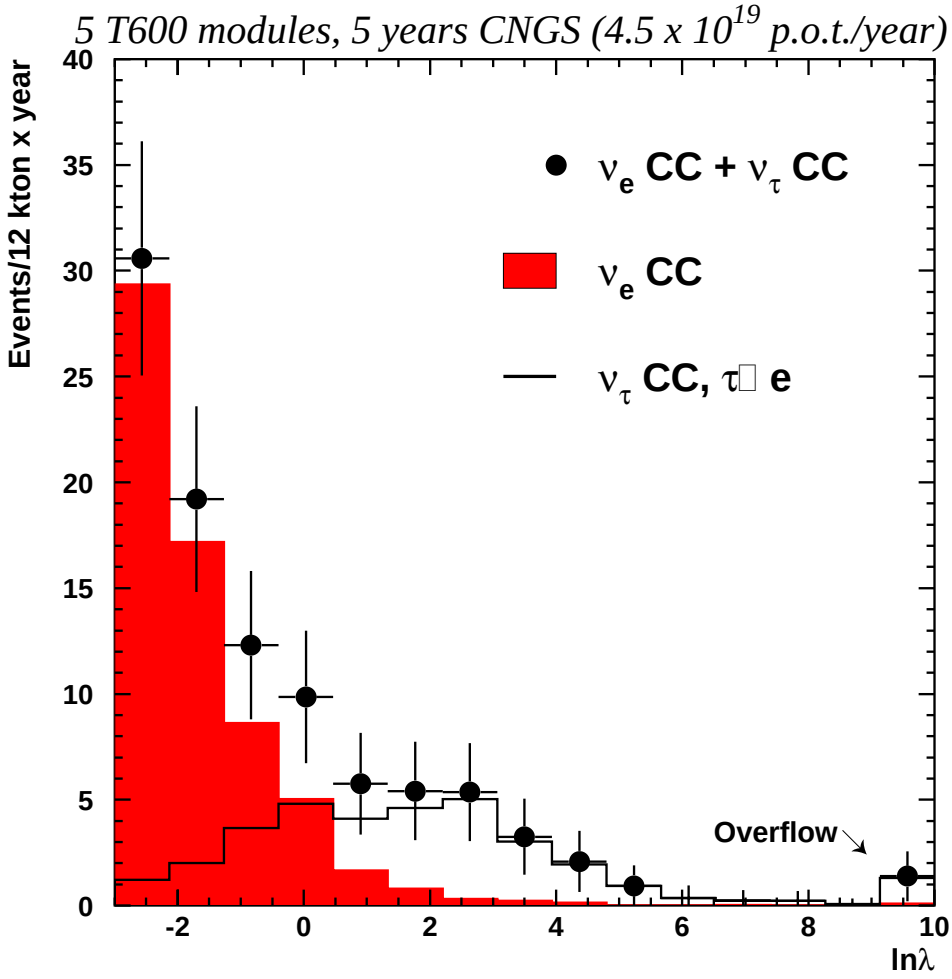

Figure 5.5: Distribution of the multi-dimensional likelihood for ν_e CC and $\tau \to e$ events. The last bin in signal includes the event overflow. Figure shows all events passing the whole set of applied cuts but $\ln \lambda$.

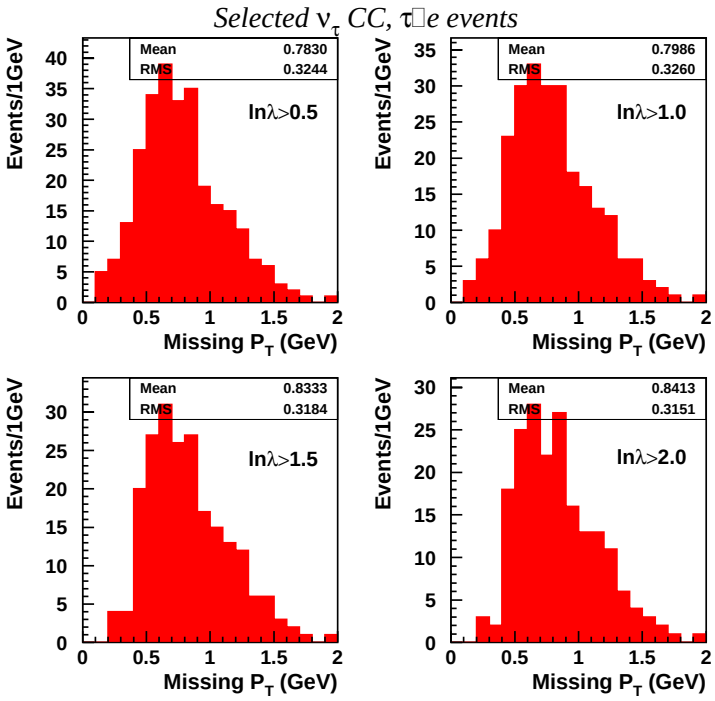

Figure 5.6: P_T^{miss} distributions of the selected signal for different likelihood cuts. All other cuts have been already applied. Note that for $\ln \lambda > 2$ events with P_T^{miss} values down to 0.2 GeV are selected by our likelihood function.

Cuts	ν_τ Eff. (%)	ν_e CC	ν_τ CC $\Delta m^2 = 3 \times 10^{-3}$ eV^2
Initial	100	262	49
Fiducial volume	63	169	31
One candidate with momentum > 0.5 GeV	57	165	28
$\ln \lambda > 0$	45	5.4	22
$\ln \lambda > 0.5$	39	2.8	19
$\ln \lambda > 1.0$	33	1.6	16
$\ln \lambda > 1.5$	31	1.2	15
$\ln \lambda > 2.0$	**26**	**0.7**	**13**
$\ln \lambda > 2.5$	18	0.6	9
$\ln \lambda > 3.0$	14	0.4	7
$\ln \lambda > 3.5$	10	0.3	5
$\ln \lambda > 4.0$	8	0.2	4

Table 5.3: Expected number ν_e CC background and signal events in the $\tau \to e$ analysis. A multi-dimensional likelihood function is used as the unique discriminant. Figures are normalized to 5 "shared" years running of CNGS.

- Tracks traveling at least 3λ ($\lambda_{Ar} = 84$ cm) without producing a secondary interaction are labeled as muons and the event is discarded.

- Tracks followed by an electromagnetic cascade are identified as a muon and the event is rejected.

These criteria reduce ν_μ CC background, where a charmed meson decays into an electron, to a negligible level. The muon veto represents a modest reduction of 3% in tau selection efficiency.

Cuts	$\nu_\mu + \bar{\nu}_\mu$ CC **(charm)**
Initial (N_{charm})	158
Fiducial volume	120
One candidate with momentum > 0.5 GeV	84
$\ln \lambda > 2$	16
Muon Veto	< 0.1

Table 5.4: Charm induced ν_μ, $\bar{\nu}_\mu$ CC background for the $\tau \to e$ analysis. Results are normalized to 5 years of CNGS "shared" running.

5.5.2 $\nu_\mu \to \nu_\tau$ appearance – hadronic channels

The hadronic decays of the τ can be used to search for $\nu_\mu \to \nu_\tau$ oscillations, as well. To enhance our sensitivity, we consider two orthogonal event samples:

- **Deep-inelastic (DIS)**. Events with an energetic hadronic jet. The usually have large final state multiplicity.
- **Quasi-elastic (QE)**. Events with a very soft hadronic system and small final state multiplicity.

The largest background before kinematics cuts comes from ν NC events. Charged current events where the muon is not identified can be a serious background, as well.

The intrinsic missing momentum related to the outgoing neutrino in NC events does not allow to search for these decay modes by selecting the momentum imbalance in the transverse plane like for the $\tau \to e$ channel. For the hadronic channels, the isolation of the candidate is the most discriminating variable against background. Isolation is defined as the transverse momentum of the hadron w.r.t. to the jet direction. A hadron coming from tau decay will be more isolated than hadrons produced in the fragmentation of the jet.

We define Q_T as the transverse momentum of the hadron candidate with respect to the total reconstructed momentum (see Figure 5.7). As we will see in the following subsections, a hard cut on the Q_T allows a large suppression of the NC background, however, at a high cost in terms of tau efficiency.

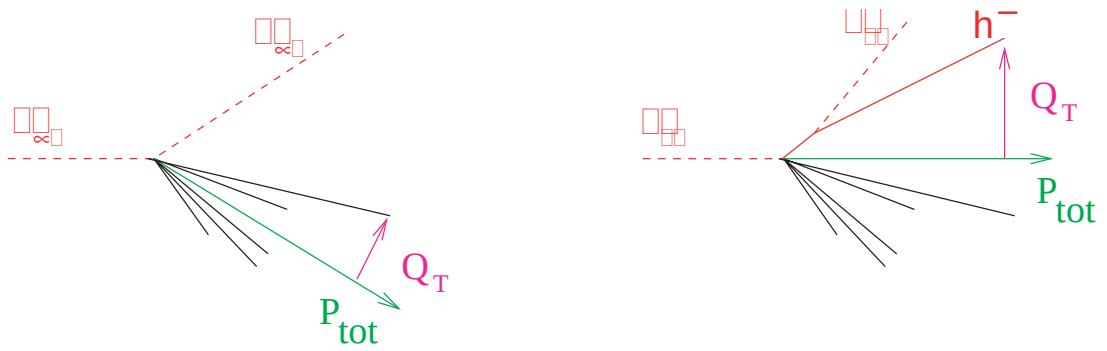

Figure 5.7: Q_T definition of a $\tau \to$ hadron candidate for both ν_τ CC and NC events.

$\tau \to \rho$ search

The ρ meson decays into a charged pion and a π^0. Therefore a rho candidate consists of a reconstructed charged hadron and a particle compatible with π^0 hypothesis. No condition on the charge of the pion candidate have been applied, since no charge determination can be performed given the present detector configuration. In case several candidates exist, we take the one with the highest Q_T.

The two pion system is required to be hard ($P_\rho > 5$ GeV) and with invariant mass in the vicinity of that of the ρ, $m_\rho = 770$ MeV (see Table 5.5). After these requirements, we

expect 15 taus and more than 300 background events. The latter ones are further reduced making use of the event kinematics. In addition to the Q_T cut already mentioned, we also imposed the condition of $M_T < 1.5$ GeV. M_T, the transverse invariant mass, is defined as $M_T \equiv \sqrt{4P_T^{tau}P_T^{miss}sin^2(\phi/2)}$, where ϕ is the angle in the transverse plane between the hadron candidate momentum (P_T^{tau}) and the missing transverse momentum. For tau events, M_T is restricted by kinematics to values smaller than the tau lepton mass ($m_\tau = 1.777$ GeV). For an overall tau efficiency of 1.6%, we expect two DIS $\tau \to \rho$ candidates and a negligibly small background contamination.

Cut	τ eff (%)	NC eff (%)	Signal ($\Delta m^2 = 3 \times 10^{-3}$ eV^2)	Background
Initial	100	100	139	10638
Candidates	76.6	46.9	106	4992
Fiducial volume	49.5	30.1	69	3202
$P_\rho > 5$ GeV	22.2	7.9	31	842
$0.65 < M_\rho < 0.8$ GeV	10.8	2.9	15	308
$M_T < 1.5$ GeV	8.6	1.0	12	110
$Q_T > 1.2$ GeV	**1.6**	–	**2.2**	**< 0.1**

Table 5.5: Expected τ and ν NC background events for the DIS $\tau \to \rho$ search.

We consider that events having a hadronic jet with momentum smaller than 1.0 GeV are potential $\tau \to \rho$ QE candidates. The signal to background ratio after this cut is S/B=1/10. The remaining background can be reduced to a negligible level just imposing that the candidate $\pi - \pi^0$ system be compatible with the ρ meson hypothesis. For a five year run, we expect 2 $\tau \to \rho$ QE events (see Table 5.6).

Cut	τ eff (%)	NC eff (%)	Signal ($\Delta m^2 = 3 \times 10^{-3}$ eV^2)	Background
Initial	100	100	139	10638
Candidates	76.6	46.9	106	4992
Fiducial volume	49.5	30.1	69	3202
$P_{had} < 1.0$ GeV	4.3	0.60	6	62
$P_\rho > 5$ GeV	3.0	0.03	4	3
$0.65 < M_\rho < 0.8$ GeV	**1.4**	–	**2**	**< 0.1**

Table 5.6: Expected τ and ν NC background events for the QE $\tau \to \rho$ search.

Charged current background rejection

Charged current events, where the muon is not identified, are a potential source of background for $\tau \to \rho$ searches. Table 5.7 shows that kinematics criteria alone are insufficient to reduce this background to a tolerable level. Once kinematics cuts have been applied, the expected background amounts up to 25 events for the DIS search while

6 are expected in the QE analysis. A veto similar to that described is subsection 5.5.1 has been adopted to enhance the ν_μ CC discrimination power. Muon identification criteria allow to reduce CC backgrounds to a negligible level. The loss in tau sensitivity is $\sim 3\%$.

Cut	$\nu_\mu + \bar{\nu}_\mu$ CC Background
Initial	33252
Candidates	18954
Fiducial	12400
DIS	
$P_\rho > 5$ GeV	3164
$0.65 < M_\rho < 0.8$ GeV	1070
$M_T < 1.5$ GeV	509
$Q_T > 1.2$ GeV	25
Muon Veto	< 0.1
QE	
$P_{had} < 1.0$ GeV	227
$P_\rho > 5$ GeV	21
$0.65 < M_\rho < 0.8$ GeV	6
Muon Veto	< 0.1

Table 5.7: Expected CC background events for DIS and QE $\tau \to \rho$ searches. Figures are normalized to five years of CNGS "shared" running.

The study of the misidentified electrons in neutral current events has also been carried out in the ICANOE proposal[18]. These backgrounds coming mostly from π^0 decays can be suppressed by requiring that the electron candidate does not have an unusually high dE/dx before it showers. Full simulation shows that before any other kinematic cut is applied, such backgrounds can be reduced to $\approx 10^{-3}$ of the NC event rate by requiring an electron energy exceeding 1 GeV. This is illustrated for a 3 family mixing scenario in which $\Delta m^2_{32} = 3.5 \times 10^{-3}$ eV^2, $\theta_{23} = 45^o$ and $\theta_{13} = 7^o$. The NC background is well below the ν_e CC, $\nu_\mu \to \nu_e$ CC and $\nu_\mu \to \nu_\tau$, $\tau \to e$ contributions (see Figure 5.8).

5.5.3 $\nu_\mu \to \nu_\tau$ appearance – combined expectation

Table 5.8 displays the expected signal and background events for 5 T600 modules and 5 five years of "shared" CNGS operation. When combined electron and rho decay channels, 17 taus are expected for a total estimated background smaller than one event.

5.5.4 $\nu_\mu \to \nu_e$ appearance

The excellent electron identification allows to look for electron excess coming from $\nu_\mu \to \nu_e$ oscillations. At high energy, we cannot neglect in addition the $\nu_\mu \to \nu_\tau$ oscillations with $\tau \to e\nu\nu$ to distort the electron sample. We adopt an approach in which both $\nu_\mu \to \nu_e$ and

ICARUS					
Decay mode	Signal 1.6×10^{-3} eV^2	Signal 2.5×10^{-3} eV^2	Signal 3.0×10^{-3} eV^2	Signal 4.0×10^{-3} eV^2	BG
$\tau \to e$	3.7	9	13	23	0.7
$\tau \to \rho$ DIS	0.6	1.5	2.2	3.9	< 0.1
$\tau \to \rho$ QE	0.6	1.4	2.0	3.6	< 0.1
Total	**4.9**	**11.9**	**17.2**	**30.5**	**0.7**

Table 5.8: Expected number of τ and background events collected by 5 T600 modules in five years of "shared" data taking. Signal events correspond to full mixing and four different Δm^2.

$\nu_\mu \to \nu_\tau$ oscillations are fitted simultaneously. A kinematical analysis is used to separate the two contributions.

Figure 5.9 shows the visible energy spectrum and the missing transverse momentum of events contributing to the electron charged current sample. Both $\nu_\mu \to \nu_e$ and $\nu_\mu \to \nu_\tau$ oscillations were assumed to take place simultaneously with the 3 family mixing parameters $\Delta m^2_{32} = 3.5 \times 10^{-3}$ eV^2, $\theta_{23} = 45^o$ and $\theta_{13} = 7^o$. Both oscillations distort the visible energy spectrum at low energy, given the chosen Δm^2 value. Tau charged current events occur at higher energies but the presence of the neutrinos in the final state lowers the visible energy of these events. Hence, both $\nu_\mu \to \nu_e$ and $\nu_\mu \to \nu_\tau$ will create an excess of electron charged current events at low neutrino energy. The spectrum at energies above 20 GeV can still be used to normalize the electron sample.

In terms of events, one can see in Table 5.9 the different contributions expected for a normalization of 8 years running in "shared" mode or five years running in "dedicated" mode. Different values of the mixing angles θ_{13} are shown in the first column. The third, fourth and fifth columns list the contribution from ν_e CC (intrinsic beam contamination), the amount of ν_τ CC with electron decay of the tau for $\Delta m^2 = 3.5 \times 10^{-3}$ eV^2 and maximal mixing, and the amount of $\nu_\mu \to \nu_e$ oscillated events. The last column shows the statistical significance of the $\nu_\mu \to \nu_e$ excess. Hence, ICARUS can test the θ_{13} angle down to a few degrees.

In order to disentangle $\nu_\mu \to \nu_e$ and $\nu_\mu \to \nu_\tau$ oscillations, we considered the transverse missing momentum. The $\nu_\mu \to \nu_e$ events are balanced, while $\nu_\mu \to \nu_\tau$ show a sizable transverse momentum due to the presence of two neutrinos in the final state. The visible energy, the missing transverse momentum and the electron transverse momentum are combined into a binned χ^2-fit, in which the three oscillations parameters Δm^2_{32}, θ_{23} and θ_{13} are allowed to vary (see Addendum II of the ICANOE proposal[47]).

The sensitivity to θ_{13} in presence of $\nu_\mu \to \nu_\tau$ oscillations, which play in this case the role of background, was estimated with the χ^2 method. The 90% C.L. exclusion region, obtained with $\chi^2_{min} + 4.6$ (2 parameter C.L.) for $\sin^2 2\theta_{13}$ is shown in Figure 5.10. In this case, the mixing angle between ν_μ and ν_τ was set to $\theta_{23} = 45^o$. Clearly, for high Δm^2_{23} values, the improvement with respect to CHOOZ is almost two orders of magnitude. For $\Delta m^2_{32} = 3 \times 10^{-3}$ eV^2, the limit could be improved by more than a factor 6.

Table 5.9: Rates at CNGS from $\nu_\mu \to \nu_e$ oscillations in three family mixing. The cuts $E_e > 1$ GeV, $E_{vis} < 20$ GeV have been applied. For $\Delta m^2_{23} = 3.5 \times 10^{-3}$ eV^2 and $\theta_{23} = 45^o$ and varying θ_{13}. Rates are normalized to 20 kton×years (for a 5 T600 modules configuration this corresponds to 8 years "shared" running, $8 \times 4.5 \times 10^{19}$ pots, or 5 years running of dedicated mode ($5 \times 7.6 \times 10^{19}$ pots).

θ_{13} (degrees)	$\sin^2 2\theta_{13}$	ν_e CC	$\nu_\mu \to \nu_\tau$ $\tau \to e$	$\nu_\mu \to \nu_e$	Total	$S/\sqrt{B}$
9	0.095	79	74	84	237	6.8σ
8	0.076	79	75	67	221	5.4σ
7	0.058	79	76	51	206	4.1σ
5	0.030	79	77	26	182	2.1σ
3	0.011	79	77	10	166	0.8σ

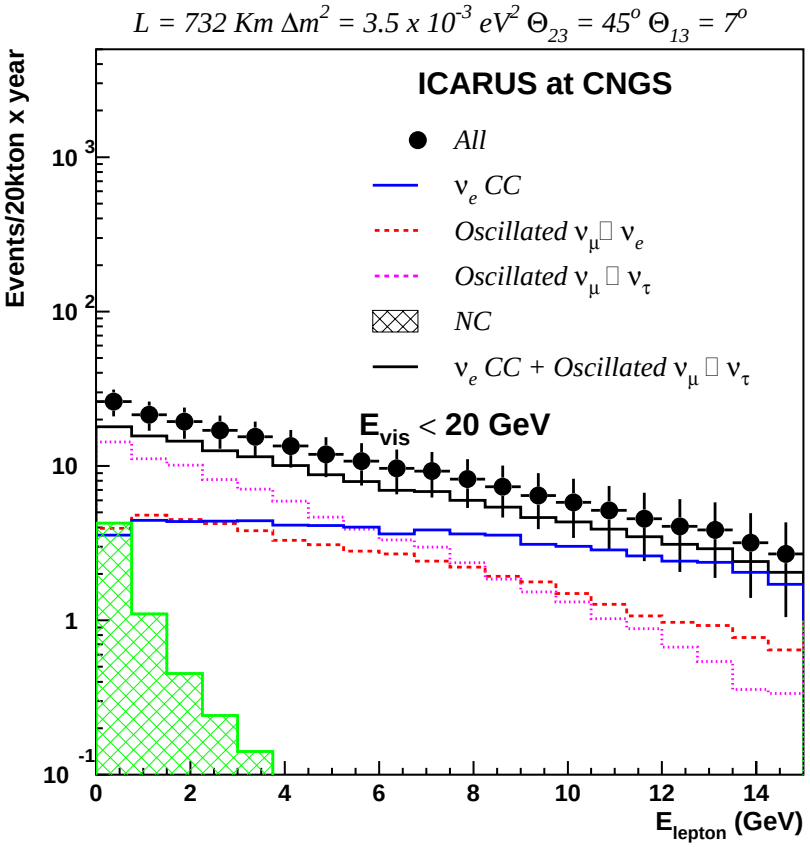

Figure 5.8: Electron candidate energy for events contributing to the electron charged current sample including background from NC.

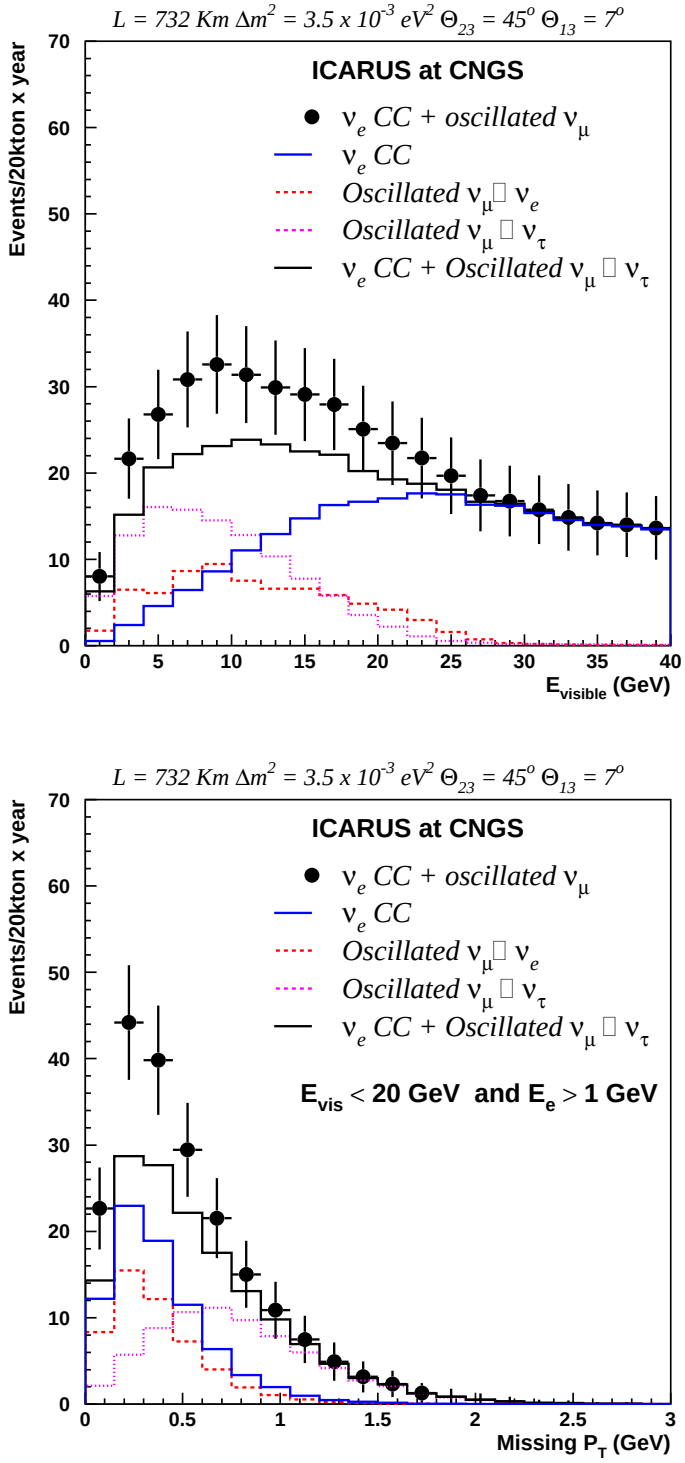

Figure 5.9: Visible energy spectrum (top) and missing transverse momentum (bottom) for events contributing to the electron charged current sample.

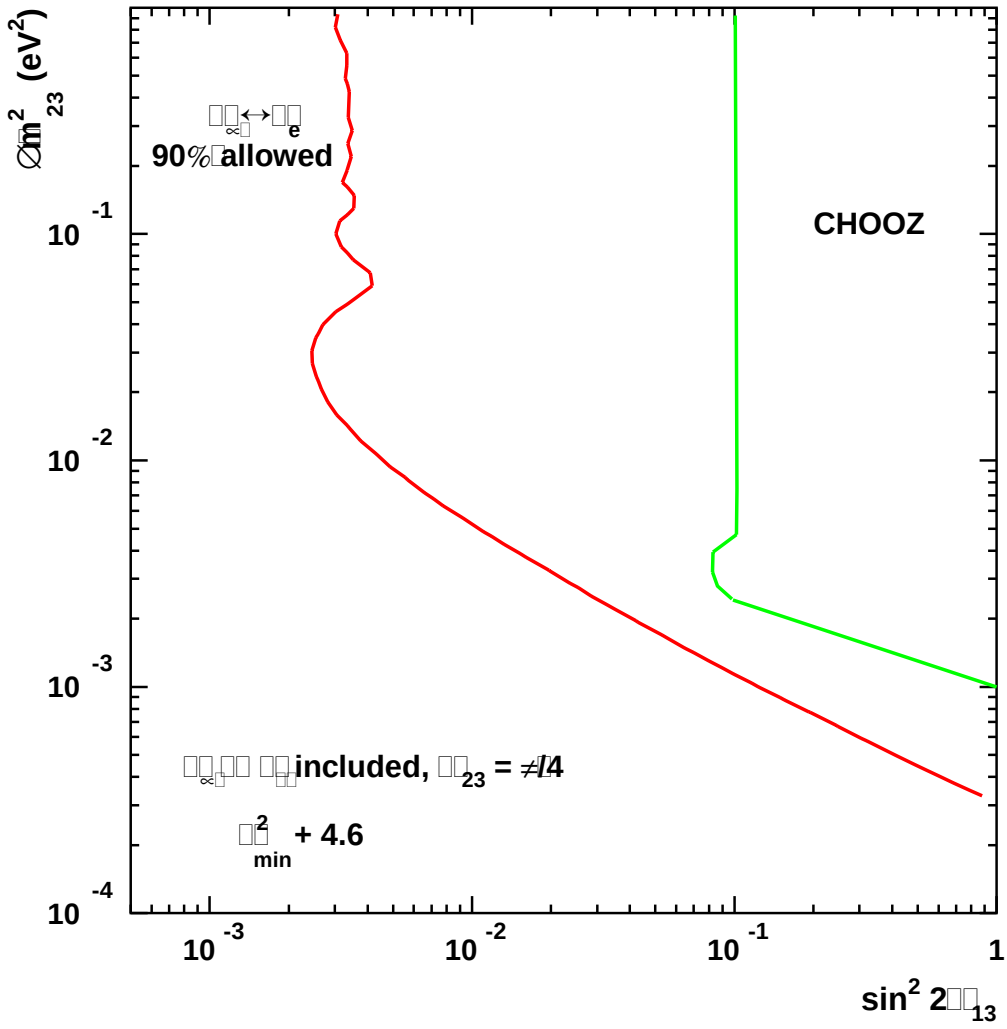

Figure 5.10: Sensitivity to the parameter θ_{13} at the 90%C.L. ($\chi^2_{min} + 4.6$, 2 parameter C.L.) in a three family mixing scenario, in presence of $\nu_\mu \to \nu_\tau$ oscillations with $\theta_{23} = 45^o$.

5.6 The nucleon decay experiment

Thanks to its large sensitive mass and to its spatial and energy resolution capabilities, ICARUS is an ideal device for nucleon decay detection. Unlike the other large detectors for nucleon decay, ICARUS, with its excellent tracking and particle identification capabilities providing a much more powerful background rejection, can perform exclusive decay modes measurements. Inclusive searches are also possible and they benefit of the detector energy and space resolution to reduce the atmospheric neutrino background to very low levels.

In addition, using the *(dE/dx)* versus range information, an excellent separation is obtained between kaons and pions. As a consequence, many exclusive channels will be searched for simultaneously, both for proton and neutron decays which discoveries can occur at the one-event level.

Nucleon decay events are characterized by a definite value of the total energy and by the fact that the total momentum of the decay products must be zero. These features, which are true for a free nucleon, are also approximately verified for a nucleon bound in a nucleus, provided the decay products do not rescatter before escaping the nucleus. These nuclear effects, the distortions of the energy and momentum distributions due to the nucleon Fermi motion, and the reinteraction of decay particles with the nucleus have been included in the Monte Carlo simulation.

Table 5.10 shows the summary of the results obtained on the nucleon decay search [48]. The first column gives the list of the studied nucleon decay modes. In order to maximize the efficiency over background ratio, separate exclusive and inclusive selections were applied to those channels with presence of pions in the final state that can be absorbed by the nucleus (pions between brackets in the table). The selection efficiencies and the expected background events at an exposure of 5 kton×year (corresponding to two years of data taking) are listed in the second and third columns. The exclusive channels show a high detection efficiency being almost background free at this exposure.

The partial lifetime lower limits, (τ/B), are given by

$$(\tau/B)_p > \frac{2.69}{S} \times Expo \times \epsilon \times 10^{32} \ \ yrs \quad (for \ \ proton \ \ decay)$$

$$(\tau/B)_n > \frac{3.29}{S} \times Expo \times \epsilon \times 10^{32} \ \ yrs \quad (for \ \ neutron \ \ decay)$$

Here, $Expo$ is the full detector exposure in kilotons per year, ϵ is the selection efficiency, and S is the constrained 90% CL upper limit on the number of observed signal events (made equal to the expected background to get the *detector sensitivity*).

The top (bottom) part of Figure 5.11 shows the predictions on the number of background events as a function of the exposure, for the proton (neutron) decay channels. The exclusive channels ($p \rightarrow e^+ \ \pi^0$, $p \rightarrow K^+ \ \bar{\nu}$, ...), almost background free up to 1 Mtons×year exposure (!), will give the possibility to discover proton decay at the one-event level. At the same time, the inclusive channels ($p \rightarrow e^+ \ (\pi^0)$, $p \rightarrow \mu^+ \ (\pi^0)$, ...), with a non zero contamination, can also be used to check the detector efficiencies by comparing the expected and obtained distributions of events.

Channel	Efficiency (%)	Background (5 kton×year)	PDG'00 limit (10^{30} years)	Needed Exposure (in ktons×year)
$p \to e^+ \pi^0$	45.3	<0.1	1600	30.2
$p \to K^+ \bar{\nu}$	96.7	<0.1	670	5.9
$p \to \mu^- \pi^+ K^+$	97.5	<0.1	245	2.1
$p \to e^+ \pi^+ \pi^-$	18.6	0.13	82	3.8
$p \to \pi^+ \bar{\nu}$	41.8	3.9	25	0.5
$p \to \mu^+ \pi^0$	44.8	<0.1	473	9.0
$n \to e^- K^+$	96.0	<0.1	32	0.2
$n \to e^+ \pi^-$	44.3	<0.1	158	2.5
$n \to \mu^- \pi^+$	44.7	0.12	100	1.6
$n \to \pi^0 \bar{\nu}$	45.1	2.4	112	2.4

Table 5.10: Summary of nucleon decay searches with the ICARUS detector. The table shows, for the studied proton and neutron decay channels, the detection signal efficiency (second column) and the expected number of background events for an exposure of 5 kton×year (third column). The two last columns show the present PDG'00 limits and the needed exposures to reach these limits.

The quoted proton (neutron) limits on (τ/B) as a function of the exposure are illustrated on the top (bottom) part of Figure 5.12.

Finally, we have studied how the previous limits on (τ/B) compare with the current ones. The third column of Table 5.10 gives the present PDG'00[49] limit for each channel, while the fourth column contains the exposure needed by ICARUS to reach these limits. Already with a 2 kton×year exposure, some of the present limits can be increased.

5.7 Solar and supernovae neutrino experiment

The ICARUS goal is not only to confront the Standard Solar Model (absolute event rate), but also to provide Solar Model independent measurements by observing various independent processes differently affected by possible oscillations.

ICARUS can detect solar neutrinos by observing the electron produced in the following two reactions:

1. Elastic scattering on electrons ($\nu_x + e^- \to \nu_x + e^-$) which occurs with all types of neutrino flavours and for both charged and neutral exchange;

2. Absorption on the Argon nucleus ($\nu_e + {}^{40}Ar \to {}^{40}K^* + e^-$) which only occurs with the electron neutrino.

These interactions usually result in the production of a primary electron track eventually surrounded by lower–energy secondary electron tracks. Small prototypes have demonstrated that, by the TPC technique, electrons with kinetic energy as low as 150 KeV can be detected. This performance allows a detailed reconstruction of the

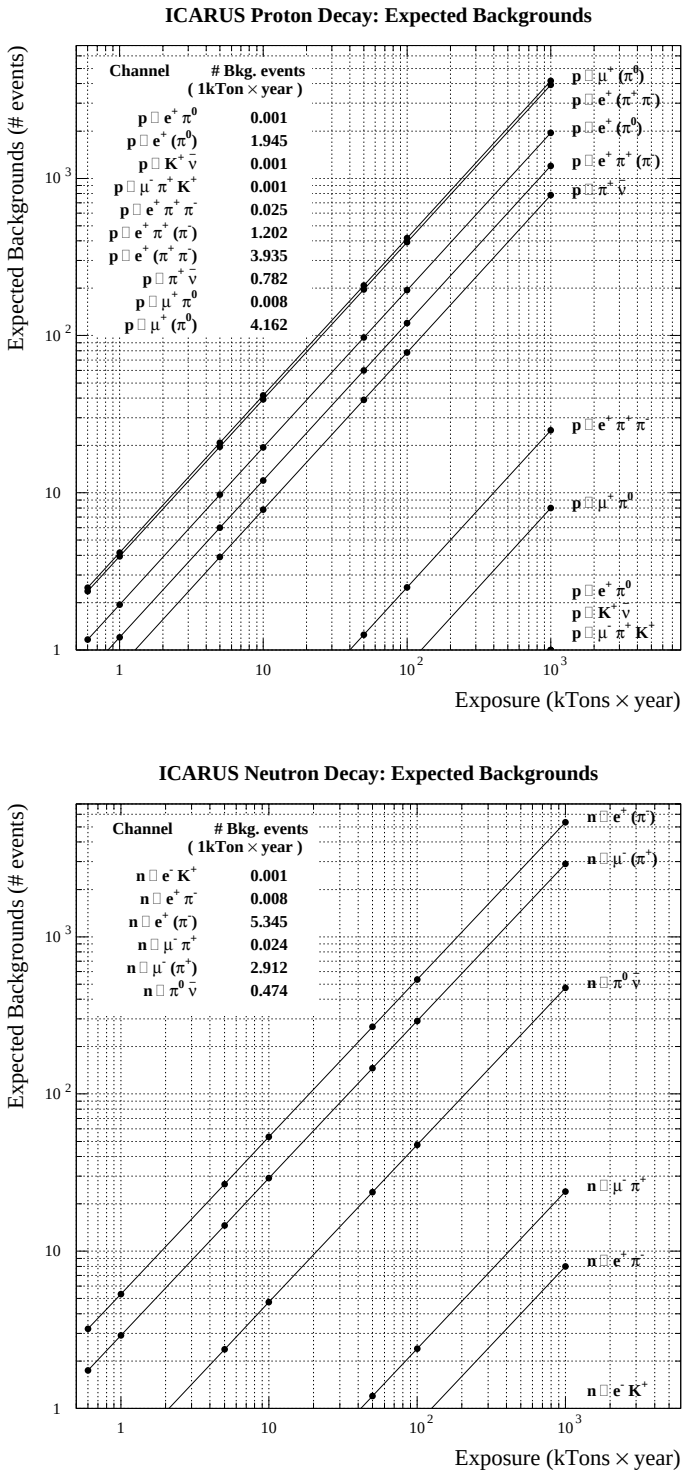

Figure 5.11: Estimated number of background events on the ICARUS detector as a function of the exposure for the different proton (top) and neutron (bottom) decay channels. The tables in the plots give the precise values for an exposure of 1 kiloton × year.

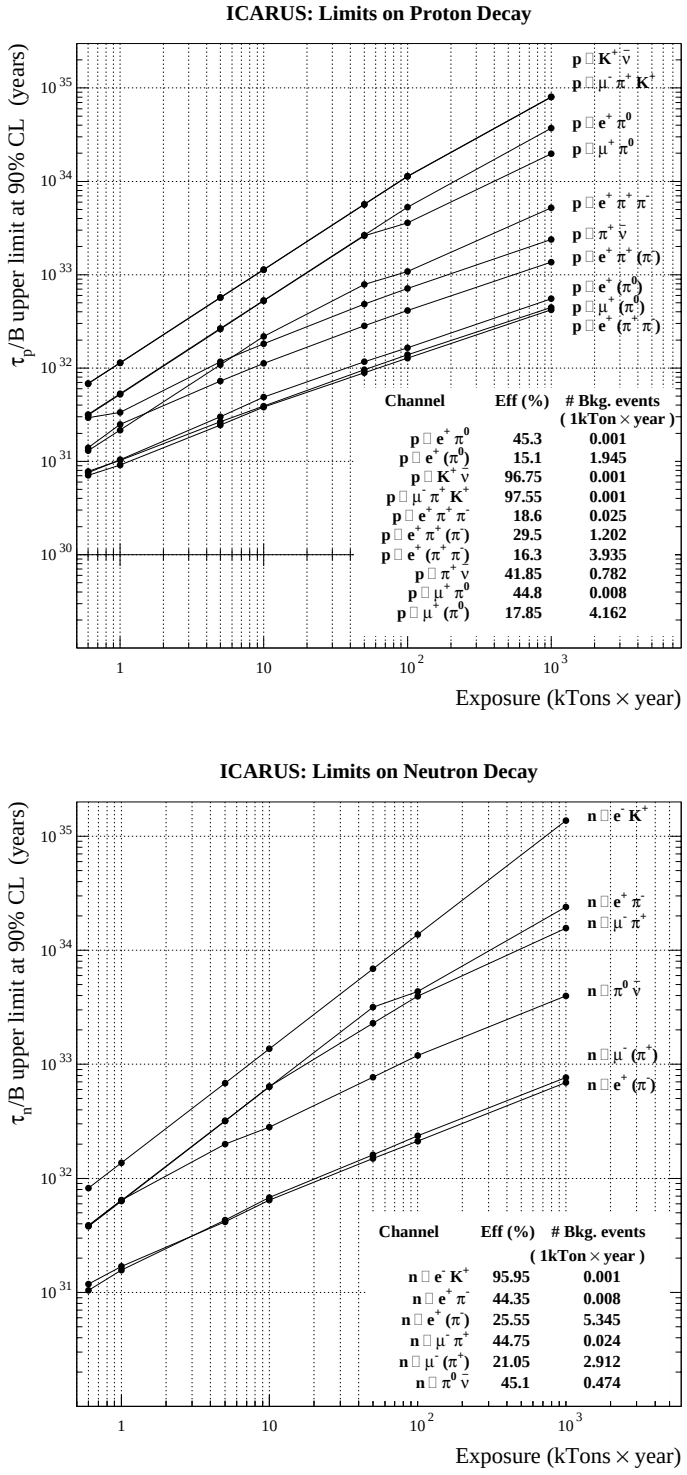

Figure 5.12: Running of the proton (top) and neutron (bottom) decay lifetime limits (τ/B) with the exposure. The limits are at 90% confidence level. The tables indicate the selection efficiencies and the estimated number of background events for each decay mode, at an exposure of 1 kiloton $\times$ year.

neutrino interactions. However, because of the increasing backgrounds (mainly natural radioactivity) at low energy, there is a minimum threshold (5 MeV) below which electrons produced by solar neutrinos can not be distinguished from other sources. Our detector is only sensitive to the ^{8}B part of the solar neutrino spectrum.

For the elastic scattering reaction, we expect in case of no oscillations 1925 events per year for a 5 T600 modules configuration. The electron produced in this process has an angular distribution, with respect to the initial neutrino direction, strongly peaked in the forward direction. We use this signature to discriminate neutrino events from background. For example if one chooses the tracks within a 25° cone around the Sun direction, the angular efficiency is 72%.

The absorption reaction is expected to proceed through two main channels: a superallowed Fermi (F) transition to the 4.38 MeV excited isobaric analog K* state; Gamow–Teller (GT) transitions to several excited K states. The two processes are distinguished by the energy and multiplicity of γ–ray emitted in the de-excitation and by the energy spectrum of the primary electron. The expected events per year are 1866 for the Fermi transition and 3913 for the Gamow–Teller reaction assuming the Standard Solar Model flux.

The fast neutron background in the LNGS tunnel has been measured[50]. This flux has been used to estimate the photon background produced by the neutron capture in Argon or in the detector and dewar materials. Most of these photons will however yield Compton electrons below the 5 MeV threshold.

The ICARUS detector is also capable of detecting neutrinos coming from a stellar explosion in our Galaxy. When the core of a massive star collapses, nearly all the gravitational binding energy is released in form of neutrinos of different flavors. Neutrinos are emitted over a total time scale of tens of seconds and their average energies will be about 10-20 MeV.

In analogy to solar neutrino detection, ICARUS has sensitivity to supernova neutrinos via elastic scattering on electrons and absorption on Argon. Assuming that a collapse occurs at a distance of 10 kpc from the Sun and a temperature of 3.5 MeV for the ν_e's, we expect to collect with ICARUS about 170 events (one fourth of them corresponds to elastic scattering events) in 2.38 kton.

5.8 A technology for a future neutrino factory

A neutrino "factory" [51, 52] is based on the decay of muons circulating in a storage ring. Neutrino factories raised the interest of the physics community, since they appear natural follow-ups to the current experimental long baseline programme and could open the way to future muon colliders.

Neutrino sources from muon decays provide clear advantages over neutrino beams from pion decays. The exact neutrino helicity composition is a fundamental tool to study neutrino oscillations. It can be easily selected, since $\mu^+ \to e^+\nu_e\bar{\nu_\mu}$ and $\mu^- \to e^-\bar{\nu}_e\nu_\mu$ can be separately obtained.

At a neutrino factory, one could independently study the following flavor transitions:

$$\begin{aligned}
\mu^- \to e^- \quad \bar{\nu}_e \quad & \nu_\mu \\
& \to \nu_e \to e^- \text{ appearance} && (5.4)\\
& \to \nu_\mu \text{ disappearance, same sign muons} && (5.5)\\
& \to \nu_\tau \to \tau^- \text{ appearance, high energy nu}'\text{s} && (5.6)\\
\to \quad & \bar{\nu}_e \text{ disappearance} && (5.7)\\
\to \quad & \bar{\nu}_\mu \to \mu^+ \text{ appearance, wrong sign muons} && (5.8)\\
\to \quad & \bar{\nu}_\tau \to \tau^+ \text{ appearance, high energy nu}'\text{s} && (5.9)
\end{aligned}$$

plus 6 other charge conjugate processes initiated from μ^+ decays.

As many studies have shown [53], the physics potential of such facilities are indeed very vast. Neutrino factories provide ideal conditions for the neutrino oscillation physics: a precise measurement of the mass difference and mixing matrix elements is achievable, a test of the unitarity of the mixing matrix can be performed, a direct detection of Earth matter effects is feasible and CP violation effects could be studied on the leptonic sector. Neutrino factories might be the only way to determine θ_{13}.

We illustrate in Table 5.11 the expected rates for three different baselines assuming 10^{21} muons decays of each sign in the storage ring, in absence of oscillations. The numbers are normalized to two years of data taking with a detector configuration consisting of 5 T600 modules.

Baseline →		L=732 km	L=2900 km	L=7400 km
Muon Energy →		$E_\mu = 5$ GeV	$E_\mu = 30$ GeV	$E_\mu = 30$ GeV
	ν_μ CC	6150	72000	11300
μ^-	ν_μ NC	1590	20600	3400
10^{21} decays	$\bar{\nu}_e$ CC	2150	27600	4370
	$\bar{\nu}_e$ NC	630	9950	1500
	$\bar{\nu}_\mu$ CC	2450	31900	5000
μ^+	$\bar{\nu}_\mu$ NC	750	11200	1750
10^{21} decays	ν_e CC	5550	64500	9900
	ν_e NC	1350	18300	2900

Table 5.11: Expected events rates (without oscillations) normalized to 10^{21} muon decays/year for a 5 kton detector (or two years of data taking).

With an ICARUS liquid Argon target followed by the muon spectrometer, we can achieve muon charge and momentum measurements, to provide discrimination between ν_μ and $\bar{\nu}_\mu$ charged current (CC) events. In addition, excellent ν_e CC versus ν NC separation can be achieved thanks to the fine imaging of the target. Finally, the identification of ν_τ CC events can be performed with kinematics analysis of all final state particles.

As an example of possible event classification that will provide information on the oscillation patterns, we show in Figures 5.13, 5.14, 5.15 and 5.16 the reconstructed

visible energy of events (at the baseline $L = 7400$ km normalized to $10^{20}\mu$'s) for specific event classes in case of a given oscillation scenario (see plot inserts). The different contributions including backgrounds for each event class have been evidenced in the plots. For example, in Figure 5.14, the different processes that contribute to the right-sign muon class are unoscillated muons, taus and background events. For quantitative estimations on the precision with which neutrino oscillation scenarios can be studied from such measurements, See Ref. [54]).

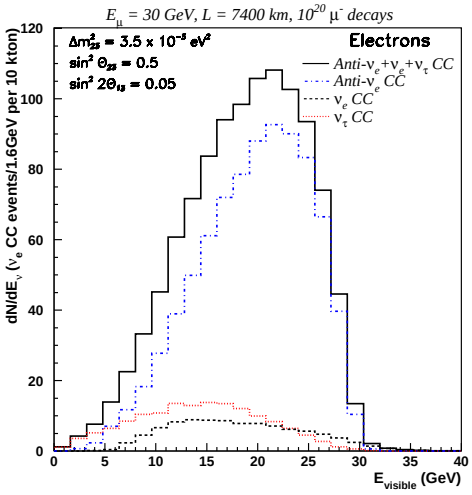

Figure 5.13: Visible energy spectrum for electron events: ν_e CC (dashed line), ν_τ and $\bar{\nu}_\tau$ (dotted line) and $\bar{\nu}_e$ CC (dot-dashed). The solid histogram shows the sum of all contributions.

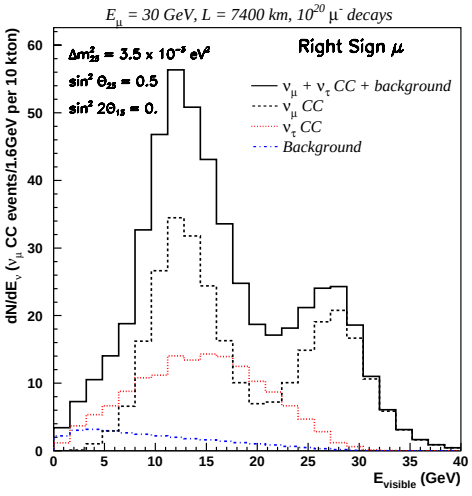

Figure 5.14: same as Figure 5.13 for right-sign muon sample: ν_μ CC (dashed line), ν_τ and $\bar{\nu}_\tau$ (dotted line) and meson decay background (dot-dashed). Solid histogram shows the total contribution.

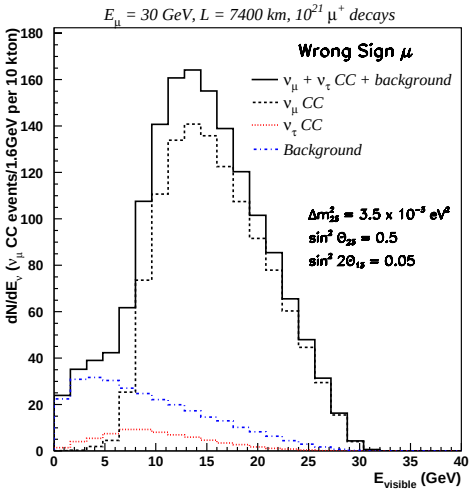

Figure 5.15: same as Figure 5.13 for wrong sign muon sample: ν_μ CC (dashed line), ν_τ and $\bar{\nu}_\tau$ (dotted line) and meson decay background (dot-dashed). Solid histogram shows the total contribution.

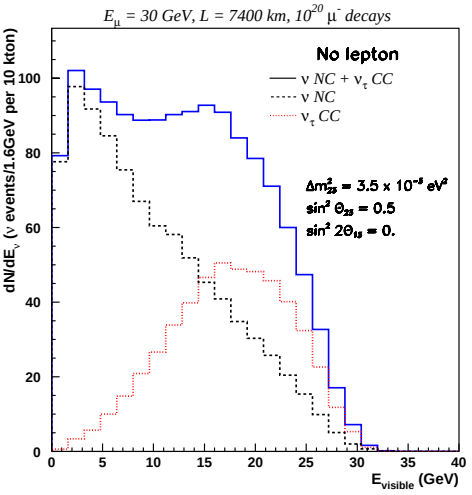

Figure 5.16: same as Figure 5.13 for the no-lepton sample: ν NC (dashed line), ν_τ and $\bar{\nu}_\tau$ (dotted line). The solid histogram shows the sum of NC and CC processes.

Chapter 6

THE T1200 SUPERMODULE

6.1 Cryogenics and Purification

The cryogenics and purification systems for the T1200 detector have to be able to purify and keep pure liquid argon with a concentration of electronegative impurities smaller than 0.1 ppb (O_2 equiv.) for a period of several years. The main Dimensions and shape of the cryostat were fixed by the following requirements:

- fit the largest number of T600-like half-modules in the Hall B cross-section;
- the supporting structure for the upper LAr containers has to comply to the MCE (Maximum Credible Earthquake) specifications and to the alignment requirements for the internal detector positioning;
- properly dimensioned anti-seismic shock absorbents are installed below the cryostat to cut the most dangerous frequencies;
- safety requires a suitable containment of the liquid argon in case of major failure of one of the LAr containers;
- thermal insulation thickness has to be large enough to provide adequate insulation also in case of vacuum breaking inside the panels.

Current limitations on the maximum electrical power assigned to the experiment and the decision to use liquid nitrogen (LN_2) recondensers as the primary supply for the nitrogen used to cool the apparatus, lead to a maximum consumption of LN_2 for cooling of about 1000 lt / hour / T1200 unit (the corresponding electrical power needed for recondensation is about 400 kW). This corresponds to an upper limit on the insulation heat input of about 10 W / m^2. Due to the limitation on the insulation maximum thickness (500 mm) we are obliged to adopt a solution somewhat different than the one originally foreseen for the T600: evacuated honeycomb panels. This solution, successfully verified during the T600 test run, ensures a performance as the one specified while preserving part of the original functionality that motivated the choice of a purely passive insulation: in case of vacuum breaking, the heat conduction will rise about a factor 3 (from 7 W / m^2 to 24 W / m^2) thus maintaining an acceptable thermal insulation capability with limited consequences on the cooling system requirements.

Good temperature uniformity is required due to the dependence of the electron drift velocity with temperature and also to avoid large convective motions inside the LAr. The main specification for the cooling system is that the LAr temperature has to be kept uniform within 1°C.

LAr purification is the most critical issue. Few facts, extensively verified during our experience with smaller prototypes, have driven the basic choices:

- We obtain a high LAr purity after the filling, using standard procedures for high vacuum (materials, cleaning procedures, design of internal components) and a good vacuum conditioning of the internal surfaces;
- pollution of the LAr is mainly produced by the outgassing of surfaces located in the gas phase, while contamination from objects immersed in the liquid is negligible; in absence of large convective motions, recirculation of the gas is sufficient to preserve the LAr purity;
- filling speed has to be as fast as possible, to limit the contamination of the LAr during the filling period from the larger exposed surfaces;
- Standard Oxisorb / Hydrosorb filters provide a purity level which is well above our present needs.

Purification speed during the detector filling (2 LAr m^3/hr) was defined extrapolating data from small sized prototypes, taking into account the outgassing rates of materials used for the T600 internal detector. Gas recirculation power (50 GAr m^3/hr per container) was also defined extrapolating data from the 3 ton prototype and taking into account the gas volume in the T600. A fast recirculation system working in the liquid phase was added to the traditional gas recirculation system to restore the purity of the liquid in case of inadequate purity level after the filling or due to some accidental contamination during the running. The LAr recirculation system was dimensioned (recirculation speed = 2 m^3/hr) in a way to restore the operating conditions, starting from an electronegative impurities contamination of 10 ppb, in less than one month. The main specifications for cryogenics and purification systems are summarized in Table 6.1.

All the above considerations lead to the definition of the purification and recirculation systems installed in the T600 module. The very satisfactory results obtained during the T600 test run convinced us to keep the same solutions for the T1200.

6.1.1 The T1200 liquid argon containment

The LAr will be contained in four mechanically independent vessels (see Figure 6.1). The volume of the elementary container will be about 270 m^3. According to our experience, to outgas efficiently the internal surfaces and obtain an adequately pure LAr, the cold vessels must be evacuated to less than 10^{-3} mbar. This implies that the containers have to be able to mechanically stand the vacuum condition and that they have to be tight to better than 10^{-5} mbar lt sec^{-1}. Maximum overpressure inside the cold vessels is limited to less than 1.5 bar abs, to avoid the hydraulic test mandatory for pressurized vessels according to Italian regulations and that would compromise the cleanliness of the inner

Table 6.1: Summary of the basic specifications for cryogenics and purification of the T1200 detector.

Max LAr container external size: height width length	 4.5 m 4.5 m 21.0 m
Maximum own weight per unit	90 ton
Insulation type	evacuated and superinsulated honeycomb panels
Max insulation thickness	500 mm
Max thermal gradient in the LAr	1^oC
Max operating pressure	1.5 bar abs
Max load (vacuum)	1 bar
Purification speed during filling	2 LAr m^3 / hr
Gas recirculation speed (per unit)	50 GAr m^3 / hr
Liquid recirculation speed (per unit)	2 LAr m^3 / hr
Target purity for LAr (concentration of e-negative impurities)	 0.1 ppb O_2 equiv.

volume.

As stated in the previous paragraph the LAr containers have to be a parallelepipe with approximate external dimensions $4 \times 4 \times 20$ m^3. Parallelepiped shape is a rather inconvenient from the mechanical point of view, as the vessels have to stand the vacuum condition. A preliminary evaluation of a standard reinforced structure made of stainless steel lead to a container with weight about 70 ton. Added to the own weight of the internal detector structures (20 ton) this leads to a mass close to the 90 ton limit imposed by maneuverability during transportation.

Air Liquide industry proposed a solution based on aluminium honeycomb. The honeycomb structure, finally adopted for the T600, with equivalent mechanical performance as the one formerly studied, weights only about 25 ton per container. The use of aluminium for the LAr vessels was also particularly attractive in view of the very good shielding offered against external electronic noises and the large thermal conductance that ensures a very good temperature uniformity inside the LAr. On the other hand, there was much less industrial experience in welding aluminium vacuum tight containers. To avoid blowholes of fake welds, special care had to be taken in the preparation and cleaning of the surfaces to be welded and in the choice of welding materials and parameters.

Figure 6.2 shows the basic elements of the cold vessels. They are panels (approximately 2×3.8 m^2) made of aluminium honeycomb sandwiched between two thin aluminium skins (4 mm thick) and surrounded by a frame made of aluminium profiles (for the connection to adjacent panels / profiles). Panel thickness is 150 mm. Aluminium honeycomb is perforated to allow air (or nitrogen) circulation or evacuation of the whole panel. The

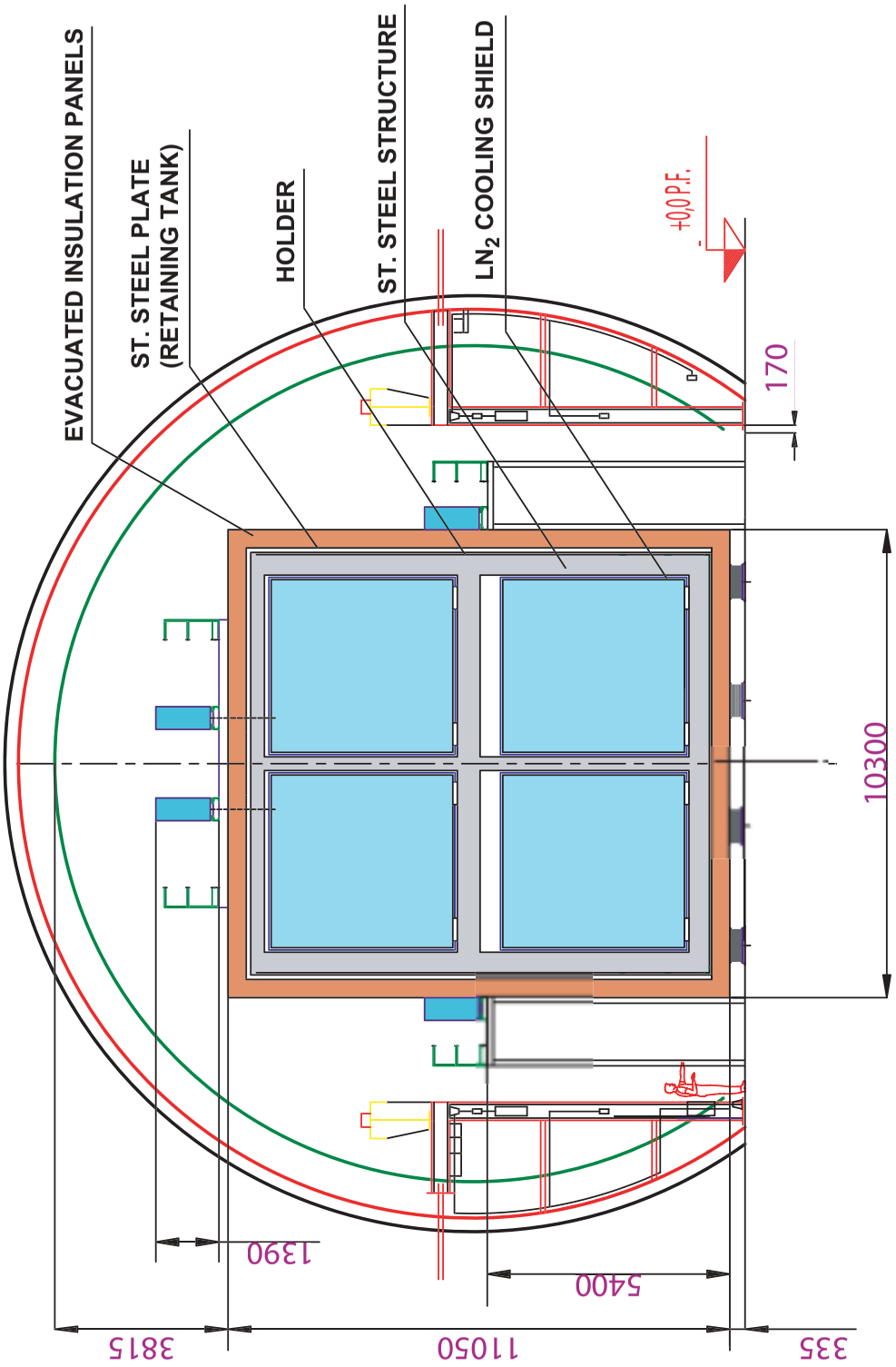

Figure 6.1: T1200 module cross-section.

panels are assembled by gluing the two skins to the aluminium honeycomb and to the surrounding profiles under hydraulic press at about 60 ^{o}C for 8 hours.

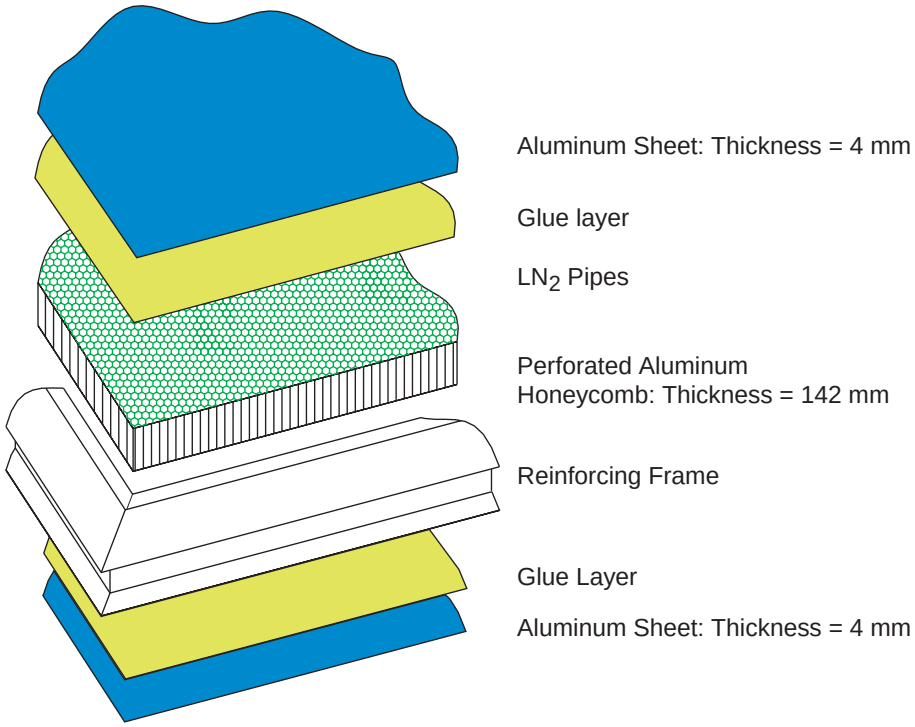

Figure 6.2: Basic aluminium panels layout.

The gluing was tested at LN_2 temperature for mechanical resistance after having heated the test samples up to 300^{o}C (to simulate the effect of heating due to the panels welding). No degradation of mechanical performance was seen for samples heated up to 200^{o}C.

The panels are joined together along the 3.8 m long side to form the lateral, the top and the bottom walls (all about 20 m long). The walls are then connected by means of angular profiles. The two end caps (about 3.5$\times$3.8 m^2), both formed by two special panels joined by an "H" shaped profile (to reach the required dimensions) are added at the end. An end cap (the backward one) is welded to the other walls through angular profiles, while the other one has to be removable to allow for the installation of the internal detector. On the front side there is a flange with the same aperture as the cryostat internal dimensions and the end cap is bolted on it. A thin aluminium plate welded all around the flange ensures the vacuum tightness of the container. To open the vessel, the aluminium plate has to be cut (and removed) and the bolts removed.

All the apertures for the wire chamber readout are located on top of the container. For each container, there are 18 apertures with internal diameter 200 mm each one reading out 576 wires at $\pm 60^o$. The apertures are equally spaced at about 1 m from each other and are organized in one row located near the edge of the top wall (just above the wire chamber). Two additional 250 mm diameter apertures near the corners of the top wall host the cables for the horizontal wires and for the last portion of wires at $\pm 60^o$. Also on the top are the ports for the LAr filling, for GAr recirculation and other services

(vacuum, safety disks, instrumentation, etc.). The output port to the LAr recirculation system is approximately at the center of the backward end cap. Finally, an aperture in the backward bottom edge is the port for the container emptying.

Due to the severe requirements on vacuum tightness, we decided to use for the argon circuit ConFlat flanges. On all the output ports of the main LAr containers, special vacuum tight bi-metal (aluminium to stainless steel) joints are installed with the inner aluminium part welded to the container body and the outer stainless steel part machined as a standard ConFlat flange. On these flanges, ConFlat joints are installed according to the schemes in Figure 6.3 to move the ports outside the insulation layer. Signal feedthrough flanges are therefore installed outside the insulation at room temperature. The container is transported sealed at the level of the bi-metal joints, without the additional connections.

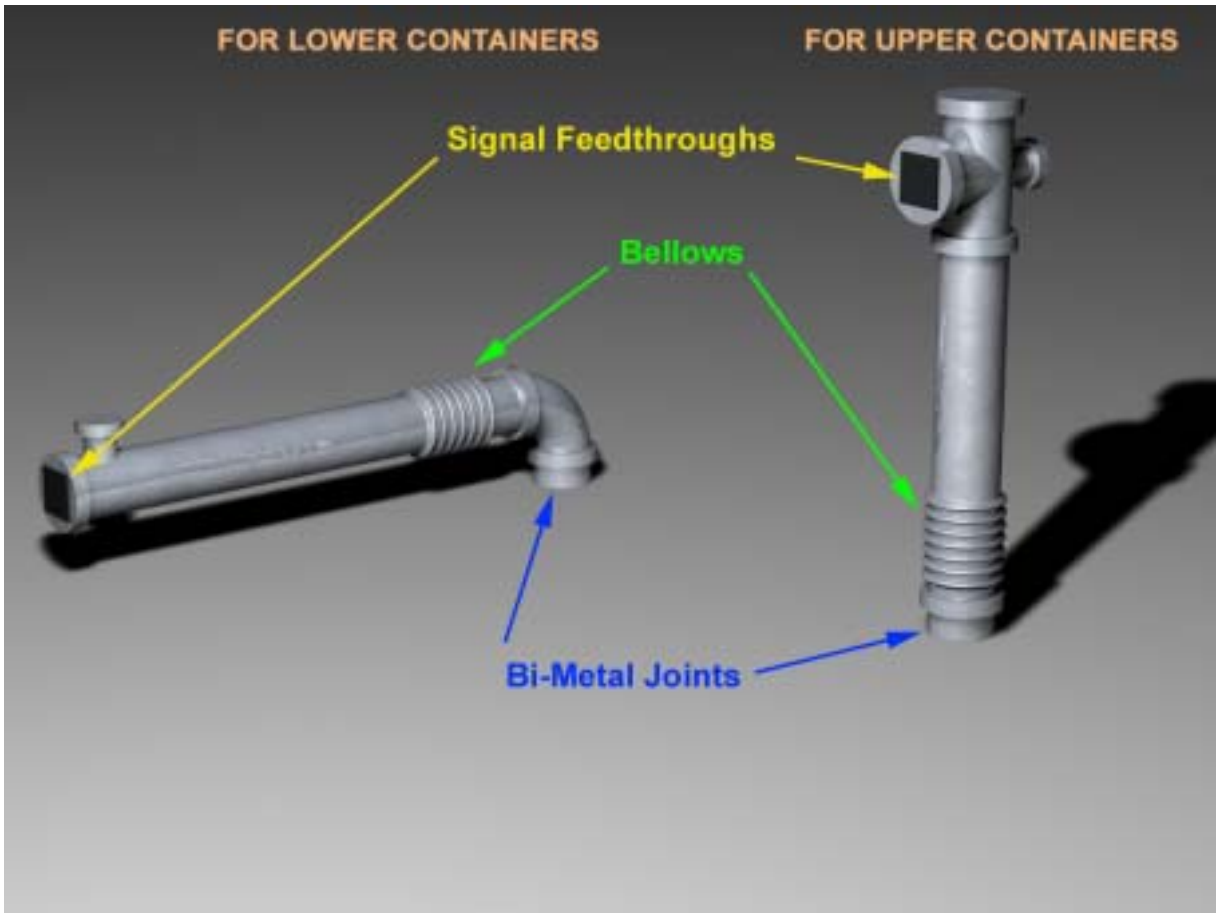

Figure 6.3: Vacuum tight connection elements for installation of signal and auxiliary instrumentation feedthroughs.

On the bottom side of the container, special beams and supporting blocks are inserted where the wire chamber structure supports are located. The wire chamber structure lies on eight points (in two rows of equally spaced four points), where special supports are installed to allow for longitudinal and transverse movements due to differential thermal

contractions of the stainless steel structure and the aluminium container (the differential contraction is about 1.1 mm / m integrated from room to LAr temperature). Two additional supports for the wire chambers are inserted in the central part to hold the transverse displacement during the transportation. Requirements on the supporting points for the container are: a reciprocal alignment within ± 2 mm, a precision in the absolute transverse positioning within $\pm$ 3 mm and a precision in the inter-axes within $\pm$ 3 mm. Special inserts (laminated aluminium blocks) are installed in the container bottom wall to be machined at the required precision after the full container assembly. The container itself is sustained on the same points on the insulation bottom part, which is adequately reinforced in these regions, or on the transverse beams of the stainless steel supporting structure (for the upper two containers). In this way, the load of the wire chamber structures and of the LAr is directly transmitted through inextensible supports, to the floor. The initial chamber alignment is therefore maintained, after the filling with LAr, within the deformations of the supporting beams of the floor basement and of the shock absorbents (installed below the insulation to cut mechanical frequencies occurring in case of an earthquake). The cold vessel structure for the T600 was calculated under the maximum load conditions (vacuum load). Special code had to be developed to correctly account for the composite materials that constitute the container (the honeycomb panels). For the T1200 LAr containers we foresee to use a higher density aluminium honeycomb and newly designed reinforcing profiles in order to attain a larger safety factor.

During and after the assembly all the welds are tested for helium tightness by pumping vacuum inside the internal volume of the walls. After the completion of these tests, the internal surface of the container is cleaned by pickling and passivation, followed by washing with de-mineralized water and drying with hot filtered air. Final test before the container delivery is the vacuum pumping inside the main volume.

The four independent containers will be accommodated in a suitable sustaining structure made of stainless steel beams (see Figures 6.4 and 6.5). The purpose of this structure (weighting 20 tons) is to keep deformations within the specifications for the alignment of the internal detector. Welded stainless steel plates close the external boundary of the structure. They act structurally as reinforcements against transverse displacements due to an earthquake but they also form a closed retaining tank (see Figure 6.6). This tank will be the third retaining surface (the first two are the "skins" of the honeycomb panels) and it will reduce to zero the probability of a liquid spill in the laboratory.

A common cooling shield encloses a pair of LAr containers at the same level (the lower two and the upper two). The cooling shield is made of panels (1×2 m^2) obtained from co-lamination of two deep-drawn stainless steel sheets. This solution, tested on the second T600 half-module[1] offers the advantage of a very large conductance together with a widespread distribution of the liquid nitrogen on the surface. A thermal insulation layer made of evacuated honeycomb panels (thickness ≈ 450 mm) is placed around the retaining tank and surrounds completely the four LAr containers assembly. This completes the main cryostat assembly.

[1] We recall that the cooling circuit for the first T600 half-module is made using pipes embedded into the LAr container walls. This solution was later considered too risky as the cooling circuit is not accessible after the completion of the assembly of the container.

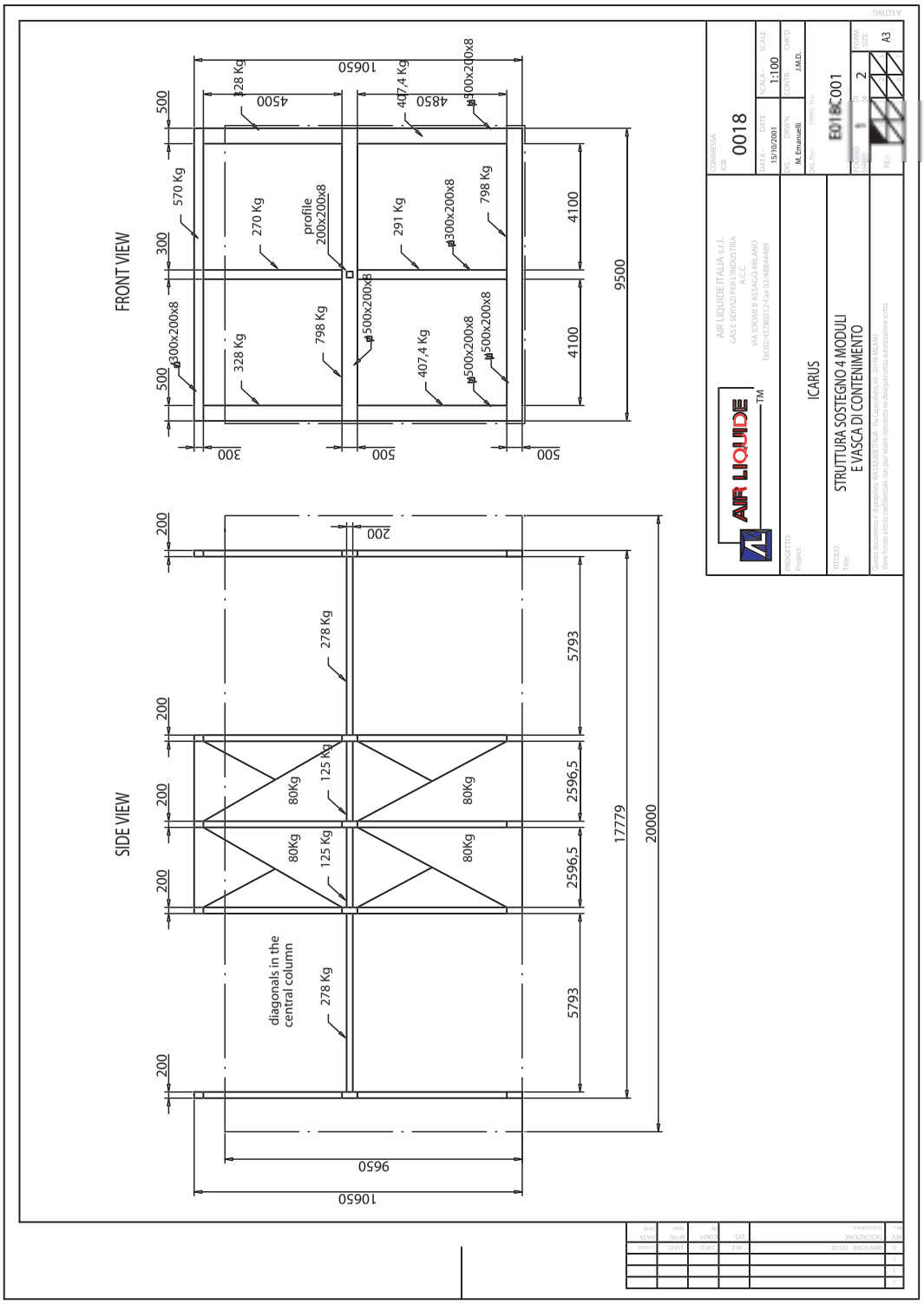

Figure 6.4: T1200: stainless steel sustaining structure.

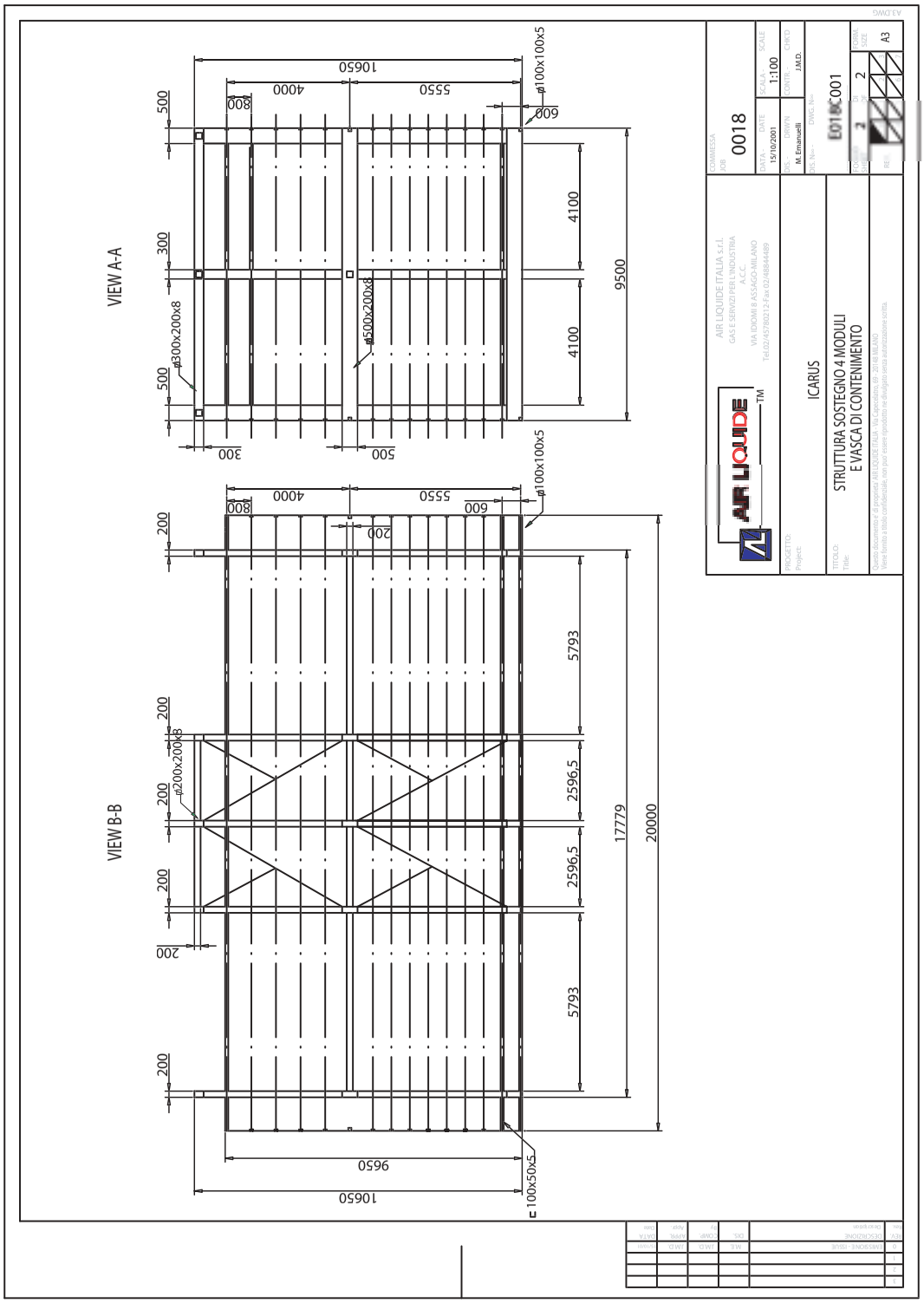

Figure 6.5: T1200: stainless steel containment vessel.

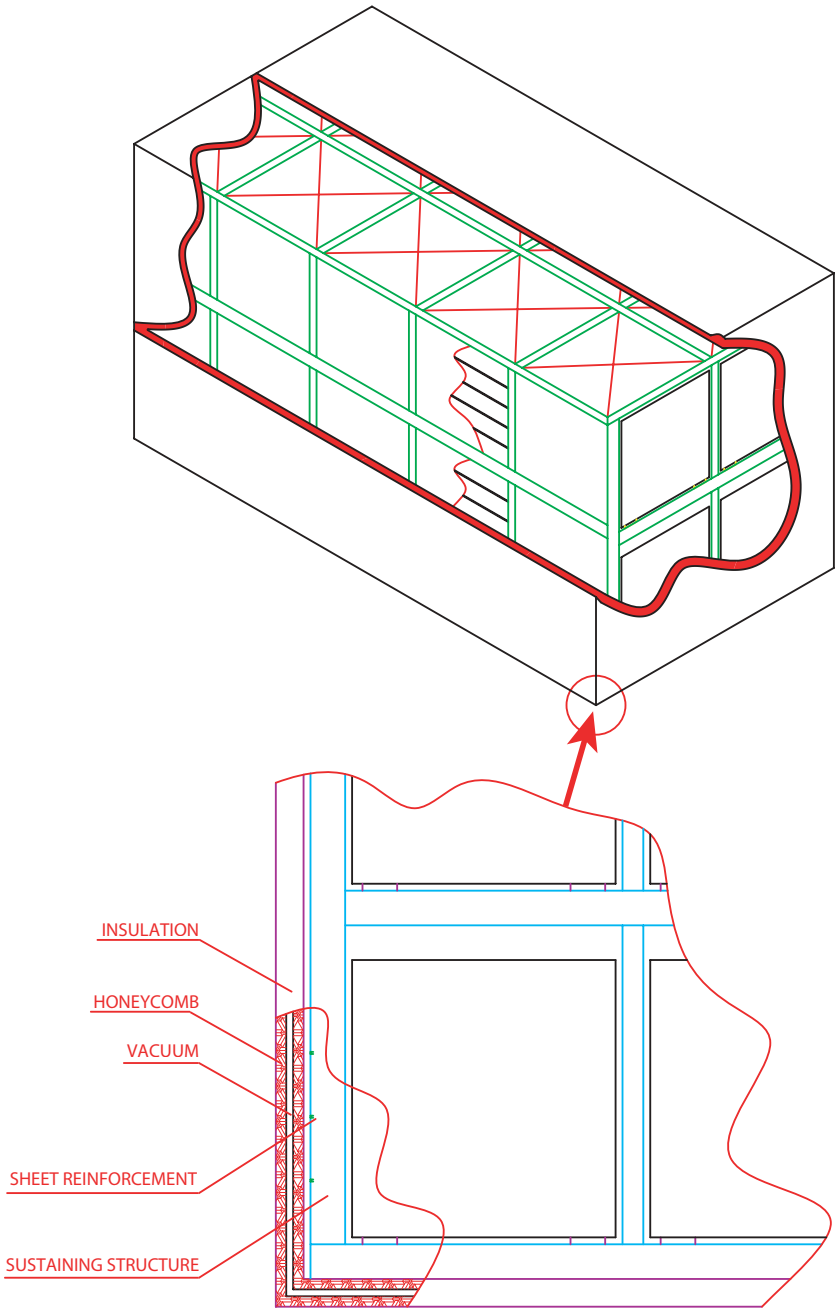

Figure 6.6: T1200: thermal isolation and containment tank.

Table 6.2: Geometrical characteristics of the ICARUS T1200.

Number of independent containers	4
Single container internal dimensions	
height	3.9 m
width	3.6 m
length	19.3 m
Single container external dimensions	
height	4.2 m
width	3.9 m
length	19.6 m
Container material (honeycomb structure)	aluminium
Walls thickness	150 mm
External insulation thickness (honeycomb+cold shield)	465 mm
Single container own weight	24.0 ton
Dimension limits for transportability on the Italian highways	1 bar
height	4.5 m
width	5.9 m
length	25.0 m
cross section of the entrance doors to the LNGS	
height	4.67 m
width	4.95 m
Total (cold) internal volume	1068 m^3
Total LAr mass	1470 ton

6.1.2 The vacuum system

The first operation of the start up procedure is the vacuum pumping into all the volumes that are going to be filled with liquid or gas argon. The purpose of the vacuum phase is the removal of air and other polluting gases from the LAr volume. Target pressure is 10^{-3} mbar or less, in order to reach the so-called "molecular regime" and let all the surfaces (in particular cables and plastic components) to out-gas the impurities.

For T600, the vacuum pumping system (see Figure 6.7) consists of 4 identical groups composed by a 24 m^3/hr primary dry scroll pump and a 1000 lt/sec turbodrag pump installed on four DN200 ports on top of the LAr container. In the T600 test run in Pavia, the pump-down time, to evacuate the argon volume down to 10^{-1} mbar, was about 20 hours. We recall that all materials installed in the internal detector have been subject to a specified cleaning procedure:

- ultrasound washing with de-mineralised water and appropriate detergent;
- rinsing (also in ultrasound bath) with de-mineralised water;

- drying in a vacuum oven or (for very large components) with hot air.

Figure 6.7: Picture of the T600 vacuum pumping units, on the top of the dewar.

Vacuum pumping was stopped 10 days after the beginning of the operations (about 175 hours of effective pumping time). The final pressure reached was 10^{-4} mbar, corresponding to a global leak rate of about 3×10^{-1} mbar lt s^{-1}, in good agreement with expectations (see Figure 6.8). The analysis of the residual gas inside the dewar showed a good agreement with expectations. Ten days after the beginning of the operation, vacuum pumping was stopped, the dewar was filled with purified gas argon and the cooling phase was started. The relative concentration of air and water was around 1/10 showing that outgassing was the dominant source for residual gas. Contributions from other components were negligible. The same vacuum system can be used for the T1200 units. In this case, having half the number of readout wires, the outgassing surfaces (dominated by the signal cables and by feedthroughs) are also approximately half and we expect, for the same pumping speed, a substantially better vacuum level. The pumping units will be connected, through appropriate joints, to one of the manholes.

According to the present procedure, the vacuum pumping will be performed at the same time in the four LAr containers. This reduces the time interval between the vacuum breaking with purified GAr and the start-up of the cooling process. An alternative procedure is presently under evaluation. It allows vacuum pumping in one container at a time, thus minimizing the possible consequences of a container mechanical failure during the vacuum pumping. In this case a fast recirculation system of hot GAr is required

to preserve the purity in those containers that have been already evacuated and refilled with purified gas argon while the others are under vacuum.

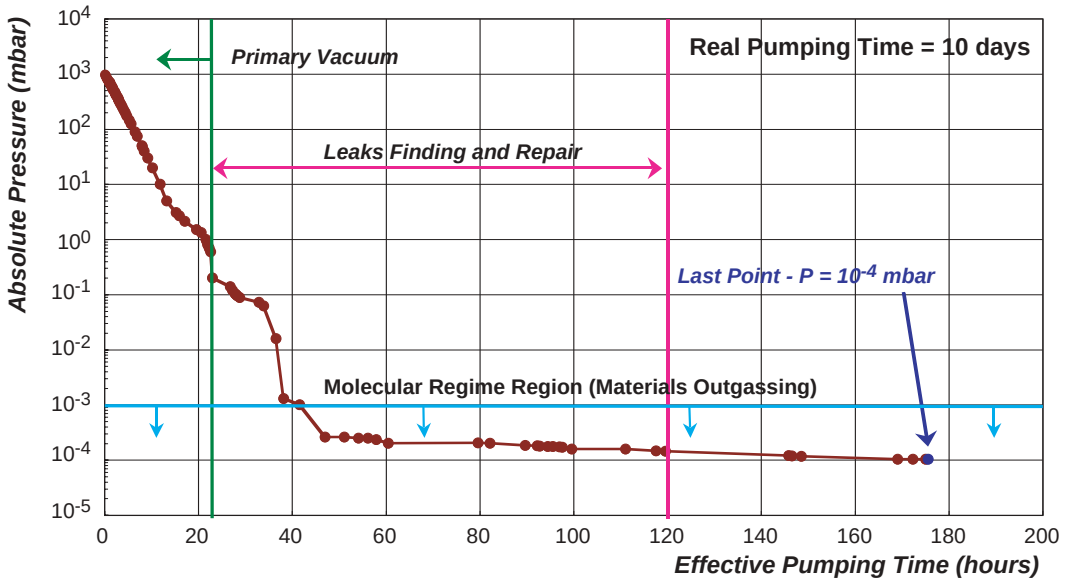

Figure 6.8: Pressure evolution during the vacuum phase of the T600 test run.

6.1.3 The cooling system

Cooling of the cryostat is performed by circulation of pressurized LN_2 (at 2.7 bar abs, nominal temperature = 89 K) inside the cooling shields of the two LAr container pairs. The former solution for the T600 was pure liquid nitrogen circulation. The circulation speed was defined by the requirement to maintain a maximum thermal gradient lower than 1^oC on the nitrogen circuit to ensure temperature uniformity in the LAr. Taking into account the actual thermal losses of the insulation, this leads to a LN_2 circulation speed of about $10m^3$/hr/LAr container (8000 kg/hr/LAr container). The corresponding LN_2 consumption due to the power injected by the circulation pumps themselves was about 25% of the total LN_2 consumption. Thanks to the large cooling shield conductance we foresee to use for the T1200 (see Figure 6.9), a two-phase gas and liquid nitrogen circulation; this has two advantages:

- best solution for temperature uniformity (ensured by thermal equilibrium between the gas and liquid phase);
- much lower mass circulation with respect to the pure liquid phase circulation, with considerable savings on the LN_2 consumption due to the nitrogen circulation pumps.

Minimum circulating gas to liquid mass ratio is about 5, in order to ensure saturated gas properties (thermal equilibrium with liquid). Taking into account the expected thermal losses from the insulation, the estimated mass circulation speed is only about 600 kg/hr/LAr container, while the volume circulation speed would be about 30 m^3/hr/LAr container. Each cooling shield is divided into eight sections (four sections per LAr

Figure 6.9: T1200 module cross-section.

container) into which the cooling nitrogen flows in parallel. One section covers the front and backward walls, while other three, "C"-shaped, cover the bottom, lateral and top walls (the circuit is obviously symmetrical for the two LAr containers). The cooling nitrogen is injected in a common collector running around the two LAr containers (external to the insulation) at the bottom level. The nitrogen flow is then subdivided between the different circuit branches and is recuperated on a common collector placed externally of the insulation running around the two LAr containers at the top level. A set of proportional aperture valves placed at the exit of the various circuit sections is used to regulate the relative amount of nitrogen flowing into the different branches. After the cryostat cool-down the aperture of these valves is regulated manually on the basis of the temperatures read at the exit point of the different branches. Once set the temperatures to the desired values, the aperture of the valves is definitively fixed. For each cryostat two LN_2 circulation pumps will be installed. The pumps will be standard cryogenic liquid transfer pumps with speed and prevalence regulated by a variable aperture bypass and a frequency controller (inverter). The pumps will be located near the LN_2 storage dewars installed above the T600 module. During normal, steady state operation, the two pumps will run in parallel each one serving a pair of LAr containers. In case of stop of one of the two pumps (for maintenance or substitution) the speed of the second pump will be doubled and the circuit will be automatically switched (by the automatic control system) for operation with a single pump.

The nitrogen return flow is sent to a phase separator (a small storage dewar placed on top of the main LN_2 storage dewar). The liquid is sent back to the main storage dewar while the gas is sent to one of the two re-condenser units installed above the T600 module. The nitrogen re-condenser feeds back the main storage dewar. This describes the steady state cooling operation. During the detector start up a different procedure is foreseen. The cool down of the cryostat is performed in two steps:

- Pre-cooling with a mixture of liquid and gaseous Nitrogen;
- Cooling with liquid nitrogen pressurised at 2.4 bar abs (temperature $\sim$89 K).

During this phase the LAr temperature should be reached in the fastest way, while keeping the temperature gradients on the internal detector structures within specifications (ΔT less than 50^oC along the same vertical). During the pre-cooling, a roots pump (one 500 m^3/h per LAr container pair) forces the circulation of gas nitrogen (GN_2) through the cooling circuit. The temperature of the gas is progressively and automatically decreased according to a pre-set ramp down by injection of increasing amounts of liquid Nitrogen (LN_2) in the main gas flow. During the T600 operation, that was using a single 300 m^3/hr gas circulation pump, the input temperature of the gas was decreased to -150^{o}C in 9 days. After 11 days of cooling the internal detector structure mean temperature was about -50^{o}C with a maximum gradient of about 25^{o}C (see Figure 6.10). On the 11th day of cooling the pre-cooling system was excluded and we started injecting LN_2 in the main cooling circuit. In the T1200 (and also for the next operation of the T600) we plan to shorten this phase thanks to the faster gas circulation pumps and by augmenting the ramp down slope.

During the test, when LN_2 injection started in the cooling circuit, we activated only the pump connected to the circuit of the first half-module. The second half-module, not

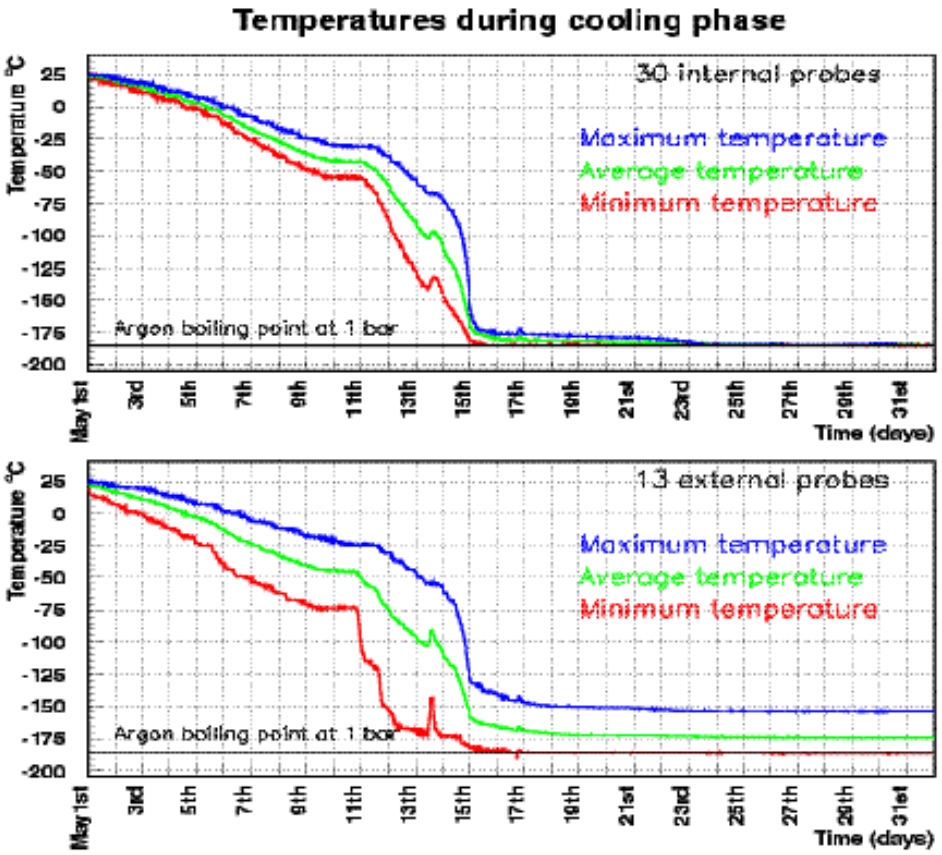

Figure 6.10: Temperatures behaviour on the internal detector structures (top graph) and on the aluminium LAr container walls (bottom graph).

filled with LAr, was cooled at the beginning by the first one through thermal conduction. After injection of LN_2 in the cooling circuit, internal temperatures started to decrease quite rapidly and, after about one day, we stopped the process several times to avoid exceeding the specified maximum gradient on the internal detector structures. The maximum gradient reached all over the internal detector was about 75^oC (6.10), while on the same vertical was just 50^oC (the maximum allowed value). The displacement of the wire holding devices (rocking frames with tensioning springs) was however quite small (≤ 0.3 mm corresponding to a variation of the wires tension ≤ 30 g to be compared to the nominal tension of 1200 g and the breaking limit of about 2900 g) (Figure 6.11). After a stop of about 10 hours we re-started to circulate LN_2 in the cooling circuit and about one day after we started to transfer LAr to the main volume. The same procedure (stopping the cooling to re-equilibrate the temperatures in case the maximum allowed gradient is reached) will be used for the T1200. In this phase, cool-down speed is less critical as the internal temperatures are already low enough to practically stop the internal outgassing. Moreover the argon gas recirculation system can be activated to purify the internal gas volume. To avoid unwanted stresses due to the dripping of LAr from the recirculators on hot portions of the internal detector, activation of the GAr recirculation system can be done only when the internal temperature approaches the LAr temperature.

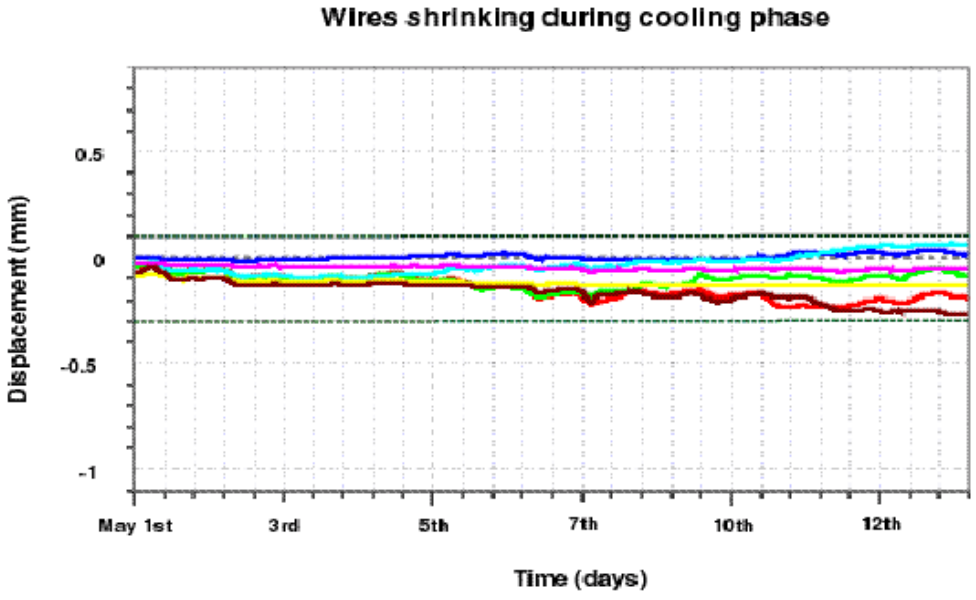

Figure 6.11: Relative displacement of the rocking frames (thermal contraction subtracted).

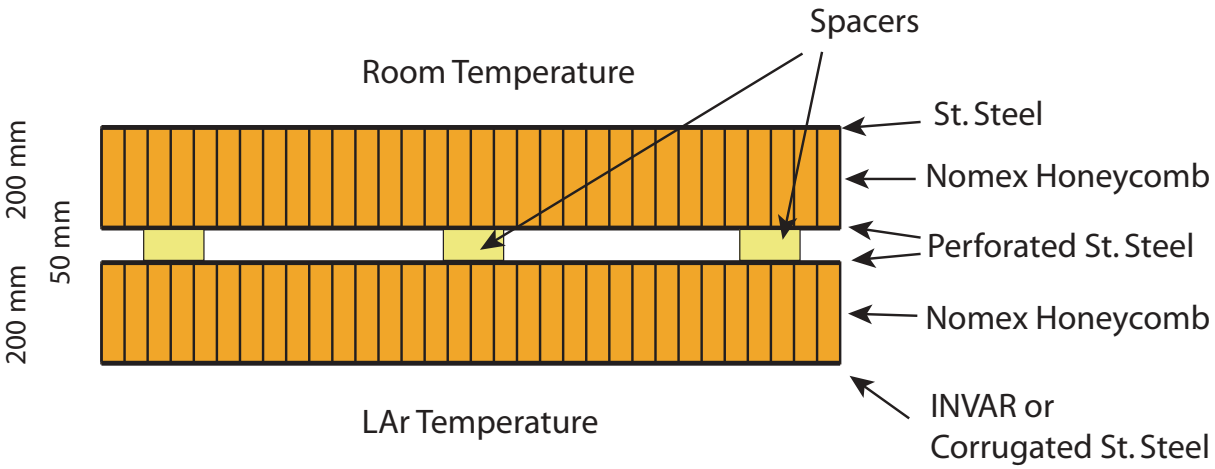

Figure 6.12: Schematic drawing of the evacuated Nomex honeycomb panel.

6.1.4 Thermal insulation

As anticipated in the introduction, we foresee to use, for the cryostat thermal insulation, evacuated panels made out of Nomex^{TM}[2] honeycomb panels as basic mechanical constituents.

The evacuated panel structure is illustrated in Figure 6.12. Two Nomex honeycomb panels (thickness = 200 mm) are separated by a set of polyethylene spacers. Inside the inter-space (50 mm) a layer of about 15 mm of super-insulation is placed. The basic Nomex honeycomb panels are realized by gluing to the Nomex honeycomb two metal sheets. The internal sheets (the ones facing the inter-space) are of perforated St. Steel (thickness = 2 mm) to allow the evacuation of the honeycomb cells. The external sheet (the one that will be at room temperature) is 2 mm thick St. Steel.

For the insulation basement and top, the sheet facing the LAr containers will be made of INVAR^{TM} in order to minimize the thermal contraction of the internal side of the evacuated panel. Thermal contraction would cause unwanted stresses on the panels corners and displacements between adjacent panels would worsen the thermal insulation by allowance of convective motions in the interstices that would be created in this case. A corrugated St. Steel sheet welded on an INVAR structure will solve this problem for the lateral walls.

The panels will be pre-assembled in the workshop to the maximum size convenient for safe transportation (the typical evacuated panel size will be about $10 \times 5 \times 0.45$ m^3). The lateral profile of each basic transportable panel will be sealed with a St. Steel sheet (1 mm thick). The panel will be tested for helium tightness and put under continuous vacuum pumping for at least 15 days and then sealed under vacuum. The vacuum level will be checked after the assembly and, if necessary, the panel will be put again under vacuum pumping.

In front of the joints for the chambers readout or the transfer lines for LN_2 and LAr, dedicated holes will be performed in the panels (obviously the external surface of the

[2]Nomex is a sort of paper saturated with a special resin that makes the material more rigid and non flammable.

panel will be sealed). After the panels installation the inter-space between the panels and the joints will be filled with insulating foam. The joints have a flexible section (bellow) to allow for relative motion between the LAr containers and the insulation due to the thermal contraction.

On the basement, where the LAr containers supports are located, holes will be performed for the insertion of evacuated and super-insulated St. Steel boxes (of adequate shape to reduce the thermal losses) for the connection of the containers to the anti-seismic shock absorbers.

Four special, angular profile, evacuated panels (about 10 m high) will be placed at the corners of the vertical insulation walls. These panels will be completely filled with Nomex honeycomb (no inter-space) and will facilitate the assembly of the vertical insulation walls.

Assembly of the thermal insulation layer will proceed as described in Chapter 8. During installation, the vertical panels will be held in place by and appropriate external structure. The panels will be joined together trough St. Steel plates bolted on the external edges of the panels themselves. After the assembly, the inter-space between adjacent panels will be filled with an insulating foam.

The evacuated Nomex insulation solution was installed on one of the lateral walls of the T600 module (see Figure 6.13) and the performance has been measured during the test run. In this case the panel's thickness was 200 mm and the dimension of the spacers was non-optimized. The performance, evaluated by means of the temperature measured on the external surface of the panel was however quite good: the thermal losses were of about 12 W / m^2. In the T1200, augmenting the panels thickness and optimizing the spacers dimensions we expect to reach thermal losses below 10 W / m^2.

6.1.5 Argon purification

Injection of argon (both gas and liquid) from the external storage dewar in the main volume is made by passing it through two identical sets of Oxy-Hydrosorb filters (purifier units) put in series. Each unit (Figure 6.14) is made of four identical cartridges put in parallel and filled 1/3 with Hydrosorb[3] (molecular sieves 5A) and 2/3 with Oxysorb. A circulation of LN_2 around the cartridges prevents the gasification of the argon, which would reduce dramatically the mass flow rate. The four filters sets are placed in evacuated stainless steel containers for thermal isolation purposes. Each set of filters is dimensioned (Oxygen adsorption capability) to allow for the purification of the LAr volume of a half-module, starting from standard commercial LAr (concentration of H_2O and O_2 0.5 ppm). The filling operation itself is quite simple and smooth. By regulating the pressure inside the external storage tank we can set the filling rate to the specified nominal value (2 m^3 / hr) as successfully verified during the T600 test run.

Most important at the end of the filling is the precise settling of the LAr level. According to specifications, the argon has to cover completely the internal detector structures (to ensure the required electrical isolation for the high voltage system) and remain at least to 65 mm from the container top (to allow for the eventual thermal expansion of the LAr). The allowed region for the level positioning is 10 mm wide. For this operation we need precise measurement of the argon level.

[3]Both Hydrosorb and Oxysorb are registered trademarks of Messers-Greisheim.

Figure 6.13: Photograph of the T600. The lateral wall insulated with evacuated Nomex panels is indicated.

In the T600 the argon level was measured by four sets of capacity level meters placed at the corners of the internal volume. Each set consisted by three, 1.2 m long, commercial level meters (nominal precision $\approx \pm$ 5 mm) and one home made, 0.5 m long, high precision level meter (nominal precision $\approx \pm$ 1 mm). The level was placed at 65 mm $\pm$ 5 mm from the container top and then, in a week after the completion of the filling, it decreased slightly (about 10 mm) due to the slow thermal contraction of the liquid. The gas evacuation valves on top of the main container were progressively closed in the few hours following the filling completion. This instrumentation has demonstrated to be perfectly adequate for measuring the level and will be used also for the T1200.

Both gas and liquid recirculation are needed to attain the desired free electrons lifetime. The same scheme used for the T600 will be implemented. Each LAr container will be separately handled with respect to the argon purification. Each container will be instrumented with:

1. two gas recirculation units with nominal speed = 25 GAr m^3 / hr / unit;
2. one liquid recirculation unit with nominal speed = 2.5 LAr m^3 / hr.

The two gas recirculation units (Figure 6.15) will collect the gas from the chimneys

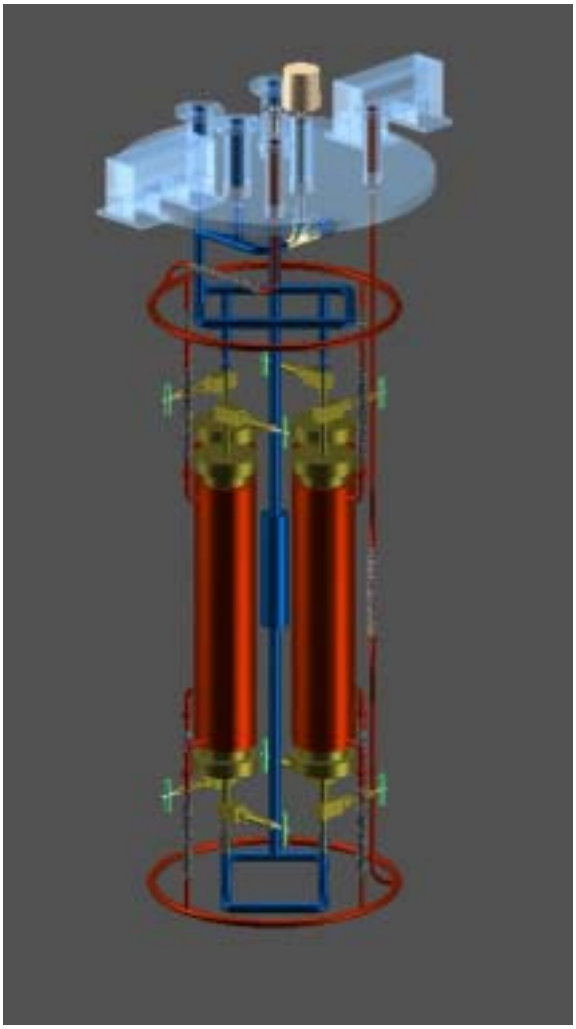

Figure 6.14: Drawing of the four filters set constituting one of the purifiers units. Both the Argon piping (in blue for colour copies) and the LN_2 circuit for cooling (in red) are shown.

that host the cables for the wire chamber readout. The gas is re-condensed into a LN_2 re-condenser with the liquid dropping into an Oxysorb filter placed below the re-condenser. The purified argon is sent back into the LAr container just below the LAr surface. Main purpose of the gas recirculation units is to prevent impurities coming from leaks on top of the container (from flanges or feedthroughs) or from the outgassing of the hot portions of the readout cables to diffuse into the liquid volume. They are expected to remain continuously active during the whole detector (not at the maximum speed). The importance of gas recirculation has been widely demonstrated in the operation of many prototypes, starting from the 2000 lt in 1991.

The liquid recirculation unit is used to purify the bulk LAr volume. The main purpose of liquid recirculation is to purify the argon just after the filling and until the target LAr purity for the detector operation is reached. In addition it has to restore the purity in case of an accidental pollution during the detector run (due for example to a sudden de-pressurization of the gas volume). Liquid recirculation units consist of an

Figure 6.15: Drawing of the gas recirculation unit. The argon (blue piping for colour copies, yellow is for LN_2 distribution piping) is liquefied in the recondenser on the top and passes through the Oxysorb cartridge to be re- injected near to the surface of the liquid in the main container. The recondenser and the filter are sealed in a vacuum tight barrel (not shown in the drawing) for thermal isolation purposes.

immersed cryogenic liquid transfer pump placed inside an independent dewar located on the backward side of the main LAr container. The dewar is fed through a vacuum insulated transfer line connected to the backward wall of the main LAr container at about 2 m from the container floor. The LAr in the pump cryostat is maintained at same level of the main LAr container by means of a connection between the two gas phases. The pump pushes the LAr into one of the two purifiers used for the container filling and the purified liquid is sent back on the front side of the LAr container (about 20 m apart from the input to the pump, to maximise the recirculation efficiency). A piping located on the bottom of the LAr container will distribute the purified liquid in order to reach possible dead zones (mainly the corners of the container).

The good functionality of the liquid recirculation system was demonstrated first in the 10 m^3 prototype and finally during the T600 test run. During the test run, the free electron lifetime in the main LAr volume measured right after the filling was of order of some tens of microseconds (30 μs to 60 μs depending on the location inside the volume), at the lower limit (or even below) of the sensitive range of our purity monitors. These figures, about a factor 2.5 lower that the nominal target value, are most likely a consequence of the increased pre-cooling time. We expect therefore that, operating according to the nominal start up planning we will reach almost exactly the target lifetime. Also, by anticipating the activation of the gas re-circulation units, we should obtain much better starting conditions.

After the filling with LAr, as soon as the pressure inside the main container was stabilised, we started the liquid re-circulation: the measured flow was 2.7 m^3 / hr at 1 bar prevalence. After few days of liquid re-circulation, as the lifetime reached definitively in the sensitivity range of our purity monitors, it became apparent the positive trend of the LAr purity. This trend was always positive (provided that the liquid and gas re-circulation units were active) for all the duration of the test run, up to the maximum reached value (1.8 ms, see Figure 6.16).

We realised indeed that the liquid re-circulation is compatible with the wires chambers readout (no microphonic noise apparently induced). So we could keep re- circulating while reading out the chambers.

At the stop-run, the lifetime was still growing with an increasing slope.

For the T600, the increasing lifetime rate was somewhat smaller than what expected on the basis of a simple full mixing model (in this case the lifetime should increase exponentially with a time constant of about 15 days). Motivation is in the presence of "dead regions" probably located in the container corners or inside the internal detector structure. In the T600 the distribution of the purified liquid was non-optimized and we plan to modify it during the installation in LNGS.

We do not expect to run the liquid recirculation continuously, even thought that the absence of induced noise on the wire chamber in principle allows it. Once reached the saturated LAr purity we plan to stop the liquid recirculation and maintain the lifetime level using the gas recirculation only. We were not able to test this procedure in the T600 due to the shortness of the test run. After about 70 days of liquid recirculation, the lifetime (1.8 ms) was not yet saturated. According to results obtained with smaller prototypes saturation should occur above 5 ms. We did not want to extend too much the test run duration so we decided to stop the run.

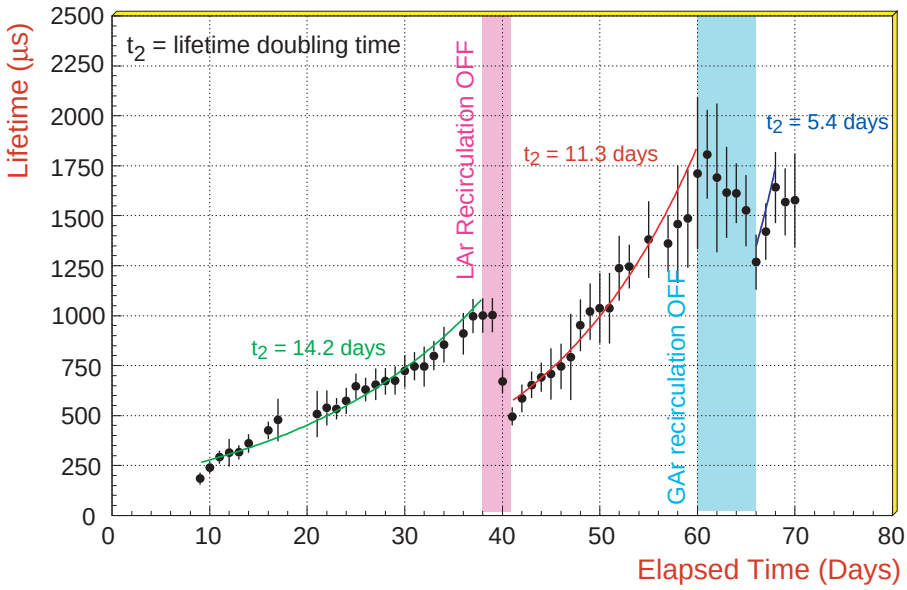

Figure 6.16: Evolution of the free electrons lifetime during the T600 test run. One can see the effect of stopping the liquid re-circulation (first negative step) and the one of stopping the gas re-circulation (second negative step).

6.2 Internal detector

Also for the basic structure of the internal detector we keep the present design of the T600. Each new sub-module will contain a high precision, high stability mechanical structure independent of the container that supports a single wires chamber with three readout planes, the field shaping electrodes and one cathode (see Figure 6.18). This gives the possibility to overcome the problems connected to the low mechanical precision of the big aluminium honeycomb boxes (of the order of cm) and the relative (sensible) shrinking between the aluminium dewar and the stainless steel frame of the wires chambers. The sustaining structure for the T600 internal detector is well visible in Figure 6.19.

Also the scintillation light detection system and all the slow control devices (level meters, position meters for the walls, temperature probes, purity monitors, etc.) will be anchored to the sustaining structure. Most of them will positioned behind the wire planes in the inter-space (about 30 cm wide) between the collection plane and the LAr container wall.

In the T600 the alignment of the whole structure has been carefully measured after the assembly. A satisfactory precision (of the order of 0.3 mm over the full detector size, that is the measuring device precision limit) was found. This result is important because the accuracy of the wire chamber event reconstruction capability, which depends on the exact distance between adjacent wires pairs and on the parallelism of the three wire planes, rely entirely on the mechanical quality of the sustaining structure. Furthermore, the good quality of the mechanics ensures that, during the cooling phase and at LAr temperature (87 K), no stress is induced on the wires and everything remains in the required precision range.

Apart from the modification required for the installation of the electrodes for the

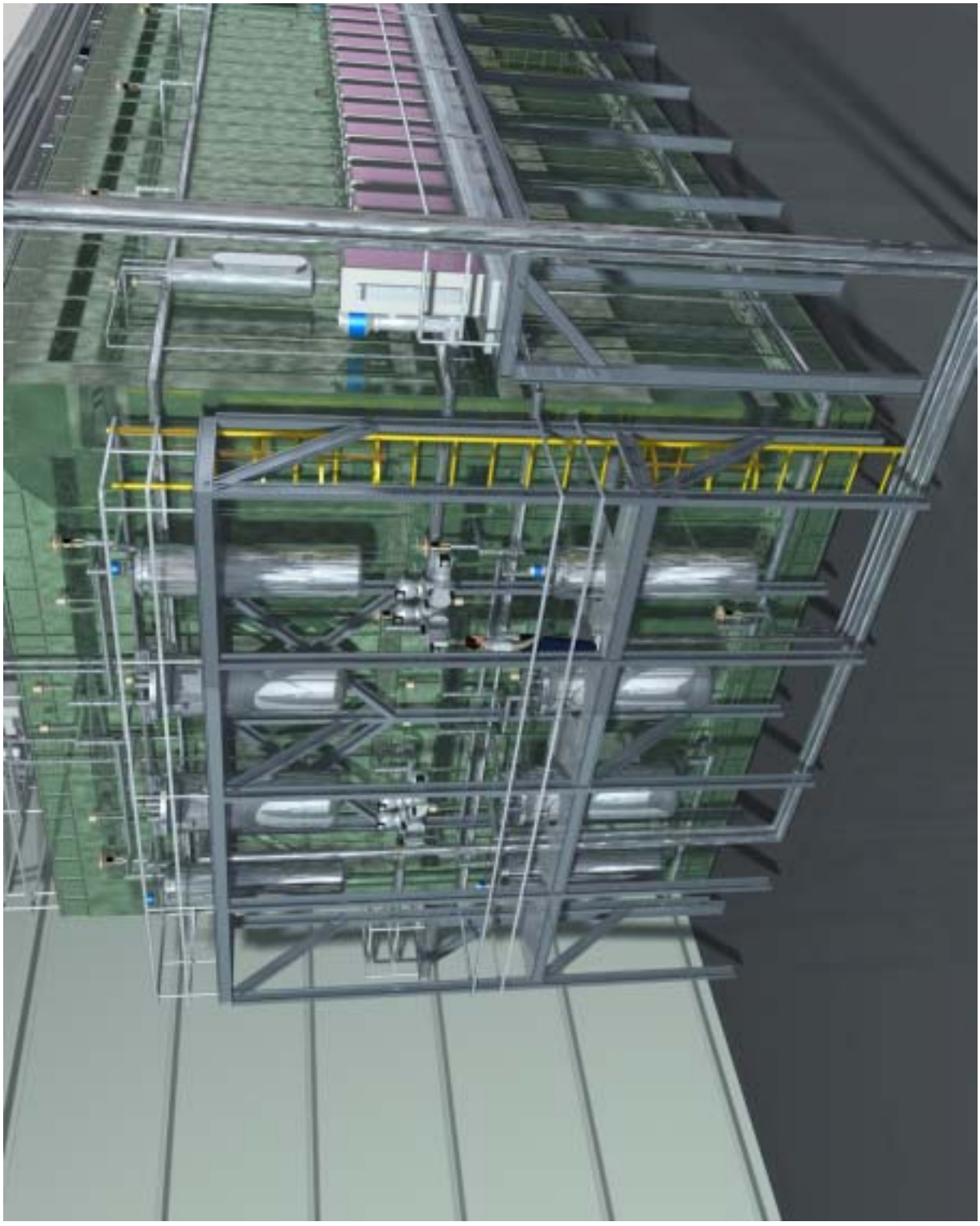

Figure 6.17: Arrangement of the main purifier units, the liquid recirculation units and the vacuum systems foreseen for the T1200 supermodule.

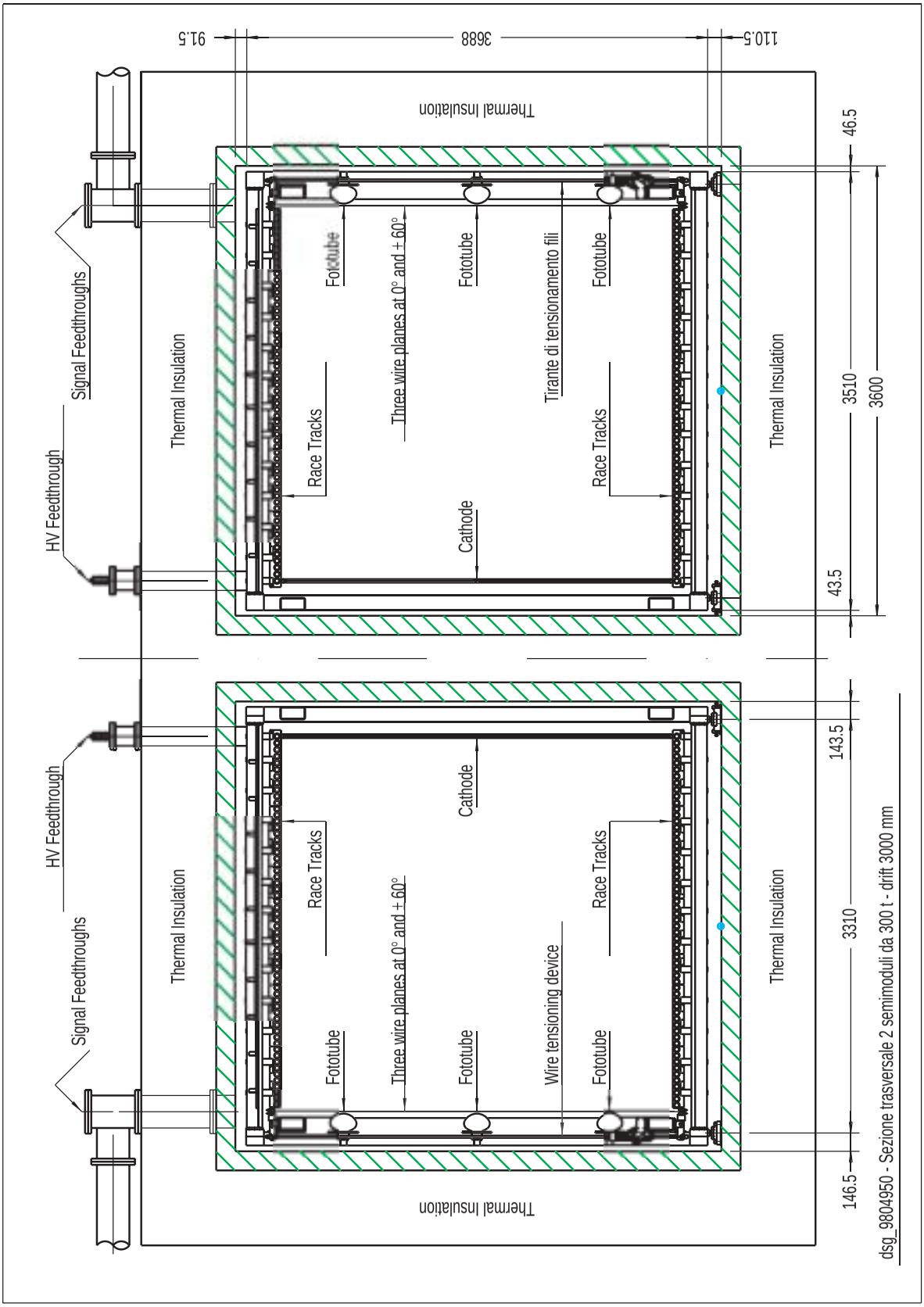

Figure 6.18: Cross-sectional view of the internal detector layout.

Figure 6.19: Photograph of the internal detector sustaining structure installed in the T600 first half-module.

non-imaging regions readout, the present mechanical and electrical solutions of the T600 inner-detector are preserved as much as possible. We plan to use

- a similar wire chambers structure with variable geometry, with three wires planes (all readout) at 0^0 and $\pm 60^0$ from horizontal and 3 mm pitch;
- a similar choice of the geometry of the field shaping electrodes made of 35 mm diameter pipes with 50 mm pitch;
- and a similar cathode structure.

Most of the components presently used for the T600 wire chambers (wires holders, combs, spacers, shock absorbers, PCB connecting boards, etc.) and for the drift HV system (voltage dividers, feedthroughs, etc.) can be used with no modifications. Also

the tooling already developed for the assembly (wiring table, assembly island) can be re-employed with minimal changes.

To reduce the number of readout channels and therefore the costs, we assumed that only one wire chamber is needed to readout a sub-module and therefore that the maximum drift can be increased from the present 1.5 m to 3 m. This will not change the basic mechanical structure of the internal detector.

In addition to the considerable savings obtained from halving the number of sensible wires and of the related electronic channels, this solution allows to put the signals extraction feed through only on one side (the "external" one) of the dewar, so reducing the vertical dimension of the apparatus.

We already verified that the drift could be expanded to more than 3 m:

- during our last tests with the T600 module we achieved LAr purities corresponding to free electrons lifetimes of about 2 ms (the corresponding drift is 3 m at 500 V/cm) constantly increasing with the argon recirculation time and limited by the total duration of the test run; in smaller prototypes, where outgassing surface to volume ratio is much larger, (24 cm, 50 lt) much longer lifetimes have been measured (> 7 ms);

- always in the T600 the full HV system has been tested up to 150 kV with stable conditions and negligible leakage currents. Therefore the operation with 3 m drift at 500 V/cm is achievable with no modifications of the present technology.

For the T600, since all components were already delivered at the end of 2000, we decided to keep the original 1.5 m maximum drift also for the second half-module.

Assembly of the internal detector will be performed in a 100,000 class clean room directly connected to the front side of the LAr container. At least for the first LAr containers, assembly will be performed in the same assembly hall that was used for the T600. If assembly rate will need to be increased, a second assembly hall may be instrumented in a relatively short time and the assembly will proceed with two teams working in parallel.

We foresee to assign the internal detector assembly to an external specialized manpower supplier. Those Collaboration members that already participated to the assembly of the first T600 half-module will control the operations. External personnel will be trained to participate on the assembly of the second T600 half-module.

6.3 Slow-control instrumentation

In order to monitor and control the operation and behavior of the first half-module of the 600 ton, a series of sensors with the corresponding readout electronics was built and tested and then installed in the detector (see Figure 6.21) [55]. Four different types of sensors have been installed and are now operated:

- sixteen liquid argon (LAr) level meters to monitor the LAr filling of the dewar;

Number of readout chambers	4
Number of wires planes per chamber	3 (all readout)
Wires orientation respect to horizontal	0^0, $\pm 60^0$
Wires pitch (normal to the wires direction)	3 mm
Wires length:	
horizontal wires	9.42 m
wires @ $\pm\, 60^0$	3.77 m
wires at the borders ($\pm 60^0$)	0.49 m $\div$ 3.77 m
Wires diameter	150 μm
Wires nominal tension	12 N
Number of wires / construction module	32
Number of modules / chamber:	
Horizontal wires	66
Wires @ $\pm\, 60^0$	2×145
wires at the borders ($\pm 60^0$)	2×30
Number of wires / chamber:	
horizontal	2112
@ $\pm\, 60^0$	2×4640
at the borders ($\pm 60^0$)	2×960
Total	13312
Total number of wires	53248
Maximum drift length	3 m
Maximum drift time @500 V / cm	2.0 ms
Distance between race tracks	50 mm
Number of race tracks / sensitive volume	58
Imaging volume / submodule:	170 m^3
length	17.95 m
width	3 m
height	3.16 m
Total imaging volume / supermodule	**680 m^3**
Total imaging LAr mass	**952 ton**

Table 6.3: Main parameters of the internal detector mechanics for T1200 supermodule

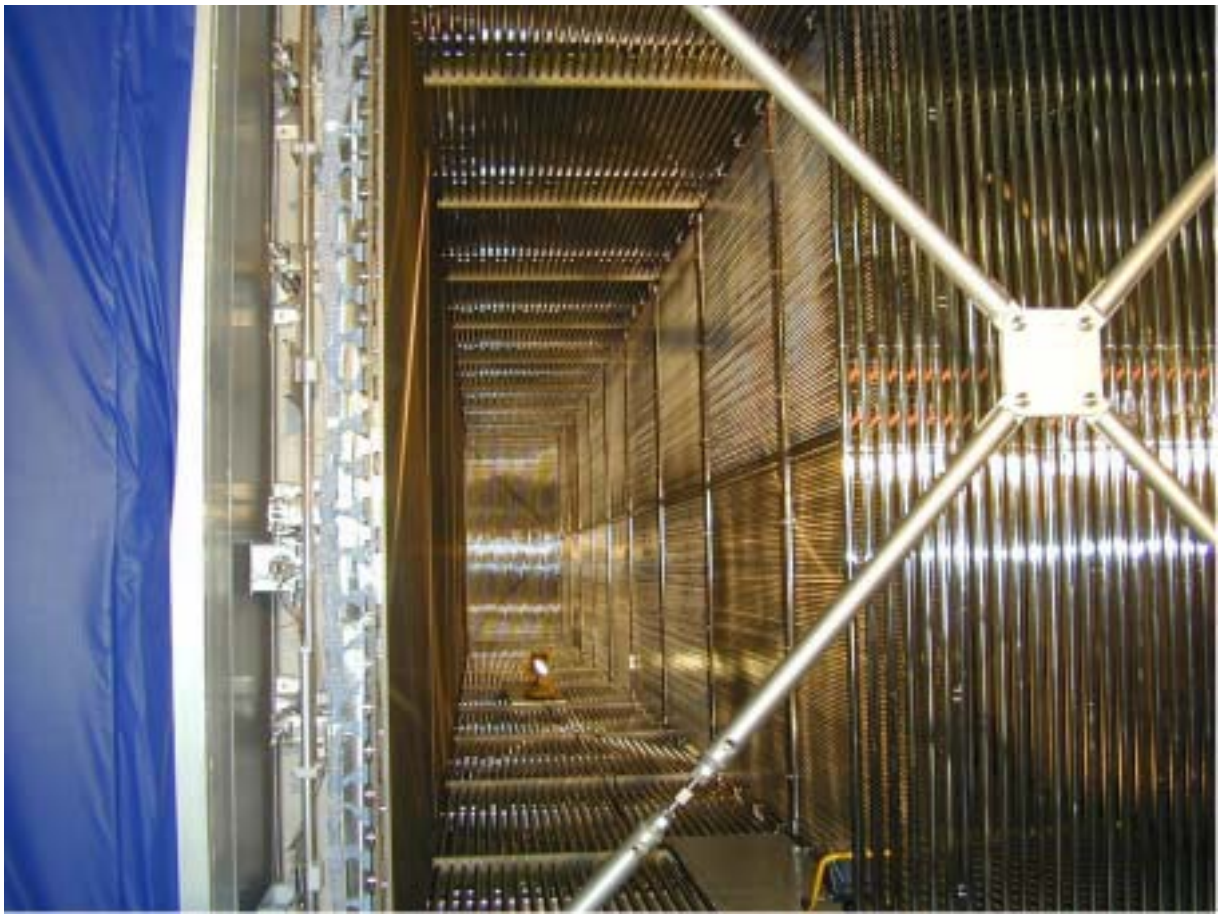

Figure 6.20: Photograph of the internal detector assembly in the T600 first half-module. Central cathode and race-tracks may be clearly identified.

- eight position meters to measure the inward movement of the dewar walls when the dewar is being pumped before filling it and the outward movement when it is filled with LAr;
- seven position meters to measure the movement of the springs, which are attached to the wires of the wire chambers, and which are intended to compensate the thermal contraction during the cooling phase from room temperature to LAr temperature (-189^{o}C) and hence maintain a constant tension on the wires;
- thirty platinum resistors (PT1000) for the temperature measurement.

The level meters are cylindrical capacitors (see Figure 6.22). The relative dielectric constant of LAr is $\epsilon_{LAr} = 1.54$; hence, the capacity of the sensors changes linearly with the length of the sensor immersed in LAr. Four level meters are mounted at all four corners of the cryostat to cover the full height of about 4 m. The sensors are all mounted inside a shielding, which is grounded to the chamber frame. The lower three sensors have a length of 1.3 m to monitor the LAr level during the filling phase with a precision of about 1cm. The four precision level meters at the top positions serve as monitors of the LAr level during the detector operation when it is full, with a precision of about 1 mm. The

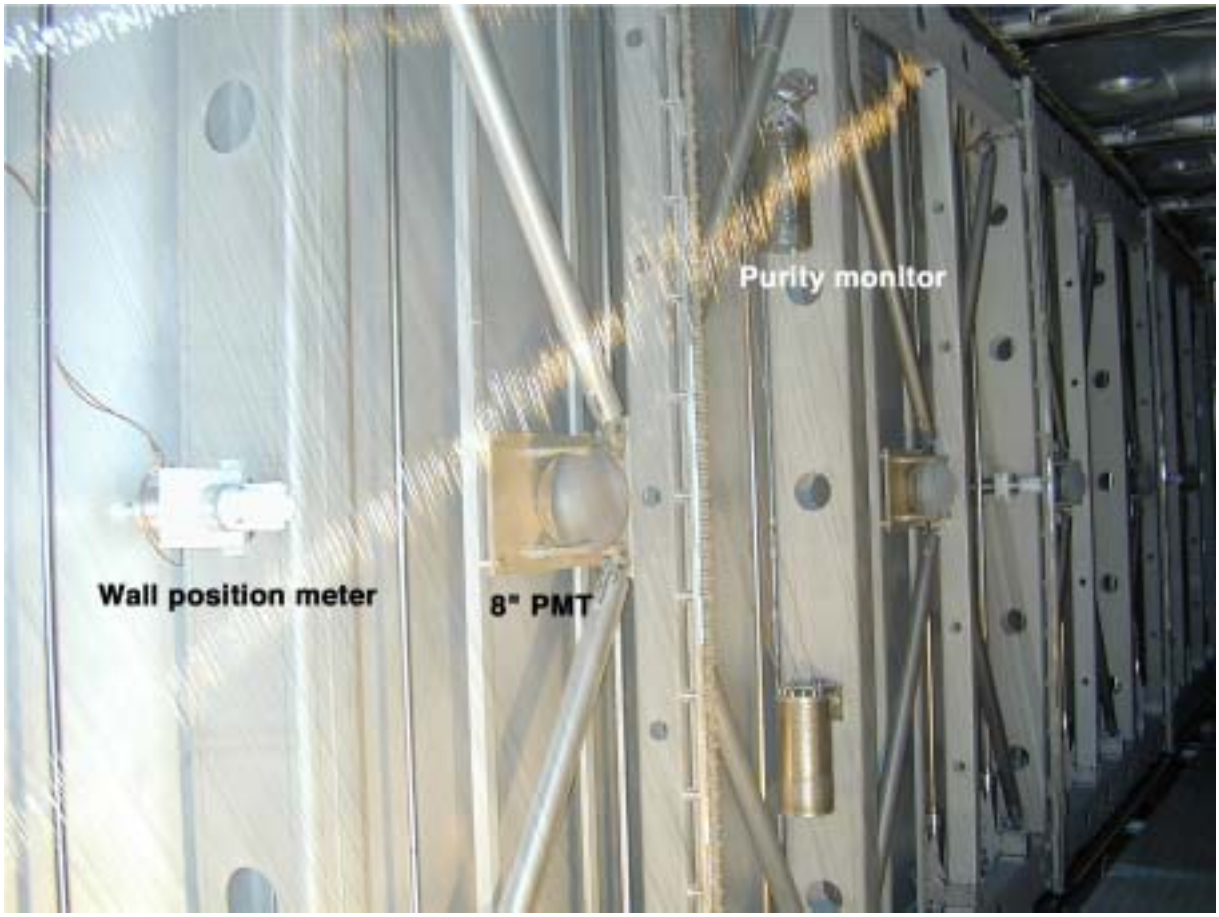

Figure 6.21: View of the wire chamber. Sensors for the wall position and liquid Argon purity are visible behind the wire planes. A PMT for scintillation light collection is also visible.

four level meters mounted at the top positions consist of two 500 mm long stainless steel tubes mounted in a 1050 mm long shielding, as shown in Figure 6.22. Two polyethylene capsules (fiberglass enforced epoxy for the sensors at the front) are holding the tubes and are used to mount the sensor inside the shielding. The radial gap of the capacitors is 0.5 mm. In air the capacity is about 730 pF and the sensitivity to a change of the LN_2 level is 0.7 pF/mm.

The position meters are cylindrical capacitors with a capacitance depending on the relative position of the inner and outer parts. The outer cylinder and the inner shaft are stainless steel, and the end caps with the precise bearings for the inner shaft are made out of glass-fiber enforced epoxy. The radial gap between inner and outer cylinder is 0.5 mm for all the position meters. Four position meters are mounted along both sides of the cryostat at the locations shown in Figure 6.23. They are mounted with polyethylene clamps at half height to the vertical poles of the wire chamber frame (see Figure 6.26). The sensors measure the inward movement of the walls when the cryostat is evacuated to vacuum, and the outward movement, when it is filled with LAr. The precision is about 0.2 mm.

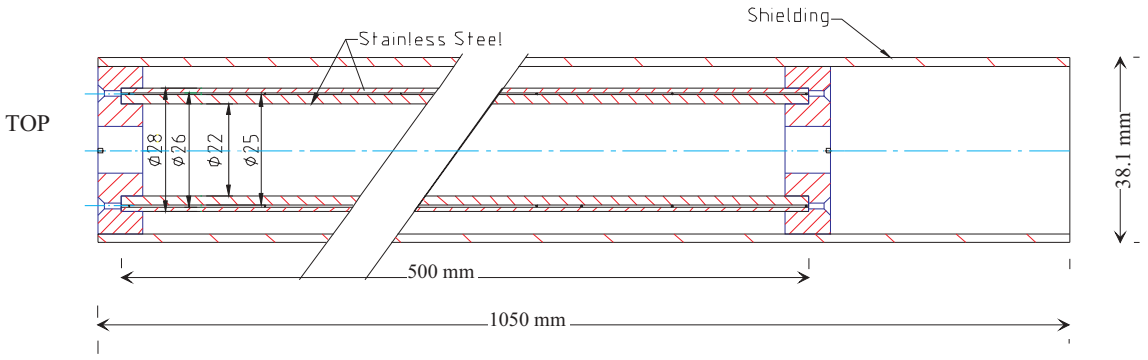

Figure 6.22: Precision level meter mounted inside the shielding.

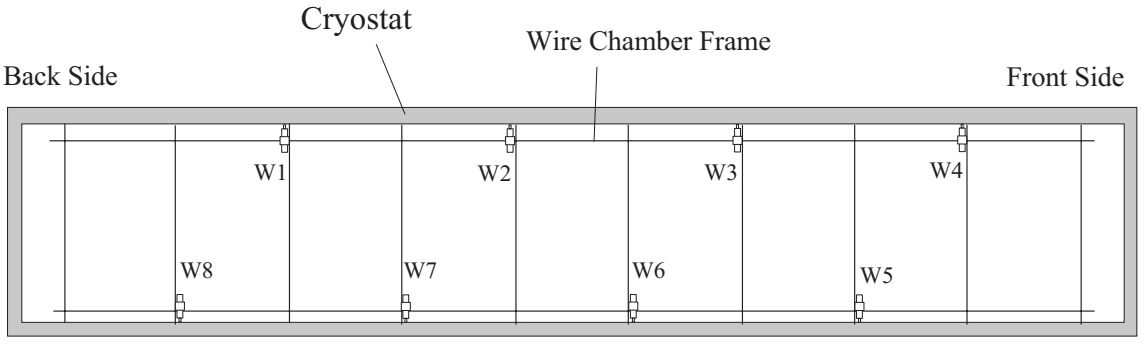

Figure 6.23: Schematic view of the cryostat, seen from top. Indicated are the locations of the wall position meters, mounted to the chamber frame.

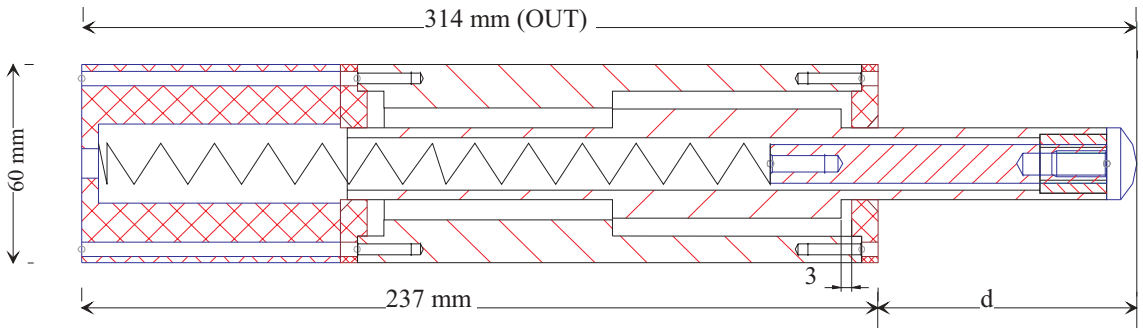

Figure 6.24: Wall position meter drawn in the OUT position.

Figure 6.24 shows the drawing of a wall position meter in the OUT position. A spring is pushing the inner and outer cylinders apart. The outer cylinder is fixed to the wire chamber frame and the inner shaft is pushing against the wall. The extension of the outer cylinder holding the spring in the IN position is made out of poyethylene. Figure 6.25 shows a picture of an assembled wall position meter (on the right) and of its parts (on the left). The wall position meters have a linear measuring range of about 65 mm.

The horizontal wires of the wire chambers are split in two halves, the front-half and the back-half. The wires of one half-chamber are 9 m long, fixed at the center of the chamber and tensioned from the front and the back sides. The wires on the left and on the right side are then grouped in three groups, each one attached to a spring, which is used for tensioning. The springs compensate the thermal contraction of the wires during the cooling phase, and hence maintain an approximately constant tension on the wires. Six position meters for the horizontal wires are attached to the springs at the front side (see Figure 6.28) to measure their movement during the cooling phase (three on the left side and three on the right side); no wire position meters are installed at the back side. Figure 6.27 shows the drawing of a position meter for horizontal wires. The inner side of the outer cylinder also has the periodic structure seen on the inner shaft. Hence, the sensor consists of ten parallel cylindrical capacitors to increase the sensitivity to a change of the relative position of the inner and outer parts. The sensors have a linear measuring range of about 15 mm, and a total (mechanical) range of 20 mm.

The position meter for the vertical wires was built as a prototype for the wire position meters. It is similar to the type for the horizontal wires, but has about twice the total range. Figure 6.28 shows how the meter is mounted behind the wire chamber.

6.4 LAr Purity Monitor

A dedicated device provides direct measurement of the LAr purity in terms of electron lifetime. The double-gridded drift chamber design for LAr purity measurement was first developed in 1989 [56] by the ICARUS Collaboration. During the operation of the 3 ton ICARUS prototype at CERN a purity monitor device has been installed inside the LAr vessel and the electron lifetime has been routinely measured over more than four years of running with the 3t prototype. Similar devices have been built and operated with

Figure 6.25: Picture of a wall position meter. On the left side the sensor is decomposed in its parts, and on the right side it is assembled.

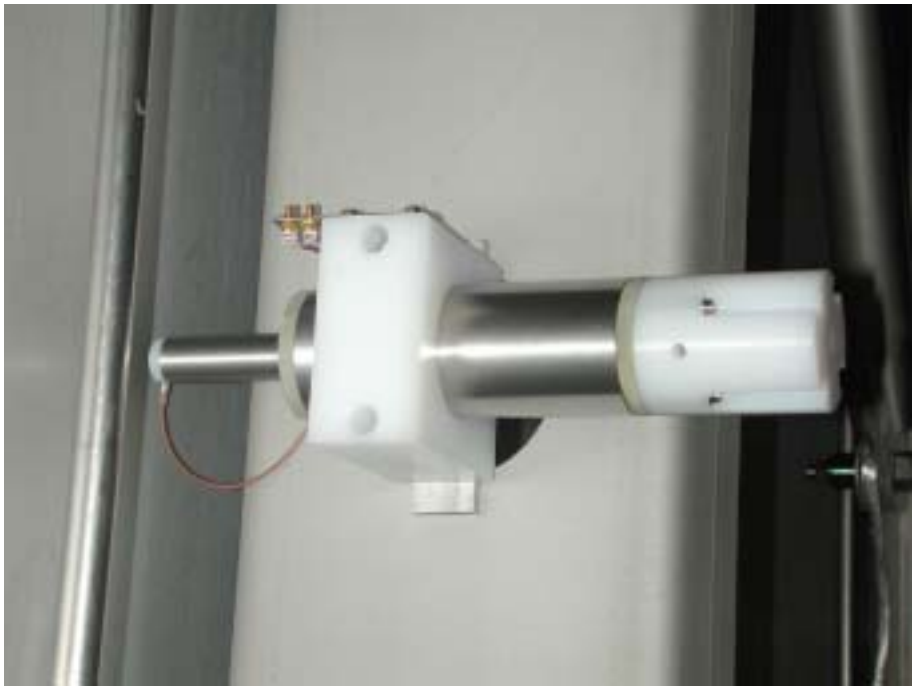

Figure 6.26: Wall position meter mounted to the wire chamber frame. The inner shaft of the sensor is pushing against the cryostat wall.

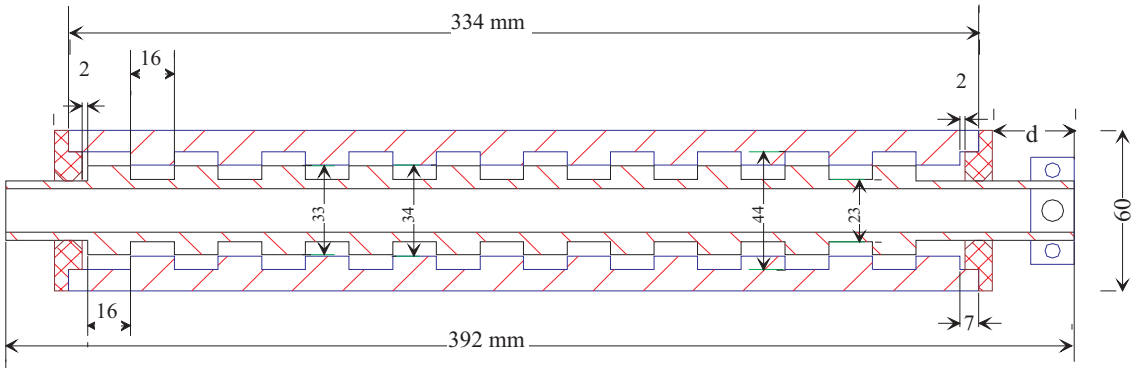

Figure 6.27: Drawing of a position meter for horizontal wires.

the subsequent prototypes. In the case of the last ICARUS prototype, the 10m^3 module operated first in Pavia and after at the Gran Sasso Lab during 1998-2000, the purity monitor design has been revised in view of the realization of the final purity monitor system for the T600 module. The major modifications concern the mechanics, the choice of the photo-cathode material and the replacement of the light source. The signal read-out system remained almost unchanged. After the experience of the upgraded purity monitor, during the $10m^3$ test, we proceeded to the realization of the purity monitors for the T600 module.

The purity monitor drift chamber basically consists of four electrodes and a field-shaping system:

- the (photo)-cathode disk (K)
- a first grid (GK), at short distance from the cathode
- an array of 15 field-shaping rings
- a second grid (GA), facing the anode
- the anode disk (A), at short distance from GA

All these elements are in stainless steel, while the mechanical structure, formed by a system of rods, bolts and spacers, is in vetronite. Both materials have similar thermal coefficient, to guarantee negligible thermal stresses during cool-down operations. The mechanical stability of the device results to be extremely satisfactory and suitable for long operation in cryogenics environment.

In Table 1 the geometrical parameters and characteristics of the device are shown.

Four independent electric potentials can be applied to K,GK,GA,A. The grids and the field-shaping rings are connected by a high-value resistor chain (50 MΩ each), so to realize a resistive divider for the electric potential applied between the two grids. This

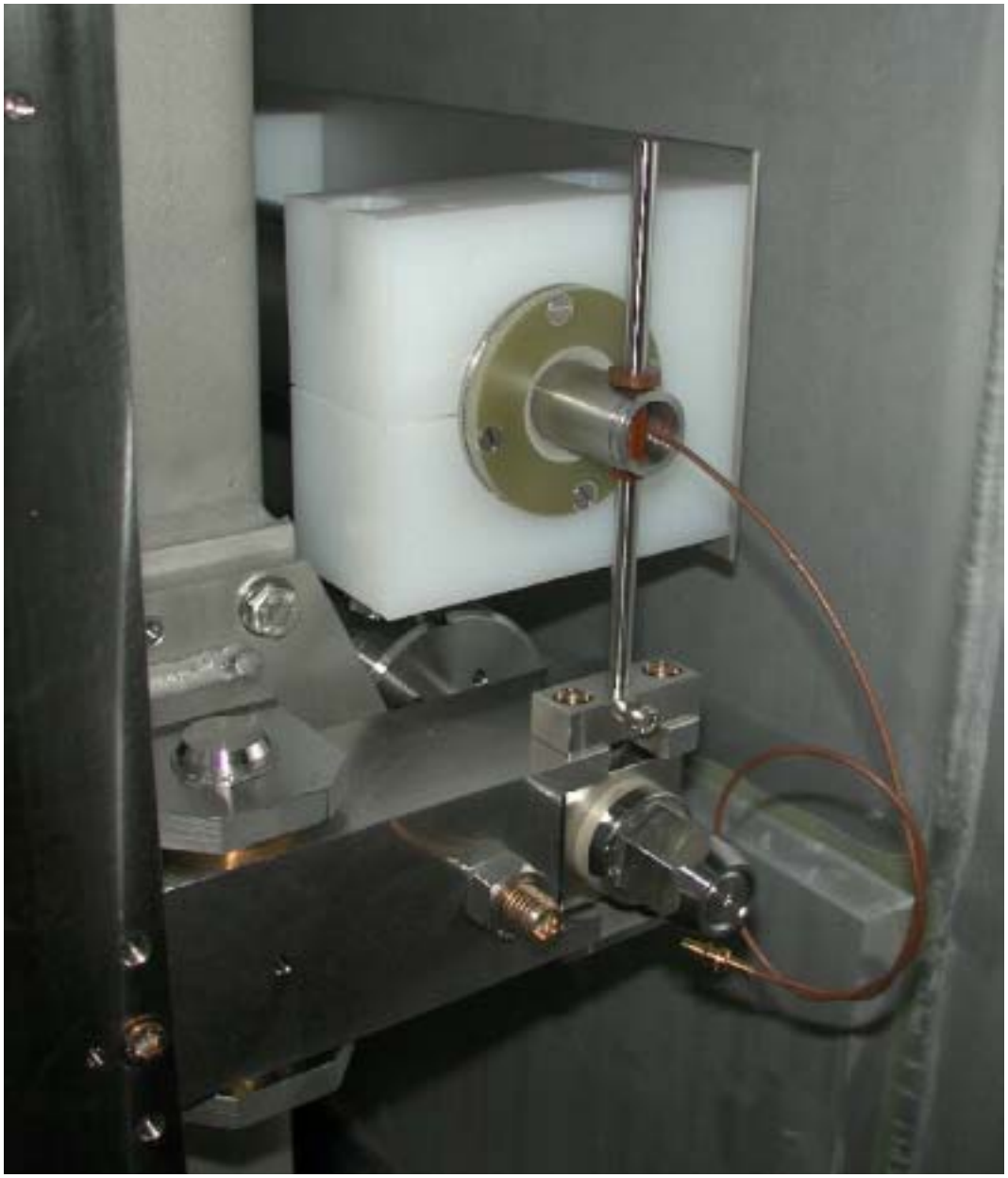

Figure 6.28: Position meter for horizontal wires attached to a spring.

Figure 6.29: Position meter for vertical wires mounted behind the wire chamber.

total length	188 mm
diameter	80 mmm
K - GK gap	18 mm
GK - GA gap	160 mm
GA - A gap	10 mm
ring pitch	10 mm
number of rings	15
fiber inclination	20^o
fiber type	HGC-M0940T (1 mm)
cable type	RG316U (teflon)

Table 6.4: Geometrical parameters of the T600 purity monitor

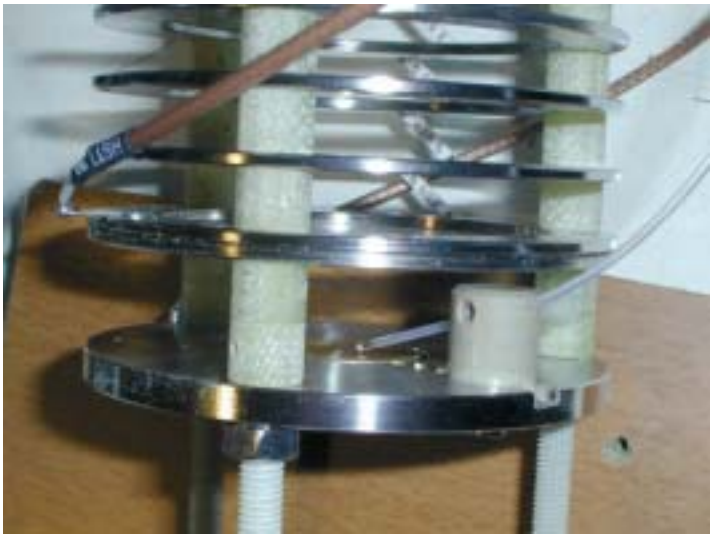

Figure 6.30: Detail of the purity monitor: photocathode, cathode grid and fiber

scheme ensures the uniformity of the electric fields (E_1, E_2, E_3) in the three drift regions (between K-GK, GK-GA and GA-A respectively). Typical field values range between few tens of V/cm and some hundreds of V/cm.

The two grids are electro-formed Nikel meshes, with 1.9 mm wire spacing, $100\mu m$ wire diameter and 89.7% geometrical transparency. The flatness of the grid plane is guaranteed by a mesh holder formed by two rings pinching the mesh in between.

The grid geometry combined with the HV bias applied to the electrodes (K,GK,GA,A) should satisfy two major requirements:

- Maximum transparency: i.e. the minimum number of drifting electrons should be lost crossing a grid.
- Maximum shielding: drifts of the electrons before a grid should not affect the field after the grid.

The two requirements are in contrast, but a reasonable compromise can be achieved.

A quartz optical fiber (1mm diameter, all silica) allows to drive UV light (down to 180 nm of wavelength) from the source, outside the chamber vessel, onto the photo-cathode. A fiber holder, realized in Peek and mounted on the cathode disk, keeps the fiber end in place at a distance of 2 mm to the cathode center and at an angle of 20^o to the cathode plane. A detail of the purity monitor structure is shown in Fig.6.30.

A cryogenics, indium sealed feedthrough, allows the fiber to exit the LAr vessel and reach the light source at the other end. The light source is positioned as close as possible to the feedthrough, to minimize attenuation. The length of the fiber is determined by the position of the purity monitor inside the LAr vessel. In the case of the T600 module it ranges from 4 m to 7 m. In Fig.6.31 a fully mounted monitor is shown in the T600 setup.

The last and most important component of the purity monitor system to be described is the photo-cathode. It is the source of electrons necessary for the electron lifetime measurement. It is evident that the precision on the lifetime determination depends

Figure 6.31: A purity monitor, mounted inside the T600 cryostat

on the actual signal-to-noise conditions provided by the system, the signal being the charge amplitude extracted from the cathode and subsequently collected by the anode. A variety of different electron extraction or production methods at the cathode have been investigated, in order to define the most efficient source.
In recent years there was a growing interest in developing electron sources based on semiconductor photocathode, able to produce much larger charge yield than metal-based photocathodes, thanks to the combined effect of their (typically) higher QE and lower surface barrier. In spite of the promising properties of SC, their use as photo-cathodes in our purity monitor systems is severely limited by the chemical reactivity shown by the SC with alkaline elements and by the NEA emitters. The oxidation of the surface during the exposure to atmosphere, before deployment in LAr, turns into a large degradation of the QE value. All elemental SC with stable chemical characteristics, like Si, GaAs, CdTe, have higher surface barrier (4 to 6 MeV), therefore requiring the use of adequate UV photon source. Their QE is in general higher than metals, at least one order of magnitude better. This is the motivation for equipping the purity monitor with elemental SC photo-cathodes.

A first set of measurements have been pursued, aiming to the characterization of a number of SC samples of various types [57]. The tested samples were of metals (Au, brass, Cu) and of semiconductors (GaAs, CdZn, InSb, etc. with different levels and types of doping). All the tested materials emit only under UV radiation. Some SC have photo-electron yields significantly higher than metals. The best results in term of QE have been shown by GaAs and Cd(Zn)Te. This lead to the choice of equipping the purity monitor for the first T600 half-module with these types of SC as photo-cathode material. A second set of tests is on-going. Samples of Si, p-type doped, show even larger QE when microstructured surfaces are realized (porous surface by electrolytic method). This option will be considered in view of the installation of the purity monitor systems in the second

T600 half-module.

All materials investigated so far, and compatible for the particular application as photo-cathodes for the purity monitor system, show photo-emission under UV light, with wavelength below about 300 nm. This implies the use of suitable UV light sources and UV light transport means (from the source to the ph-cathode). The light transport has been solved by using quartz fiber, as discussed above.

The choice of the UV light source is more complicated: the light must be fed in pulsed mode, with high pulse energy and short duration. Obviously, the use of high power lasers (like for example Nd-YAG laser - 266 nm -, or KrCl excimer laser - 222 nm) looks ideal. However, this solution is expensive, not easy to handle and above all it brings to fast degradation of the fiber entrance. In the last few years an alternative option to the laser devices has been adopted, namely the pulsed Xenon flash lamps. Commercially available Xe lamps emit in a wide range from $\lambda \sim 185nm$ to $\sim 2000nm$, but with a large peak around $\lambda \sim 240nm$, with pulse width of about $1\mu s$. The optical coupling of the lamp to the fiber, for the purity monitor system, consists of a couple of biconvex fused silica lenses (transparent to UV light, 25.4 mm focal length) contained with the lamp bulb inside a PVC cylinder. At one end of the cylinder a pipe hosts the fiber end keeps it in the focal point by means of a micrometric adjuster. This system (Xe lamp + optical coupling + fiber) is an easy handling, portable device well suited for the LAr measurement with the purity monitor device described above.

The LAr purity level was continuously measured during T600 filling and steady state operation. The purity monitor readout was accomplished by manual operation of a digital scope. Each pulse of the light source is seen as a waveform of a roughly trapezoidal shape, whose three main features (rising edge, flat top, falling edge) correspond to the three main drifting gaps of the purity monitor. The typical, total duration of the waveform is of the order of hundreds of microseconds. A typical waveform is shown in Fig. 6.32. The measurement of the rise and fall amplitudes, along with the pulse duration, gives a direct estimation of the charge degradation in the LAr.

This purity monitor system can be transferred with the same layout to equip the T1200 modules.

6.5 High-voltage system

In the T600 modules, the two active volumes –width: 3 m, height: 3.2 m, length: 18 m– are configured with a cathode centered in the cryostat facing the two side walls and two wire chambers on the sides. The maximum drift path is 1.5 m and, for an electric field of 500 V/cm, the applied high voltage is -75 kV. The crucial parameter that allows for a re-design of the TPC chamber geometry (see figure 6.33) –with a maximum drift path of 3 m, a single wire chamber per volume and half of the wires and electronic channels– is the possibility to safely employ high voltages up to -150 kV. In this new configuration, the relevant economy results in halving the number of channels, this more than compensates the greater cost of the required HV components and power supplies.

The design of the overall high voltage system for the T600 module was performed having in mind this possible working conditions. Safe margins were adopted in the design of the high voltage feedthrough (dielectric strength of the insulator > 1 MV), in the choice

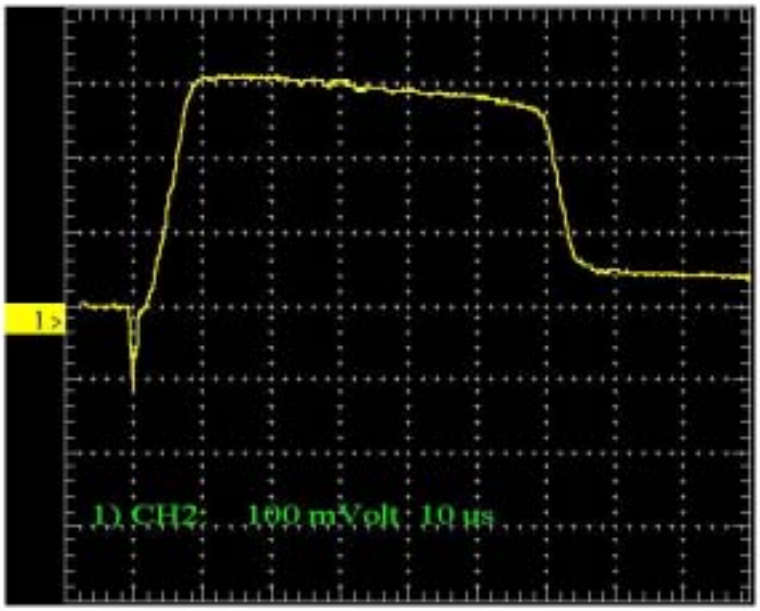

Figure 6.32: Typical waveform generated by a purity monitor

of the resistors for the inner voltage degrader (maximum operating voltage in air more than 10 times the operating voltage in LAr) and in the configuration of the divider chain (four resistors in parallel at each degrader step). During the two-months test run of the first T600 half-module the possibility to run the system at -150 kV has been successfully proved (see next section).

6.5.1 High voltage for the drift in the first T600 half-module

On June 2nd 2001 the first T600 half-module, filled with liquid Argon and stabilised in temperature, was ready to be set in operation. After having verified the level of the liquid Argon over the electrostatic top screen and the absence of bubbling inside the liquid Argon, the negative high voltage for the drift was applied together with the positive high voltage bias for the wire chamber planes. Immediately after that, the first events were recorded.

The systematic work of design, simulation, prototyping and test of the high voltage (HV) system is reported in Ref. [58]. The mechanical parts of the HV system, including the cathode and the field shaping electrodes, were installed inside the first half-module during the period November 2000/February 2001.

In the same period, we carried out the installation of the HV feedthrough (Figure 6.34), the resistive voltage divider (Figures 6.35, 6.36 and 6.37) and the voltage monitoring feedthroughs.

During the installation, the correct positioning of the HV electrodes was verified.

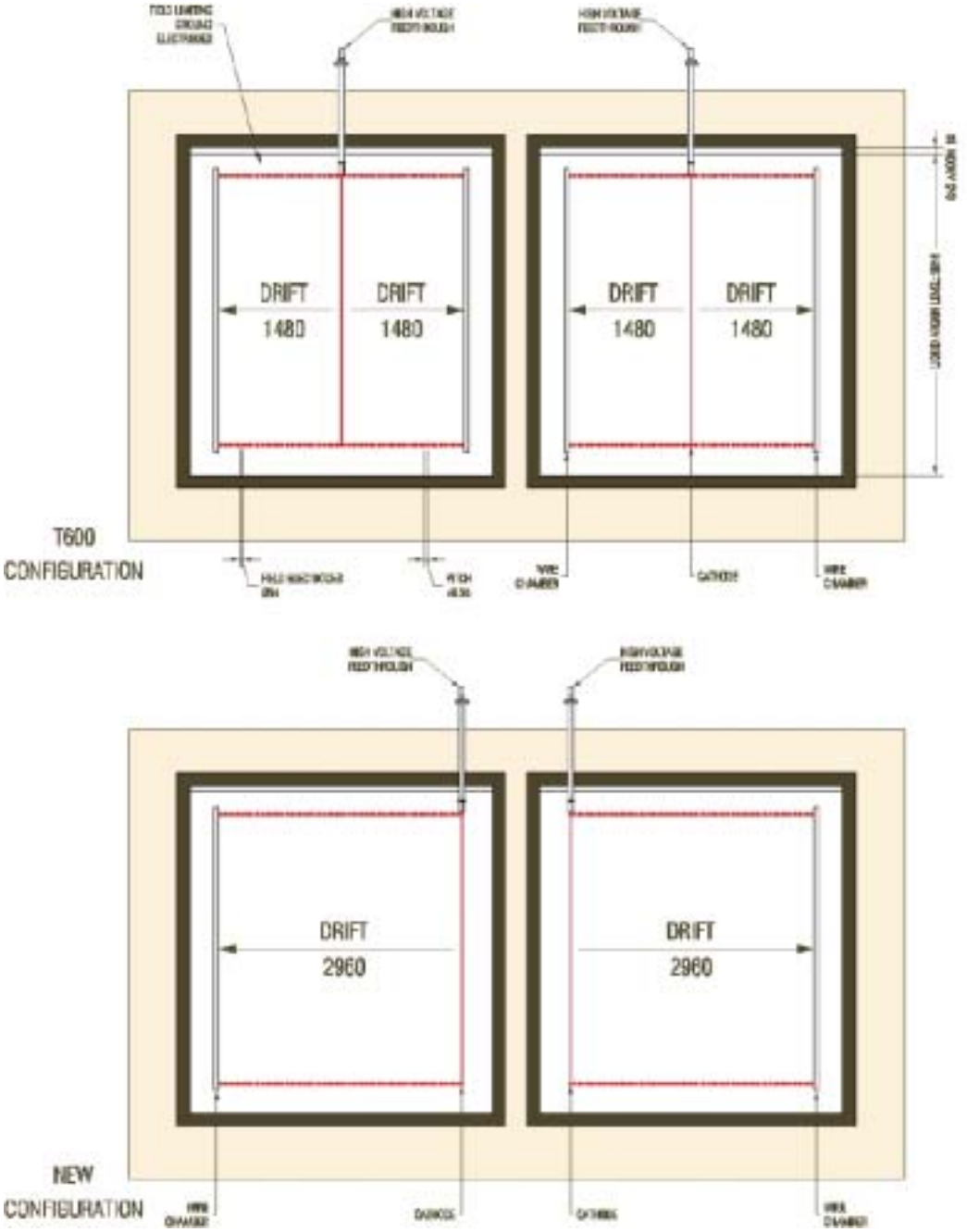

Figure 6.33: Configuration of the TPC chambers for the T600 module (top) and for the new proposed modules (bottom).

Figure 6.34: Left: the HV feedthrough positioned on the T600 roof flange. Right: details of elastic contact between the feedthrough and the receptacle connected to the cathode.

Before closing the cold body, a final test was performed on the HV system. The monitoring voltages for the left and the right drift volumes, measured through a special voltage divider in the last degrader step (Figure 6.37) gave a proportionality of 10^{-4} with the HV applied to the cathode, as calculated (see also the measurements on figure 6.41). All the 240 resistors of the HV divider were operated in air, in their working position, at 5 kV – twice the nominal running voltage– by measuring the absorbed current. The deviation from uniformity along the divider chain resulted less than 5×10^{-3} in both left and right chains.

The HV power supply and cable, assembled with a custom-made plug, were installed on May 2001 together with an analog interface to an EDAS–1002-2A module (Digital I/O and Multifunction Ethernet DAQ System, Burr-Brown) and connected to the network for the remote monitoring and control of the HV (see Figure 6.38).

After a first check to verify the absence of possible short circuits (phase 1, in Figure 6.39), the detector was activated (02/06/2001). The high voltage was raised, by a programmed ramp-up slope of -0.5 kV/min, up to -112.5 kV (1.5 times the nominal running voltage, phase 2 in Figure 6.39) to verify the safe running at -75 kV. After one hour, the voltage was lowered (ramp-down slope = +1 kV/min) down to the working voltage -75 kV (electric field = 500 V/cm).

The complete HV system operated during the 2 months run in an ultra stable and reliable way (top plot in Figure 6.39). Effects of eventual residual power supply ripple

Figure 6.35: Installing the resistors for the HV divider.

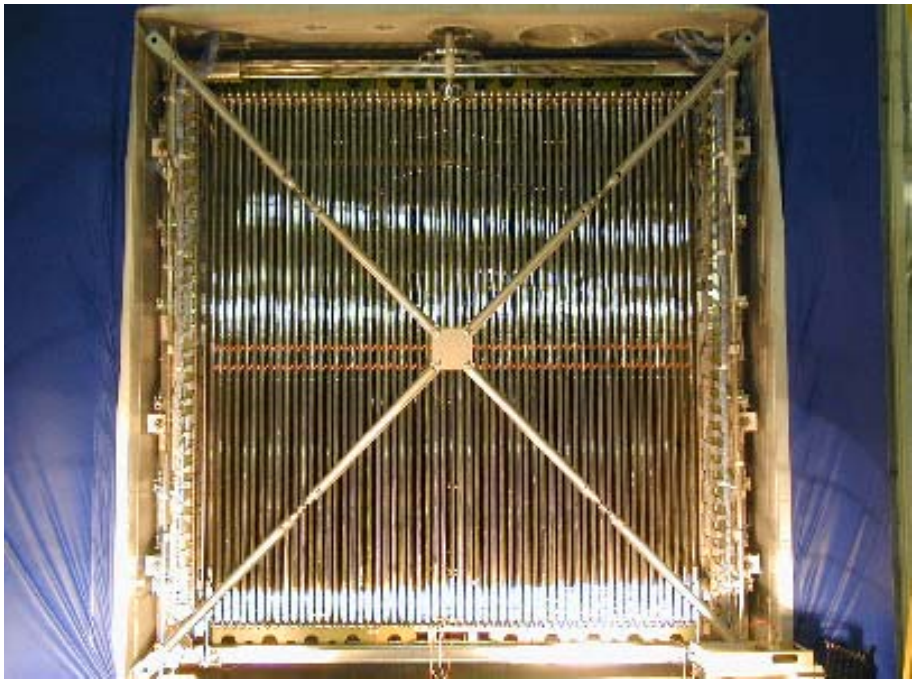

Figure 6.36: The complete HV system (feedthrough, cathode, field electrodes, voltage divider) for the first T600 half-module.

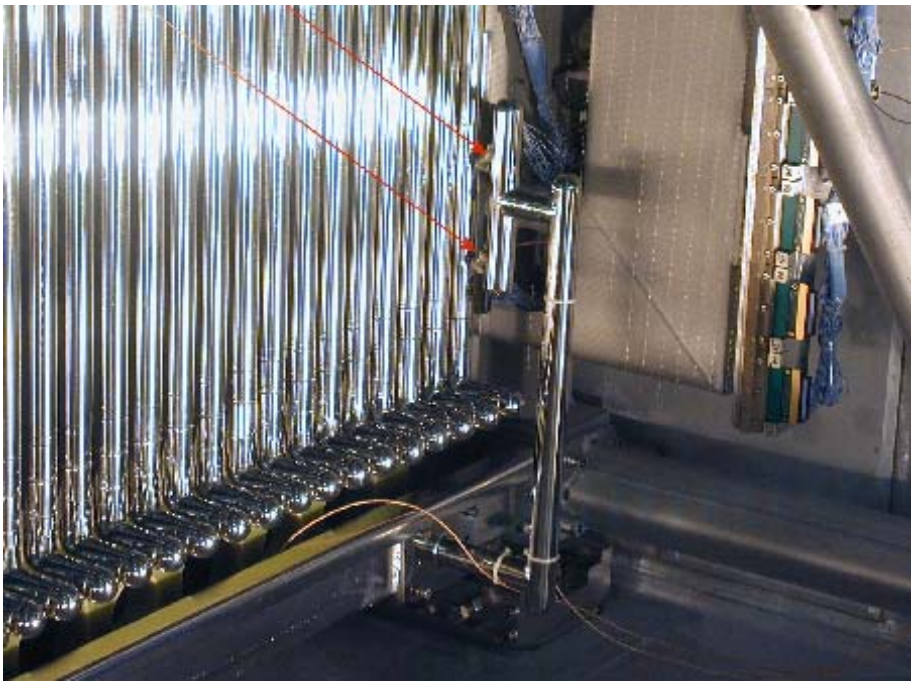

Figure 6.37: The monitoring resistors on the right side of the voltage degrader (arrows).

Figure 6.38: HV equipment on the top of the T600 detector (HV power supply, HV monitor, interface to Ethernet, remote control and monitoring software running on a PC).

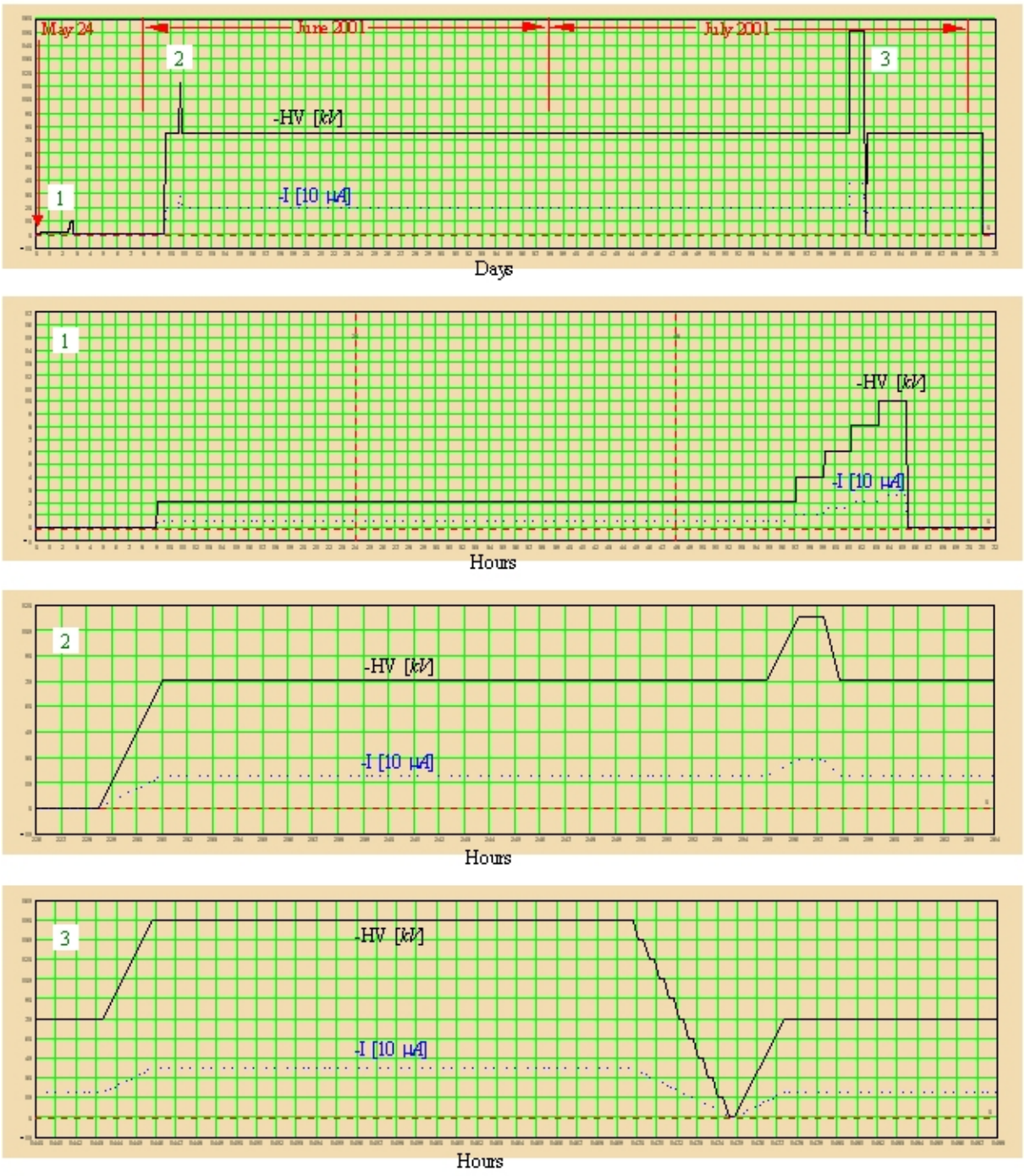

Figure 6.39: Record of the high voltage (solid line) and current (dotted line) dependencies on time, over the full test period (top plot). 1: pre-run check; 2: setting up at -75 kV; 3: test at -150 kV.

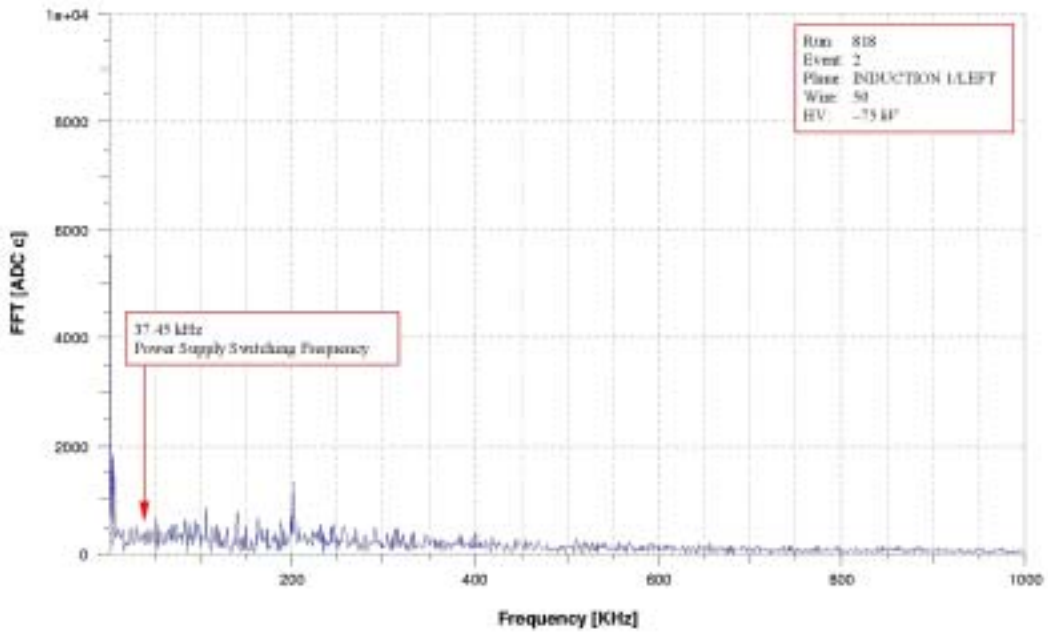

Figure 6.40: Frequency spectrum, at 75 kV, of the signals on a wire of the first wire plane facing the cathode (Induction 1), showing the absence of the peak corresponding to the power supply switching frequency.

(filtered by a custom made HV filter) are not observable on the wire signals and the power supply characteristic switching frequencies are not present in the signal frequency spectrum (Figure 6.40). On July 23^{rd} (see phase 3 plot in Figure 6.39), the HV was raised up -150 kV, the maximum power supply voltage. No problem was observed during this operation. This voltage was kept during 24 hours to demonstrate the capability of the HV system to be employed in a detector configuration with 3 m long drift path. This is the maximum high voltage ever tested in noble liquids. After the test, the HV was lowered in steps of 15 kV down to zero. At each step, data were collected, with a trigger for diagonally passing through particles, in a vertical plane containing the drift. From the analysis of these data (under progress), it is possible to get a direct estimate of the drift velocity and an alternative check of the electron charge attenuation at different electric field intensities. After that, the HV was restored at -75 kV for the final period of normal data taking and, finally, brought to zero on August 1st.

The remote control and monitoring system, for which further improvements are in progress, providing a reliable and flexible remote operation and data recording (Figure 6.41).

The test run confirmed the good design of the complete high voltage system and the correct choices for its components (feedthrough, power supply, ripple filter, degrader resistors, ...).

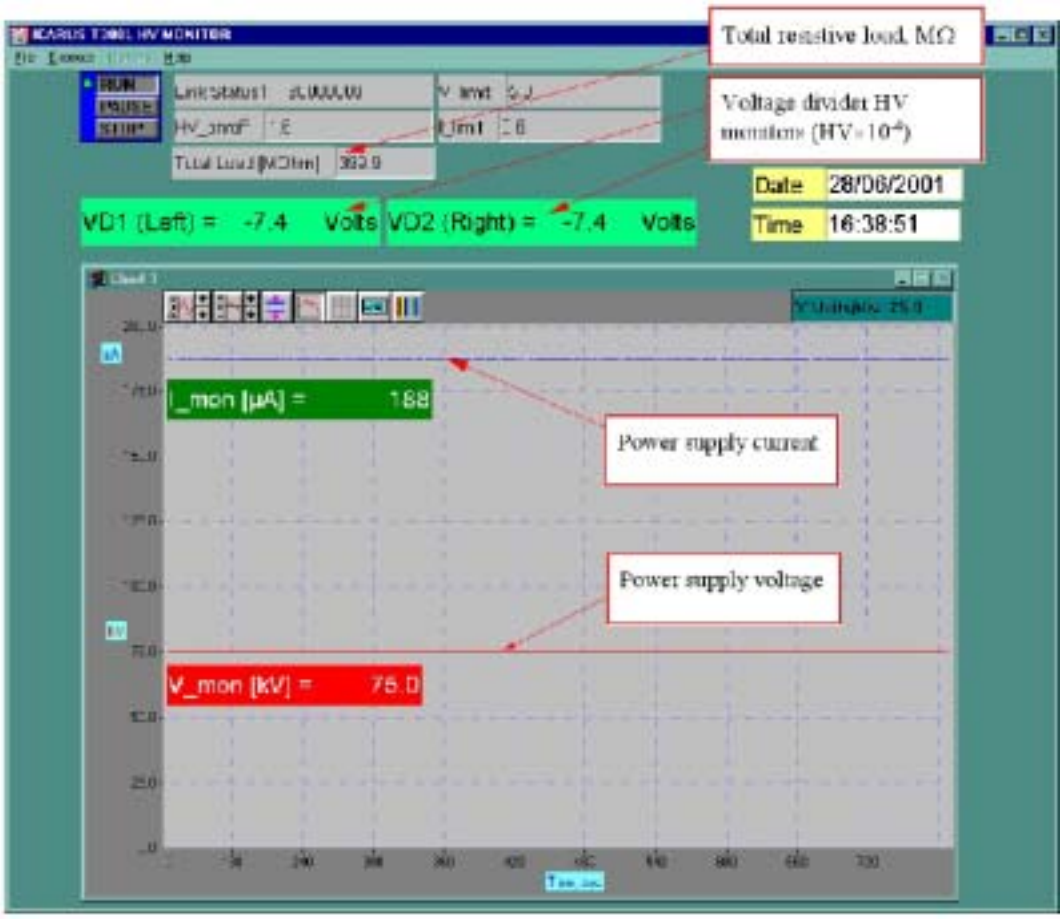

Figure 6.41: The remote monitoring of the HV operating conditions in ICARUS T600 via the EDAS interface.

6.6 The internal PMT system

A photomultiplier (PMT) system able to detect light from liquid argon scintillation will provide an effective method for absolute time measurement of the ionizing events. This information will allow the proper track reconstruction along the drift coordinate and will provide an internal trigger signal.

The system set-up is suggested by experimental results coming from an intense R&D study on different methods and devices able to detect the LAr scintillation light [59, 60]. The adopted solution, which has been validated during the T600 technical run, makes use of Electron Tubes 9357FLA PMTs. This model is a 12-stage dynode PMT with hemispherical glass window, 200 mm (8") diameter (see Figure 6.42). The device has a blue sensitive bialkali photocathode on a platinum under-layer which allows the PMT functioning at low temperature. The nominal PMT gain is 5×10^7 which is reduced to about 10^7 at LAr temperature (87 K). The PMT glass window is not transparent to the 128 nm light coming from the LAr scintillation. Nevertheless it can be made sensitive to the VUV photons by means of the window coating with TetraPhenyl-Butadiene (TPB) which acts as a fluorescent wavelength shifter. The resulting global quantum efficiency to the LAr scintillation is better than 10%.

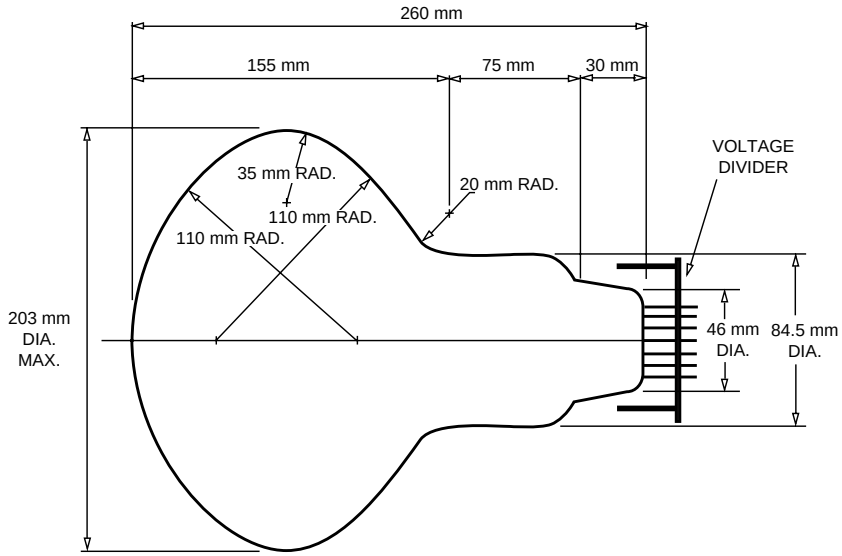

Figure 6.42: The Electron Tubes Limited D727KFLB photomultiplier outline drawing.

The T1200 photomultiplier system mainly reproduces the scheme designed for the T600 second half-module. The PMT dimensions are compatible with the detector mechanical constraints which impose their mounting in the 300 mm space left behind the wire planes (Figures 6.43 and 6.44). In each sub-unit, a minimal set of about 30 PMTs will be placed following the geometry shown in Figure 6.43 which was designed taking into account the detection efficiency, dimension of the photomultipliers as well as the goal of detecting solar neutrino events (down to E = 5 MeV). In the case of the current T1200 design, it is no more possible to instrument both sides of the dewar with PMTs, since one cannot place PMTs close to the cathode. The increased distance yields a lower detection efficiency due to the light attenuation in the Argon and to the solid angle,

which must be compensated by an increased number of PMT's relative to the current T600 design. In addition, the doping of the LAr with Xe can extend the VUV light attenuation length. Overall, we foresee to be able to reach a detection threshold of about 20-30 MeV for events occurring near the cathode and lower for other events closer to the PMTs.

The PMT readout will be based on the same instrumentation used for the ionization charge. A voltage divider, especially designed to work at low temperature, will be welded directly on the PMT output leads. Coaxial cables will be connected to pick-up the current signal and to provide the device with the power supply (see Figure 6.45). For each PMT the output signals will be integrated over the 2 μs LAr photon emission by means of "ICARUS-like" amplifiers and the corresponding charges will be sampled (50 MHz) by means of 10-bit ICARUS ADC boards with a resolution of about 10 ADC counts for a single photoelectron ($> 10^7$ electrons). This will allow to place the event along the drift coordinate, by means of the correlation between the ionization signals and the PMT pulses. A parallel electronic system, based on discriminators and custom designed coincidence units, will be used to provide a signal for the detector trigger logic.

A demonstration of the PMT system capability to determine the track absolute time is shown in Figure 6.46. The event was taken during the T600 test run by means of a trigger logic accepting horizontal tracks, which was based on the coincidence of at least 4 PMTs in the same chamber. The time sampling of the four PMT outputs is shown on the right side of Figure 6.46. Two PMTs (1 and 2) are positioned, along the 18 meter-long wire chamber structure, in the same position of the ionization event shown in the left side of Figure 6.46 (which is only a fraction of the full image corresponding to the whole drift volume): one can see three tracks, one of which is horizontal. The PMT pulses inducing the trigger signal, generated by the horizontal track ionization, can be identified in the data sampling at $t \approx 0$ μs. The PMT pulses generated by the two additional tracks, placed at time > 400 μs, are present only in the photomultipliers (1 and 2) facing the event. This shows that the tracks correspond to events crossing the detector drift volume at three different times.

6.7 Trigger System

The Trigger System of the T600 in the Pavia setup exploited three independent subsystems:

- internal photomultipliers;
- external scintillators for "horizontal" muon selection (HM);
- external scintillators for "vertical" muon slection (VM).

6.7.1 Internal PMT system

As described in the previous section, a row of 9 PMT (Electron Tubes 9357FLA, 200 mm diameter) per chamber were present. Their characteristics (photocathode and wavelength

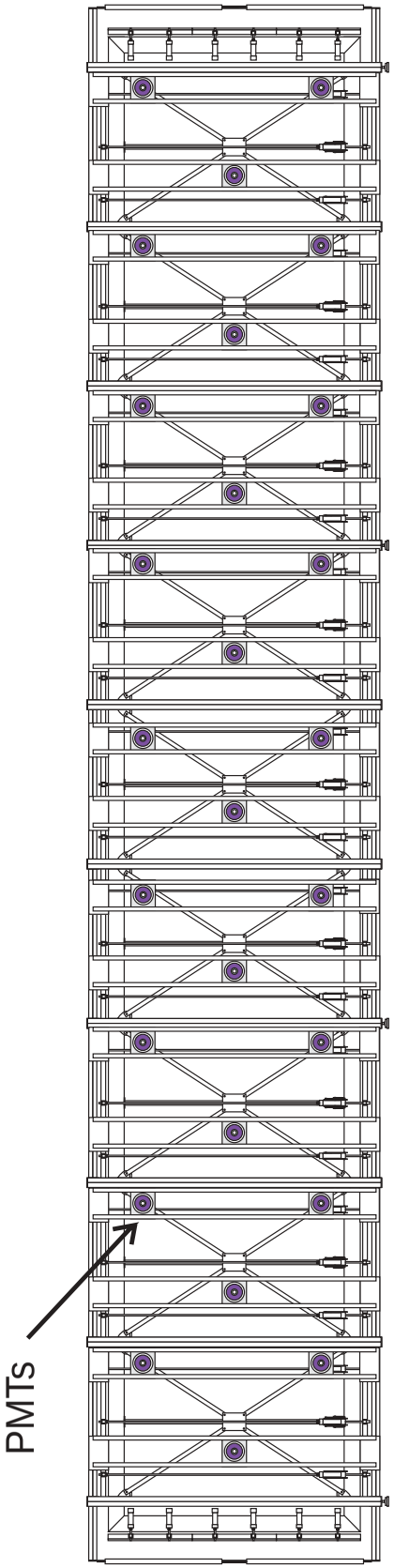

Figure 6.43: PMT mounting in the chamber structure.

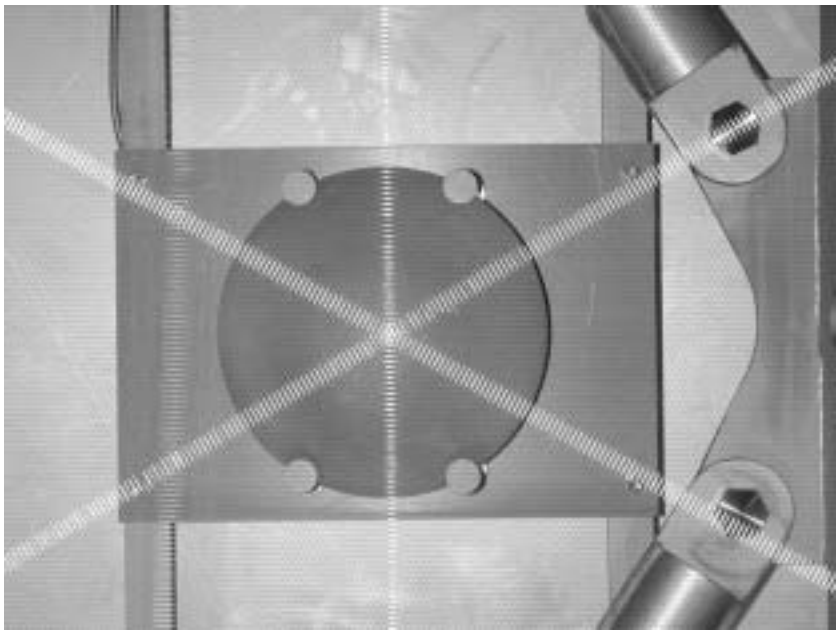

Figure 6.44: Picture of a PMT in the final mounting behind the three wire planes.

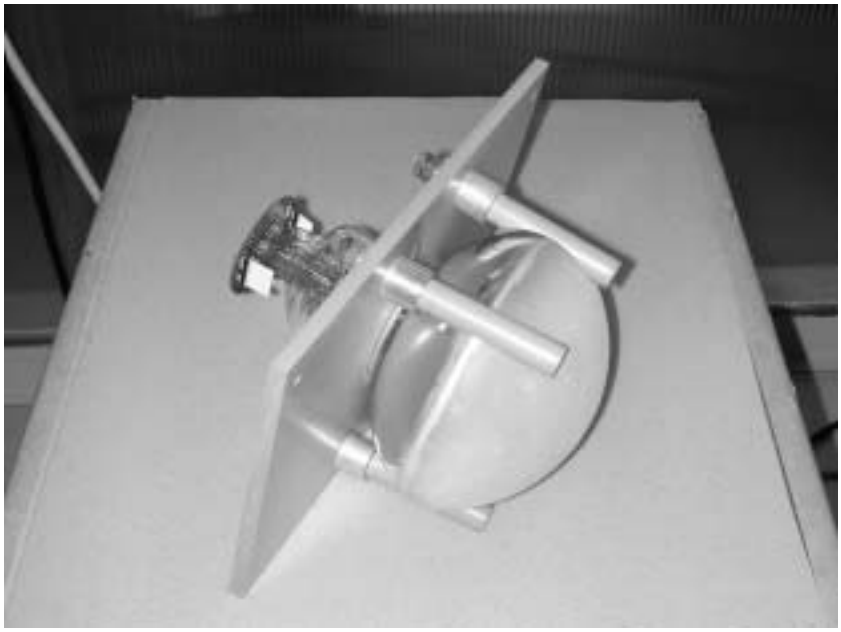

Figure 6.45: PMT final assembling. The TPB coating on the PMT glass window is clearly seen. The voltage divider has been mounted directly on the PMT output leads.

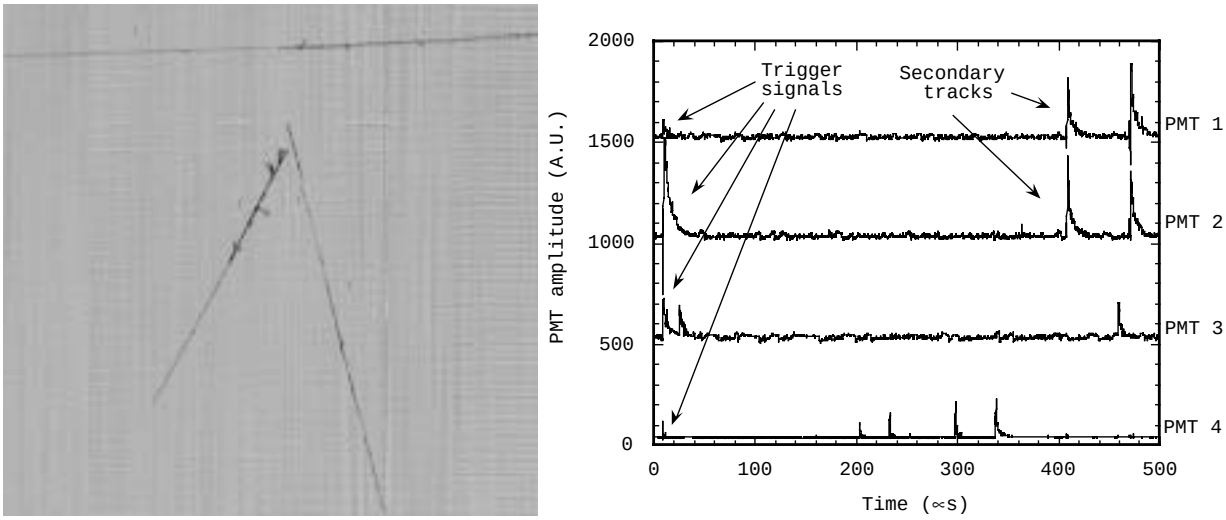

Figure 6.46: T0 event reconstruction in the T600 detector.

shifter) made them suitable for use at LAr temperature and sensitive to the 128 nm LAr scintillation light.

The PMT signals were all connected, via RG58 coaxial cables, to a dedicated rack where they were individually discriminated. The resulting logic signals could be used for triggering the T600 DAQ, selecting different logics. Several trigger logics were implemented by use of standard majority and coincidence units. The most frequently used trigger logics were:

- majority of *n/total* PMTs, either on one or on both chambers. This was one of the most versatile logics, allowing to select long muon tracks crossing longitudinally the T600, or more localized events with complex electromagnetic and/or hadron interactions.

- "muon stop" trigger, in which one or more of the PMT were set in anti-coincidence with a majority of the others, trying to select long tracks stopping in the detector.

Other trigger modes, mainly for test purposes, were tried. The PMT system allows to select different kinds of events in an easy and flexible way.

In the second T600 half-module, a more complete coverage of the detector inner surface is foreseen, employing 30 PMT per chamber. Obviously, the even rate and number of different event topologies will be largely reduced in the underground environment.

The trigger logic will be a compromise between the necessity to cover the entire volume at low energy threshold with a selectable track geometry and the requirement to keep low the noise rate. This will be done either with standard VME commercial modules or custom boards with loadable patterns.

6.8 Electronics and Data Acquisition System

The readout electronics is the latest evolution of the traditional solution developed in the past years by the ICARUS collaboration and tested on many prototypes [22].

The readout system is structured as a multichannel wave form recorder that stores the charge information collected by each sense wire during the drift of the electrons. Each wire is equipped with a current integrating amplifier followed by a 10 bit ADC that samples the signal every 400 ns. The converted data are stored in a digital memory (Figure 6.47).

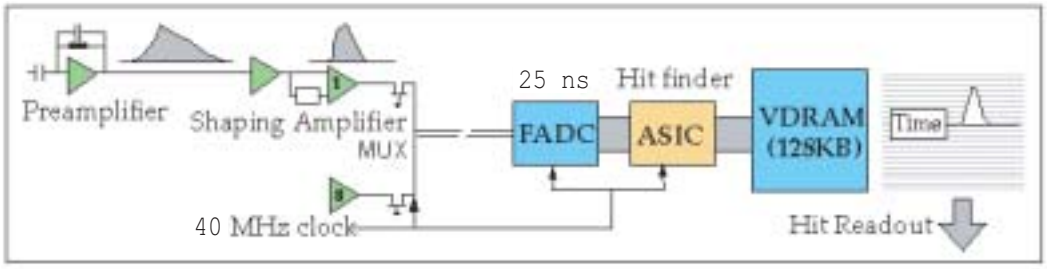

Figure 6.47: Block diagram of the hit finder chip.

The collected data can be highly reduced by recognizing Regions Of Interest (ROI) of the signal, by means of a dedicated hit finding unit, pipelined in the data acquisition path. Only data inside ROI's will be saved, obtaining a highly efficient zero skipping. Contiguous ROI's can be correlated to enhance detector self-triggering capability.

The developed hit finding algorithm can be easily implemented in hardware. It has been extensively tested on real and simulated events to evaluate its efficiency and robustness as a function of the signal shape with different S/N ratio.

This process is made flexible through the parametrization of all the thresholds and the window size. Their values can be tuned depending on signal characteristics and signal to noise ratio. Furthermore it allows to resolve signals of different tracks that hit the same wire closely in time.

As the selection of the ROI's has to be done in real time, a specific hardware signal analyzer, named DAEDALUS, has been designed in VLSI CMOS technology [33]. To preserve the signal shape and to have, at the same time, a compact hardware structure, data acquisition is performed grouping channels in set of 16 and multiplexing then to one 40 MHz ADC in order to sample each channel every 400 ns. As shown in the block diagram of Figure 6.48, the signal analyzer processes four groups of four channels, demultiplexing the 10 bits input data.

The chip architecture is a six stage pipeline; one stage is dedicated to demultiplex inputs, one to multiplex outputs, one to perform median filtering, while the hit finder requires three stages. Data move through the pipeline at a frequency of 2.5 MHz that matches the input data rate. The chip features programmable operating parameters: median filter size (up to 15 points), window size (up to 15 counts) and all the threshold values.

Few prototype chips, operating on four channels, have been designed in VLSI $0.7\,\mu m$ CMOS standard cell technology [34]. They performed according to the specifications and a 16 channels prototype readout module (named ARIANNA) has been

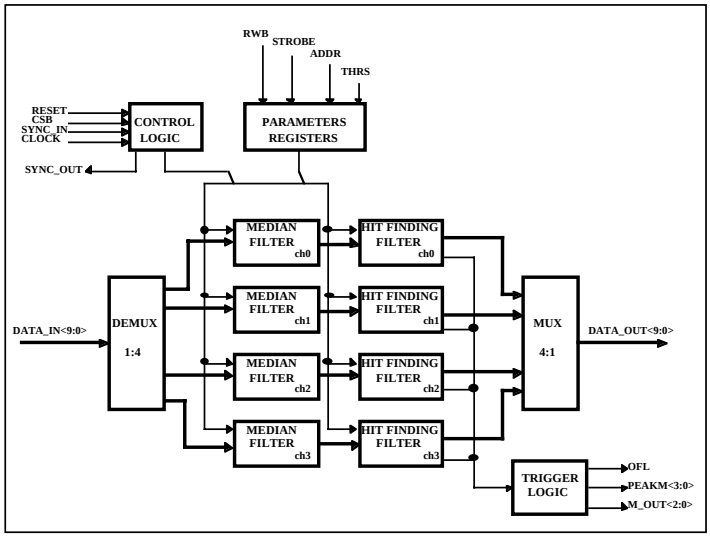

Figure 6.48: Block diagram of the hit finder chip.

designed and built in VME standard as a demonstrator for functionality and performance test [63, 64, 65].

The final version of the chip, has been designed in VLSI $0.5\,\mu m$ CMOS gate array technology and it operates on a set of 16 channels [35]. The final readout module serves a set of 32 channels.

The readout electronics (Figure 6.49), which resides entirely outside the detector, is hosted on racks positioned just in front of the signal flanges (on the sides of the cryostat for the two lower LAr containers and on top of the cryostat for the upper ones), to minimize the input capacitance due to the cables. Each rack hosts all the readout channels needed to handle the set of wires connected through the corresponding feed-through. For the T600 technical run we had 36 identical racks, 576 channels on each, plus 8 additional racks tailored for the side corner feed-through (which, due to the internal cabling, carry a larger number of wire connections, about three times more) (Figure 6.50). Every rack has:

- One analogue Crate:
  - Distribution and decoupling of the bias voltage to the wires
  - Test pulse distribution and setting of baselines [CAEN A793]
  - 9+9 analogue boards [CAEN V791] providing amplification and shaping, according to the two different configurations (charge and current reading) required for the different planes
- One digital Crate:
  - 18 digital boards, where waveforms are buffered and processed to achieve zero skipping [CAEN V789]
  - Distribution of absolute clock and trigger signals [CAEN V816]

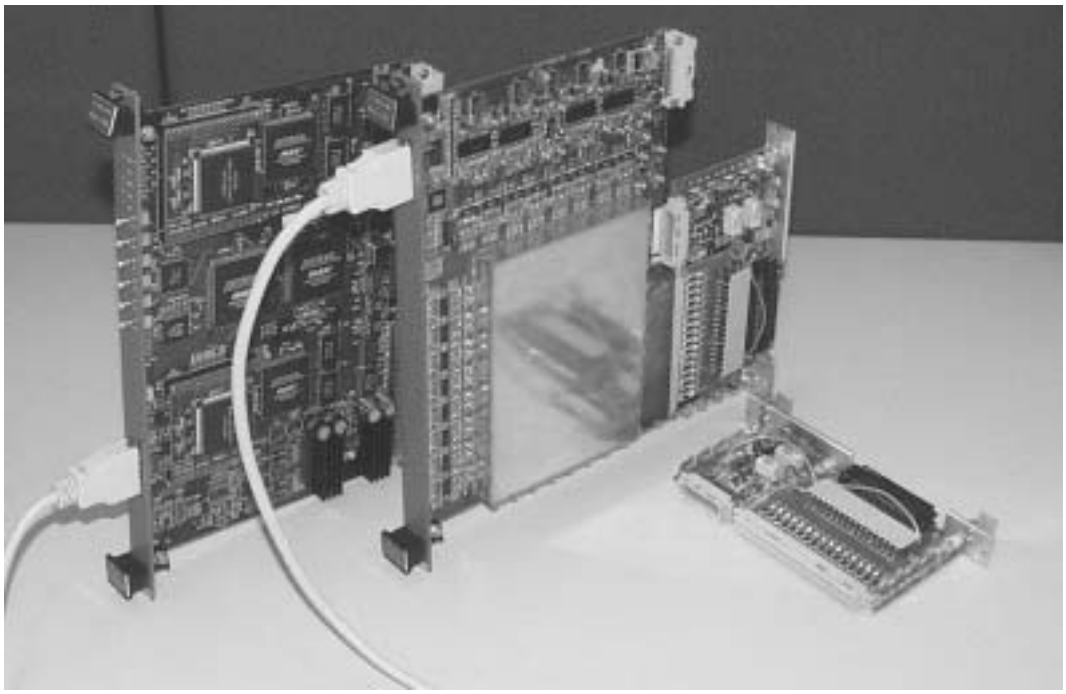

Figure 6.49: The three basic electronics modules: -the small Decoupling Board (DB) that receives 32 analogue signals from the chamber via the feedthrough and passes them to the analogue board. It also provides biasing of the electrodes and distribution of the test signals. It is housed (not shown in the photo) in the back side of VME-like crate that houses in front the analogue board. The Analogue Board (V791 by CAEN) houses the amplifiers for 32 channels, based on the proprietary analogue BiCMOS VLSI (2 channels per chip) and provides the data convertion (10 bit) at 40MHz rate. The data are transmitted to the digital module via the cable connected to the front panel connector. The Digital Board (V789 by CAEN), Arianna, has the two DAEDALUS VLSI, mounted on small piggy back PCBs. The board serves 32 channels and receives the digital data (multiplexed) via the small cable plugged in the front panel. The data out are available via the VME bus.

  - 1 embedded CPU, controlling data collection and forwarding data to event builder [motorola mvme 2100]

- One linear power supply, [5V 6A-12A-18V] for analogue crate
- One rack monitor, which monitors internal temperatures and ventilation flow, and allows remote control (via i2c bus) of power supplies and of several I/O signals 220V distribution
- Radiators and fans to provide air tight heat exchange

The networking system has been designed for a total bandwidth of 100 kHz of small sized events and a data throughput of 100 Mbit/s. These figures largely exceed the data rate that we expect to have in the underground lab, on the basis of our background measurements.

Figure 6.50: Photograph of the T600 top showing the disposition of the electronic Racks for one chamber.

All the electronics installed on the T600 has been verified on a test-bed before installation. Typical rms noise levels measured on the detector for the two versions of the front-end were respectively 1.5 and 1.7 ADC counts, giving a corresponding signal/noise ratio for minimum ionising tracks ranging from 7 to 10. A small number of channels were found over those levels (rms up to 30 ADC counts), but for all of them the noise source was inside the dewar (probably due to a defective connection on the feedthrough or on the internal cabling).

Following the first results from the analysis of collected events, the possibility of rising amplification gain in order to reduce quantization noise on low ionisation tracks is under investigation. A first modified set of boards is already being tested on the small 50L chamber.

The interconnection of the racks for data acquisition purposes was completed with the deployment of the ethernet network, following the scheme in [[62]]. A switch on the top of the dewar aggregates all the 100 Mbps links coming from the CPU of a chamber into a 1Gbps optical link, going down to the farm of the event builder. Four *linux* machines were dedicated to the data acquisition, provided with 500GB of on line disk space and two DLT units for long-term storage. One of the computers was in charge of the synchronisation, being interfaced to the trigger system through a busy signal.

Performance of the building was found within design requirements, with a total throughput of collected data around 40 MB/s and a sustained disk writing over 15 MB/s. Given the diagnostic purposes of the data taking run in Pavia, most of the events

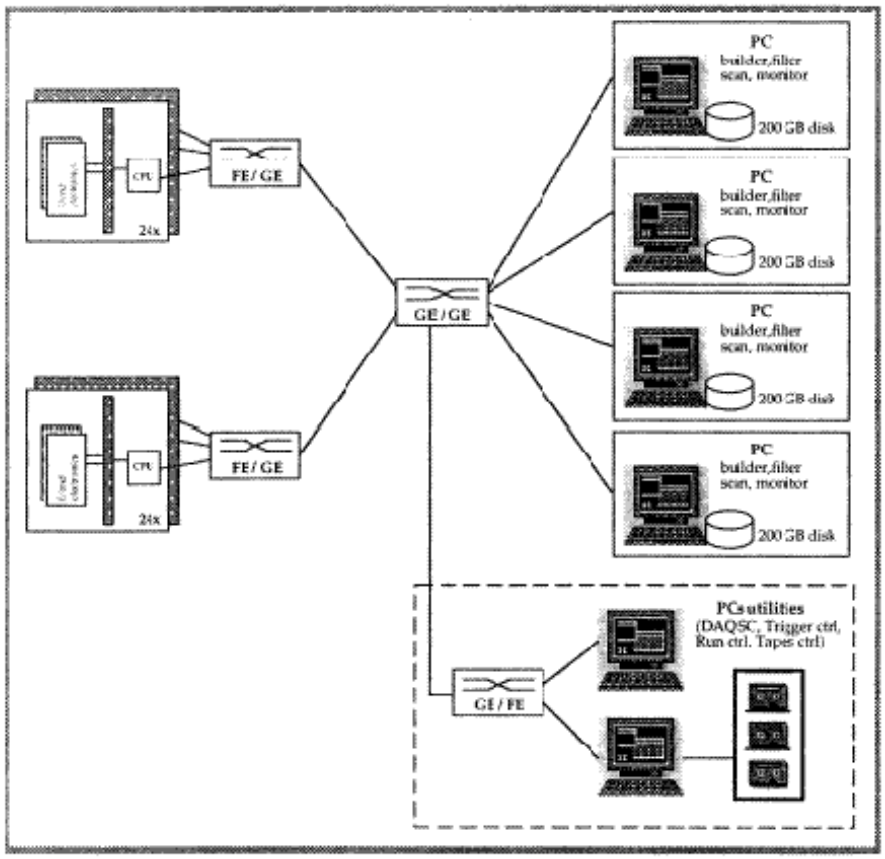

Figure 6.51: DAQ scheme of the T600 module.

have been taken in "full drift imaging" mode, thus implying quite large sized events (200MB/evt) to be handled. In such conditions, the required time to merge all data chunks belonging to a single event ranges from 2.5 to 10 seconds (depending whether events are distributed on more than one machine or not). Several data runs were taken with the front end zero skipping enabled, obtaining a reduction of the dead time (which was rarely near the effective rate of the selected trigger configuration). Since the reduction algorithm parameters were estimated prior to the data analysis, a low selection efficiency was observed. An optimized set of parameters has been obtained from the analysis of collected events (see Section 3.5.6). The technical run put under test the functionality of the data acquisition system and allowed to verify its behaviour under real data taking conditions. Thanks to this experience, several software and hardware upgrades are now planned, mainly concerning the user interface and the computers gigabit network card, which showed some instabilities. According to the confirming results following the T600 test, the collaboration proposes that the new ICARUS modules will adopt the same architecture on both electronics and the data acquisition system.

6.9 Calorimetric readout of the non-imaging regions

We foresee to instrument the non imaging LAr in such a way to provide a calorimetric readout also for this region in order to have a continuous connection (from the calorimetric point of view) between the active and inactive LAr regions. This will largerly improve the energy resolution measurement for neutrino beam events.

The basic idea is that ionization charges are produced everywhere in the LAr, also outside the main drift volume. Here we naturally have an electric field, in most zones rather high, produced by the field shaping electrodes and by the cathode (see Figures 6.53 to 6.57). Hence, ionization electrons produced in the non-active region are transported to the detector walls. Readout of these charges can be obtained simply by a set of readout electrodes (strips) placed in front of the walls (Figure 6.52).

The behaviour of the equipotential lines is shown in Figure 6.53, for the back region outside the field electrodes (the front region is symmetrical). Figures 6.54 through 6.57 show in detail the field and the potential near the cathode and near the wire chambers.

A solution for the calorimetric readout can be based on a set of 5 mm thick plane electrodes distributed along the inner walls, except the one facing the wire chambers, and segmented into strips each connected to an amplifier. The same scheme used for the wires readout can be also applied for the "pads" readout with few modifications. Due to the very different fields in the various regions, the amplifiers, with a charge integration configuration, have a decay constant sufficiently long to measure with equal efficiency signals due to charges drifting with different velocities. The gain of the amplifiers and possibly the dynamic range of the ADC's might require some small optimizations. The strip electrodes have width and spacing from the walls adjusted in order to keep their capacitance less than 500 pF. They are positively biased ($\sim$400 V) to collect also the charges in the gaps between them and the walls.

Strip parameters for the different walls are listed in Table 6.5 for LAr sensitive volume 18 m long.

Wall	Width [cm]	Length [cm]	Pitch [cm]	Gap [cm]	Capacitance [pF]	Number
Front	9.5	380	10	1	480	35
Back	9.5	380	10	1	480	35
Top	9.5	350	10	1	440	192
Bottom	9.5	350	10	1	440	192
Cathode	4.5	380	5	0.5	450	384
Total						858

Table 6.5: Strip number and parameters for a 18 m long LAr sensitive volume.

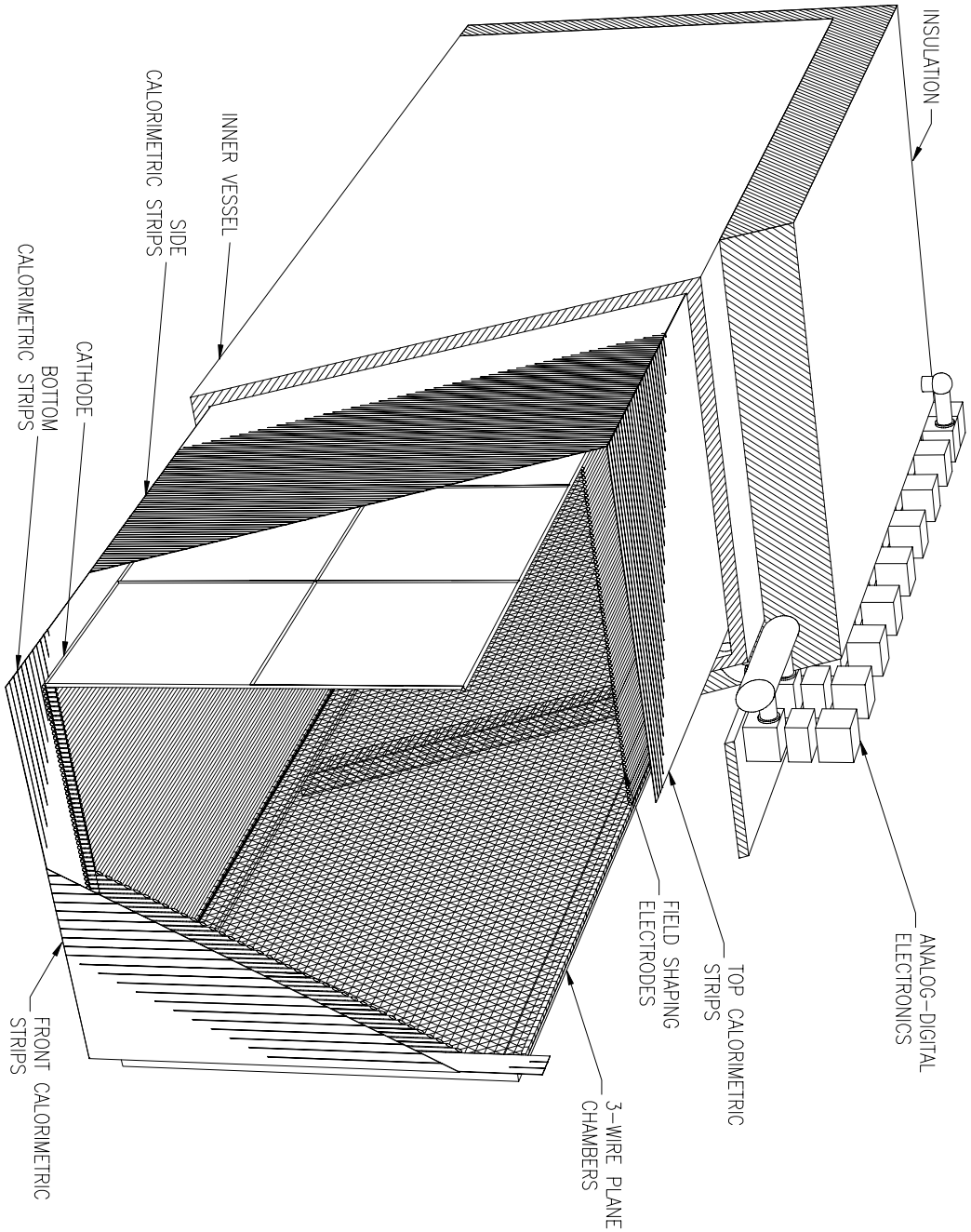

Figure 6.52: Layout of the calorimetric readout in the non imaging regions of each LAr submodule.

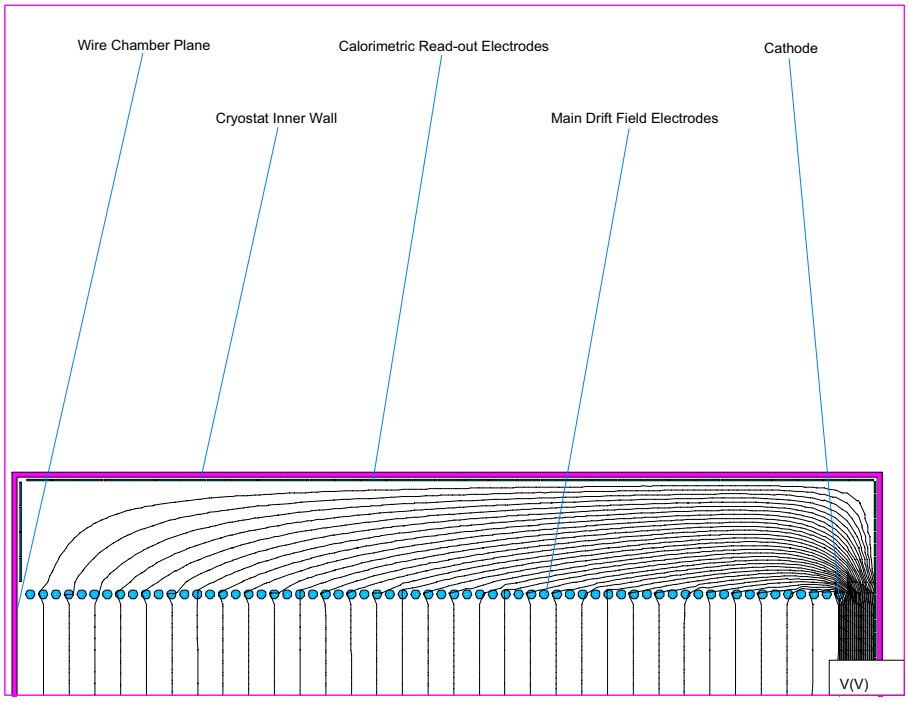

Figure 6.53: Equipotential lines in the back region of a LAr submodule (top view). For the front region, equal pattern, but mirrored along the median horizontal line.

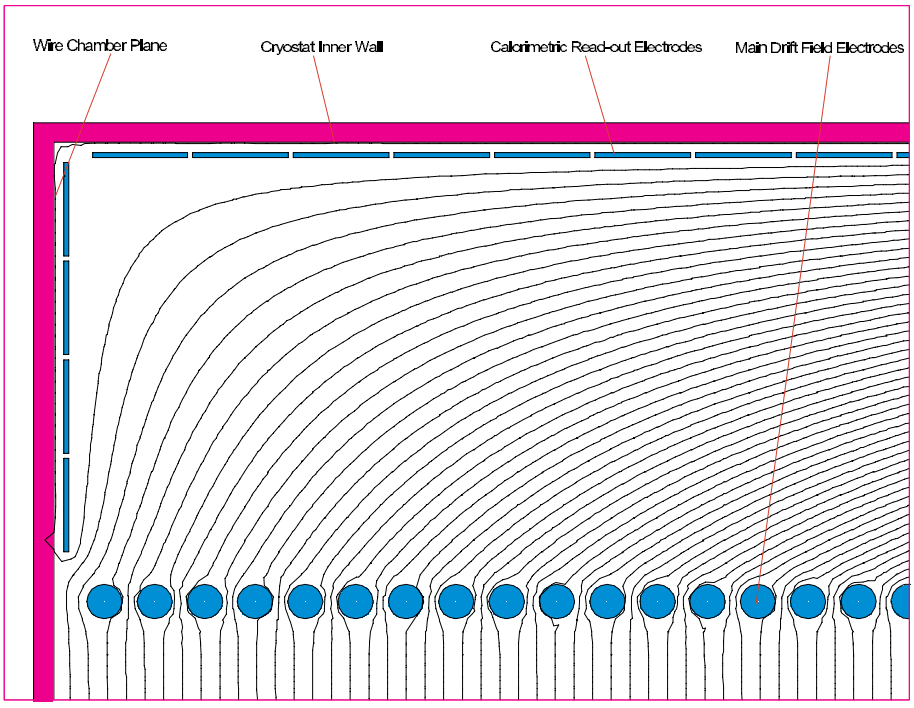

Figure 6.54: Equipotential lines in the back region of a LAr submodule. Magnification around the wire chamber end.

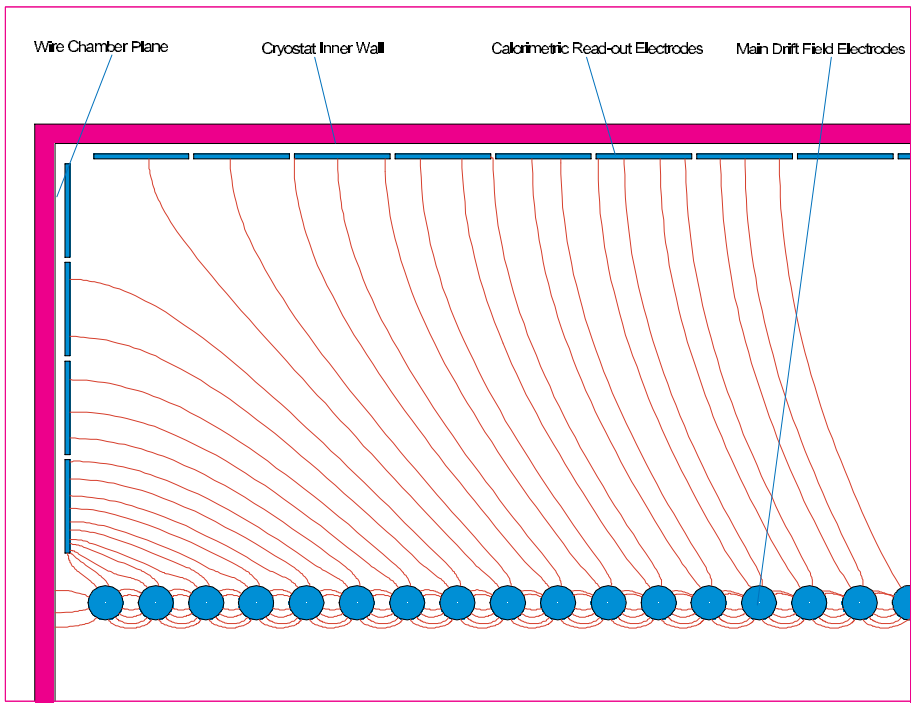

Figure 6.55: Electric field streamlines in the back region of a LAr submodule. Magnification around the wire chamber end.

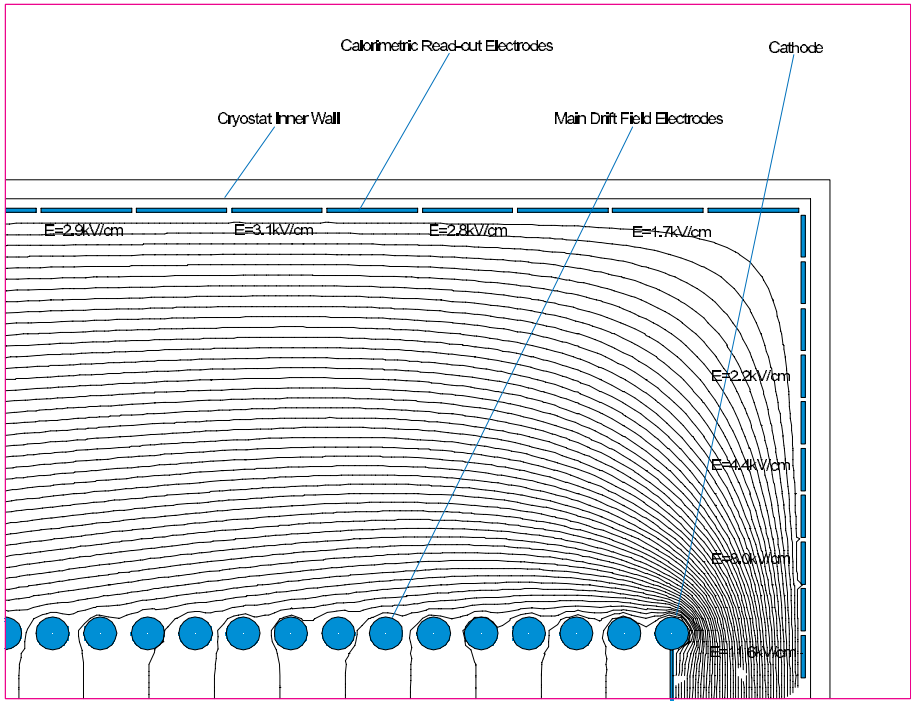

Figure 6.56: Equipotential lines in the back region of a LAr submodule. Magnification around the cathode end.

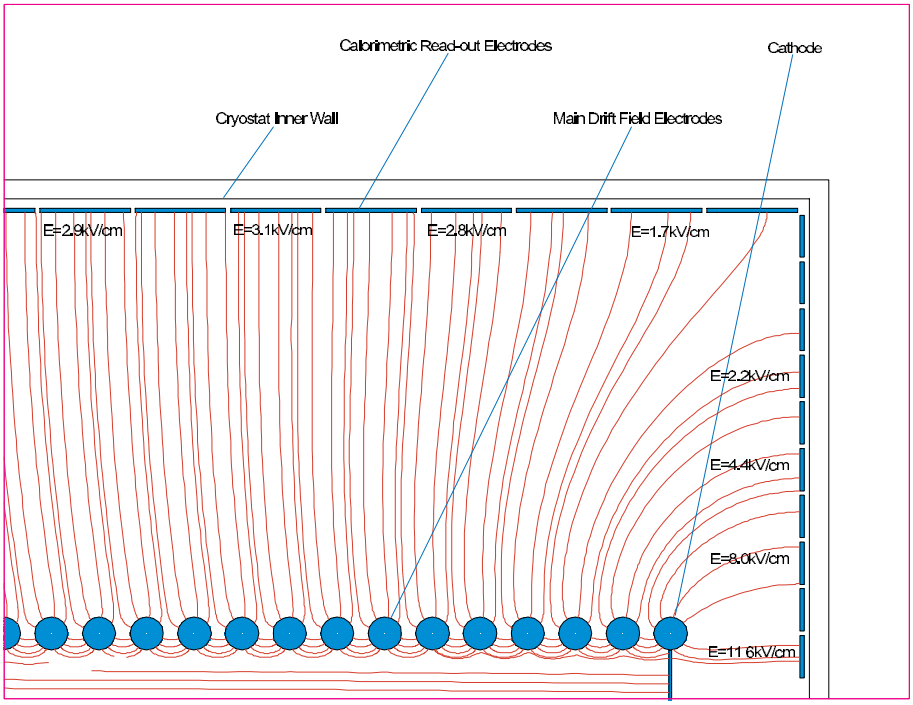

Figure 6.57: Electric field streamlines in the back region of a LAr submodule. Magnification around the cathode end.

Chapter 7

THE OPTIONAL MUON SPECTROMETER

7.1 Introduction

The spectrometer is relevant for the physics programme with the CNGS beam, and could be important in the event of future neutrino beams beyond the CNGS.

In the original ICANOE proposal[18], the liquid Argon modules were complemented by instrumented magnetized calorimeters, in order to measure the charge and the momentum of the muons and to provide coarse calorimetric information on the non-contained events leaking outside the liquid Argon.

In the meantime, we have further improved our understanding of the requirements of the spectrometer. It became clearer that the most important purpose of the external iron is to provide magnetic bending of penetrating muons, and hence the calorimetric performance could be reoptimized. In fact, we are now convinced that the small fraction of non-contained beam events can be recovered by a careful "shower-shape" analysis, within the imaging liquid Argon target. Hence, we can consider, without dramatic loss of fiducial mass, a basic solution, in which the spectrometer is only playing the role of magnetic bending and does not contain an instrumented part.

The spectrometer would then be composed of non-instrumented, magnetized iron, which after optimization of achievable momentum resolution and charge confusion, could have a length of 3 meters. Compared to the original ICANOE proposal, in which the amount of iron was minimized, in order not to degrade the calorimetric performance of the spectrometer, we now opt for a more conservative 3 meter long bending. In this way, we gain bending power (which grows linearly with length) over multiple scattering (which is proportional to the square-root of the length).

A more precise design of a muon spectrometer will be part of a future document, if its construction is retained as relevant for the accelerator physics programme. For the moment, we present the expected performance of an optional muon spectrometer as an starting-point to be further investigated.

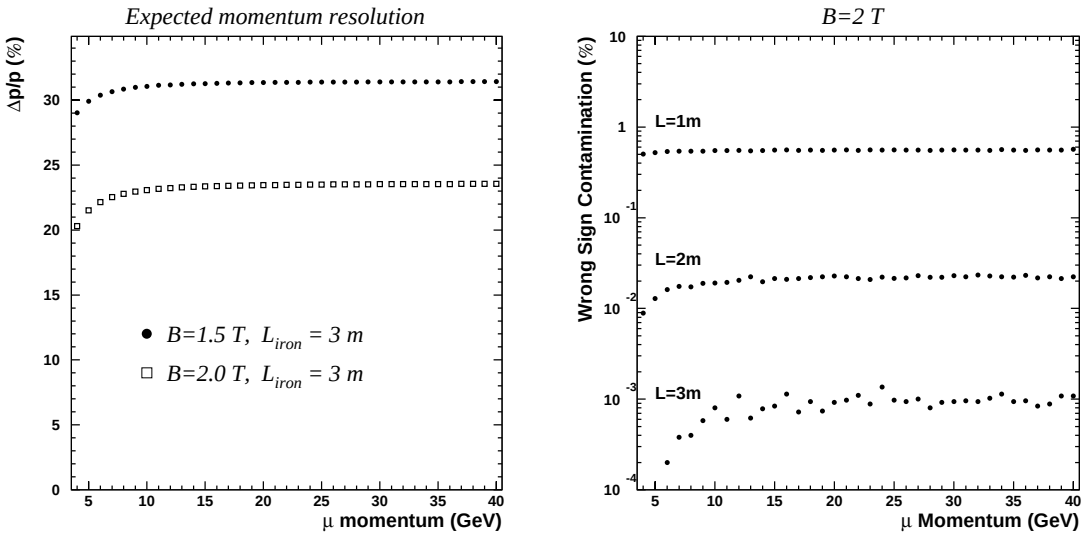

Figure 7.1: (left) Expected momentum resolution as a function of the muon momentum. Two different magnetic fields have been considered. (right) Wrong sign muon contamination as a function of the muon momentum for three different lengths of iron spectrometer.

7.2 Expected performance

The bending angle of penetrating muon tracks will then be easily estimated with the measurement of the track segment directions provided by the two consecutive LAr modules, before and after the iron spectrometer.

The performance of this setup has been estimated. The deflection due to a 2 Tesla bending is always larger than the one provided by multiple scattering. Figure 7.1(left) shows the expected momentum resolution as a function of the muon momentum for two different magnetic fields. The error in the measurement is dominated by multiple scattering. The expected resolution is $\approx 25\%$. For comparison, an instrumented iron block (2 m long with $n_{samples} = 20$ and 1 mm spatial resolution) immersed inside a 1T field, provides a momentum resolution $\Delta p_\mu / p_\mu \approx 20\%$. The wrong sign contamination due to charge mismeasurement is shown in Figure 7.1(right) for three different track lengths. The expected charge confusion is of the order of 10^{-5} for 3 meter long bending.

Chapter 8

ASSEMBLY IN THE GRAN SASSO HALL B

The construction of the large mass ICARUS detector will begin with the T600 detector installation. The T600 will be placed on a set of anti-seismic shock absorbents dimensioned to MCE specifications. A neutron absurder shield (thickness $\sim$ 70 cm) made of polyethylene hollow pipes filled with boric acid powder will surround the apparatus, see Figure 8.1.

#	Description	Characteristics
3	Storage dewars for LN2	30000 lt / unit
1	Storage dewar for LAr	30000 lt / unit
2	N2 re-condensation units	"cold" power = 40 kW / unit
6	LN2 circulation pumps	max speed = 24 m3 / hr / unit
1	Electrical supply cabinet	Max power = 1.2 MW
3	Automatic control system racks	One per module

Table 8.1: Auxiliary plants installed on top of the T600.

The space left on top of the T600 will be conveniently used to install the auxiliary systems needed for cryogenics (storage dewars, nitrogen re-condensers, etc., see Table 8.1). This solution offers two main advantages:

- optimisation of the use of the available space in Hall B;
- the system can be easily expanded to serve additional T1200 modules (simply by prolongation of the argon and nitrogen transfer lines and eventual addition of re-condensation units).

In Figures 8.2, 8.3 and 8.4 the above-mentioned solution is schematically shown. The auxiliary systems are organised on a platform located above the T600. In this space can take place:

- the storage dewars for liquid nitrogen (3);

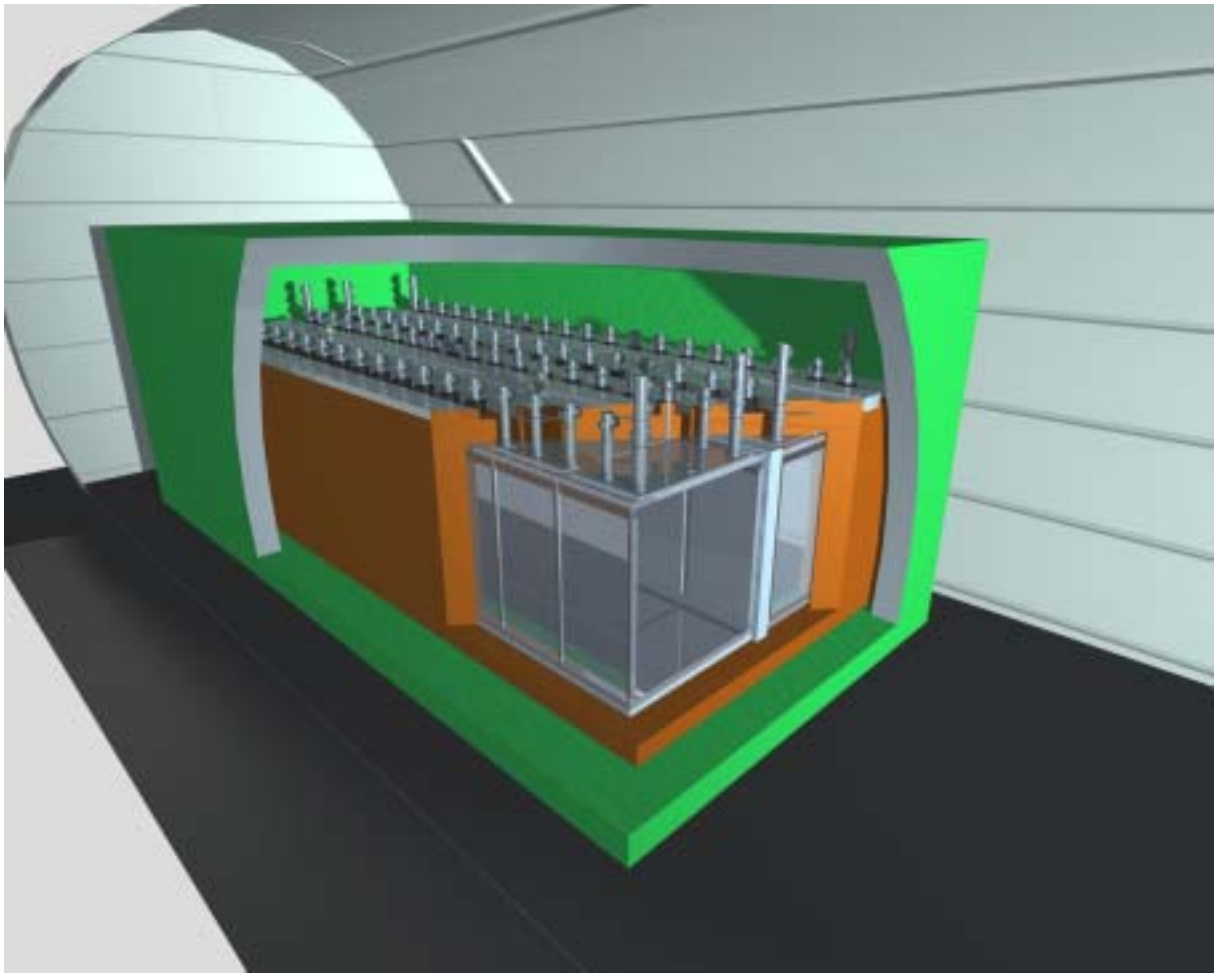

Figure 8.1: T600 installation in Hall B. The external box represents the neutron shield.

- the storage dewar for liquid argon (1);
- the nitrogen re-condenser units;
- the liquid nitrogen circulation pumps;
- the electrical power supply cabinets and the automatic control system racks for cryogenic and purification devices.

The apparatus is dimensioned to operate the T600 and two T1200 supermodules.

The first T1200 supermodule will be assembled just in front of the T600 module. In first place, the anti-seismic shock absorbers will be positioned and anchored to the cave floor. The bottom insulation layer will be then assembled out of four evacuated panels (single panel approximate dimensions: $5.5 \times 0.45 \times 10$ m^3) over the anti-seismic shock absorbers. The lower sheet of the retaining tank will be then installed together with the basement of the sustaining structure for the LAr containers (500 mm stainless steel "I" beam profiles), see Figures 8.5 and 8.6.

The structure is therefore ready for the positioning of the lower two LAr containers (Figure 8.7). The assembly sequence is the following:

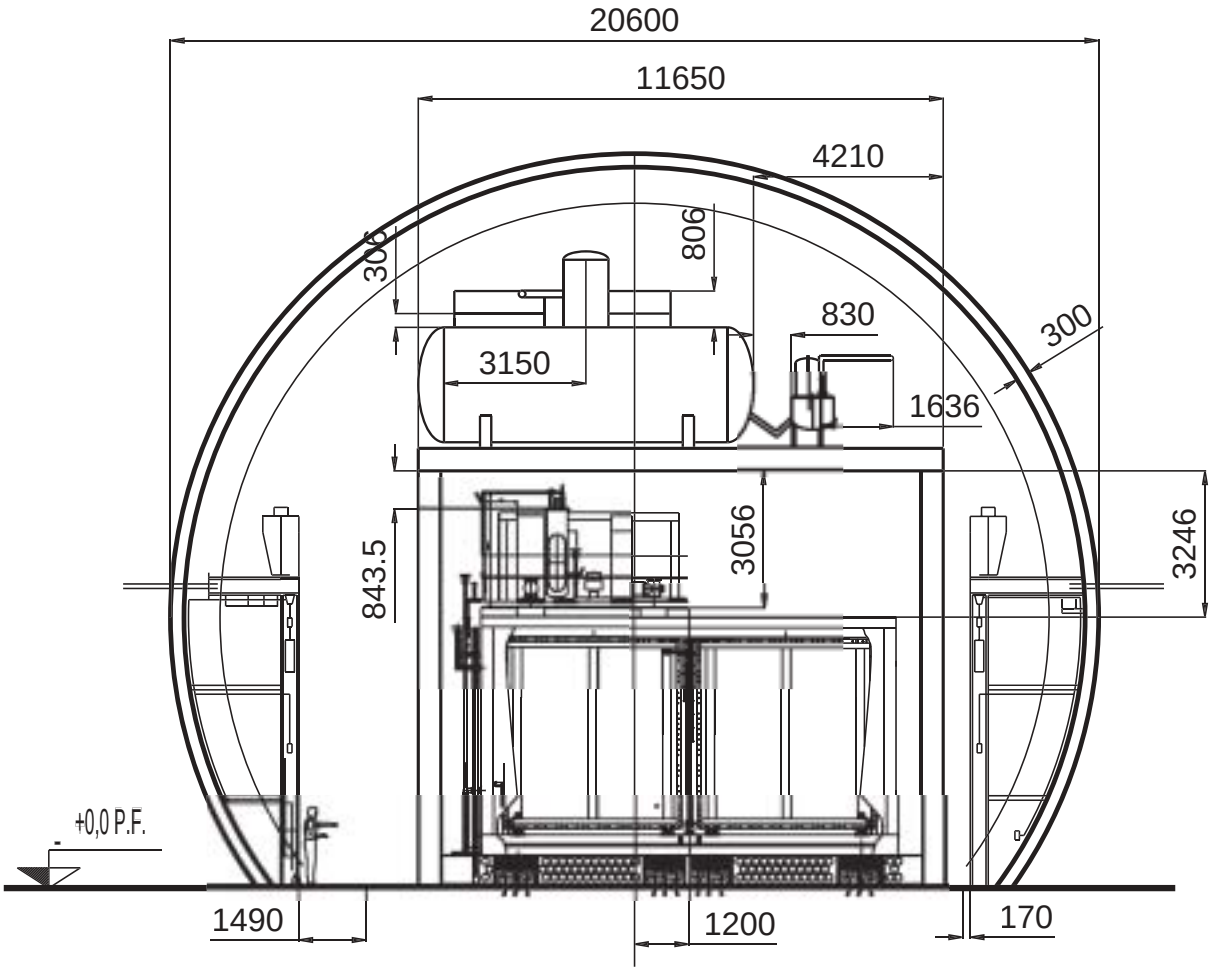

Figure 8.2: Front view of the auxiliary systems installation above the T600, the neutron shield is only sketched on the bottom of the T600, anti-seismic shock absorbers are also visible.

- Installation of the lower part of the cooling shield for the first and the second LAr container;
- First LAr container positioning;
- Assembly of the central vertical beams of the sustaining structure (300 mm stainless teel "I" beam profiles);
- Second LAr container positioning;
- Installation of the cooling shield vertical walls;
- Assembly of the external part (on the external side of the LAr containers) of the sustaining structure (500 mm stainless steel "I" beam profiles with diagonal reinforces in the central region);

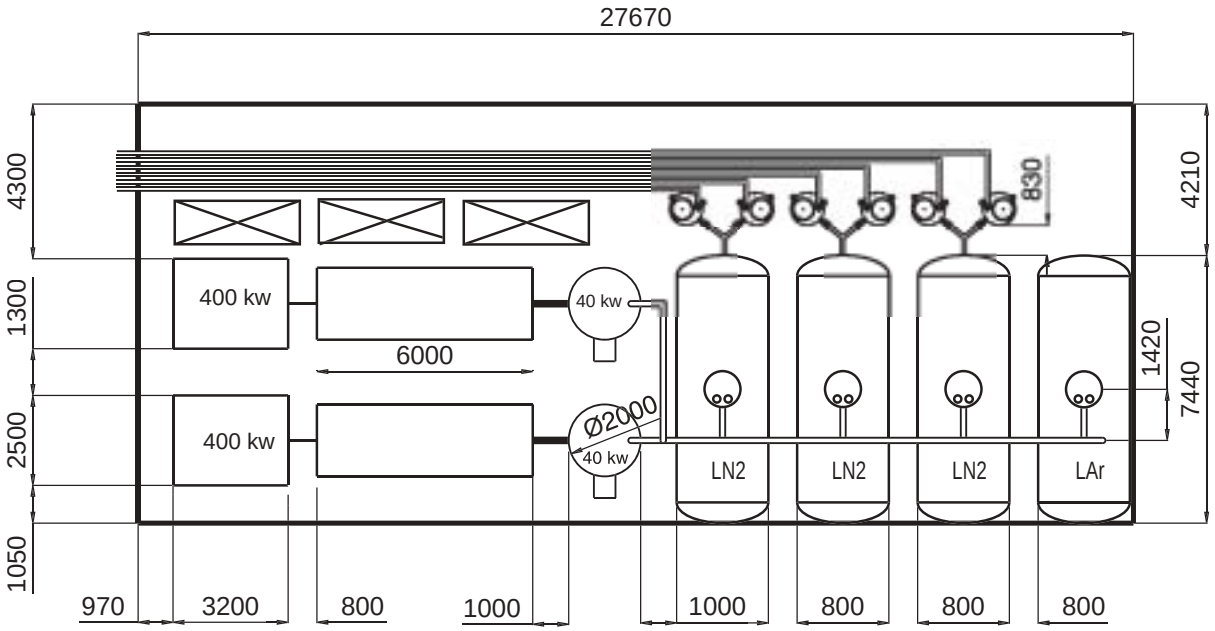

Figure 8.3: Top view of the auxiliary systems installation above the T600.

- Installation of vacuum tight joints with signal and HV feedthroughs for the connection of the readout electronics for the lower two LAr containers (completion of the internal detector cabling);
- Installation of transfer line segments for LAr filling and recirculation;
- Pressurization test (1.4 bar abs) of the lower two containers (rough tightness test);
- Completion of the cooling shield installation (top) for the lower two LAr containers;
- Cooling shield pressurization test (7 bar abs);
- Assembly of the platform for the upper two LAr containers (500 mm St. Steel "I" beam profiles).

Installation of the two upper LAr containers proceeds with an identical sequence as the one used for the lower two containers (see Figure 8.8).

At this point stainless steel plates will be welded all around the vertical part of the sustaining structure. These plates act as a reinforce of the structure to cope with transversal accelerations occurring in case of an earthquake and also form a retaining tank able to contain the LAr in case of a major failure of one of the LAr containers. In correspondence to the joints for the wire chambers readout and the LN_2 and LAr transfer lines, flexible joints will be installed in order to allow for differential thermal contraction of the aluminium containers and the stainless steel supporting structure.

The thermal insulation vertical and top layers will be finally installed (see Figure 8.9). Lateral walls will be built of 4 evacuated honeycomb panels with approximate dimensions $10 \times 5 \times 0.45$ m^3. Front and backward insulation walls are made out of two panels also of about $0.45 \times 5 \times 10$ m^3. Special angular profile evacuated panels will be used on the

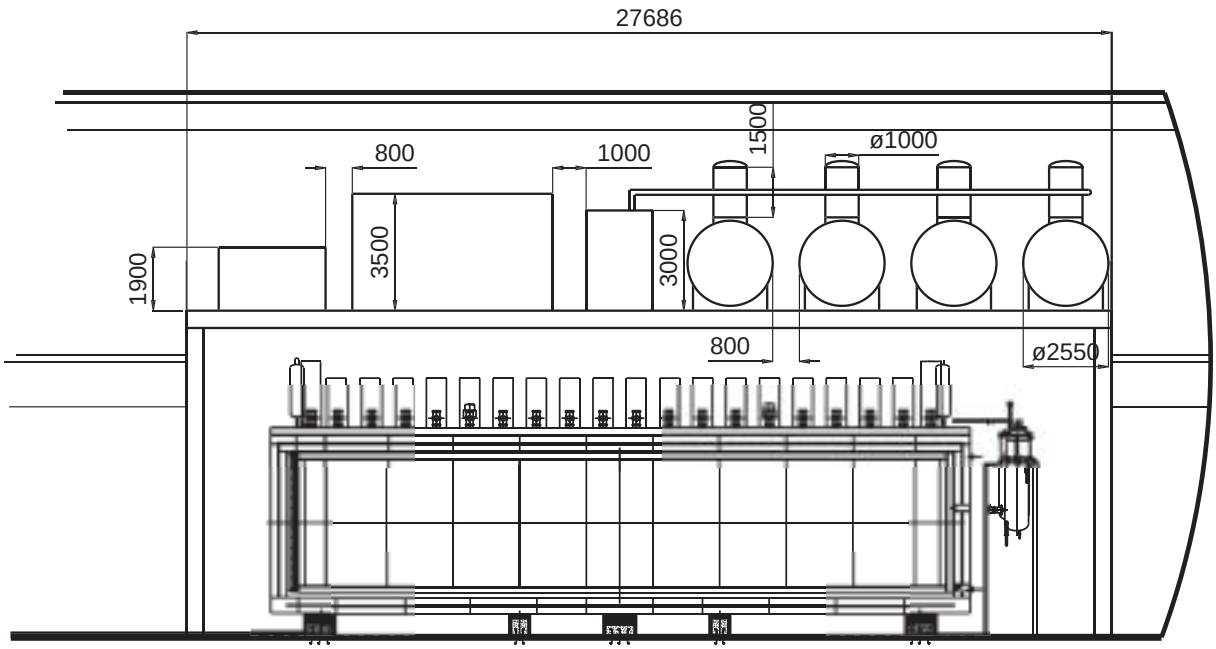

Figure 8.4: Side view of the auxiliary systems installation above the T600.

vertical corners to facilitate the connection between the lateral and front and backward walls. The top layer will be made of 4 evacuated honeycomb panels with approximate dimensions $5.5 \times 0.45 \times 10$ m^3.

T1200 assembly will be completed by installing (see Figure 8.10):

- External transfer lines and regulating valves for LN_2 distribution and connection to the auxiliary plants installed on top of the T600 module;
- Electronics and external devices sustaining carpentry;
- Main purifiers and liquid argon recirculation units (4 units installed on the backward side the supermodule);
- Vacuum system (4 units);
- Gas argon recirculation units (8);
- Readout electronics;
- HV power supplies;
- Readout electronics for auxiliary instrumentation.

Assembly of the additional T1200 modules (up to 2) can proceed in similar way. The assembly process makes use of the available space in Hall B (about 10 m) are needed in front of each supermodule for temporary storage of the various apparatus elements. A second crane (min. load 15 ton) has to be installed in order to move and position the LAr containers and the insulation panels.

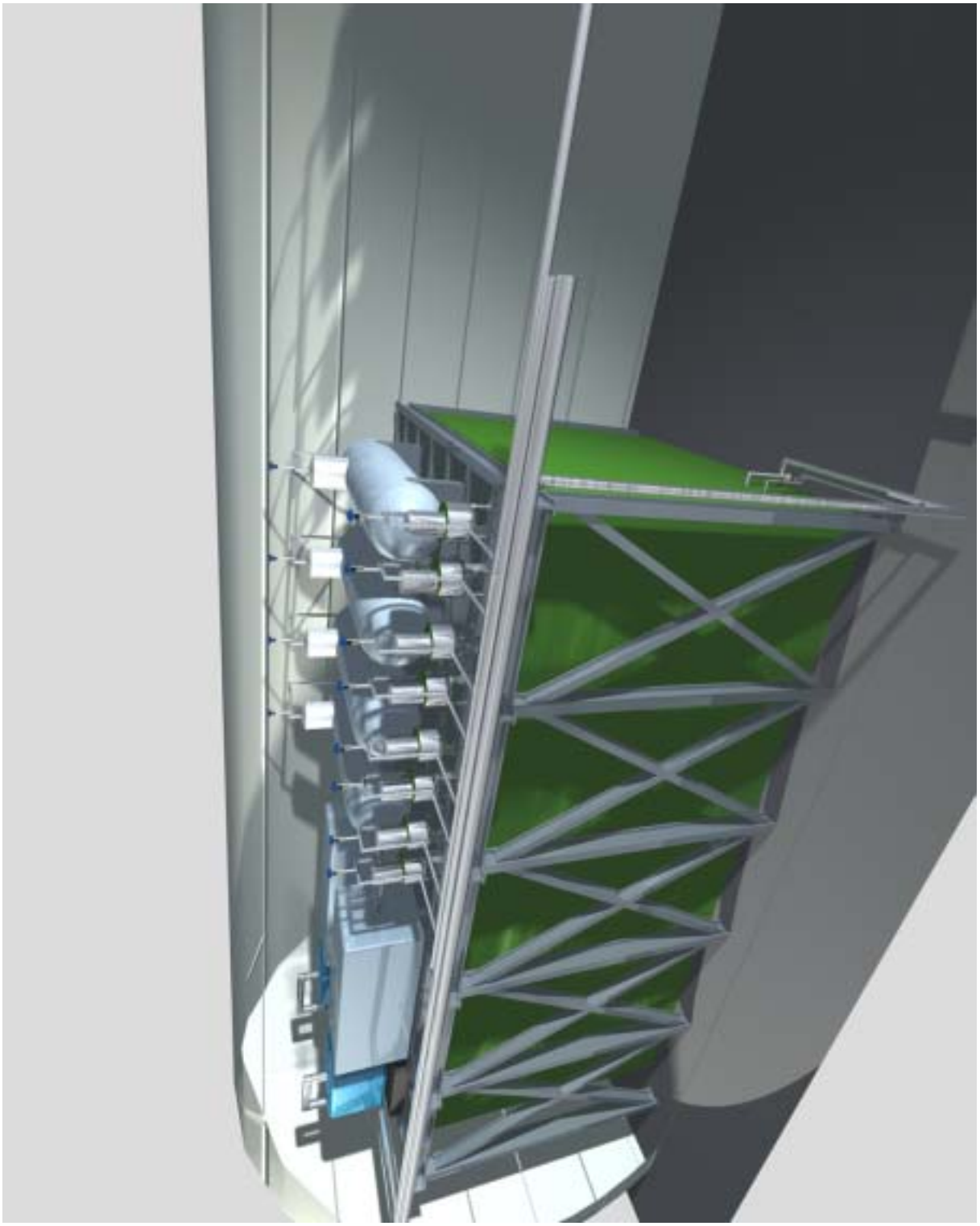

Figure 8.5: T600 and auxiliary plants assembly in Hall B.

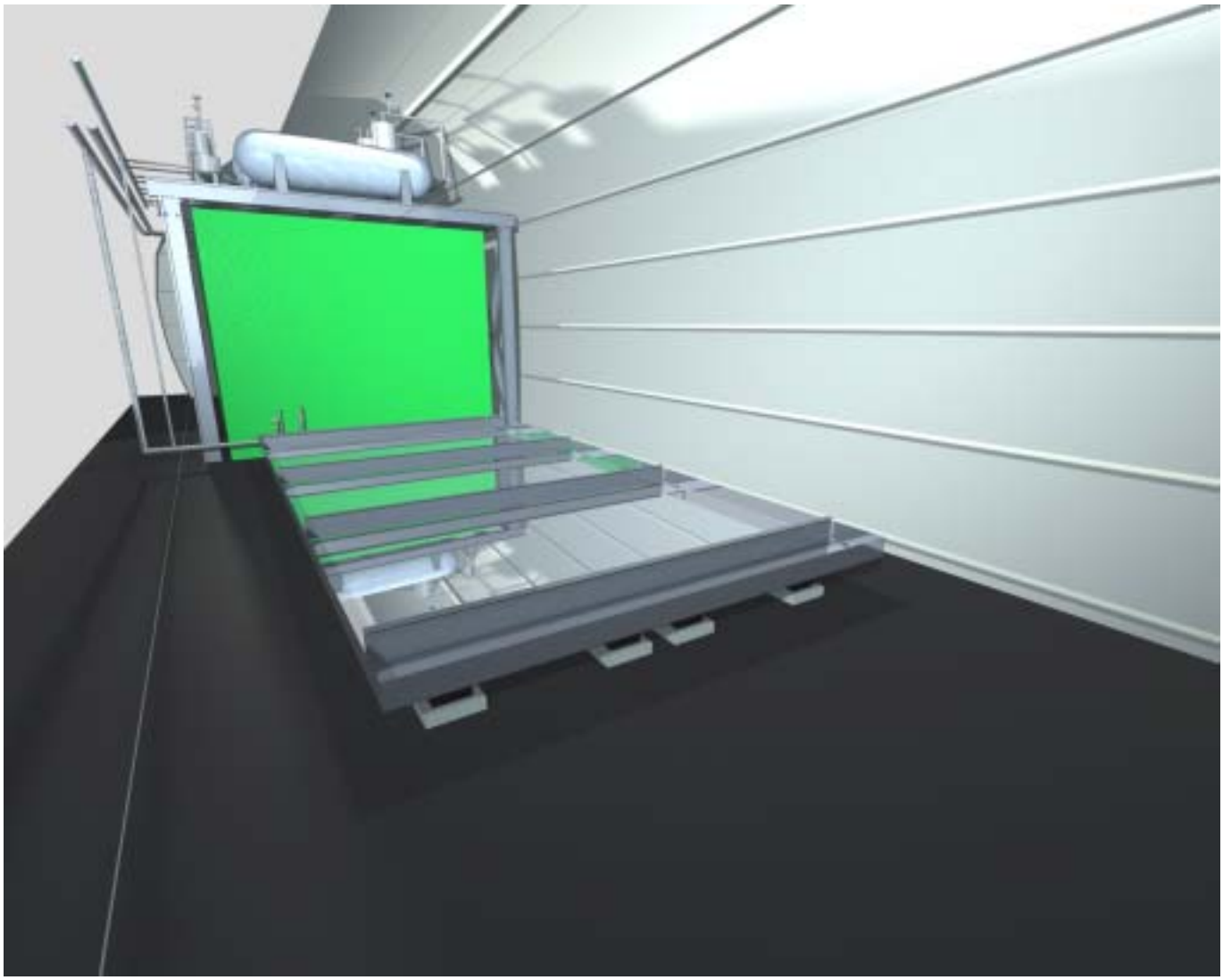

Figure 8.6: T1200 installation: insulation bottom layer and lower part of the LAr containers sustaining structure.

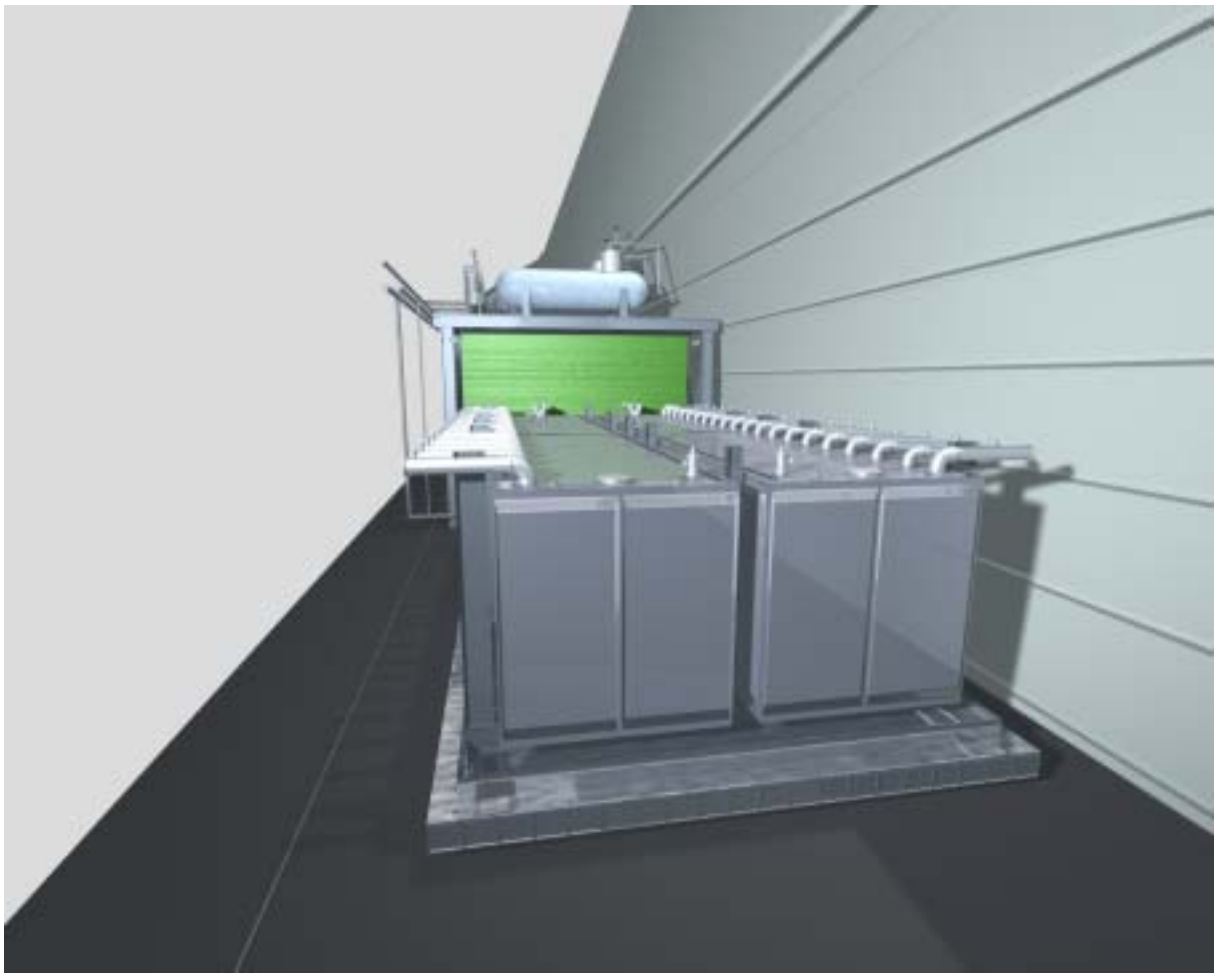

Figure 8.7: T1200 installation: lower two LAr containers.

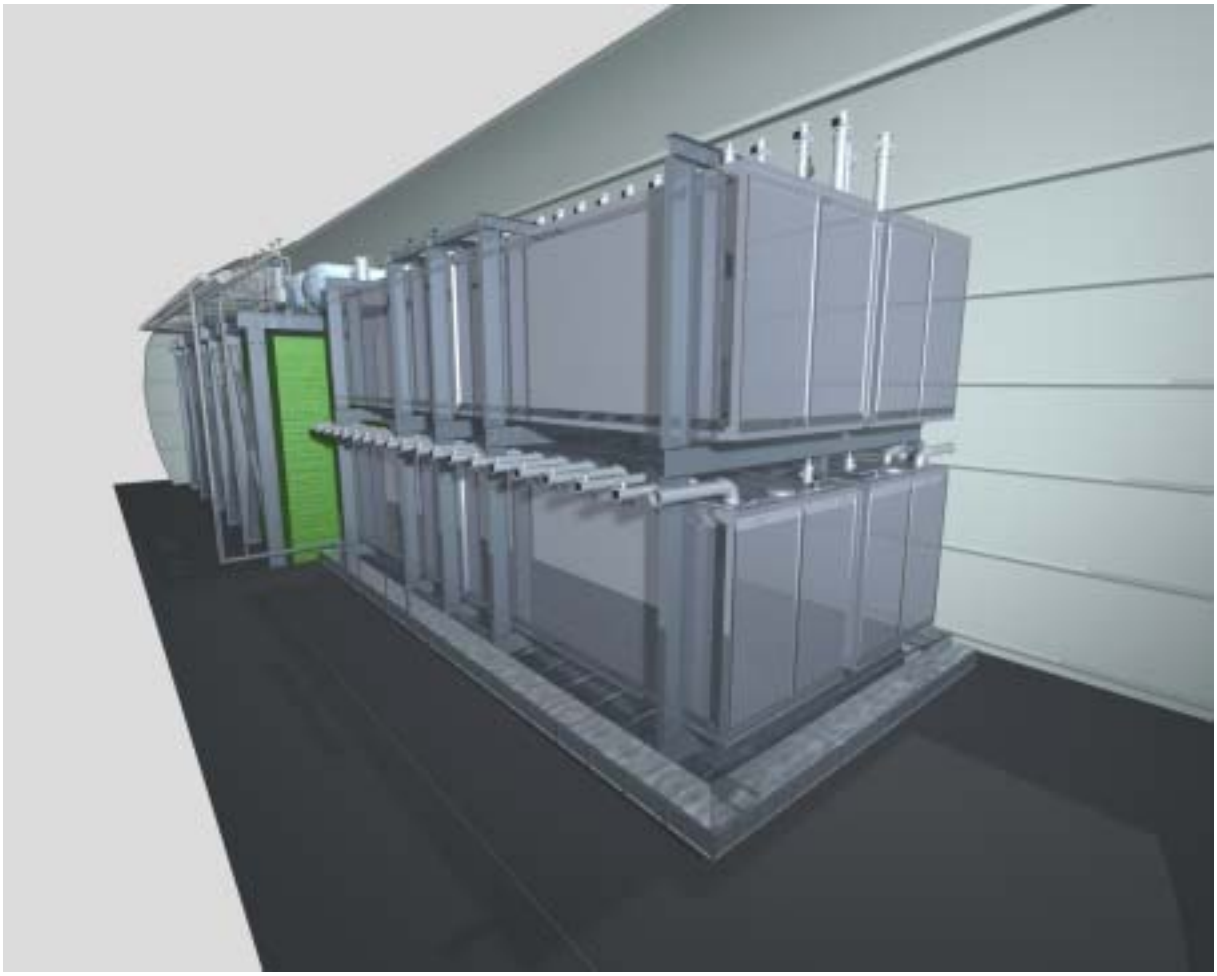

Figure 8.8: T1200 installation: upper two LAr containers

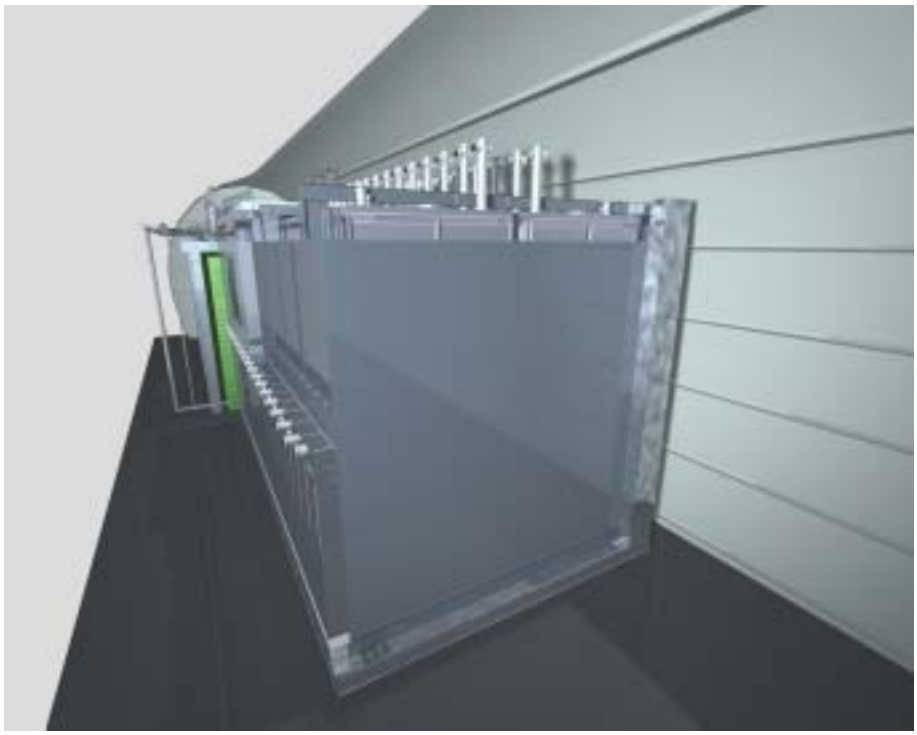

Figure 8.9: T1200 installation: assembly of the retaining tank and of the thermal insulation.

Figure 8.10: First T1200.

Bibliography

[1] C. Rubbia, "The Liquid-argon time projection chamber: a new concept for Neutrino Detector", CERN-EP/77-08 (1977)

[2] E. Aprile, K.L. Giboni and C. Rubbia, "A study of ionisation electrons drifting large distances in liquid and solid argon", Nucl. Instr. and Meth. A241, (1985), 62.

[3] ICARUS Collab., "ICARUS-I: a proposal for the Gran Sasso Laboratory", INFN/AE-85/7, Frascati (Italy, 1985).

[4] E. Buckley et al., "A study of ionization electrons drifting large distances in liquid argon", Nucl. Instr. and Meth. A275, (1989), 364.

[5] G. Carugno, B. Dainese, F. Pietropaolo and F. Ptohos, "Electron Lifetime Detector for Liquid Argon", Nucl. Instr. and Meth. A292, (1990), 580.

[6] ICARUS Collaboration, "A Study of The Factors Affecting The Electron Life Time in Ultra-Pure Liquid Argon", Nucl. Instr. and Meth. A305, (1991), 177.

[7] ICARUS Collaboration, "The ICARUS liquid argon TPC: a complete imaging device for particle physics", Nucl. Instr. and Meth. A 315, (1992), 223.

[8] ICARUS Collaboration, "The ICARUS R&D program and results" , Nucl. Instr. and Meth. A 327, (1993), 173.

[9] ICARUS Collaboration, "Argon purification in the liquid phase", Nucl. Instr. and Meth. A 333, (1993), 567.

[10] ICARUS Collaboration, "Performance of a three-ton liquid argon time projection chamber", Nucl. Instr. and Meth. A 345, (1994), 230.

[11] ICARUS Collaboration, "A 3-D image chamber for the liquid argon TPC based on multi-layer printed circuit board" , Nucl. Instr. and Meth. A 346, (1994), 550.

[12] ICARUS Collab., "ICARUS-II. A Second-Generation Proton Decay Experiment and Neutrino Observatory at the Gran Sasso Laboratory", Proposal Vol. I (1993) & II (1994), LNGS-94/99.

[13] Program presented to Commissione II and to LNGS Scientific Committee between 1996 and 1997. Approved by LNGS Scientific Committee and approved and founded by Commissione II. The technical report is described in: "CRIOSTATO DA 600

T: STUDIO DI INGENERIA DI BASE". Presented to LNGS management and to Commissione II in July 1997.

[14] ICARUS Collab., "A first 600 ton ICARUS detector installed at the Gran Sasso Laboratory", Addendum to Proposal, LNGS - 95/10, (1995).

[15] ICARUS Collaboration, "A study of the Electron Image due to ionizing events in a two-dimensional liquid argon TPC with a 24 cm drift gap", Nucl. Instr. and Meth. A286, (1990), 135.

[16] ICARUS Collaboration, "A three-ton liquid argon time projection chamber", Nucl. Instr. and Meth. A 332, (1993), 395.

[17] ICARUS Collaboration, "Detection of scintillation light in coincidence with ionizing tracks in a LAr TPC", Nucl. Instr. and Meth. A 432, (1999), 240.

[18] F. Arneodo *et al.* [ICARUS and NOE Collab.], "ICANOE: Imaging and calorimetric neutrino oscillation experiment," LNGS-P21/99, INFN/AE-99-17, CERN/SPSC 99-25, SPSC/P314; see also A. Rubbia [ICARUS collaboration], hep-ex/0001052.

[19] F. Arneodo *et al.* [ICARUS collaboration], "The ICARUS experiment, a second-generation proton decay experiment and neutrino observatory at the Gran Sasso laboratory," LNGS P28/01, LNGS-EXP 13/89 add.1/01 and arXiv:hep-ex/0103008.

[20] E. Gatti et al., IEEE Trans. Nucl. Sci. NS-26 (1970) 2910.

[21] E. Bonetti et al., Nucl. Instr. and Meth. A286 (1990) 135.

[22] P. Benetti et al., Nucl. Instr. and Meth. A332 (1993) 395. P. Benetti et al., Nucl. Instr. and Meth. A333 (1993) 567. P. Benetti et al., Nucl. Instr. and Meth. A346 (1994) 550.

[23] P. Benetti et al., Nucl. Instr. and Meth. A345 (1994) 230.

[24] S. Ragazzi *et al.*, *'Request for a test of liquid argon TPC on the neutrino beam'*, SPSLC/M 594, 1997.

[25] ICARUS Collab., *'ICARUS-II. A Second-Generation Proton Decay Experiment and Neutrino Observatory at the Gran Sasso Laboratory'*, Proposal Vol. I & II, LNGS-94/99, 1994.

[26] ICARUS Collab., *'A First 600 ton ICARUS Detector Installed at the Gran Sasso Laboratory'*, Addendum to proposal, LNGS-95/10, 1995.

[27] P. Cennini *et al.*, *Nucl. Instrum. Methods* A **345**, 230 (1994).

[28] P. Cennini *et al.*, *Nucl. Instrum. Methods* A **333**, 567 (1993).

[29] P. Cennini *et al.*, *Nucl. Instrum. Methods* A **355**, 660 (1995).

[30] P. Cennini *et al.*, ICARUS-TM-97/24, 1997.

[31] ICARUS Collaboration, "Short report on performance evaluation of the ICARUS $10m^3$ prototype", ICARUS-TM-99/09.

[32] ICARUS Collaboration, "Operation of a $10m^3$ ICARUS Detector Module", Proceed. of the Frontiers Detectors for Frontier Physics Conference I.la d'Elba (Italy, May 2000), Nucl. Instr. & Meth. A461 1-3 (2001) 286,
ICARUS Collaboration, "The ICARUS Liquid Argon Time Projection Chamber", Proceed. of the Imaging 2000 Conference Stockholm (Sweden, July 2000), Nucl. Instr. & Meth. A471 (2001) 272.

[33] P.Arcaro et al., "DAEDALUS: a proposal for a VLSI implementation of a feature extractor for Icarus signals" ICARUS-TM-96/02 (1996).

[34] C.Carpanese et al., "DAEDALUS: a feature extractor for ICARUS signals" ICARUS-TM-97/06 (1997).

[35] C.Carpanese et al., "DAEDALUS: a feature extractor for ICARUS signals" ICARUS-TM-98/08 (1998).

[36] K.S. Hirata *et al.* [KAMIOKANDE-II Collaboration], Phys. Lett. **205B**, 416 (1988).

[37] Y. Totsuka to appear in the Proceedings of TAUP2001, 8-12 Sep 2001, Assergi (Italy).

[38] W.W. Allison *et al.* [Soudan-2 Collaboration], Phys. Lett. **B449**, 137 (1999) hep-ex/9901024.

[39] F. Ronga *et al.* [MACRO Collaboration], "Neutrino oscillations at high energy by MACRO", hep-ex/9905025.
The MACRO Coll. (M. Ambrosio et al.), Phys. Lett. **B478**, 5 (2000).

[40] K. Nakamura (for SuperK Collaboration), NUFACT00, Monterey, USA, May 2000.

[41] M. Apollonio *et al.* [CHOOZ Collaboration], Phys. Lett. **B420**, 397 (1998), hep-ex/9711002.

[42] M. Apollonio et al., Phys. Lett. **B466**, 415 (1999), hep-ex/9907037.

[43] A. Ferrari, I. Gil-Botella, A. Rubbia, "ICARUS T600 Geometry Simulation", ICARUS TM-2001/05.

[44] A. Rubbia, NUX code, private communication.

[45] F. Arneodo *et al.*, Nucl. Instrum. Meth. **A449** (2000) 42.

[46] A.Bueno, A.Rubbia, "ν_τ appearance search at CNGS for a detector configuration based on the T600 module geometry", ICARUS/TM-2001/07.

[47] F. Cavanna *et al.* [ICANOE Collab.], "Addendum 2: Answers to Questions and Remarks Concerning the ICANOE project", LNGS-P21/99-Add2, CERN/SPSC 99-40, SPSC/P314 Add.2

[48] A. Bueno, A. Ferrari, S. Navas, A. Rubbia and P. Sala, "Nucleon decay searches: study of nuclear effects and backgrounds", ICARUS/TM-2001/04.

[49] C.Caso et al., *"Review of particle physics"*, **Eur. Phys. J. C 15** (2000).

[50] F. Arneodo *et al.*, Nuovo Cim. **A112** (1999) 819.

[51] S. Geer, Phys. Rev. **D 57** (1998) 6989, hep-ph/9712290.

[52] Information on the neutrino factory studies and mu collider collaboration at BNL can be found at *http://www.cap.bnl.gov/mumu/*. Information on the neutrino factory studies at FNAL can be found at *http://www.fnal.gov/projects/muon_collider/*. Information on the neutrino factory studies at CERN can be found at *http://muonstoragerings.cern.ch/Welcome.html/*.

[53] A. de Rújula, M. B. Gavela and P. Hernández, *Nucl. Phys.* B **547**, 1999 (21); V. Barger, S. Geer, R. Raja and K. Whisnant, Phys. Rev. **D 62** (2000) 013004, hep-ph/9911524; Phys. Rev. **D 62** (2000) 073002,hep-ph/0003184; A. Bueno, M. Campanelli and A. Rubbia, Nucl. Phys. **B573** (2000) 27; V. Barger, S. Geer and K. Whisnant, *Phys. Rev.* D **61**, 2000 (053004); M. Freund, M. Lindner, S. T. Petcov and A. Romanimo, Nucl. Phys. **B578** (2000) 27; A. Donini, M. B. Gavela, P. Hernández and S. Rigolin, Nucl. Phys. **B574** (2000) 23; M. Koike and J. Sato, Phys. Rev. **D 61** (2000) 073012; G. Barenboim and R. Scheck, Phys. Lett. **B475** (2000) 95; H. Fritzsch and Z. Xing, Acta Phys. Polon. **B31** (2000) 1349.

[54] A. Bueno, M. Campanelli and A. Rubbia, Nucl. Phys. **B589** (2000) 577.

[55] A. Badertscher, J. Rico and A. Rubbia, "Slow Control Results from the Technical Run in Pavia with the First T600 Half-Module", ICARUS/TM-2001/06.

[56] G.Carugno et al. **NIM A292** (1990) 580-584

[57] F. Arneodo et al. "Electron beam generation from semiconductor photocathodes", Review of Scientific Instruments, 72, 1, 63

[58] D. Cline, S. Otwinowski, F. Sergiampietri, H. Wang and J. Woo, "The High Voltage System for ICARUS-T600", ICARUS/TM-2001/01.

[59] P. Cennini et al., Nucl. Instr. and Meth. A432 (1999) 240.

[60] G.L. Raselli, M. Rossella, C. Vignoli and A. Votano, LAr scintillation light detection in the ICARUS T600 Apparatus, INFN Report FNT/AE-2001/12.

[61] An external trigger system for the ICARUS T600 test, ICARUS-TM/2000-05.

[62] F. Arneodo et al., "ICARUS DAQ back-end hardware proposal", ICARUS/TM-2000/02.

[63] C.Carpanese et al., "ARIANNA: the readout module for ICARUS, prototype version" ICARUS-TM-98/07 (1998).

[64] C.Carpanese et al., "DAEDALUS: a hardware signal analyser for Icarus" Proc. of the 7th Pisa Meeting on Advanced Detectors, La Biodola, Isola d'Elba, Nucl. Instr. and Meth. A 409 (1998).

[65] C.Carpanese et al., "ARIANNA: the ICARUS experiment readout module" IEEE Transactions on Nuclear Science, Vol. 45 no. 4 (1998).